DEPARTMENT OF ELECTRONIC & ELECTRICAL ENGINEERING

University of Strathclyde Engineering

GAS-SOLID INTERFACES STRESSED WITH HV IMPULSES: SURFACE FLASHOVER BEHAVIOUR AND CONTROL

A thesis presented in the fulfilment of the requirement of

The degree of

Doctor of Philosophy

Ruairidh Worthy Macpherson, BEng (Hons), MPhil

2023

Department of Electronic and Electrical Engineering

University of Strathclyde

Glasgow, UK

DECLARATION OF AUTHENTICITY AND AUTHORS RIGHTS

‘This thesis is the result of the author’s original research. It has been composed by the author and has not been previously submitted for examination which has led to the award of a degree.’

Signed:

Date:

ACKNOWLEDGEMENTS

I would firstly like to thank Dr Mark Wilson and Dr Igor Timoshkin for providing me with excellent support when completing my PhD by continually offering fantastic advice throughout the duration of the project/degree. I would also like to express my thanks to Dr Martin Given and Dr Michelle Maclean for providing me with invaluable support. Additionally, I would like to thank Professor Scott MacGregor for also giving me the opportunity to do an MPhil with the HVT department prior to my PhD study.

Thanks must also be extended to Andy Carlin, Sean Doak and Louis Cooper of the mechanical workshop within the High Voltage Technologies Department for their excellent work in preparing test cells and machining solid dielectric samples for use within my experiments, and to Maureen Cooper for her administrative assistance over the course of the study.

I would finally like to thank my fiancé, Sarah, for putting up with me during this process, and providing me with continued encouragement and much needed moral support. I would also like to thank my Mum, Dad, and Sister for all their support throughout all of my degrees, could not have done this without you all! Finally, A special acknowledgment goes to my Gran, Susan Currie Maxwell, who has consistently been a source of encouragement and belief in me.

ABSTRACT

In pulsed power engineering, solid spacers are used to insulate high voltage parts from extraneous metal parts, providing electrical insulation as well as mechanical support. The breakdown/flashover voltage, at which a discharge process initiates across the gas-solid interface, is important in the design process, as it informs designers of specific threshold 'failure' voltages of the insulation system. In this thesis, a method to potentially increase the failure voltage, tested under multiple environmental conditions, without increasing the length of the solid spacer, was investigated. Three dielectric materials: High-Density Polyethylene (HDPE), Polyetherimide (Ultem) and Polyoxymethylene (Delrin), were tested under 100/700 ns impulse voltages. Cylindrical spacers made of these materials were located in the centre of a plane-parallel electrode arrangement in air, which provided a quasi-uniform field distribution. Breakdown and flashover tests were performed in a sealed container at air pressures of −0.5, 0 and 0.5 bar gauge, with varying relative humidity (RH) level of <10%, ~50% and >90%. The materials were tested under both, negative and positive, polarity impulses. Additionally, the surfaces of a set of solid spacers were subjected to a 'knurled' finish, where ~0.5 mm indentations are added to the surface of the materials, prior to testing, to allow comparison with the breakdown voltages for samples with 'smooth' (machined) surface finishes.

The results show that the flashover voltage is controlled by the physical insulation system and environmental parameters, where the multiple test conditions yielded results where the V_{50} breakdown voltage for samples with a smooth surface finish was higher than for knurled, by up to ~55 kV; where there were similar V_{50} breakdown voltages for each type of surface finish; and where the knurled spacer resulted in a higher (by up to ~66 kV) hold-off voltage than the corresponding smooth spacer. Each of these results is discussed herein, particularly in terms of the location of the discharge channel at breakdown, where changing the physical and environmental test parameters was shown to affect the discharge path, and therefore the flashover voltage of the insulation system. The results and discussion will inform designers and operators of outdoor pulsed power systems on the design of air-solid insulation systems, and the control of the flashover characteristics, under varying environmental conditions.

TABLE OF CONTENTS

1. CHAPTER I

INTRODUCTION

This thesis focuses on the measurements obtained with a system developed that allows the behaviour of surface flashover to be investigated to allow the control of a gas-solid interface under the influence of high-voltage (HV) impulses. This introduction will include the motivation, aims and objectives, novelty of the research and thesis structure. This research endeavors to contribute to the field of pulsed power engineering by enhancing our comprehension of the intricate phenomena associated with surface flashover and by devising efficacious methods to regulate it. The primary objective of this work is to establish a foundation that allows for the optimisation of system design and the implementation of appropriate control measures to mitigate the detrimental effects of surface flashover.

1.1. MOTIVATION

Solid insulation is imperative within pulsed power systems as it provides mechanical support between conductors at different potential, but the inclusion of insulation can lead to surface flashover/breakdown of the gas-solid interface created, which can occur at a lower applied voltage than that for a gas gap without a solid spacer. Therefore, it is desirable to have information on the flashover strength of different materials within a system, for design processes to be tailored to the intended application. The influence of the surrounding environment on these insulation systems will have a large effect on the performance of the overall system. As pressure fluctuations around atmospheric pressure and humidity extremes are common in outdoor insulation systems (where the insulative parts are subject to varying environmental conditions), research is required to ultimately characterise the performance of insulation systems under a range of different environmental conditions. For outdoor pulsed power systems, the goal of creating a more compact unit has been an ongoing challenge for many years [1 – 3]. A way in which a system can be miniaturised is to understand the hold-off voltage that the system insulation can withstand between high voltage conductors and extraneous metal parts. This

information will enable designers to make informed choices in their pulsed power insulation system design, to avoid unwanted flashover.

Overall, the flashover process involving solid spacers in air is well documented, including different energisation regimes, wave-shapes, and insulation system designs, meaning that reliable material-selection criteria is readily available [4 – 7] However, less information is available on the flashover process under pulsed power conditions, particularly regarding exposed insulation systems within rapidly-changing environments, where the use of an enclosed insulation system is not required. This is of particular importance to outdoor pulsed power systems, which are prevalent in multiple sectors such as agriculture [8], food processing [9], the defence industry [10] and the automotive industry [11].

Within this thesis, solid spacers were tested in sub-optimal conditions, and the breakdown parameters recorded throughout. Three materials, High-Density Polyethylene (HDPE)), Polyetherimide (Ultem) and Polyoxymethylene (Delrin) with smooth (machined) and knurled surface finishes, were subjected to positive and negative polarity 100/700 ns impulse voltages in air, with conditions of varying humidity, and pressure. The results allow direct comparison of material performance for each set of environmental conditions. The electrode system is immersed in air, to simulate an outdoor pulsed power insulation system, which is to be subjected to a range of atmospheric conditions.

The information in this thesis can be used to underpin the design of element-open insulation systems of reduced complexity, as compared with heavier gas insulated insulation systems which require pressure vessels, as well as enabling lighter, more compact sub-systems as part of the larger system. Additionally, the use of air as external insulation is desirable as it is a cheap, clean alternative to other common insulating gases such as SF_6 that are damaging to the environment. The characterisation of environmentally-friendly gases is a prevalent area of high-voltage engineering, where many researchers are working on suitable dielectric gases for their intended applications [12–16]. The more fundamental knowledge available on air-insulated pulsed power systems, particularly operating under sub-optimal outdoor conditions, the more information will be available to engineers to design high-voltage equipment free of environmentally damaging gases, removing the requirement for

sealed and monitored systems to prevent the venting of harmful gases to the atmosphere.

Surface flashover of gas-solid interfaces during operation can result in catastrophic failure of a system, resulting in downtime for the repair and replacement of damaged solid insulation, or at least in the reduction or loss of energy delivered to the load and the loss of output data. Therefore, insulation system design should incorporate a safety margin, to ensure that the hold-off voltage is significantly higher than the flashover voltage.

This study builds upon previously published literature on the subject of insulation design [17-26], where similar work was completed on the effects of humidity, pressure, polarity, material type and surface finish on the flashover voltage. However, the characterisation of air-solid insulation systems under sub-μs fast *dV*/*dt* impulsive conditions is not well documented. Also, a lack of published information on the synergistic effect of the different environmental and physical parameters is also evident for pulsed power insulation systems. Therefore, an air-solid pulsed power insulation system was subject to a series of tests under different conditions driven by a fast *dV*/*dt* supply, with the breakdown/flashover voltages measured. The results will provide designers with information on the breakdown mechanisms of novel insulation systems, to inform the design of industrial, air-insulated pulsed power components and systems, used in situations of rapidly changing environments.

Insulation systems come in many different topologies, with the spacer ultimately separating two conductors of different electric potential. Therefore, the shape of these spacers is an important factor in the design of the insulation system, as this will alter the electric field distribution and, therefore, will greatly alter the breakdown strength of the insulation system. The work in this thesis will focus on a parallel-plane arrangement, with a cylindrical spacer positioned at the centre of the electrodes. This basic design will facilitate analysis of the effect of the impulse polarity, material, surface finish and environmental conditions on the discharge path at breakdown. The parallel-plane arrangement used is representative of the electrode arrangement that would be used in a practical system, rather than resorting to the use of a point high-

voltage electrode to control the location of the discharge as shown in literature [27 – 29].

The insulator surface finish is also an important factor in insulation systems, with studies where the potential increase in flashover voltage afforded by the addition of surface roughness and the use of different insulator shapes, [30 – 33]. Therefore, in addition to testing solid spacers with a smooth (machined) surface finish, spacers with a novel 'knurled' surface finish were also tested for comparison. The knurling process was selected to provide a quick, cheap method of adding consistent indentations to the spacer surfaces, as a way of potentially increasing the flashover voltage of the system by surface profile alone, without increasing the length of the spacer.

In order to examine the effect environmental parameters have on the insulation systems, three different humidity levels were subject to the air dielectric throughout the testing process: <10% relative humidity (RH), ~50% RH and >90% RH, in order to cover the full humidity spectrum, particularly to characterise the effect increase pressure on breakdown/flashover characteristics as well as the presence of water droplets in high-humidity environments [34 – 36]. The effect on the breakdown voltage and flashover voltage of the various insulation systems was characterised, with particular focus on changes in discharge location with increasing humidity. The polarity effect witnessed in the early investigation of open gaps, where asymmetrical electrical characteristics manifest in symmetrical electrode gaps when one electrode is grounded, as witnessed in other previously literature for varying electrode topologies, [37 – 43], prompted investigation into breakdown of all tested insulation systems under both polarities. Pressures of −0.5 bar gauge, 0 bar gauge and 0.5 bar gauge were tested, so as to understand the effect on breakdown and flashover voltage at pressures above and below atmospheric pressure.

1.2. AIMS AND OBJECTIVES

Building on the discussion in Section 1.1, more specifically, the main objectives of the study were to:

- Develop an experimental rig, incorporating a custom-design test cell, to be used with a high voltage impulse generator and diagnostic equipment to characterise the flashover behaviour of air-solid insulation systems under varying environmental parameters (air pressure of -0.5 bar gauge, 0 bar gauge and 0.5 bar gauge; and <10% RH, ~50% RH and >90% RH environments).
- Design air-solid insulation systems to consist of solid spacers bridging plane-parallel electrodes.
- Integrate into the system design controllability of the pressure and humidity parameters with a comprehensive diagnostic system to control each parameter.
- Characterise insulation system for multiple environmental parameters with an open gap, in order to establish reference breakdown voltage data to compare with the flashover of gas-solid insulation systems.
- Characterise the gas-solid insulation systems with spacers with smooth (machined) surfaces, as well as those with spacers subjected to a novel surface modification method, in order to understand the difference in flashover voltage in changing environmental conditions.
- Analyse the results spanning a wide range of experimental parameters, to explain the differences in the flashover voltages of each insulation system in relation to changing physical and environmental parameters, based upon physical discharge mechanisms.
- Apply relevant statistical analyses to provide system designers with information on the probabilities associated with these flashover voltages, and to use this information to predict the flashover performance under difference conditions.

1.3. NOVELTY

The thesis presents a number of novel contributions, which include experimental investigations focused on the physical attributes of the system, the environmental parameters that influence its behaviour, and the synergistic effects that arise from the interaction between each parameter. The experimental work conducted as part of the thesis is designed to elucidate the behaviour of the system under different conditions,

providing insights that are not currently available in the literature. These insights are used to develop new test parameters that describes the behaviour of the system to aid existing work. In addition to the experimental work, the thesis also includes a detailed statistical analysis of the data gathered during the experiments. This analysis provides a rigorous and quantitative approach to characterising the behaviour of the system.

The original contributions of the thesis are as follows:

- Characterised the effect of sub-µs impulses on the flashover voltage of a parallel-plane insulation system in varying environmental conditions.
- Comparison on High Density Polyethylene (HDPE), Polyoxymethylene (Delrin) and Polyetherimide (Ultem) flashover performance in pulsed power conditions
- Using ‘knurling’ as a surface modification technique in order to increase the flashover voltages of insulation systems.
- Determined the influence of material hydrophobicity and hydrophilicity on the flashover of materials in sub-µs pulsed power conditions.
- Explanation into the influence of physical and environmental parameters on the discharge location in an air-insulated parallel-plane pulsed power insulation system
- Execution of a detailed Weibull statistical analysis of the flashover data, where the skewed probability density function and cumulative density function have been used to define asymmetrical error bars on the flashover data.

1.4. THESIS STRUCTURE

The subsequent chapters presented within this thesis are summarised as follows:

Chapter I (Introduction):

This chapter presents an introduction to the motivation, aims, objectives and novelty of the research. The thesis focuses on the development of a system that aids in describing the behaviour of surface flashover and the control of a gas-solid interface under the influence of high-voltage (HV) impulses. This research endeavors to contribute to the field of pulsed power engineering by enhancing comprehension of

the intricate phenomena associated with surface flashover and by devising efficacious methods to regulate it. The primary objective of this work is to establish a foundation that allows for the optimisation of system design and the implementation of appropriate control measures to mitigate the detrimental effects of surface flashover.

Chapter II (Background and Literature Review): presents background information on pulsed power, gaseous insulation systems, solid insulation systems and gas-solid interface theory, with particular focus on the effect on the breakdown/flashover mechanisms with changing environmental parameters. Recent literature on the subject is also discussed, with particular focus on flashover under varying environmental conditions, outlining the novelty of this work as a contribution to the design of pulsed power insulation systems.

Chapter III (Systems and Methodology): presents information on the experimental apparatus used throughout the study. This includes high-voltage generation circuitry, gas and solid sample information, and gas control for both high-voltage generation and test-cell pressure control. Information on the humidity system and measurement circuitry, and on diagnostics, is also introduced. Supporting the subsequent presentation and discussion of experimental results, relevant information on statistical analysis and data representation is provided.

Chapter IV (No Spacer (Open Gap) Breakdown): the breakdown characteristics of an open-air gap, with no insulating spacer between the electrodes, are detailed, to provide baseline reference information for comparison to the breakdown characteristics of air-solid insulation systems that follow in Chapters V and VI . The breakdown data were generated using a step-up testing procedure, with the V_{50} breakdown voltage of the gas gap found for positive and negative polarity at the three different pressures, and three different humidity levels. This chapter also focuses on the asymmetrical electrical behaviour of the geometrically-symmetrical electrode arrangement observed under certain conditions, which is key to describing the mechanisms governing the breakdown process for both polarities, including when comparing the behaviour to that of the air-solid insulations systems characterised in Chapters V and VI.

Chapter V (Smooth Machined Surface Dielectric Flashover): the breakdown/flashover characteristics of air-solid insulation systems, with smooth (machined) insulating spacers made of HDPE, Polyetherimide and Polyoxymethylene bridging the electrodes, are presented. The flashover voltages recorded are directly compared to those found for the open air-gap tests reported in Chapter IV. Also included is discussion of the mechanisms governing the flashover/breakdown process under the different sets of environmental conditions, where comparisons to the open gap insulation systems are made. Conclusions on the best-performing spacer (material and surface finish) for the different sets of test conditions are drawn.

Chapter VI (Knurled Surface Dielectric Flashover): the breakdown/flashover characteristics of air-solid insulation systems, with spacers made of HDPE, Polyetherimide and Polyoxymethylene with a knurled surface finish bridging the electrodes, are presented. These tests were conducted with the aim of increasing the flashover voltage compared with that measured for spacers with a smooth (machined) surface finish. Therefore, in this chapter, the breakdown characteristics resulting from the incorporation of spacers with knurled surfaces into the electrode system are directly compared to those with smooth (machined) surfaces, as well as to the baseline open gap breakdown characteristics. Discussion on the mechanisms that govern the flashover voltage with the inclusion of surface-modified insulating spacers is also introduced, with a particular focus on the effect that the inclusion of indentations has on the effect of plasma channel location, as well as accumulation of water droplets in humid environments and on the electric field, and how this affects the discharge location. From this discussion, an overall picture of the optimal arrangements for the insulation system under different conditions is presented.

Also incorporated into Chapters IV, V and VI are 2-paramter Weibull statistical analyses of the data presented in each chapter. The 2-parameter Weibull analysis was used to plot the V_{50} corresponding to the median of the Weibull distribution for all test arrangements. The Kolmogorov-Smirnov test is first conducted, to give information on the goodness-of-fit from various distributions, with the outcome that the 2-parameter Weibull distribution, a prevalent method of statistical analysis in high-voltage engineering [44 - 46], was selected. The corresponding probability of breakdown for each dataset, particularly the 63.2% probability of the dataset, α, the

slope of the distribution, β, to understand the effect of increasing applied voltage on the breakdown characteristics, and the 0.01% probability of failure (1 breakdown in 10,000 tests) is calculated from the cumulative distribution function.

Chapter VII (Conclusions and Further Work): a summary of all work completed within the thesis is presented, highlighting the aims and objectives and novelty stated with the introduction of this these, and the major outcomes from the study. This includes conclusions drawn and recommendations on the optimal insulation system design for different sets of environmental conditions. Recommended further work is then detailed, including investigation of the effect of different parameters such as wind speed and air quality, which will provide supplementary data supporting the design of outdoor pulsed power systems.

1.5. CHAPTER I REFERENCES

[1] W. Jiang *et al.*, "Compact pulsed power and its industrial applications," *2009 IEEE Pulsed Power Conference*, 2009, pp. 1-10, doi: 10.1109/PPC.2009.5386209.

[2] J. A. Gaudet *et al.*, "Research issues in developing compact pulsed power for high peak power applications on mobile platforms," in *Proceedings of the IEEE*, vol. 92, no. 7, pp. 1144-1165, July 2004, doi: 10.1109/JPROC.2004.829006

[3] P. Deb *et al.*, "Design and development of compact pulsed power driver for electron beam experiments," *2014 International Symposium on Discharges and Electrical Insulation in Vacuum (ISDEIV)*, 2014, pp. 341-343, doi: 10.1109/DEIV.2014.6961689.

[4] A. Sivathanu Pillai *and* Reuben Hackam, "Surface flashover of solid insulators in atmospheric air and in vacuum", *Journal of Applied Physics* 58, 146-153 (1985) https://doi.org/10.1063/1.335700

[5] T. S. Sudarshan and R. A. Dougal, "Mechanisms of Surface Flashover Along Solid Dielectrics in Compressed Gases: a Review," in *IEEE Transactions on Electrical Insulation*, vol. EI-21, no. 5, pp. 727-746, Oct. 1986, doi: 10.1109/TEI.1986.348922.

[6] H. C. Miller, "Surface flashover of insulators," in *IEEE Transactions on Electrical Insulation*, vol. 24, no. 5, pp. 765-786, Oct. 1989, doi: 10.1109/14.42158.

[7] J. Sun *et al.*, "A Review on Surface Flashover Phenomena at DC Voltage in Vacuum and Compressed Gas," in *IEEE Transactions on Dielectrics and Electrical Insulation*, vol. 29, no. 1, pp. 1-14, Feb. 2022, doi: 10.1109/TDEI.2022.3148456.

[8] C. Schultheiss, H. . -J. Bluhm, H. . -G. Mayer and M. Kern, "Industrial-scale electroporation of plant material using high repetition rate Marx generators," *PPPS-2001 Pulsed Power Plasma Science 2001. 28th IEEE International Conference on Plasma Science and 13th IEEE International Pulsed Power Conference. Digest of Papers (Cat. No.01CH37251)*, 2001, pp. 207-210 vol.1, doi: 10.1109/PPPS.2001.1002029

[9] H. A. Prins, R. H. S. H. Beurskens, Y. L. M. Creyghton, N. Dutreux, S. W. H. de Haan and B. Roodenburg, "Solid state pulsed power source for pulsed electric field and plasma treatment of food products," *PPPS-2001 Pulsed Power Plasma Science 2001. 28th IEEE International Conference on Plasma Science and 13th IEEE International Pulsed Power Conference. Digest of Papers (Cat. No.01CH37251)*, 2001, pp. 1294-1297 vol.2, doi: 10.1109/PPPS.2001.1001786.

[10] T. H. G. G. Weise, M. Gowin and D. Langhans, "Solid state medium energy weapon laser," *Digest of Technical Papers. PPC-2003. 14th IEEE International Pulsed Power Conference (IEEE Cat. No.03CH37472)*, 2003, pp. 245-248 Vol.1, doi: 10.1109/PPC.2003.1277702.

[11] B. D. Min, J. H. Kim, E. Pavlov, D. W. Yoo and G. H. Rim, "A Compact Inductive Type Pulse Generator Using Diodes as Opening Switch," *2005 IEEE Pulsed Power Conference*, 2005, pp. 1364-1367, doi: 10.1109/PPC.2005.300640.

[12] T. Stadlbauer, T. Kramer, D. Kontelis, L. Ducimetière, L. Sermeus and D. Woog, "SF6 Gas Replacement in Pulsed High Voltage Coaxial Cables," *2019 IEEE 20th International Conference on Dielectric Liquids (ICDL)*, Roma, Italy, 2019, pp. 1-5, doi: 10.1109/ICDL.2019.8796780.

[13] R. W. Macpherson, M. P. Wilson, S. J. MacGregor, I. V. Timoshkin, M. J. Given and T. Wang, "Characterization and Statistical Analysis of Breakdown Data for a Corona-Stabilized Switch in Environmentally Friendly Gas Mixtures," in *IEEE Transactions on Plasma Science*, vol. 46, no. 10, pp. 3557-3565, Oct. 2018, doi: 10.1109/TPS.2018.2844954.

[14] C. McGarvey, I. V. Timoshkin, S. J. MacGregor, M. P. Wilson, M. J. Given and M. A. Sinclair, "An experimental and analytical study of plasma closing switches filled with environmentally friendly gases," *2015 IEEE Pulsed Power Conference (PPC)*, Austin, TX, 2015, pp. 1-6, doi: 10.1109/PPC.2015.7296988.

[15] Y. Yao, I. V. Timoshkin, S. J. MacGregor, M. P. Wilson, M. J. Given and T. Wang, "Breakdown Characteristics of Plasma Closing Switch Filled With Air, N2, CO2, and Ar/O2," in *IEEE Transactions on Plasma Science*, vol. 46, no. 10, pp. 3574-3583, Oct. 2018, doi: 10.1109/TPS.2018.2856306.

[16] A. C. Mermigkas, I. V. Timoshkin, S. J. MacGregor, M. J. Given, M. P. Wilson and T. Wang, "Surface flashover behaviour of insulating materials under impulsive electric fields in environmentally friendly gases," *2017 IEEE 21st International Conference on Pulsed Power (PPC)*, Brighton, 2017, pp. 1-6, doi: 10.1109/PPC.2017.8291284

[17] L. A. Lazaridis and P. N. Mikropoulos, "Positive impulse flashover along smooth cylindrical insulating surfaces under variable humidity," in *IEEE Transactions on Dielectrics and Electrical Insulation*, vol. 18, no. 3, pp. 745-754, June 2011, doi: 10.1109/TDEI.2011.5931061

[18] S. Chotigo, B. Pungsiri and S. Kanchana, "The Effect of Atmospheric Factor on Various Test Gaps Under Negative Impulse Voltages," *2008 International Conference on Condition Monitoring and Diagnosis*, Beijing, 2008, pp. 667-670, doi: 10.1109/CMD.2008.4580374

[19] P. N. Mikropoulos and L. C. Tzimkas, "Influence of humidity on surface streamer propagation in a uniform field in air," *45th International Universities Power Engineering Conference UPEC2010*, Cardiff, Wales, 2010, pp. 1-5.

[20] K. P. Morales, J. T. Krile, A. A. Neuber and H. G. Krompholz, "Pulsed Dielectric Surface Flashover at Atmospheric Conditions," *2005 IEEE Pulsed Power Conference*, Monterey, CA, 2005, pp. 1147-1150, doi: 10.1109/PPC.2005.300540.

[21] X. Meng, H. Mei, L. Wang, Z. Guan and J. Zhou, "Characteristics of streamer propagation along the insulation surface: Influence of air pressure and humidity," in *IEEE Transactions on Dielectrics and Electrical Insulation*, vol. 24, no. 1, pp. 391-400, Feb. 2017, doi: 10.1109/TDEI.2016.005966.

[22] L. LIU *et al*., "The Influence of Electric Field Distribution on Insulator Surface Flashover," *2018 IEEE Conference on Electrical Insulation and Dielectric Phenomena (CEIDP)*, Cancun, 2018, pp. 255-258, doi: 10.1109/CEIDP.2018.8544732.

[23] R. Victoria, L. E. Gockenbach, H. Borsi, H. Negle and A. Lunding, "Effects of roughness on surface flashover voltages under DC stress," *2007 Annual Report* -

Conference on Electrical Insulation and Dielectric Phenomena, Vancouver, BC, 2007, pp. 576-579, doi: 10.1109/CEIDP.2007.4451562.

[24] J. -K. Seong *et al*., "Effect of humidity and electrode roughness on the AC and impulse breakdown characteristics of dry-air," *2012 IEEE International Conference on Condition Monitoring and Diagnosis*, Bali, Indonesia, 2012, pp. 770-773, doi: 10.1109/CMD.2012.6416260.

[25] Pillai,A. Sivathanu, Hackam,Reuben "Surface flashover of solid insulators in atmospheric air and in vacuum" 1985/07/01 doi: 10.1063/1.335700 *Journal of Applied Physics* 146 153 58 1, American Institute of Physics

[26] Bauer, S., & Leu, C. (2009). Electrical breakdown and flashover of short spark gaps in atmospheric air at transient voltages. In *Information technology and electrical engineering - devices and systems, materials and technologies for the future* (Vols. 54, 2009, p. Session 6.5). https://www.db-thueringen.de/receive/dbt_mods_00014945

[27] Somesh, Vinayak & Tewari, & Kshirsagar, R. & Roy, Amitava & Sarathi, R. & Sharma, Archana & Mittal, "Optical emission spectroscopy study on flashover along insulator surface due to particle contamination." *Laser and Particle Beams*. 2014 32. 10.1017/S0263034614000718.

[28] L. A. Lazaridis, P. N. Mikropoulos, A. Darras and A. Theocharis, "Flashover along cylindrical insulating surfaces under positive lightning impulse voltages," *17th International Conference on Gas Discharges and Their Applications*, Cardiff, UK, 2008, pp. 233-236.]

[29] M. P. Wilson *et al*., "Surface flashover of oil-immersed dielectric materials in uniform and non-uniform fields," in *IEEE Transactions on Dielectrics and Electrical Insulation*, vol. 16, no. 4, pp. 1028-1036, August 2009, doi: 10.1109/TDEI.2009.5211850.]

[30] Z. Chen *et al.*, "Flashover Voltage of Epoxy FRP Insulators with Different Surface Roughness and Groove under Nanosecond Pulses in SF6," *Energies*, vol. 15, no. 6, p., Mar. 2022, doi: 10.3390/en15062202],

[31] Yushun Zhao, Yitong Xiang, Shanqiang Gu, Bin Du, Bingbing Dong, Nianwen Xiang, Heng Xu, “Effect of surface roughness on flashover characteristics of silicone rubber”, *Journal of Electrostatics*, Volume 99, 2019, Pages 41-48, ISSN 0304-3886, https://doi.org/10.1016/j.elstat.2019.04.004],

[32] R. Victoria, L. E. Gockenbach, H. Borsi, H. Negle and A. Lunding, "Effects of roughness on surface flashover voltages under DC stress," *2007 Annual Report - Conference on Electrical Insulation and Dielectric Phenomena*, Vancouver, BC, Canada, 2007, pp. 576-579, doi: 10.1109/CEIDP.2007.4451562.

[33] Vinod, P, Amizhtan, SK, Ganesh, P, Kornhuber, S, Srinivasan, B, Sarathi, R. Study on water droplet initiated discharges and charge trap characteristics of laser textured silicone rubber nanocomposites. *SPE Polymers*. 2020; 1: 139– 148. https://doi.org/10.1002/pls2.10025],

[34] P. N. Mikropoulos, C. A. Stassinopoulos, M. E. Stapountzi and B. C. Sarigiannidou, "Streamer Propagation and Flashover Along Insulator Surface in a Uniform Field in Air: Influence of Humidity," *Proceedings of the 41st International Universities Power Engineering Conference*, Newcastle upon Tyne, UK, 2006, pp. 916-920, doi: 10.1109/UPEC.2006.367613.].

[35] Adolphe, MOUKENGUE IMANO “AC discharge current characteristics and LI flashover field intensity of water droplets on insulated solid surface”. *Journal of ELECTRICAL ENGINEERING*, VOL. 60, NO. 1, 2009, 24–28

[36] Bin Cao and Shichao Shao and Xiaohan Wu and Fanghui Yin and Liming Wang and Masoud Farzaneh “Flashover characteristics of a hydrophobic surface covered by water”, *Journal of Physics* D: Applied Physics, Volume 54, Number 7

[37] F. O. McMillan and E. C. Starr, "The Influence of Polarity on High-Voltage Discharges," in *Transactions of the American Institute of Electrical Engineers*, vol. 50, no. 1, pp. 23-33, March 1931, doi: 10.1109/T-AIEE.1931.5055733.

[38] F. O. McMillan, "Polarity Limits of the Sphere Gap," in *Transactions of the American Institute of Electrical Engineers*, vol. 58, no. 2, pp. 56-61, Feb. 1939, doi: 10.1109/T-AIEE.1939.5057923

[39] A. Pokryvailo, "Calculation of breakdown voltage of gas gaps with arbitrary geometry on examples of spheres and toroids," *2017 IEEE 21st International Conference on Pulsed Power (PPC)*, Brighton, UK, 2017, pp. 1-4, doi: 10.1109/PPC.2017.8291190.

[40] Z. Qiu and J. Ruan, 'Electric Field Features and Its Application for Air Gap Breakdown Voltage Prediction', *Electric Field*. InTech, May 23, 2018. doi: 10.5772/intechopen.72230.

[41] Leandros A. Maglaras, Athanasios L. Maglaras, Frangiskos V. Topalis, "The influence of the Effect of Grounding and Corona Current on the Field Strength the Corona Onset and the Breakdown Voltage of Small Air Gaps", *WSEAS TRANSACTIONS on POWER SYSTEMS,* 2008

[42] A. Carrus, E. Cinieri, A. Fumi, and C. Mazzetti, ''Short tail lightning impulse behaviour of medium voltage line insulation,'' in *IEEE Trans. Power Del.*, vol. 14, no. 1, pp. 218–226, Jan. 1999, doi: 10.1109/61.736725.

[43] E. Kuffel and M. Abdullah, ''Corona and breakdown-voltage characteristics in sphere—Plane and rod—Rod gaps under impulse voltages of various wavefront durations,'' Proc. Inst. Electr. Eng., vol. 113, no. 6, pp. 1113–1119, Jun. 1966, doi: 10.1049/piee.1966.0182.

[44] Q. Wang, L. Hao, Y. Gao, J. Zhao and Y. Wang, "Probability distribution model of DC basin insulator flashover," *2020 IEEE International Conference on High Voltage Engineering and Application (ICHVE)*, 2020, pp. 1-4, doi: 10.1109/ICHVE49031.2020.9279493.

[45] S. Okabe, T. Tsuboi and J. Takami, "Reliability evaluation with weibull distribution on AC withstand voltage test of substation equipment," in *IEEE Transactions on Dielectrics and Electrical Insulation*, vol. 15, no. 5, pp. 1242-1251, October 2008, doi: 10.1109/TDEI.2008.4656231.

[46] Wang Can, Youyuan Wang, Lianwei Bao and Gao Jun, "A DC cable failure model by using two parameters Weibull distribution," *2014 ICHVE International Conference on High Voltage Engineering and Application*, 2014, pp. 1-4, doi: 10.1109/ICHVE.2014.7035459

2. CHAPTER II

BACKGROUND AND LITERATURE REVIEW

2.1. INTRODUCTION

In the analysis of the breakdown characteristics of air-solid insulation systems, it is important to recognise that there are three types of failure that can occur:

- gaseous bulk breakdown
- solid bulk breakdown
- gas-solid interfacial flashover

As the insulating parts of a high-voltage system are integral to both the mechanical and electrical integrity of the system, each of these types of failure will be discussed in relation to the underlying physical mechanisms, and the damage that can result once a breakdown/flashover path has been established. In terms of gaseous bulk breakdown, this breakdown mechanism is the least damaging to the system, as the discharge path does not involve contact with the solid spacer. The gaseous material can recover within a short timescale after breakdown has occurred. Solid bulk breakdown or gas-solid interfacial flashover differ, however, and can be detrimental to the insulation properties of the system. The propagation of a discharge channel either through the solid bulk or over the surface of the material can change the chemical composition of the solid material, reducing the flashover/breakdown strength under the application of subsequent impulse voltages [1], [2]. To fully understand the results associated with the surface flashover of solid insulation systems, the gaseous breakdown, bulk breakdown and gas-solid interfacial flashover mechanisms must all be understood. This knowledge will enable an insulation system to be designed that is able to withstand the voltage characteristics specific to the application.

In order to characterise the method of energy delivery, an introduction to pulsed power systems will firstly be made, with discussion on the basis of the capability to produce impulse voltages of high enough magnitude to induce one or more of the failure mechanisms. This review will focus on high-voltage systems based on capacitive energy storage. A literature review on the electrical breakdown of gaseous insulation,

solid insulation and the flashover of gas-solid interfaces follows, with particular focus on the effect of environmental conditions on the breakdown strength, as appropriate to the work and results presented and discussed in this thesis.

2.2. PULSED-POWER TECHNOLOGY

Pulsed power refers to the accumulation of energy over a relatively long charging time of storage elements, in the (ms – s) regime, and its subsequent release in a fraction of the charging time (ps - μs) [3], [4]. This gives the opportunity to achieve very high peak powers of up to the petawatt range, from relatively low average supply powers [5]. The peak power achieved can be found using equation 2.1:

$$P = \frac{E}{t} \tag{2.1}$$

where P is the peak power (W), E is the energy (J) and t is the time (s), of the pulse duration. It is clear that very high magnitudes of peak power will be reached for short discharge times, [5].

Another definition of pulsed power can be attributed to Bluhm [6], '*where stored energy is discharged as electrical energy into a load in a single short pulse or as short pulses with a controllable repetition rate*' Although pulsed power technology was originally developed to enable military and defence applications, where the output of torrents of radiation were used to simulate the explosion of nuclear weaponry, other uses have emerged that require the use of pulsed power. These include medical applications [7-11], material and mineral processing, [12–15], and, looking to the future, many applications use pulsed power technologies to drive experiments aimed at the production of fusion energy [16-18]. A recent publication details many other applications of pulsed power systems [19].

To quantify typical pulsed power conditions, impulses generally fall within the range of parameters shown in Table 2.1 [5].

Table 2.1 – Typical pulsed power parameters [5]

Parameter	Range
Energy per pulse	$1\text{-}10^{7}$ J
Peak power	$10^{6} – 10^{14}$ W
Peak voltage	$10^{3} – 10^{7}$ V
Peak current	$10^{3} – 10^{8}$ A
Pulse width	$10^{-10} – 10^{-5}$ s

The energy-storage elements used in a pulsed power system are either capacitive or inductive. In inductive systems, the achievable energy density accumulation far surpasses that of capacitive elements, [20], [21]. Therefore, when limited space is available, utilising inductive storage will be of benefit. A downside to an inductive system, however, is a plasma opening switch has to be incorporated, and the inductive system then must be charged and discharged rapidly [22], as the self-discharge time of the system is very short.

Given the capability of capacitive systems to provide impulse voltages of hundreds of kV using charging voltages of tens of kV, and their high efficiency for low-capacitance loads, this was the preferred method of impulse generation for this study. As such, capacitive storage systems will now be discussed. And although the achievable energy density is presently much greater for an inductive system, capacitive energy density is increasing [23].

With particular emphasis on pulsed power technologies, the energy density for large-format millisecond discharge capacitors capable of storing >50 kJ has increased from 0.7 J/cm^3 in the early 1990s to >2.4 J/cm^3 in 2015, with lifetimes of over 10,000 shots. [24]. Further research in megavolt Marx generator capacitors, used at Sandia National Laboratories, was driven by the ‘ZR project’, where the 2.6 μF, 100 kV capacitors (General Atomics) have doubled the energy density of the older 1.3 μF capacitors by doubling the capacitance in the same volume, while maintaining the low inductance (<30 nH) and high peak current (170 kA) capabilities. The lifetime of the capacitors is around 11,000–13,000 shots at 100 kV, decreasing to 8000 shots at 110 kV [25].

Analysing the energy associated with the electric fieldof the capacitor, the energy accumulated within the dielectric between the plates is shown in equation 2.2 –

$$E = \frac{1}{2} C.V^2 \qquad 2.2$$

where *E* is the energy (J), *C* is the capacitance (F) and *V* is the applied voltage (V).

The instantaneous current achieved in a capacitive discharge circuit is given by equation 2.3, where high peak currents can be achieved as a result of the rapidly-decreasing voltage while the capacitor discharges.

$$i = C \frac{dV}{dt} \qquad 2.3$$

Basic examples of capacitive pulsed power circuits are shown in Figures 2.1 and 2.2, where R_{CH} is a charging resistor, *C* is the capacitor and *CS* is a closing switch. The operation of the circuit consists of the capacitor, *C*, charging up from the HVDC supply through the charging resistor, R_{CH}. Once the self-breakdown level of the closing switch has been reached, or the switch has been triggered by an external source, the energy within the system is then delivered to the load. Figure 2.1 shows an example of a non-inverting capacitive energy storage circuit, while Figure 2.2 shows an example of an inverting energy storage circuit, where the relative positions of the capacitor *C* and the closing switch *CS*, have been swapped. In the inverting configuration, upon switch closure, the charged side of the capacitor is connected to ground through the shorted closing switch, so the output of the system is inverted with respect to the input polarity. Within the non-inverting circuit, the primary power supply connected can be subject to voltage reversal, and when used in the delivery of repetitive pulses, this can cause problems as the reverse voltage can result in diode bridges housed within the supply to conduct and lead to failure [26]. The inverting arrangement has a safeguard from this, however, as the power supply is completely decoupled from the load due to the shorted switch during the discharge process.

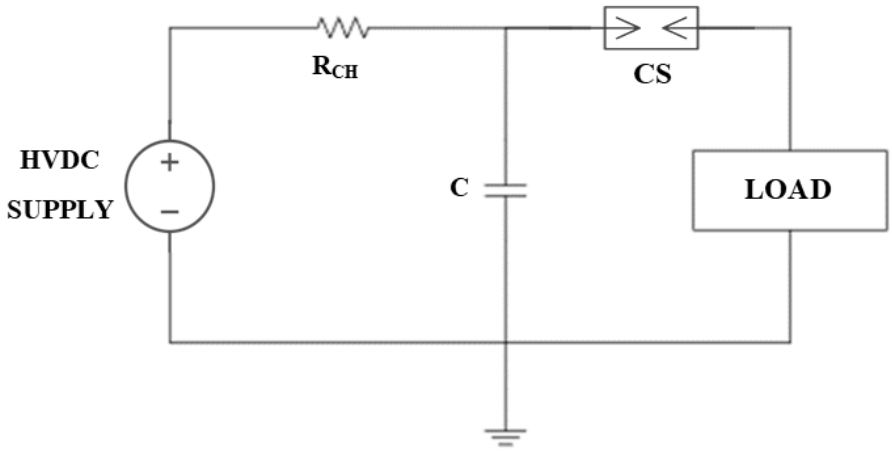

Figure 2.1 - Schematic diagram of basic non-inverting capacitive storage pulsed power circuit

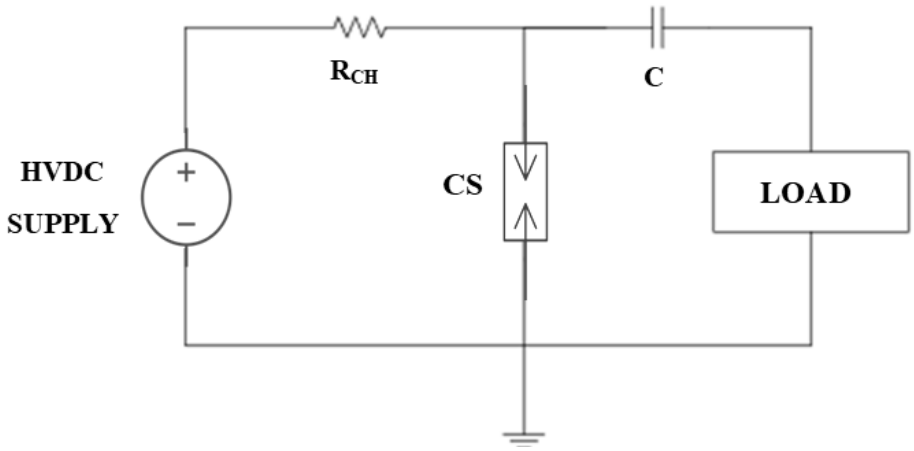

Figure 2.2 - Schematic diagram of basic inverting capacitive storage pulsed power circuit

2.2.1. Marx Generators

Utilising the capacitive energy storage principles introduced in Section 2.2.1, but with multiple capacitors (‘stages’), The Marx generator was invented by Erwin Marx in 1923 [27]. The Marx generator consists of a system of capacitor banks and resistors, configured to result in a high-amplitude, fast-rising voltage pulse. The capacitors of a Marx generator are DC charged in parallel through impedances, and then discharged in series, to enable voltage multiplication. This system can then be utilised in order to deliver very high impulse voltages to a load.

During the charging cycle of the Marx generator, each capacitor is charged up in parallel, to the charging voltage, V_0. Equation 2.4 describes the charging time of a capacitor bank within a Marx generator [28] and [29],

$$\tau_{ch} = n^2 R C_0 \quad \text{where} \quad 1 \leq n \leq N \tag{2.4}$$

where n is the n_{th} stage, R is the stage resistance, C_0 is the stage capacitance and N is the total number of stages. An simplified example of a Marx generator in the charging phase is shown in Figure 2.3.

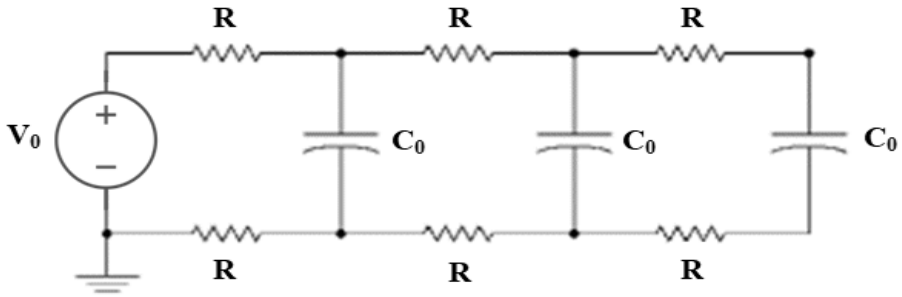

Figure 2.3. - Charging phase of Marx Generator, modified from [5]

The capacitive bank is charged in parallel and discharged in series, achieved by the closure of spark-gap switches. The Marx generator can be triggered in different ways. This can be via self-breakdown, where a fixed output voltage is directly resultant from the physical characteristics such as gap length and electrode topology. If output voltage control over a range of voltages is required, the breakdown of the spark gap can be triggered either by a mechanical or a pneumatic system. Electrical triggering can also be utilised, to control the time of discharge initiation. Regardless of the method of initiation, once the critical breakdown voltage has been reached, the gaps in the spark column close, connecting each individual capacitor in series, resulting in an output impulse voltage being a multiple of the charging voltage, defined by the number of stages of the Marx generator [30].

The maximum available energy that can be stored by the capacitors in the Marx generator is shown in equation 2.5:

$$E = n.\frac{1}{2}.C.V^2 \tag{2.5}$$

where n is the number of stages, C is the energy-storage capacitance of one stage (F), and V is the voltage to which each capacitor C is charged (V).

During the discharge process, the chain of resistors shown in Figure 2.3 add inefficiency to the circuitry, as the energy dissipated by the resistors can be considered as being lost. Therefore, to maximise the energy dissipated by the load, the discharge

time should be kept short. The discharge time of a Marx generator circuit is described by equation 2.6.

$$\tau_{discharge} = \frac{RC_0}{2} \qquad 2.6$$

It was found in [31] that, in practice, a ten-stage Marx generator had a full closure time of ~200 ns.

If the Marx generator has fully discharged, and the energy is delivered to a load, an ideal equivalent circuit can be found in Figure 2.4. This circuit assumes single polarity charging, and also that very little discharge current is drawn.

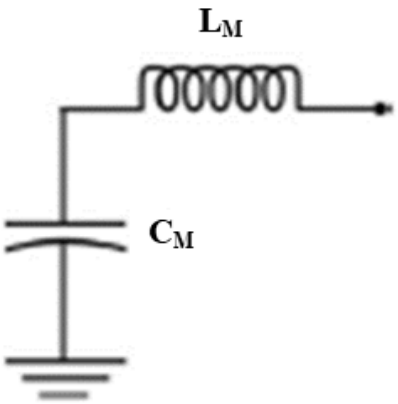

Figure 2.4. - Ideal Marx generator output circuit, modified from [5]

In Figure 2.4, the inductance, L_M, is added to represent the self-inductance of the Marx generator, that is the combined inductances from the discharge switches, the capacitors, and the discharge circuit. For unipolar impulses, the erected capacitance of the Marx generator, C_M, is given by equation 2.7. The erected impedance, Z_M, intrinsic discharge time, T_M, and inverted open circuit voltage of the erected Marx, V_{OC}, are given in equations 2.8, 2.9 and 2.10, respectively.

$$C_M = \frac{C_0}{N} \qquad 2.7$$

$$Z_M = \sqrt{\frac{L_M}{C_M}} \qquad 2.8$$

$$T_M = \sqrt{L_M C_M} \quad 2.9$$

$$V_{OC} = -NV_0 \quad 2.10$$

As discussed, the output voltage waveform can be manipulated by changing the capacitance values and number of stages within the Marx generator. Assuming fixed capacitances, control of the front time and time to half-value is affected by varying the values of the wave-shaping resistors, shown as R_e and R_d in Figure 2.5

As discussed previously in relation to single-stage circuits, the Marx generator circuit can be configured in such a way that the output voltage is inverted or not, with respect to the polarity of the charging voltage. Given the advantages of the inverting configuration discussed in Section 2.2.1, a single-stage equivalent circuits of an inverting Marx generator is shown in Figure 2.5. In this particular configuration, when the capacitance of the load is low, the voltage efficiency is higher, [32].

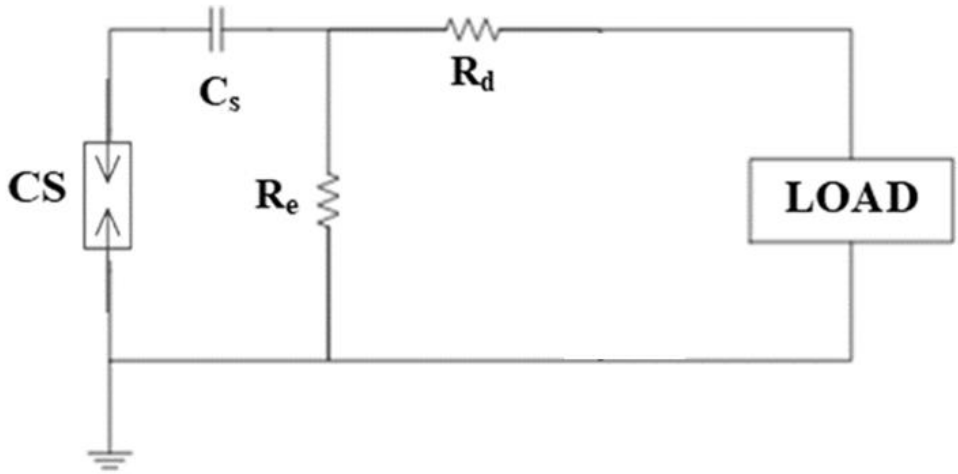

Figure 2.5. - Inverting Marx generator arrangement where the arrangement dictates that the Marx generator drives a low-capacitance load for higher efficiency; adapted from [32]

The output voltage, $v(t)$, can be determined by the double-exponential expression in equation 2.11 [32]:

$$v(t) = \frac{V_0}{R_d C_L} \cdot \frac{\tau_1 \tau_2}{\tau_1 - \tau_2} (e^{-t/\tau_1} - e^{-t/\tau_2}) \quad 2.11$$

where V_0 is the output voltage magnitude (V); R_d is the wave-front resistance (Ω); C_L is the load capacitance (F); τ_1 is the discharging time associated with the wave-tail (s); and τ_2 is the charging time associated with the wave-front (s). Referring also to Figure 2.5, providing that $R_e\ C_s \gg R_d\ C_L$), then the characteristic times τ_1 and τ_2 can be evaluated in terms of the circuit components in Figure 2.5, and can be extracted using equations 2.12 and 2.13, respectively, where R_e is the wave tail resistance.

$$\tau_1 \sim R_d \frac{(C_s(C_L))}{(C_s + C_L)} \qquad 2.12$$

$$\tau_2 \sim R_e(C_s + C_L) \qquad 2.13$$

A typical resultant output voltage waveform from a Marx generator is shown in Figure 2.6, where a faster front time is evident in comparison to the time to half-value. From this waveform, the peak voltage can be extracted, as well as the values of the front time and time to half-value, which are typically referenced when describing double-exponential waveforms (e.g. this example shows a 100/700 ns impulse). Where the 100 ns refers to the front time 0 -100% and 700 ns is time to half value.

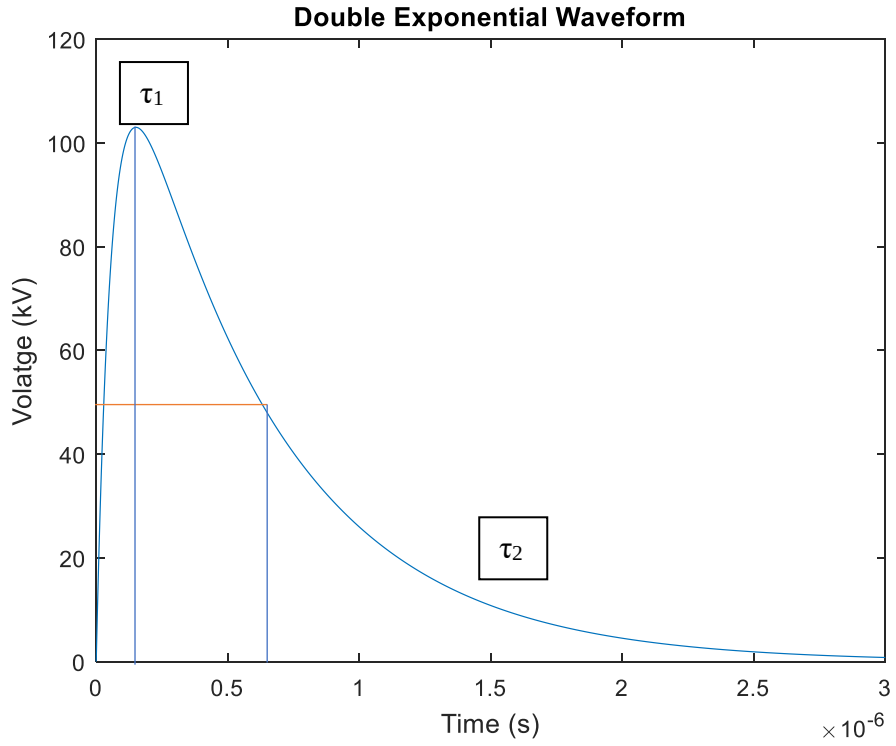

Figure 2.6 - Typical double-exponential output impulse voltage waveform from a Marx generator, showing the front time, τ_1, and tail time value, τ_2

The main advantage offered by the use of a Marx generator is the possibility to achieve a high output voltage from a relatively low DC charging voltage. A disadvantage is that the wave-shaping resistors will require maintenance. Historically, a disadvantage also was apparent from the self-inductance of the capacitors being at a level such that *di/dt* was limited. However, capacitors with a low self-inductance (<20 nH) are now readily available [25], [33]. A disadvantage is the limited pulse repetition rate of Marx generators; however, research is currently being conducted on repetitively pulsed Marx generators, [34].

Given the capability to provide impulse voltages of hundreds of kV using charging voltages of tens of kV, its high efficiency for low-capacitance loads, and its capability for control of the impulse wave-shape, a Marx generator was the preferred method of impulse generation employed for this study. Further information on the specific Marx generator used in the experimental phase of this study, in terms of design and electrical performance, will be discussed in Chapter III.

2.2.2. Conclusion

Summarising the information presented in Section 2.2, to generate the voltages required for electrical breakdown/flashover in this study, a Marx generator was utilised. This section has summarised relevant information on the operation and overall performance of a Marx generator, to elucidate the voltage multiplication process.

The next section in this literature review will focus on the loads being driven by the Marx generator, starting with background material on gas breakdown, and the mechanisms relating to the plasma discharge created within a gas gap under different environmental conditions.

2.3. GAS INSULATION SYSTEMS

A mode of insulation failure that can occur during the application of impulse voltages is the breakdown of a gas gap, which can occur between two electrodes within the overall pulsed power system. A low-impedance plasma channel will establish from

one electrode to the other. This section will explain breakdown theory as related to open gas gaps.

For conduction to occur, there must be charge carriers established within the gap, in a gas these are electrons and positive ions. If the gas has no net charge, then the number density of electrons, n_e, and the number density of ions, n_{ion}, are equal. If an electric field is applied across the gas, the electrons and positive ions will move towards the anode and cathode at drift velocities v_e and v_{ion}.

2.3.1. Ionisation Processes in Gases

The most important process in gas breakdown is ionisation, in particular ionisation of gas molecules due to electron impact. The effectiveness of this ionisation process is dependent upon the electron energy. When an electron collides with an atom or molecule, once this energy is exchanged, an elastic or inelastic process occurs. If the process is elastic, no ionisation or excitation will result from the collision. However, if the process is inelastic, the atom will have become excited, and if the energy exceeds the ionisation energy, the atom or molecule will become ionised by this energy absorption from the incident electron.

Small particle collisional ionisation occurs when a fast-moving electron, *e*, which has been accelerated by an external electrical field, comes into contact with a neutral particle, *A*. The energy transfer that takes place has sufficient magnitude such that an electron can escape the particle; thus, the kinetic energy can free another electron. This results in a situation where the result will be a positive ion, A^+, and two free electrons, 2*e* [35], as shown in equation 2.14:

$$A + e \leftrightarrow A^+ + e^- + e^- \qquad 2.14$$

Large particle collision [36] takes place when two neutral particles, *A* and *B*, collide, with the kinetic energy freeing an electron from one of the particles.

$$A + B \leftrightarrow A + B^+ + e^- \qquad 2.15$$

The process of ionisation is started when energy of sufficient magnitude is introduced into a system occupied with neutral particles. Ionisation takes place where this energy results in interactions with neutral particles and, in terms of positive ionisation, displaces an electron [37]. The minimum magnitude of the energy required for the process is known as the ionisation potential. The gain in energy must be greater than or equal to the ionisation potential of the gas, as in equation 2.16:

$$V_i \leq \lambda_e E \qquad 2.16$$

where λ_e is the average distance that an electron travels between collisions, termed the mean free path, E is the magnitude of the applied electrical field and V_i is the ionisation potential.

The ionisation potential varies by gas type. Table 2.2 shows the ionisation potential of gases found in zero grade air and relevant to this study [38].

Table 2.2 - Ionisation potential of relevant gases [38]

Gas	**Ionisation energy (eV)**
N_2	15.6
O_2	12.1

Another method of ionisation is photoelectric ionisation, [39], [40], a process that can take place from either a natural source, such as cosmic rays, x-rays or nuclear radiation; or from radiation emitted from excited atoms returning to their ground state.

Photoelectric ionisation takes place when a photon of sufficient energy manages to release an electron from a neutral atom. If *A* represents the neutral atom and *e* is an electron, *KE* is the kinetic energy associated with the electron and *A** is the excited atom of the gas the following reaction, a chemical reaction equation is produced as shown in equation 2.17.

$$A + e^- + KE \rightarrow A^* + e^- \qquad 2.17$$

Afterwards, once the neutral atom has recovered from its excited state after ~10^{-8} seconds, the atom radiates a photon that has the potential to ionise another neutral

molecule, if the ionisation potential of the neutral atom is less than or equal to the photon energy. This is shown in Figure 2.7, where a photon is seen to collide with an atom which consequently frees an electron, leaving behind a positive ion [40]. The energy, *E*, of the photon, is given by equation 2.18:

$$E = h\nu \tag{2.18}$$

where Planck's constant, $h \approx 6.626 \times 10^{-34}$ J.s, and ν is the frequency (Hz). Equation 2.19 characterises the photoionisation process [40].

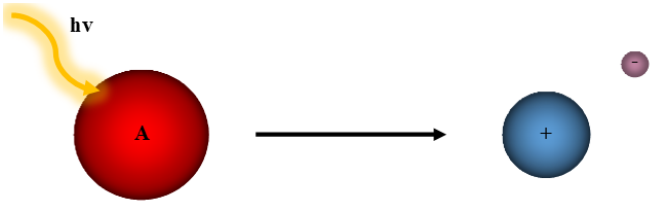

Figure 2.7 - Illustration of photoionisation process

$$A + h\nu \rightarrow A^{+} + e^{-} \tag{2.19}$$

A collision between particles, as incorporated in equations 2.14 and 2.15, will occur if the centre of one of the particles passes within a distance of $\frac{d_1 + d_2}{2}$ within the other particle. Therefore, the area which particle one must pass through to collide with a second particle is given by equation 2.20 -

$$\sigma = \pi\left(\frac{d_1 + d_2}{2}\right)^2 \tag{2.20}$$

where σ is the collision cross section, d_1 is the diameter of particle one and d_2 is the diameter of particle two.

If particle one is moving at a certain velocity, ν, the resultant cylindrical volume created by the moving particle is $V = \sigma\nu$. The number of particles, *N*, in volume, V, determines the collisional frequency, $f = N\sigma\nu$, therefore the higher number density, the higher the collision frequency. As the collision frequency increases, the mean free path will decrease, which relates to the distance the particle will travel between collisions, given by equation 2.21.

$$\bar{\lambda} = \frac{1}{N\sigma} \qquad 2.21$$

As particles, in this case free electrons, traverse the gas gap, each electron can initiate different processes along its path, where each collision will have its own specific cross-section. Therefore, the energy of the colliding pair will create elastic collisions, excitation or ionisation. These individual processes have their own specific cross-sections, as described in equation 2.22:

$$\sigma(v) = \sigma_{el}(v) + \sigma_{ex}(v) + \sigma_{ion}(v) \qquad 2.22$$

where $\sigma(v)$ is the total cross-section, $\sigma_{el}(v)$ is elastic impact cross-section, $\sigma_{ex}(v)$ is the excitation cross-section and $\sigma_{ion}(v)$ is the ionisation cross-section. Each of these collisions will also have their own independent mean free path in relation to equation 2.21. The collision path of an electron through a gas under the influence of an electric field is illustrated in Figure 2.8.

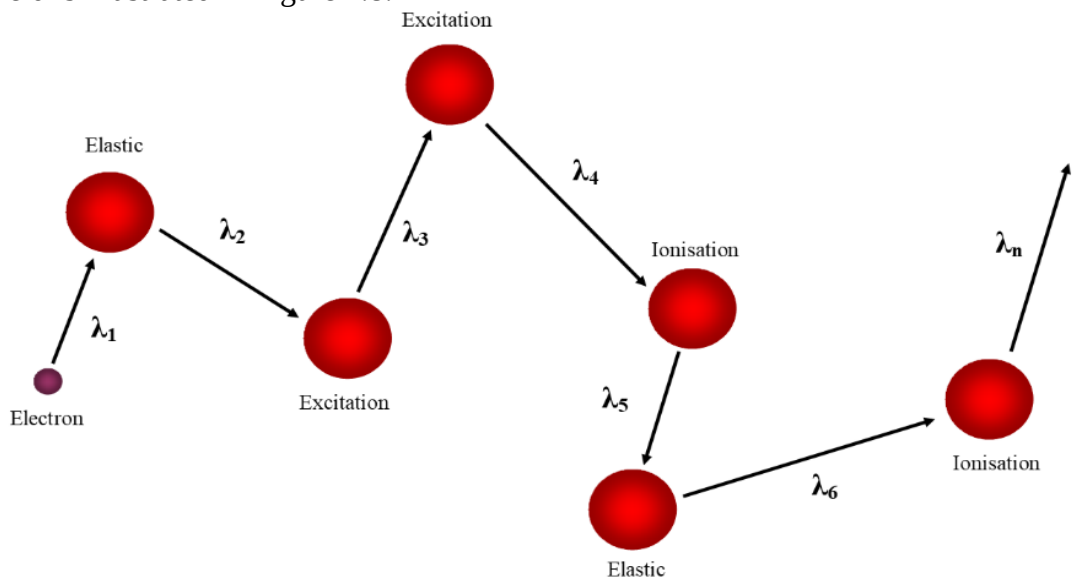

Figure 2.8 - An electron moving through a gas from the influence of an electric field, modified from [5]

2.3.2. Loss of Free Electrons

Referring to equation 2.19, recombination is the reverse process of the photoelectric ionisation process. Recombination results when a free electron recombines with a positive ion, resulting in a neutral particle being formed, as well as a photon given off. This process can be seen in equation 2.23 [40].

$$A^+ + e^- \nrightarrow A + hv \quad (2.23)$$

Electron attachment occurs when a neutral molecule accepts a free electron, which in turn creates a negative ion. This process occurs mainly in electronegative gases such as air or SF_6, [39], where the gas is missing electrons from the outer shell of its molecules. This can be illustrated by equation 2.24:

$$A + e^- \nrightarrow A^- + hv \quad (2.24)$$

When an electron attaches to a neutral particle, a negative ion is formed, and a photon of light is given off. The free electron being absorbed by the atom results in a much heavier negative ion, which is a much larger and slower particle. The probability for the negative ion to go on to cause further ionisations is reduced, compared to that for an electron. This results in higher applied voltages being required in order for the negative ions to go on to cause further ionisations.

In the reverse process, the collision of a photon and a negatively charged ion can release the attached electron, leaving a neutral particle and a free electron. This process is known as photoelectric detachment [40].

For a negative ion to exist and remain stable, its total energy has to be lower than that of the atom in the ground state. After a free electron attaches itself to a neutral particle, the change in energy is known as electron affinity. Dependent upon the attraction between the electron and the neutral particle, this will alter the amount of energy released; the larger the attractive force, the higher the energy.

2.4. BREAKDOWN MECHANISMS

In this section, Townsend's seminal work will be examined, followed by Paschen's law. This will be followed by Townsend's criterion for spark breakdown, and a focus on streamer structure and propagation. Finally, the effect of environmental parameters will be discussed, including how these affect the breakdown process in compressed gases.

2.4.1. Townsend discharge

Townsend was the first to study the electric current through a gas as a function of voltage [40]. When a voltage is applied between two electrodes insulated by a gas such that a uniform electrical field is established, the current in the gas can exist in three different regions. The relationship between current, *I*, and voltage, *V*, is now discussed as is the nature of these three regions.

In order to understand the mechanisms behind the Townsend breakdown of gases, firstly it is important to determine the sources of initiating electrons in the gas. For breakdown to occur, a single initiating electron is required. This can be initiated within the gas, due to heavy particle impact or photoionisation as discussed in Section 2.3.1, or from the electrode due to field-related injection or photo emission (discussed in Section 2.4.1.1).

2.4.1.1. Initial electron production

Field emission

This phenomenon is a prominent factor during a process where high electrostatic fields are present, which results in field emission. When an electron leaves the surface of the material, the resultant field can be loosely determined by a point charge and equipotential plane, where the electron is infinitely far from the surface and the fermi level. This is what is referred to as the work function, in eV.

The work function can be defined as an energy value that represents the energy required to remove an electron from a solid. In the context of an electrode in a gas, the work function can be understood as follows: When attempting to transfer an electron from the electrode into the gas, a force arises between the electron and the positively-charged region left behind. In order to move the electron, work must be done, specifically that for moving a charge in an electric field resulting in a potential difference. This creates a potential well, which confines electrons in close proximity to the surface of the solid. At elevated temperatures, certain electrons will have enough energy to surpass the work function and escape from the solid (in this case, the electrode), allowing them to transition into the gas phase. This phenomenon occurs

due to the increased thermal energy associated with higher temperatures. Additionally, the application of an electrical field modifies the profile of the barrier that governs the ease of electron emission from the cathode. Therefore, apart from the influence of the field resulting from charge separation, as an electron moves away from the cathode, it also experiences a change in potential due to the external electrical field, leading to alterations in the shape of the barrier, as illustrated in Figure 2.9, modified from [41].

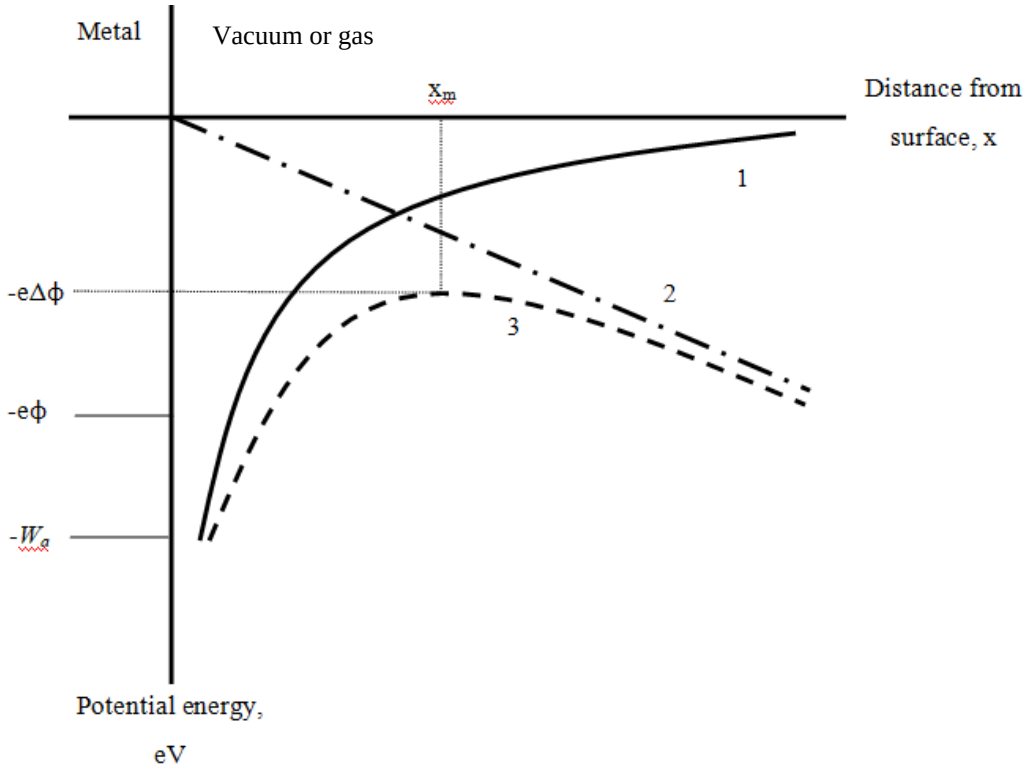

Figure 2.9 - Energy required in order for an electron to leave a metal surface, modified from [41]

The energy which is required for an electron to escape from the surface of an electrode is dependent upon multiple parameters. Using Coulomb's law and integrating, the potential energy (W_e) of the electron can be found at a distance, *x*, from the surface. A potential energy (W_f) is also produced by the electric field perpendicular to the surface. Each individual potential energy as well as the combined energies are shown in Figure 2.9. From [40], [41], 'The lowering of the potential barrier by an external field: curve 1 – energy curve with no external field, - $W_e = e^2/16\pi E_0 x$; curve 2 – energy due to applied field, - $W_f = eE_x$; curve 3 – total energy curve, $W_t = W_f + W_e$.

From Figure 2.9, as the field is increased the combined potential energy distribution has a maximum, if this is situated close to the electrode surface this can result in

tunnelling effects. The tunnelling effect is where an electron with an energy less than the barrier may tunnel through to the other side of the barrier, if a high enough field exists to cause the barrier to be sufficiently narrow for tunnelling to occur. The tunnel probability, which is exponentially dependent on the tunnelling distance, is inversely proportional to the applied electric field, and the probability of an electron tunnelling through the barrier is exponentially decreasing function of tunnelling distance. As a result, emission or current density is an exponential function of the reciprocal of the applied field. The equation for the emission current of the emitted electrons is called the Fowler-Nordheim equation (equation 2.25):

$$j = f.\frac{E^2}{\phi}.e^{\frac{-g\phi(V)^{\frac{3}{2}}.u}{E}} \qquad 2.25$$

Where j is the Current density (A/m^2), E is the Electric field (V/m), f is 1.54 x 10^{-6}, g is 6.83 x 10^9, u is 1-1.4 x 10^{-9} E/ϕ^2 and $\phi(V)$ is the work function, which varies by material.

Photoelectric emission

Another type of electron emission is photoelectric emission. If a photon of sufficient energy impacts the surface of the electrode, and if the transfer of energy to an electron gains a sufficient amount to overcome the work function, then the electron is released. Equation 2.26 is an expansion of equation 2.19, [40].

$$\frac{1}{2}.m_e.{u_e}^2 = hv = \phi(V) \qquad 2.26$$

Where –

- m_e = mass of electron (kg)
- u_e = electron velocity (V/m)
- h = Planck's constant (kg m^2/s)
- v = photon frequency (1/s)
- $\Phi(V)$ = work function (V)

2.4.1.2. Electron Avalanches

An illustration of an electron avalanche is provided in Figure 2.10. An electron emitted from the cathode collides with a neutral particle within the inter-electrode gap spacing and transfers its kinetic energy, resulting in the creation of another free electron and a positive ion. Further collisions then take place as the electrons accelerate away from the formed positive ion at an exponential rate. Thus, a Townsend electron avalanche is formed.

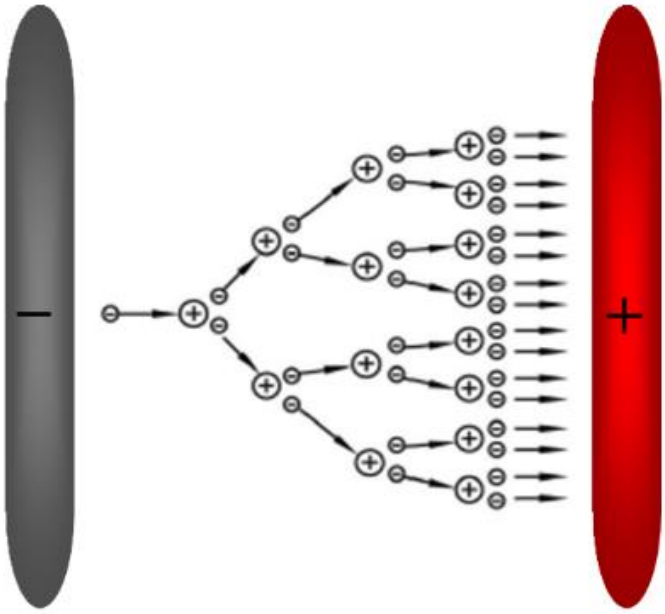

Figure 2.10 - Electron avalanche illustration, modified from [42]

The ionisation coefficient, α, which is known as Townsend's first ionisation coefficient, defines the number of ionising collisions per unit length of path travelled by a free electron.

Having defined the sources of initiating electrons in the gas, then for a gas to breakdown, there must be a multiplication process of those electrons. An electron avalanche requires an initiatory electron, either occurring naturally or emitted from an external source (electric field or thermionic), and present due to the action of an applied electric field. This free electron then moves in the applied field to collide with neutral gas molecules at a drift velocity, v_d, in relation to the electric field, E, and mean free path, λ. The cumulative effect of ionising collisions results in a 'cascade ionisation', as illustrated in Figure 2.10, where the number of free electrons within the

gas gap grows exponentially. This is referred to as an electron avalanche, [40], [42]. The current density (*J*) is related to the electron number density through equation 2.27:

$$J = q_e n_e v_d \quad 2.27$$

where q_e is the electronic charge, n_e is the number density of electrons and v_d is the drift velocity.

The electron number, n_e, in a thin layer, dx, within the electron avalanche is given by equation 2.28.

$$dn_e = n_e \alpha dx \quad 2.28$$

In order to analyse the change in electron population as the electron avalanche moves throughout the gap, this can be expressed as shown in equation 2.29.

$$\frac{dn_e}{dx} = \alpha n_e \quad 2.29$$

Where the integration of equation 2.28, with a set initial condition of $n_e(x) = 0$, yields equation 2.30:

$$n_e(x) = n_0 \, e^{\alpha x} \quad 2.30$$

The term $e^{\alpha x}$ in equation 2.30 is the exponential growth term.

- $n_e(x)$ = number of electrons produced by collisions at distance, *d*
- n_o = number of electrons generated at cathode
- α = Townsend's first ionization coefficient
- *d* = inter-electrode gap spacing

2.4.1.3. Secondary ionisation

Additionally occurring within the gas under breakdown conditions is a process known as secondary ionisation, where the positive ions formed by the collisions in the electron avalanche then drift towards the cathode. Their bombarding collisions with the cathode, assuming the ions gain enough energy, then creates further injection of electrons from the cathode. This process is accounted for by the addition of the secondary ionisation coefficient, γ, to the governing equation 2.32, from 2.31. [39], [40].

Analysing a specific region between the electrodes, dx, a single electron creates αdx electron-ion pairs. Representing the current at x as I_e, the current increases by the following equation 2.31.

$$dI_e = I_e \alpha dx \tag{2.31}$$

The integration of equation 2.31 yields 2.32.

$$I_e(x) = I_0 e^{\alpha x} \tag{2.32}$$

In terms of cathode current, a single electron will generate $(e^{\alpha d} - 1)$ electrons and positive ions. The created positive ions which collide with the cathode will then go on to generate γ secondary electrons. Therefore, the current generated from the new electron population will add to the initial cathode current, I_0, as shown in equation 2.33.

$$I_{cathode} = \frac{I_0}{1 - \gamma(e^{\alpha d} - 1)} \tag{2.33}$$

As the (positive) ions move towards the cathode, the anode current will only consist of electronic current, as shown in equation 2.34.

$$I_{anode} = I_{cathode} e^{\alpha d} = \frac{I_0 e^{\alpha d}}{1 - \gamma(e^{\alpha d} - 1)} \tag{2.34}$$

During energisation, with the increase in applied voltage potential, the coefficients α and γ will increase. In the case where $I_0 = 0$, this will result in a non-self-sustaining discharge, as the current generated from equation 2.34 will be 0.

However, if $\gamma(e^{\alpha d} - 1) = 1$, this will then yield a situation where the anode current, I_{anode}, cannot be 0, even if $I_0 = 0$. This means that an external ionisation source is not needed to sustain a discharge. The transition from non-self-sustaining discharge to self-sustaining discharge is referred to as breakdown, as defined in equation 2.35.

$$n = \frac{n_0 e^{\alpha d}}{1 - \gamma(e^{\alpha d} - 1)} \tag{2.35}$$

In the steady state, the circuit current will be given by equation 2.36:

$$I = \frac{I_0 e^{\alpha d}}{1 - \gamma(e^{\alpha d} - 1)} \qquad 2.36$$

The process can be seen as self-sustaining when the condition in equation 2.37 is met:

$$\gamma(e^{\alpha d} - 1) = 1 \qquad 2.37$$

As a result of the ion attraction and mass collision with the cathode releasing electrons, the process repeats. Thus, electron avalanches will continue to occur without the need for external systems having to deliver energy for the continuation of the avalanche process [39], [40]. Equation 2.37 is referred to as the Townsend criterion for breakdown.

$$\delta = \gamma(e^{\alpha d} - 1) \qquad 2.38$$

Equation 2.38 refers to the number of electrons generated per single electron moving across the gap. When δ = 1, this is known as the Townsend criterion for spark breakdown, when $\delta < 1$ external energy delivery is required.

2.4.1.4. Townsend graphical representation

Relating equation 2.37 to the regions identified in Figure 2.11, at low field strengths (low voltages) $e^{\alpha d}$ is closer to 1, and the current is then equal to $I_0 e^{\alpha d}$ in the region between V_1 and V_2. As the voltage continues to increase, $e^{\alpha d}$ and $\gamma e^{\alpha d}$ both continue to increase until $\gamma e^{\alpha d}$ is unity, when $e^{\alpha d}$ approaches infinity. In practice, the current is limited by the resistance of the power supply. For a gap spacing of distance, d, breakdown will occur when α and γ reach their critical values [40], [43], [44].

Accounting for electron attachment, η, which defines the number of attachments that occur for an electron travelling unit length in the gas, equation 2.37 becomes equation 2.39:

$$\gamma\left(e^{(\alpha-\eta)d} - 1\right) = 1 \qquad 2.39$$

Analysing equation 2.39, if the electron attachment coefficient (η) is greater than the first ionisation coefficient, then breakdown will not occur, due to the absence of electron multiplication [40].

The relationship between current, *I*, and voltage, *V*, can be seen in Figure 2.11.

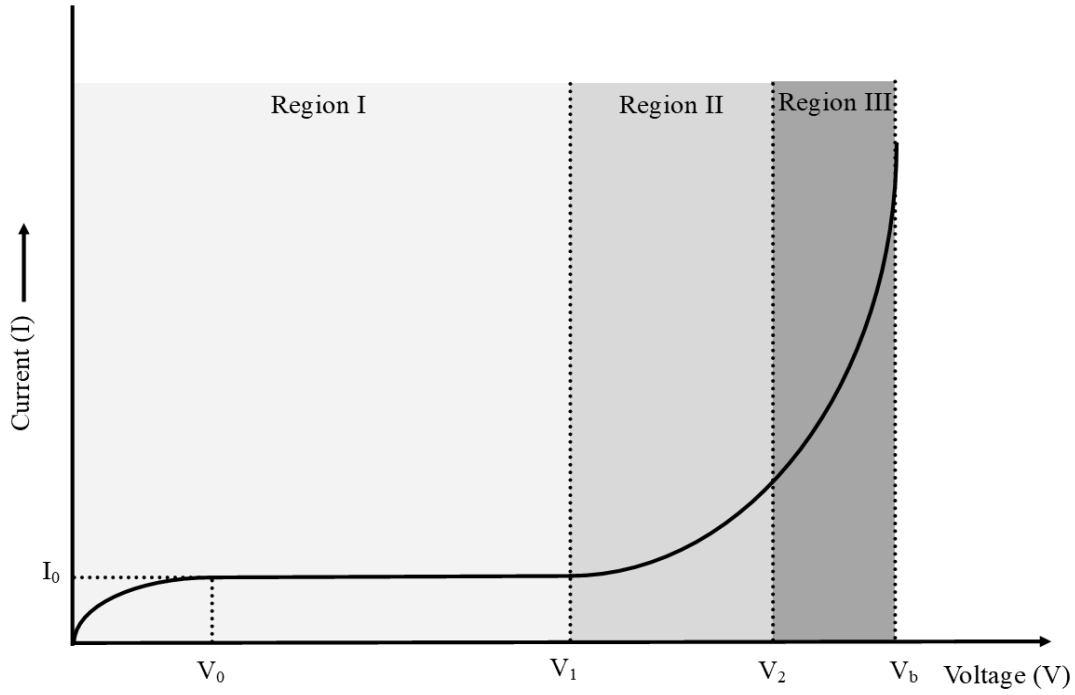

Figure 2.11 - I-V characteristics of two-electrode spark gap, modified from [42]

As shown in Figure 2.11, the development of breakdown can be described in three distinct *I-V* regions, as now discussed.

Ionisation free region (Region I)

At first, *dI/dV* is proportionate, where the current increases proportionally with voltage up until point I_0 has been reached. In this region, the electrons within the gas gap start to drift from the cathode to the anode. During this process, many of these electrons could be lost to processes such as electron attachment or electron recombination, dependent upon the gaseous dielectric. This electron velocity will be determined by the level of electric field due to the applied voltage [45], where as the field increases the time taken for the electrons to cross the gap decreases and the probability of attachment or recombination decreases this leads to the current saturating at value I_0. Between V_0 and V_1, the current remains constant at I_0, known as the saturation current. This occurs once all of the electrons and ions within the gas reach and are absorbed

by the anode or cathode, where if there is cathode emission due to illumination then all of the electrons introduced to the cathode transit to the anode. In the case of ion electron pairs generated in the gap by photoionisation or ionising radiation then again all are being absorbed by the cathode or anode.. This current does not increase until an electron amplification mechanism becomes dominant, which occurs in region II.

Townsend first ionisation region (Region II)

Once the applied voltage reaches V_1, the current then increases to a value greater than I_0. This increase in current is due to the flow of additional electrons from the more frequent ionising collisions of electrons with gas molecules as the electric field is increased in the gap. In this region, there is an exponential relationship between the current and voltage after V_2, as has been described in Section 2.4.1.1 and 2.4.1.2, in relation to Townsends first ionisation coefficient, α.

Townsend second ionisation region (Region III)

In the phase above V_2, the increasing electric field then accelerates electrons, produced by secondary ionisation at the cathode, which in turn creates more collisions, leading to further ionisation of the gas. The current is found to increase much faster in this section in comparison to the first ionisation region. At V_b the discharge has become self-sustaining and the breakdown voltage of the gas has been reached. In addition to α describing the growth of the population of electrons within the gap, Townsend's second ionisation coefficient, γ, which relates to the number of secondary electrons produced at the cathode due to ion bombardment from the primary avalanche, is now active in this region.,

2.4.2. Paschen's law

Subsequent to Townsend's work, one of the first studies of electrical breakdown, again between two parallel plates, was undertaken by Paschen [46]. In a plane-plane electrode geometry under DC stress, the field strength within the inter-electrode gap will be uniform. Under these conditions, equation 2.40 applies, [43]:

$$E = \frac{V}{d} \qquad 2.40$$

where E is the electrical field strength (V/m), V is the applied voltage (V) and d is the inter-electrode gap distance (m). The coefficients α and γ are both defined by gas pressures and functions of electric field, as shown in equations 2.41 and 2.42, respectively:

$$\alpha = pF_1\left(\frac{E}{p}\right) \quad 2.41$$

$$\gamma = F_2\left(\frac{E}{p}\right) \quad 2.42$$

When combining equations 2.41 and 2.42 with equationa 2.39 and 2.40, this yields equation 2.43:

$$\left(F_2\left(\frac{V_b}{pd}\right)\right)\left[e^{\left(pF_1\left(\frac{V_b}{pd}\right)\right)d} - 1\right] = 1 \quad 2.43$$

Where:

- E = electrical field strength
- p = gas pressure
- d = inter-electrode spacing
- α = Townsend's first ionisation coefficient
- γ = Townsend's second ionisation coefficient
- V_b = breakdown voltage

Analysing equation 2.43, the value of the breakdown voltage, V_b, is only related to the pressure (p) of the gas and the inter-electrode spacing (d) within the system [40].

Therefore, the breakdown voltage is the same for a given value of the product pd, which is shown in equation 2.44:

$$V_b = F(pd) \quad 2.44$$

Equation 2.44 is known as Paschen's law, which states that the breakdown voltage, V_b (or sparking potential), is a unique function of the (pd) product for a given gas and electrode material. The typical relationship between the breakdown voltage of a gas and the pressure-distance (pd) product is illustrated in Figure 2.10 (DC distribution shown from [40], [43], [47] and microsecond and nanosecond performance from [48] and [49], respectively).

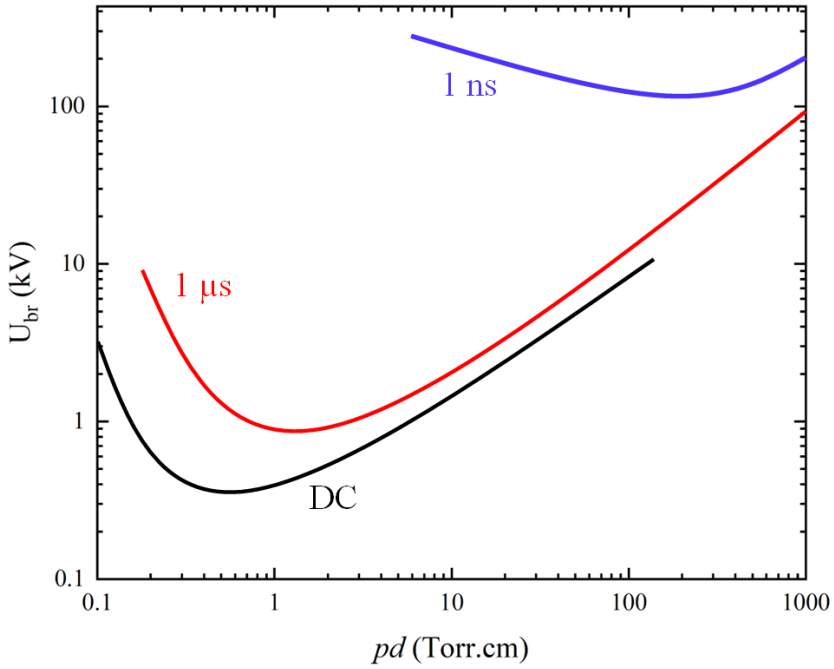

Figure 2.12 - Typical Paschen curves under DC, microsecond impulse and nanosecond impulse, showing relationship between breakdown voltage and pd product, modified from [49], in air.

When analysing Figure 2.12, V_{min} is the minimum voltage required to break down the gas, occurs at the Paschen minimum, labelled as pd_{min}. For each energisation regime, there are different V_{min} and pd_{min} values, and Table 2.3 shows the minimum breakdown voltages for different voltage profiles, taken from the values shown in Figure 2.12.

Table 2.3 - Minimum breakdown voltage for air under different energisation regimes [40], and approximated from the modified Figure 2.12,[48]

Regime	V_b (min) (V)	pd at V_b (min) (Torr.cm)
DC	327	0.754
µs	900	1.2
ns	90,000	300

What is evidently clear from the work conducted in [48] and [49], is that the applied voltage characteristics alter the Paschen curve for gas breakdown. Compared to the DC characteristics, as the applied pulsed voltage becomes shorter in duration, both V_b (min) pd (min) increase. This effect is due to the shorter pulse duration meaning less time for a discharge to develop at a given level of applied field. Whereas for DC (and AC) voltages, there are generally sufficient initiatory electrons to initiate breakdown at lower applied fields [40], due to the increased time under energisation having enough time to initiate a formative process.

What can also be seen from Figure 2.12 is that there are two distinct regions at $pd > pd_{min}$, the breakdown voltage is higher than that at pd_{min}. For a fixed gap distance, d, the reason for this is due to the shorter electron mean free path at higher pressure, whereby electrons traversing the gap collide with gas molecules more frequently compared to the lower pressure at pd_{min}, reducing their kinetic energy. Therefore, for the breakdown process to commence, a higher potential has to be applied. When $pd < pd_{min}$, the breakdown voltage also increases, although the free electrons have the possibility to cross the gap making very few or no ionising collisions in the process, as the lower number density will result in a longer mean free path. At a fixed pressure, p, as the gap length decreases, the number of electrons in an avalanche decreases, and some electrons could collide with the anode before sufficient ionisation has occurred. For long gaps, the increased distance results in a lower electric field, therefore α decreases, resulting in fewer ionisation events occurring.

The breakdown behaviour identified in the Paschen curve shown in Figure 2.12 is linked to Townsend's first ionisation coefficient, α, as well as to Townsend's second ionisation coefficient, γ. Townsend proposed that α is a strong function of electric field, as well as pressure, above the Paschen minimum - this can be shown from typical values of A and B ionisation constants in equation 2.45:

$$\frac{\alpha}{p} = Ae^{\left(\frac{-Bp}{E}\right)} \qquad 2.45$$

where -

- α = Townsend's first ionization coefficient (cm^{-1})
- A = ionisation constant related to temperature ($cm^{-1}.Torr^{-1}$)

- B = ionisation constant due to type of gas (V/cm.Torr)
- P = pressure (Torr)
- E = electric field (V/cm)

The ionisation coefficients for air are listed in Table 2.4

Table 2.4 - Ionisation coefficients for air

Gas	A ($cm^{-1}.Torr^{-1}$)	B (V/cm.Torr)
Air	15	365

2.4.3. Propagation of Streamers

In Townsend breakdown theory, the effect of space charge, which distorts the electric field across the gap, is not considered. The streamer onset criterion has two prominent theories of explanation. First is Meek's theory [42], in which the space-charge field will lead to the generation of a streamer discharge when the electric field at the head of the electron avalanche (E_r) is approximately equal to the external applied field (E_0). Similarly, the theory of streamer onset was created by Raether, which states that the electron avalanche will transition to a streamer when the number of electrons in the avalanche head exceeds 10^8 [50].

Streamer polarity is dependent upon the polarity of the applied voltage. Therefore, the location of the formation of a streamer determines the polarity of said streamer [43]. Streamers propagating from the cathode are known as 'negative streamers'; as such streamers travel towards the anode, they can also be called 'anode-directed streamers'. Positive polarity streamers propagate from the anode of the system and can also be called 'cathode-directed streamers' [42].

Streamers form in the shape of long, thin, ionised channels. The channel of a positive streamer has been shown to be thicker than that of a negative streamer in [51], at a gap distance of 4 cm, which corresponds to the gap distance used in the present study.

The space charge that is produced influences the growth of the electron avalanche. The minimum breakdown strength of gases has been shown to correspond to a critical

charge density of 10^8 per cm^3; when the charge density was measured as between 10^6 and 10^8, the growth of an impending avalanche was weakened [40], [42], [43], [44].

2.4.3.1. Streamer Structure

The basic structure of both, negative and positive, streamers is illustrated in Figure 2.13, with the electron avalanche emanating either from the cathode or the head of the negative streamer.

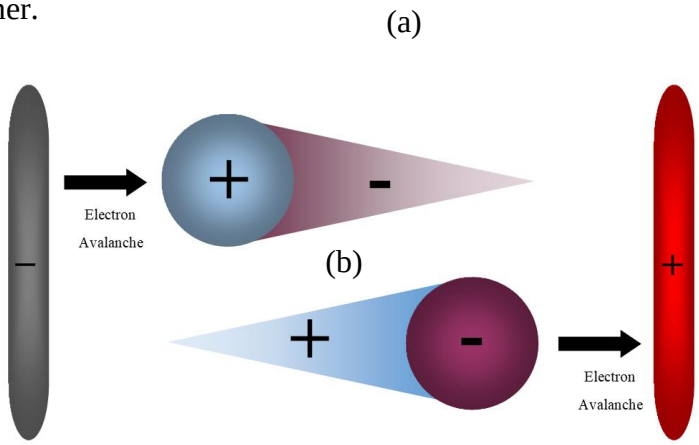

Figure 2.13 - Structure of a) positive (cathode-directed) streamer and b) negative (anode-directed) streamer

Following Meek's work on positive streamer mechanisms [42], and with reference to Figure 2.14 (adapted from [42]), an electron avalanche is developed at the cathode and moves under the action of the applied electric field. If the avalanche reaches the anode, this will result in the electrons being absorbed into the anode. This process will leave positive ions in a cone-shaped structure across the inter-electrode gap. A positive streamer will then develop from a region of high electric field local to the anode and propagate towards the cathode. The streamer development is supported by photoionisation in the densely ionised gas around the anode, which drives the production of more free electrons These electrons produced by the photoionisation

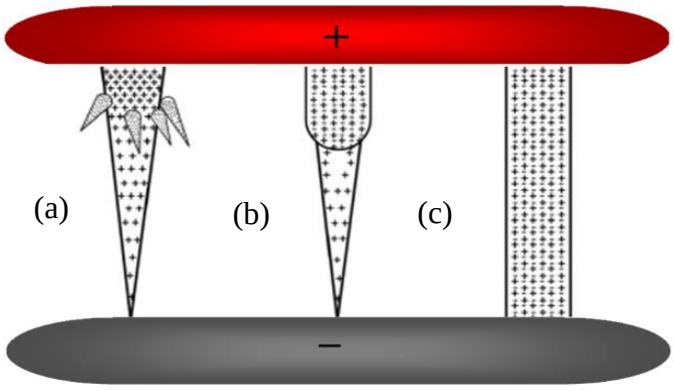

Figure 2.14 - Positive streamer development, modified from [42], [50] a) first avalanche crossing the gap b) streamer extending from the anode and c) streamer crossing the gap

process create auxiliary avalanches from the main streamer channel, which are attracted to the positive space charge at the head of the advancing streamer.

Figure 2.15 (modified from [43]) illustrates the negative streamer mechanism, following Raether's work. Within the Raether criterion, it is stated that streamer transition occurs when the number of electrons within the avalanche head exceeds $e^{\alpha x} = 10^8$. At this point, the electric field produced due to space charge is comparable with the applied electric field. Auxiliary avalanches are then produced culminating in a negative streamer, as seen in Figure 2.15.

In Figure 2.15, there is a strong electric field between the head of the negative streamer and the anode due to space charge. Ionisation takes place as the electrons are dislodged, leaving behind positive ions. The electrons move at a significantly greater speed than the heavier positive ions [40], [43], [44].

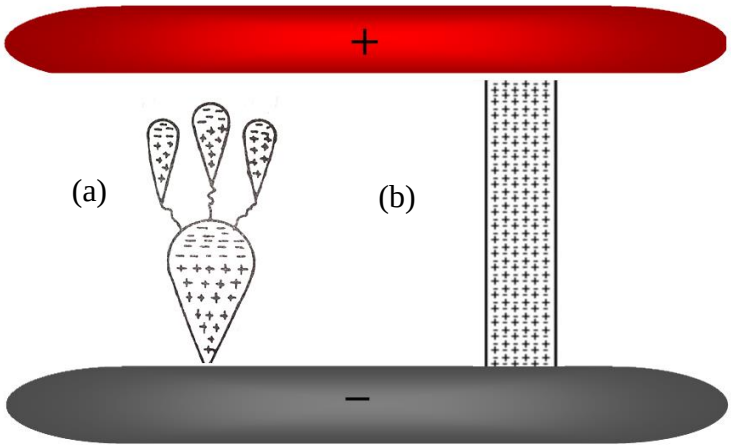

Figure 2.15 - Negative streamer development, modified from [43], a) avalanches travelling from cathode to anode b) negative streamer crosses gap

2.4.3.2. Streamer Electric Field Distribution

The different electrical field distributions associated with negative and positive streamers are illustrated in Figures 2.16 and 2.17, respectively.

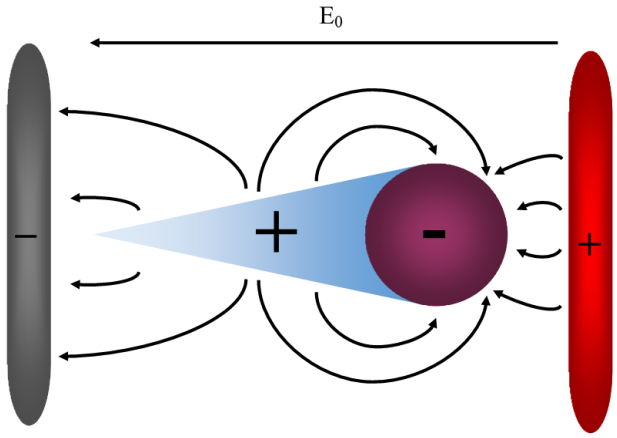

Figure 2.16 - Negative streamer electrical field line distribution

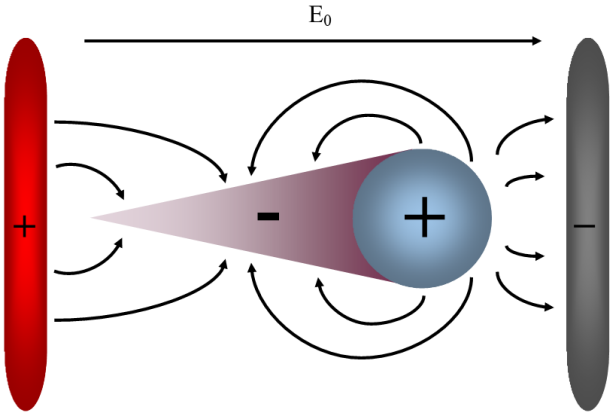

Figure 2.17 - Positive streamer electrical field line distribution

In Figure 2.16, a local electrical field is formed between the negative streamer head and the positive streamer body, which is in the opposite direction to the applied electrical field, reducing the overall electrical field strength, as seen in the associated graph in Figure 2.17. In Figure 2.17, for the positive streamer, the electrical field distribution creates a local field between the positive head of the streamer and negative streamer body, just like in the case of the negative streamer [44].

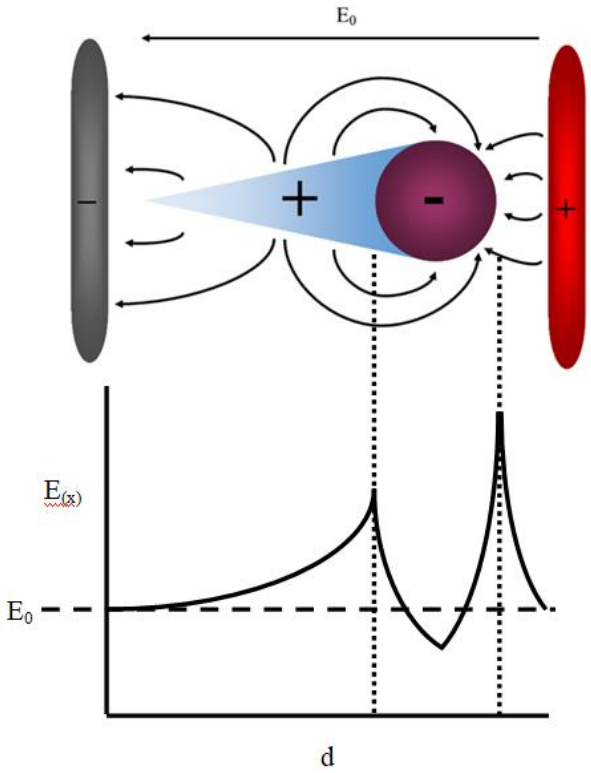

Figure 2.18 - Electrical field distribution of negative streamer, modified from [40]

Figure 2.18 shows the change in electrical field strength over the length of a negative streamer within the electrode gap. It shows a negative streamer where the local field creates a region of reduced electrical field strength between the space charge head and the positive streamer body due to the opposing electric fields. Due to the external applied field and the space charge formed, the avalanche head can experience intense ionisation, which can result in the field strength at this point being the strongest at any point across the gap. This will then result in more ionisation and secondary ionisation from electron bombardment occurring, which can end with full breakdown and with an ionised spark channel becoming formed.

Work completed on the propagation of streamers in atmospheric air is described in [51], [52], with the authors concluding that positive streamers propagate faster than negative streamers. This is because positive streamers are initiated by the ionization of neutral gas molecules by electrons accelerated towards the anode, which causes a positive space charge ahead of the streamer. This positive space charge enhances the electric field ahead of the streamer, leading to faster propagation. In contrast, negative streamers result in the attachment of electrons to neutral molecules, which creates a negative space charge ahead of the streamer [51], [52]. This negative space charge

reduces the electric field ahead of the streamer, leading to slower propagation. However, there is research that disputes this as in [53], the authors concluded from their results that negative streamers had a higher velocity than positive streamers. This was attributed to the increase of charged particles in negative streamer channel, which increases the electric field in the streamer channel, this causes the ionisation of the gas by accelerated electrons.

So, from these two cases, it is apparent that the type of streamer propagation in the system is important in determining the breakdown voltage. Interestingly, the negative breakdown voltage is higher than the positive where DC electric fields are applied, [54], under lightning impulses [55], and under nanosecond impulses [56]. However, the opposite behaviour has been recorded for the application of sub-nanosecond discharges with high overvoltage levels, which resulted in positive polarity breakdown voltages becoming higher than those for negative polarity [57].

2.4.4. Effect of Environmental Parameters on the Breakdown of Gases

The breakdown voltage of an insulation system is influenced by the amount of water vapour within the environment, where the presence of water vapour, which is electronegative in nature, results in the attachment coefficient increasing. In general, the authors of [58] showed that the breakdown voltage will increase with the addition of water vapour into a gaseous environment. By increasing the relative humidity and therefore the water vapour in the air, the attachment coefficient (η) of the air mixture would increase, while the ionisation coefficient (α) would stay constant, or not increase as rapidly [59]. Breakdown of humid air can be partly explained by the space charge generated within the gap due to the presence of humidity-induced ions. It is shown in [59] and [60] that the negative ions that affect the electrical breakdown strength of air are O^- and O_2^-. The ions lose electrons by means of detachment after colliding with a neutral molecule, as shown in equations 2.46 and 2.47, [58].

$$O^- + O_2 \longrightarrow O + O_2 + e^- \quad (2.46)$$

$$O_2^- + O_2 \longrightarrow 2O_2 + e^- \quad (2.47)$$

Alternatively, electrons can be lost by auto-detachment due to the instability of the ion, as shown in equation 2.48.

$$O_2^{*-} \longrightarrow O_2 + e^- \qquad 2.48$$

In a process called conversion, the oxygen ions can transform into others that do not detach. Two examples of this process are shown in equations 2.49 and 2.50 [59].

$$O_2^- + H_2O \longrightarrow O_2^-.(H_2O) \qquad 2.49$$

$$O^- + O_2 + O_2 \longrightarrow O_3^- + O_2 \qquad 2.50$$

When an electron is absorbed by an oxygen molecule, the process creates a negative ion, as shown in equation 2.51.

$$e^- + O_2 \longrightarrow O^- + O \qquad 2.51$$

However, when adding water molecules to the gas mixture, deionisation also occurs [61]. Electron attachment to water molecules yields three kinds of negative ion fragments, as shown in equations 2.52, 2.53 and 2.54.

$$e^- + H_2O \longrightarrow O^- + H_2 \qquad 2.52$$

$$e^- + H_2O \longrightarrow H^- + OH \qquad 2.53$$

$$e^- + H_2O \longrightarrow OH^- + H \qquad 2.54$$

Due to the addition of the extra electronegative molecules within the gas mixture, the attachment coefficient of the gas mixture increases. Reported in [62], as the humidity is increased, the lower mobility of ions will result in a reaction with the water molecules.

This ion mobility is found from the equation 2.55, [62] -

$$\frac{1}{K_i} = \frac{P_w}{P(K_i)_w} + \frac{P - P_w}{P(K_i)_d} \qquad 2.55$$

Where K_i is the ion mobility in humid air and is either associated with $P(K_i)_w$ for wet air or $P(K_i)_d$ for dry air. As humid air is a mixture of dry air at 0% RH and water vapour at 100% RH, P_w is the partial pressure of water vapour and P is the air pressure.

This effect also showed that it influenced the corona onset voltage as the humidity increased, [63].

To further understand the influence of humidity on the breakdown voltage of an insulation system, the discussion will now focus on the effect that the humidity has on the mechanism of streamer current growth.

Figure 2.19 shows a schematic representation of the current generated by electrons crossing the gap from the cathode to the anode, based on [58], [64].

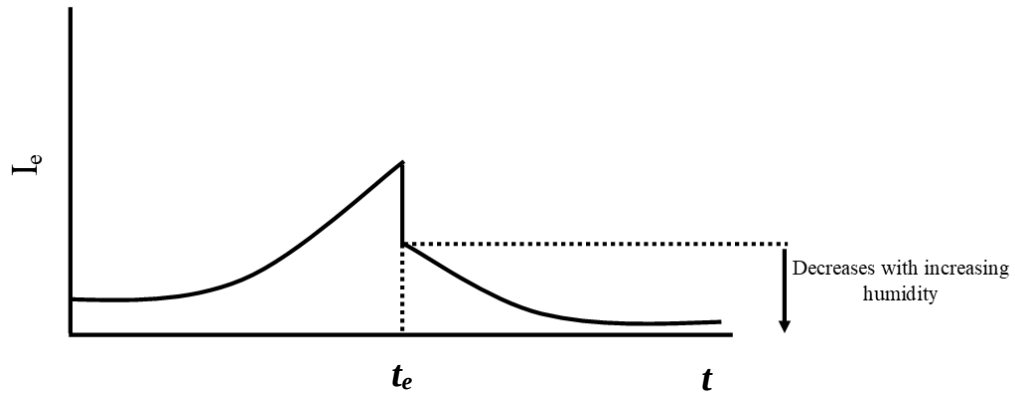

Figure 2.19 - Streamer current growth with changing humidity modified from [58], [64]

From Figure 2.19, modified from [64], it is evident that the current increases until a time, t_e, and then decreases. The initial rise in current with respect to time is due to increasing arrival of electrons at the anode. At time t_e, there is a steep drop in the current due to the arrival of the head of the electron avalanche at the anode. At this point, the electron current does not drop to zero, but does follow a decreasing trend until time, t, caused by electrons that arrive after the avalanche head. The electrons that arrive at this point are those that have been detached from unstable ions in the gap. The electrons' arrival at the anode is later than that of the free electrons due to the time that is required for the detachment process to take place. This secondary ramp after time t_e, is referred to in the literature as 'after current' [58],[64].

When relating this to humidity, with increasing humidity a reduction in the after current beyond t_e has been reported in [64]. This is caused by the decreased number of electrons that have detached within the gap [58]. The number of electrons that have been incorporated into non-detaching ions due to conversion reactions is increased with the increase of humidity, resulting in a reduction in the number of detached electrons. The electron detachment processes are independent of the electric field. However, the amount of conversion reactions is a function of the partial pressure of water vapor. The times involved in detachment and conversion processes are different, with the detachment time being virtually constant. Conversion reaction times are a function of humidity and are shortened substantially for humid air when compared to the values for dry air. This behaviour has been observed practically in [65], where with the increase of humidity of up to 65% RH, the number of negative ions and free electrons were reduced by factors of 5.8 and 2.7, respectively. Also reported in [58] were minor changes in breakdown strength due to increased relative humidity. Particularly at lower levels of humidity, with the limited source for the ions due to the low concentration of water molecules within the gap, the electric field is strong enough to clear most of the O_3^-, O_2^- and O^- ions, so the trapped charge remains low. Relating this to the breakdown strength of the gas gap, trapped charge has a negative effect, reducing the breakdown strength, but the reduction in the population of free electrons has a positive effect, increasing the breakdown strength.

In [64], decreases in the breakdown voltage with increasing humidity were seen to follow the phenomenon illustrated in Figure 2.19. As the humidity was increased, the magnitude of the after current termed 'drop phase', t_e, of decreasing current originates, resulting in a progressive reduction in breakdown strength. A reduction in streamer current can lead to a reduction in breakdown strength because streamer current is directly related to the strength of the electric field in the ionisation region. A higher streamer current results in a stronger electric field, which promotes the ionization of sample molecules. Additionally, a reduction in streamer current may also result in a decrease in the plasma density, which can further reduce the ionisation efficiency and the breakdown strength of the system. This can be explained also due to the conversion reaction in equation 2.49, which is a function of humidity and quickly becomes the dominant reaction for humid air. The authors of [64] showed that the time required for

conversion by equation 2.49, reduced from 32 ns for dry air to 3 ns for humid air, resulting in a faster detachment process. The large amount of H_2O molecules present in the high humidity gas increases the number of conversion reactions taking place by almost an order of magnitude. In [61], it was reported that heavy ions created via the reaction in equation 2.49, the $O_2^-\cdot(H_2O)$ ions, have a slower drift velocity than that of O^-. These $O_2^-\cdot(H_2O)$ ions can create clusters with additional water molecules [65]. These clusters are of the form $O_2^-\cdot(H_2O)x$, where x is the amount of water molecules in the cluster. Collision cross-sections of the ionic clusters increase with additional H_2O molecules, decreasing their mobility. Also, collision cross-sections of these water clusters vary with the electric field magnitude, further hindering their movement [65], this could result in a higher breakdown voltage being resultant, [66]. However, for much higher humidity, it is probable that a large amount of $O_2^-\cdot(H_2O)x$ ions have not been cleared from the gap. These trapped charge carriers are responsible for the subsequent reduction in breakdown strength at very high levels of humidity. This could account for the dramatic decrease in the breakdown voltage at high humidity which is reported in [67] and [68].

As discussed previously, the electron detachment processes are independent of the electric field, where increasing humidity is shown to increase the breakdown strength of air. However, this section will discuss the electric field effect on the breakdown voltage of an open-air gap at high humidity. The addition of aerosol into the system at very high levels of humidity also has an effect on the breakdown voltage of the insulation system. In [69], it is shown that the effect of aerosol short distances away from HV electrodes, or forming on the HV electrodes, can have a detrimental effect on the breakdown voltage due to the high electric field forming local to the HV electrode, as shown in Figure 2.20.

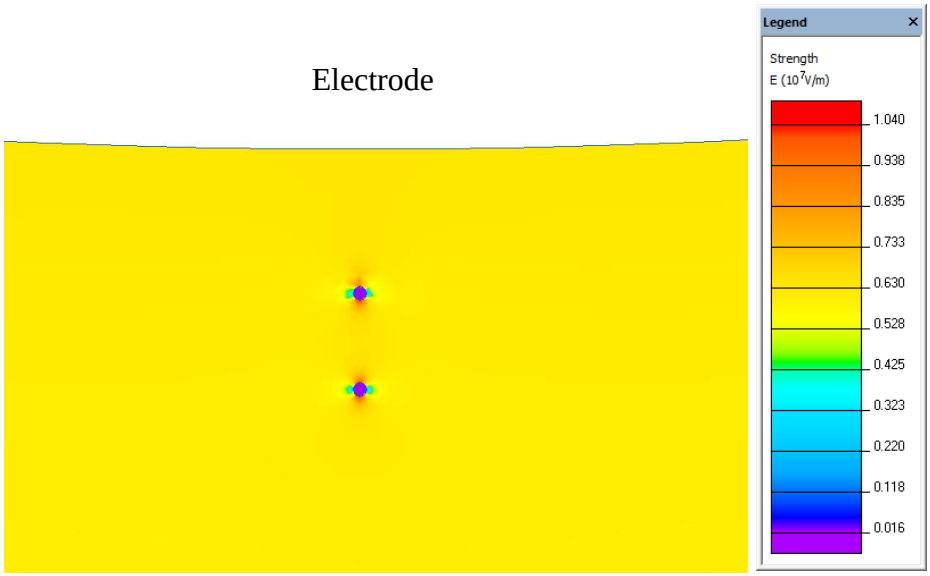

Figure 2.20 - Electric field distribution of spherical electrode with aerosol, based on work conducted in [69]

Due to the high permittivity of water (ε_r = 80), a high field region is created between the HV electrode and the aerosol, resulting in the generation of electrons, ultimately leading to breakdown. The impact of the added water molecules is to introduce another possible source of electron emission, playing a guiding role in the development of the streamer.

The results in [67], [68], [70] show the effect of high humidity on the breakdown strength of gas gaps. From these studies, it is clear to see that under very high humidity, typically >90% RH, the breakdown strength of the gas gap is reduced due to the high aerosol content of the air. The breakdown strength of a gas is affected, manifested as the disruptive discharge voltage becoming irregular, typically at humidity levels of >80% RH as shown from the high voltage testing standard. [70]. In [71], an increase of the relative humidity was shown to result in the formation of water droplets, with the increased electric field in the vicinity of the HV electrode potentially leading to breakdown.

The influence of gas pressure is also a factor which determines the breakdown voltage of an insulation system. The higher probability of collisions resulting from the increased number density with increasing air pressure results in the collision frequency increasing, meaning that a higher applied field is needed in order to drive the development of an electron avalanche to the point of breakdown, as discussed in

Sections 2.4.1. ans 2.4.2. Experimentally, it is well known that increasing pressure causes an increase in breakdown voltage, as shown experimentally in [72].

2.5. SOLID INSULATION SYSTEMS

In a gas-solid insulation system, another potential method of failure is a bulk breakdown of the solid insulating material. This is a more severe method of failure, as a solid does not have the self-healing capabilities of a gas, or even a liquid. This failure mechanism will be only briefly discussed here, as within this work the probability of bulk breakdown is very low due to the level of applied field.

2.5.1. Basic Principles

For bulk breakdown of solids to initiate, the electric field which is induced by the application of a voltage has to be high enough in order for free charge carriers to acquire a sufficient amount of energy that is not dissipated by photon emission alone. Within solid dielectrics, free charge carriers are not usually present. Therefore, for breakdown to initiate, the injection of charge carriers from the electrodes is required. As the applied electric field is increased, this causes charge-carrier injection, with the high fields accelerating these charge carriers, leading to breakdown [73]. Processes of field-enhanced thermionic emission, as described by Schottky [74], and direct field emission, as described by Fowler and Nordheim [75], account for charge-carrier emission at different levels of applied field. The breakdown channel will become filled with a gas of low relative permittivity, causing local electric-field enhancement, and increasing the probability of streamers forming and propagating to the point of breakdown upon application of subsequent voltage stress.

As shown in Figure 2.21, [76], the bulk solid breakdown mechanism can be classified into four categories.

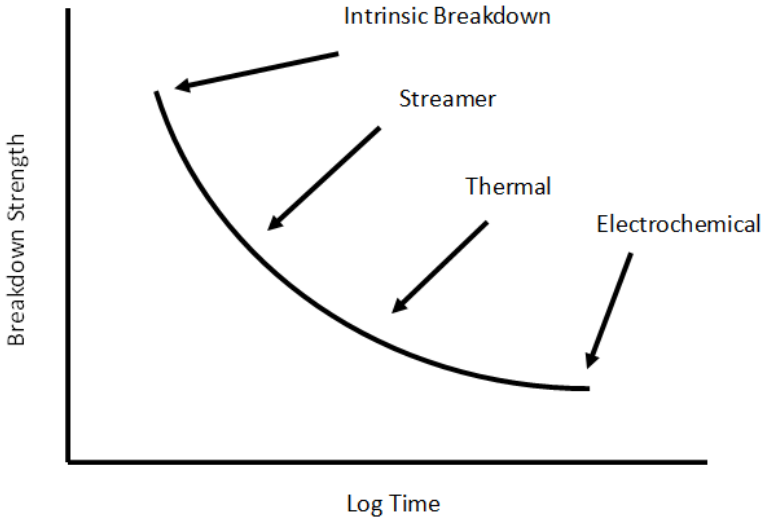

Figure 2.21 - Breakdown of solid dielectrics with respect to time, modified from [76]

For intrinsic breakdown, upon applying an electric field, electrons absorb energy and move from the valence band to the conduction band, traversing the energy gap that separates them. As this process continues, an increasing number of electrons accumulate in the conduction band, and eventually, the system experiences breakdown, [76]. For the streamer mechanism, electrons starting from the cathode will drift towards the anode, during this motion gaining energy from the field and losing it during collisions. When the energy gained by an electron exceeds the lattice ionization potential, an additional electron will be liberated due to collision of the first electron, [76]. This process repeats itself, resulting in the formation of an electron avalanche, and eventually streamer, if the number of electrons exceeds 10^8, if a void has been created in the solid, creating a dielectric lens and promotes breakdown. The thermal breakdown process is related to the conduction current heating up the dielectrics under applied voltage stress, leading to an increased thermal conductivity. If the heat generated by the energisation regime exceeds the heat that can be dissipated by the dielectric, thermal breakdown will occur. Over time, when exposed to different environmental conditions and continuous electrical stress, chemical reactions may take place within the solid, which will lead to breakdown.

2.5.2. Selection of Solid Dielectrics

The materials chosen for study in this project were High Density Polyethylene (HDPE), Polyetherimide (Ultem) and Polyoxymethylene (Delrin)

(Polyoxymethylene)), due to their prevalence in pulsed power applications. The differences in mechanical strength, permittivity and moisture absorption properties were deemed to provide suitable potential to result in different breakdown mechanisms and yield differences in measured breakdown voltages.

Further literature on the bulk breakdown of the selected solid samples can be found in [77 – 81].

2.6. GAS-SOLID INTERFACE SYSTEMS

As the basis of this thesis, the physics of the breakdown of gas-solid interfaces will be discussed in terms of basic processes leading to flashover. Many of the mechanisms occurring during the flashover process are linked with the gas breakdown theory from Section 2.3. Therefore, this section will reference these mechanisms, but be tailored in order to describe the flashover process specifically.

The flashover process follows the following phenomena [82] –

- Initial electron production
- Secondary electron generation process
- Electric field modifications
- Effect of environmental parameters on the flashover voltage

2.6.1. Initial Electron Production

2.6.1.1. Field emission

Field emission during a flashover follows a similar process in relation to the work function discussed in Section 2.4.1.1.

2.6.1.2. Photoelectric emission

Photoelectric emission specific to a surface flashover event can involve the dielectric material, which is in addition to the processes discussed in Section 2.4.1, in relation to gas breakdown.

The photoelectric yield, γ, is an important material property and characteristic of photoelectric emission in surface flashover events. The photoelectric yield is the

number of electrons per incident photon. Significant photoelectric yield, ~10^{-2} to 10^{-1}, typically occurs in the far UV or below the 200 nm range [45]. The dielectric primarily utilized for all flashover experiments discussed in [83] using different dielectric materials, for which a work function between 4.08 and 4.85 eV. Therefore, this work function will differ dependent upon the solid dielectric used in the insulation system.

2.6.2. Secondary Electron Emission

Miller [84] defined the secondary electron emission avalanche (SEEA) mechanism contributing to surface flashover in vacuum. This SEEA takes the form of the emission of electrons from the material surface, with secondary emission occurring due to electrons striking the surface of the electrodes, which can also be used to produce initial electron emission as discussed in Sections 2.4.1.1 and 2.6.1, to then go on to produce third generation electrons during the flashover process. A large amount of emission of electrons from the surface will create a positive surface charge on the material, as described in Figure 2.22, which will cause an electric field to be produced which is perpendicular to the surface of the dielectric. This process will then create a force where the electrons within the gap are attracted to the surface of the dielectric. A cascade effect, also known as an electron avalanche (shown in Figure 2.23) can then occur. However, during this process, the material surface will reach a neutral state, but under a fast-rising (ns) impulse voltage, there may not be time for the dielectric surface to neutralise. An important characteristic of SEEA is the secondary electron emission yield, δ, defining the number of secondary electrons emitted for every primary electron. For $\delta > 1$, more secondary electrons are escaping the material than incident primary electrons. If $\delta < 1$, there are more incident electrons than emitted secondary electrons [85]. Other factors which are important in the secondary ionisation process are the material absorption coefficient and the probability of escape. These factors are incorporated in the Gerald Dionne model in equation 2.56 [86] –

$$\delta = \left(\frac{B}{\xi}\right).\left(\frac{An}{\alpha}\right)^{\frac{1}{n}}.(\alpha d)^{\frac{1}{(n-1)}}.(1 - e^{-\alpha d}) \qquad 2.56$$

where –

- δ = secondary electron emission yield
- B = Secondary escape probability
- ξ = Secondary-electron excitation energy
- A = Primary-electron absorption constant
- n = Power-law exponent
- d = Maximum penetration depth

The secondary electron emission can be graphed to understand the secondary electron emission yield associated with the escape of a secondary particle, with respect to the energy of an incident particle. This graph is show in Figure 2.23 [86].

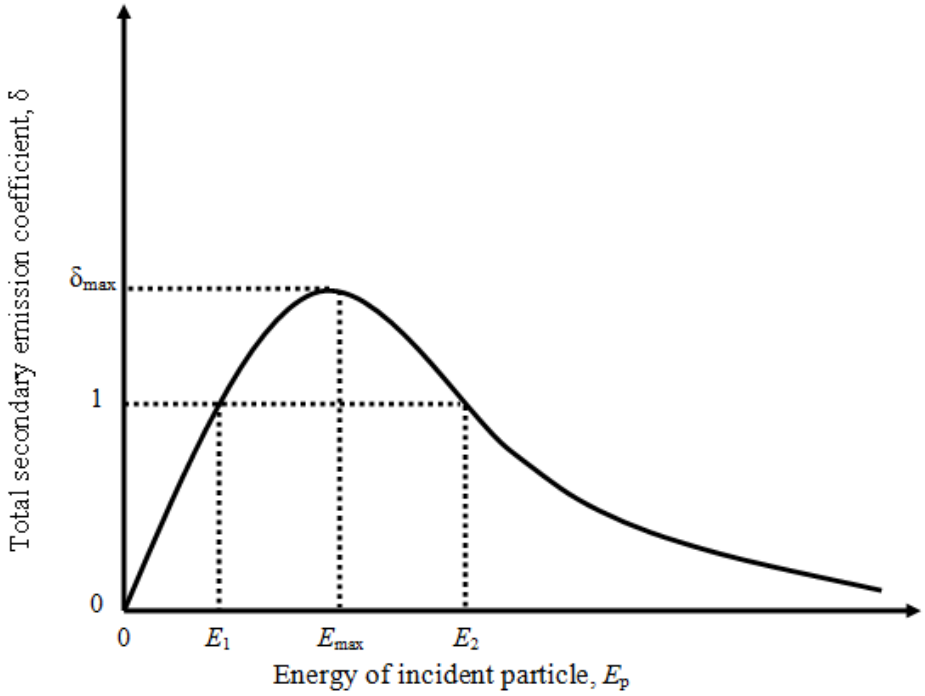

Figure 2.22 - Secondary electron emission versus the energy of incident electron, reproduced from work in [86]

Figure 2.22 shows the crossover points, where the yield is equal to 1. The maximum point associated with the graph is from electrons penetrating deep into the surface. Above E_2 , the penetration depth is such that the secondary electrons have a lower probability of reaching the surface.

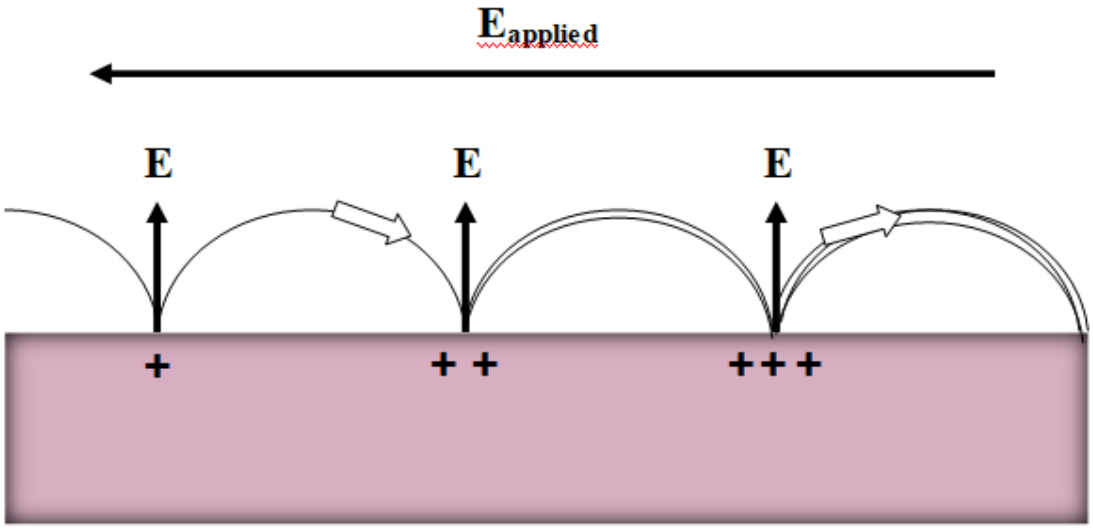

Figure 2.23 - Surface cascade flashover with associated electric fields

Shown in Figure 2.23 is an illustrative example of the flashover process over a dielectric material. The top layer of the surface is the interface between vacuum and the solid material. When a dielectric material is subjected to an increasing applied voltage, the emission of primary electrons due to the Schottky effect increases exponentially. These primary electrons, in turn, cause the multiplication of secondary electrons on the surface of the dielectric. The cumulative effect of this electron multiplication eventually leads to the formation of a flashover channel.

In this work however, pressurised gas will be used. As Miller's work was conducted in vacuum, this means that the mean electron mean free path would be much greater compared to a system with elevated pressures. The distance which an electron can travel within a vacuum and not collide with another particle is up to nearly 80 μm [87]. However, during flashover or breakdown within an atmospheric-pressure gaseous environment, an electron mean free path of the order of 100 nm can result, a distance of almost three orders of magnitude shorter than in a vacuum [41]. As surface flashover in pressurised gas is an important theme which will run throughout this thesis, this has been further explained in Section 2.6.3.

2.6.3. Electric Field Manipulation

Discussed in this section are key parameters that will determine the field distribution in a gas-solid insulation system, and ultimately the flashover voltage.

2.6.3.1. Permittivity Effect

The permittivity of the material has an effect on the flashover strength of solid insulation, shown in [88], [89]. Increasing the permittivity of the material was seen to decrease the flashover strength, due to field enhancement. This enhancement of the electric field strength is comprised of normal and tangential fields established due to the specific properties of the material tested. Under applied voltage, the electric field created will result in the ions within the material moving towards the electrode of opposite polarity. Interfacial polarization can occur due to the migration of charge carriers to the interfacial boundaries under the effect of an applied field [90]. This results in an enhanced field at the surface of the material. This can be determined by equation 2.57, in terms of the conduction current densities associated with the air, J_a, and the solid dielectric, J_s. [91] -

$$J_a - J_s = \sigma_a E_0(t) - \sigma_s E_s(t) = \frac{\partial \gamma_s(t)}{\partial t} \qquad 2.57$$

where -

- σ_a = Conductivity of gaseous dielectric (air) (S/m)
- $E_0(t)$ = External applied field (kV/cm)
- σ_s = Conductivity of solid dielectric (S/m)
- $E_s(t)$ = Electric field in the solid dielectric (kV/cm)
- $\gamma_s(t)$ = Non-compensated free surface charge

This surface charge is related to the electric flux density on either side of the gas-solid interface, as shown in equation 2.58 -

$$\gamma_s(t) = \varepsilon_0 \varepsilon_a E_0(t) - \varepsilon_0 \varepsilon_s E_s(t) \qquad 2.58$$

where –

- ε_0 = Permittivity of free space (~8.85*10^{-12} F/m)
- ε_g = Permittivity of gaseous dielectric (air)
- ε_s = Permittivity of solid dielectric

Therefore, if the permittivity of one material is increased when the other is kept constant, the field strength will increase for the constant permittivity material, and decrease for the material where the permittivity is being increased resulting in a higher field strength at the surface of the solid dielectric. This enhancement of the field strength due to varying permittivity is shown on Figure 2.24, which shows the effect on the field lines with changing permittivity. The first illustration in Figure 2.24a shows the dielectric when there is perfect contact with the electrode, where the full edge of the dielectric is normal to the electrode surface. The second and third parts show the field distribution when there is an air gap included between the dielectric and the electrode. Figure 2.24b shows the behaviour when the permittivity of the dielectric is high (ε = 10), and the bottom illustration in Figure 2.24c, when the permittivity of the dielectric is low (ε = 3). This results in a stronger field strength at the triple junction point, and due to the field enhancement at higher permittivity values, results in a lower discharge initiation voltage under an applied field.

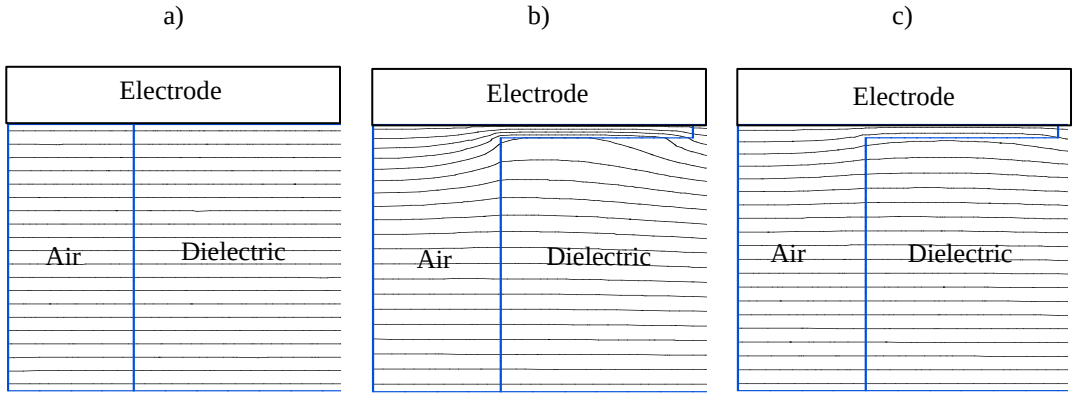

Figure 2.24 - Effect of permittivity and spacer material on the electric field lines under applied voltages

2.6.3.2. Dielectric shape and surface modification

Another property that will have an effect on the flashover strength of air-solid interfaces is the surface roughness of the solid materials, as illustrated in Figure 2,25. Work has been completed in order to coat the insulator surface with a semi-conductor

material in [92], [93]. Other work to improve the flashover strength focused on changing the angle of the triple junction, which will be discussed in the next section, as well as changing the angle of the insulator to prevent secondary electrons from returning to the surface, [94]. The work in [95] shows some flashover data with the manipulation of the shape of the solid dielectric, which ties into discussion of the angle of the triple junction. The results showed that a positive-angled cone (example given from angle β in Figure 2.26) had higher flashover voltage compared to negative-angled cone (example given showing angle α in Figure 2.26). It was shown that a positive-angled cone design results in a higher flashover strength, due to the inclined electric field drawing electrons away from the surface of the insulator, thus preventing most of the field-emitted electrons from the triple junction from colliding with the insulator surface. Also, due to the angle, any secondary electrons which are developed are then directed away from the insulator surface. For the negative-angled cone, the electrons emitted from the cathode easily strike the insulator and initiate flashover [94]. In the interest of reduced complexity, when reduced space is available, a cylindrical spacer is often used in flashover systems, [96].

Work was completed in [97], [98] in order to see the effect of the surface roughness of the solid spacer on the flashover voltage. Ultimately, the effect of increasing the roughness of the insulator from 0.1 µm to 1.4 µm was found to decrease the flashover strength by 25 kV. This effect was also found to be more prominent (greater reductions in flashover strength) for negative polarity lightning impulses compared to positive. Recent work has been completed in [99], where the behaviour of modified surfaces was simulated, in order to determine the effect on streamer propagation along the surface. The authors found that a longer time was taken for the streamer to reach the ground electrode for rough surfaces than for smooth surfaces, due to charge being trapped in the indentations, affecting the streamer propagation along the surface. Experimental work on surface modification to a dielectric surface is shown in [100] where the researchers show that an increase in the flashover of a profiled surface in comparison to a smooth surface can be increased by 26.5 kV.

The way in which the surface of a dielectric material has an effect on the flashover voltage of an insulation system can be shown by the illustration in Figure 2.25. from [101]

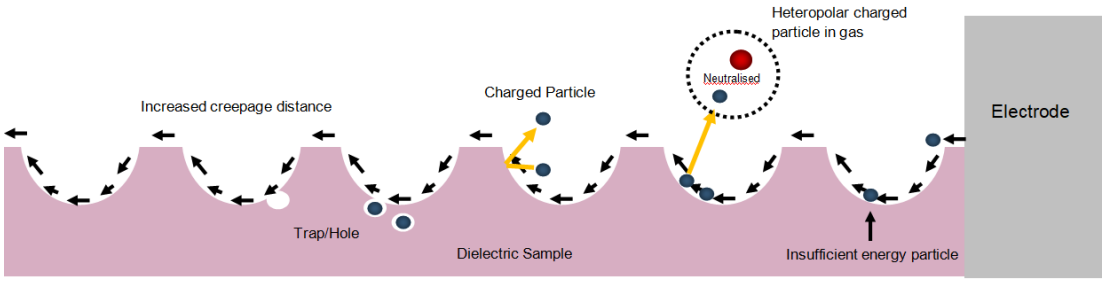

Figure 2.25 – surface discharge characteristics of roughened sample modified from [101]

When examining a surface that has been intentionally made rough, we observe the emergence of uneven grooves and small pits on the sample's surface. These surface irregularities indirectly influence the distance electrons can travel (referred to as creepage distance) and impede the smooth progress of electrons across the sample's surface. Concurrently, a subset of charged particles lacking sufficient energy encounters obstacles as they move toward these grooves or pits. These charged particles lack the necessary energy to maintain their forward momentum. They either neutralize other charged particles in the air or their trajectory is altered due to reflections off the surface, which results in an increase in the voltage needed to induce a discharge (flashover voltage). This effect is especially pronounced when the surface texture is oriented perpendicularly to the direction of the external field. The combined influence of these effects contributes to further hindering the occurrence of flashover along the surface. Nevertheless, the uneven surface may also lead to inadequate contact between the sample and the electrode, leading to distortions in the electric field strength near the electrode. The initial electrons are generated at the point where the gas, electrode, and sample meet, known as the triple junction point (TJP). This phenomenon further encourages the progression of a flashover event. Therefore, at lower degrees of roughness, the primary mechanism is the barrier effect obstructing the movement of charged particles, across a material's surface. However, as the roughness increases, the gap between the sample and the electrode widens, making the promotion effect, which encourages the acceleration or enhanced movement of charged particles more influential in the process.

As discussed previously in Section 2.6.3, the permittivity of the solid material can have an effect on the field enhancement at the surface of the material, and therefore

on the flashover strength of the insulation system. Another important factor in relation to the discussion related to Figure 2.25, is the angle that is created at the triple junction point of the insulation system, due to the surface profile of the material. The triple junction point is the point where the electrode, insulator and gas (air) contact, and generally where the flashover is initiated from due to the enhancement of the electric field at this point. The characteristics of a triple junction point with respect to angle of contact and permittivity of material are illustrated in Figure 2.26, which shows a cross-section of a triple junction point, where the cathode, solid dielectric and vacuum contact [102]. The work completed in [102] shows the field behaviour which is associated with different triple junction point angles. This paper deals with the flashover behaviour in a vacuum, so it is assumed that the flashover initiates over the surface of the material. The contact angle is changed from +90 degrees to -90 degrees. As the angle is changed, there is a dramatic effect on the field strength, as discussed in the following text, using Figure 2.27 also. This will now be discussed in relation to triple junction point angle.

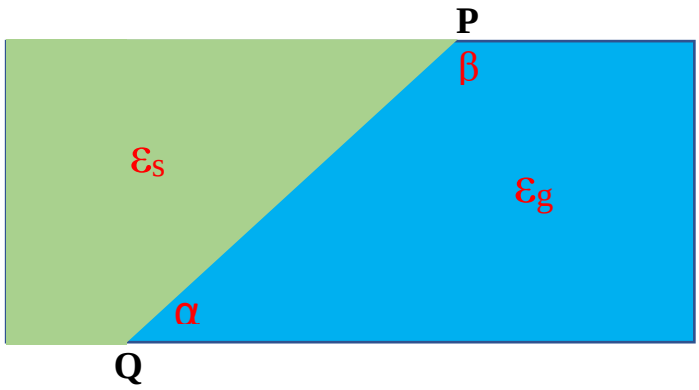

Figure 2.26 – Dielectric triple junction properties modified from [102], P and Q are triple junction points with α and β denoting the angle characterised at each triple junction point. ε_s related to the permittivity associated with the solid dielectric and ε_g is associated with the permittivity of the gas dielectric.

Figure 2.27 illustrates the behaviour of the electric field distribution at the surface of the material for three different spacer contact angles, as shown at the top of Figure 2.27. As the material shape is changed, the electric field changes correspondingly, due to the new angles created at the triple junction point.

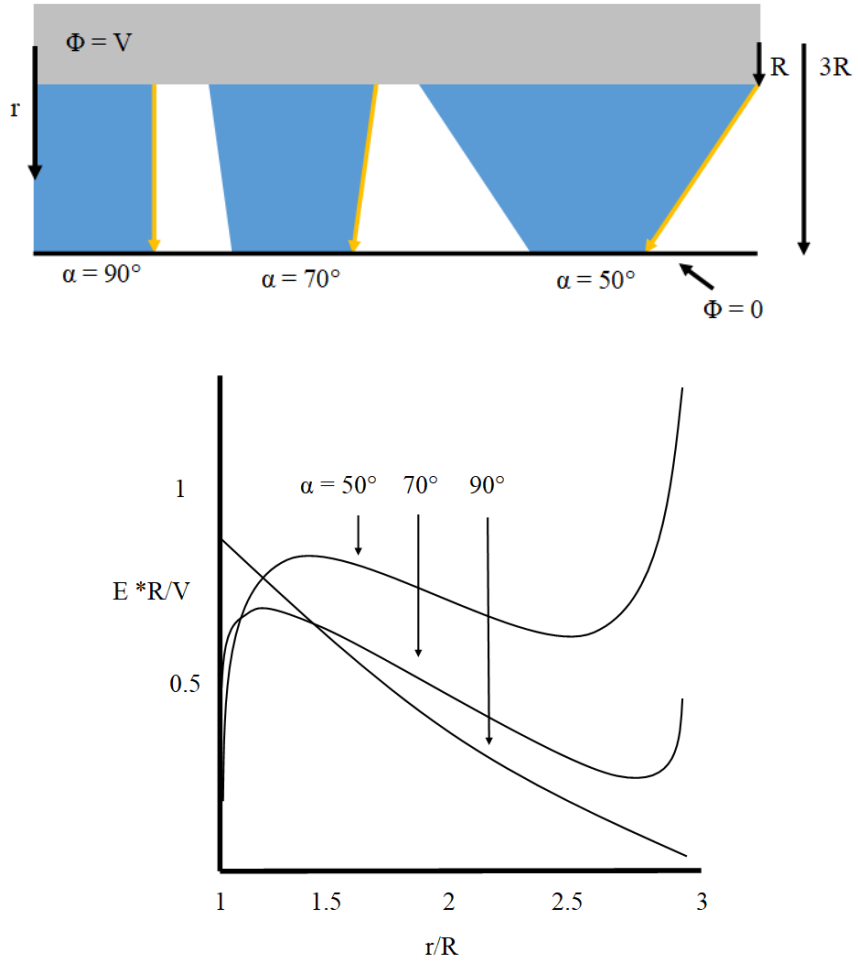

Figure 2.27 - Electric field strength along the surface of different spacer shapes modified from [102], permittivity of material used ε = 6

Figure 2.27 shows the field distribution along the dielectric spacer. It shows that when the angle is 50° or 70°, there is an increase in the field strength at the triple junction point when r/R = 3, as shown in Figure 2.26.

From Figure 2.28, the field strength E, at the point of contact near P or Q, shown in Figure 2.26, can be expressed as equation 2.59, [102], [103].

$$E = K.l^m \qquad 2.59$$

where –

- l = the distance from P or Q (shown in Figure 2.26)
- K = a constant dependent upon the angle, α, and the permittivity ratio
- m = exponent, the sign of which is dependent upon the two permittivity's

$m < 0$ when $\varepsilon_s > \varepsilon_g$ and $m > 0$ when $\varepsilon_s < \varepsilon_g$ at $\alpha < 90°$, where ε_s and ε_g are shown in Figure 2.26, but the opposite is true for $\alpha > 90°$. This means that approaching point P, the field strength is theoretically infinitely high when $\varepsilon_s > \varepsilon_g$ and theoretically zero when $\varepsilon_s < \varepsilon_g$. The value of m can be shown as Figure 2.28 in relation to the contact angle of the dielectric, as well as the permittivity's and the relationship between the two permittivity's.

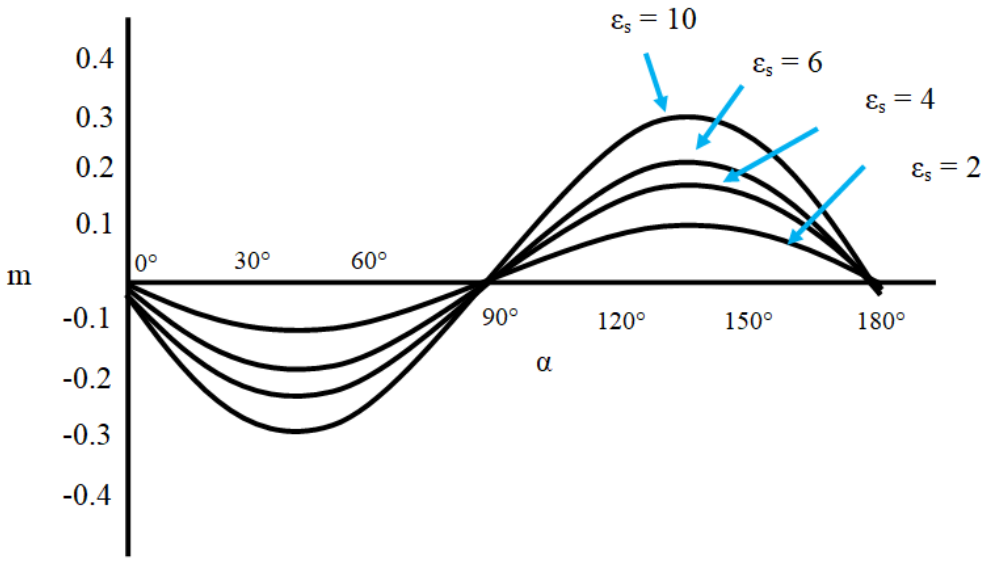

Figure 2.28 - Permittivity and contact point angle effect on 'm', modified from figure in [102]

As the permittivity ε_s increases, the absolute value of m is increased; m can be found using equation 2.60 [102] –

$$n\alpha + \varepsilon_s . tan.n(\pi - \alpha) = 0 \qquad 2.60$$

where $\varepsilon_s = \varepsilon_d / \varepsilon_g$.

In relation to Figure 2.28, it is explained in [102] that m is relative to contact angle, α, for $2 \leq \varepsilon_s \leq 10$. The absolute value of m increases with ε_s, but it is only 0.3 at the maximum, even for $\varepsilon_s = 10$. This means that the field strength increases only slowly when approaching a contact point. As can be seen in Figure 2.28, $m = 0$ at $\alpha = 0$ and at $\alpha = 90°$, indicating that the field does not exhibit a singularity, 0, in these cases.

It should be noted that these results were gathered under vacuum, where the effect of environmental conditions such as air quality and relative humidity will not impact the flashover voltage. In air, variation in these parameters could cause partial discharge activity, leading to different mechanisms of flashover. The work completed in [104] shows simulation results regarding the electric field distribution from the triple junction point over the spacer material. It was shown that as the angle increased from 10 degrees to 140 degrees, the electric field intensity decreases. The maximum field intensity found by the authors was between 10 and 20 degrees at the contact point. Overall, the findings resulted in a 90° insulator angle being selected, to minimise the field enhancement.

2.6.3.3. Environmental Parameters

It has been widely published that elevated air humidity is seen to decrease the flashover strength of solid insulation. In [105], the authors showed that for an increase in relative humidity from 10% to 90%, a corresponding decrease in flashover voltage of around 50% was evident. It was also seen that as the percentage of moisture increases with increasing relative humidity, a film of water was accumulated on the surface of the solid material, leading to a consistent discharge path across the surface of the material, rather than through the bulk of the air. A similar system design was used in [106], where the effect of increasing humidity was seen to reduce the flashover strength of the insulating system. This conductive area, which is related to the film of water on the material surface as the humidity is increased, increases the probability of the production of secondary electrons, leading to flashover. Under positive polarity, the flashover strength has been found to generally increase with increasing humidity, whereas for negative polarity, the flashover voltage decreases with increasing RH. This can be attributed to the finding that humidity inhibits the inception and development of positive impulsive discharges but exerts minimal influence upon negative streamers [107]. The influence of RH on breakdown voltage can be explained by the following phenomena. For negative polarity, the reduction in breakdown voltage with increasing RH can be attributed to the reduced pre-stressing effect, associated with an increase in humidity. For positive polarity, the increase in breakdown voltage with increasing RH could be due to the lesser amount of space

charge generated under positive polarity at high humidity. There is experimental evidence [108 – 110] that supports the notion that positive space charge diminishes with increasing humidity. Results reported in [111] also show a difference in corona inception voltages, with negative inception voltages being lower than positive due to the effect of humidity.

The hydrophobic/hydrophilic nature of a material will also be an important factor in determining the flashover strength in humid air, as outlined in [112 – 114]. When the material is hydrophobic, the ability of the droplet to move along the surface is important when close to the triple junction point, resulting in a lower field intensity, due to the movement of the droplet towards, and coming into contact with, the electrode, which eliminates any air gap, and therefore increases the flashover voltage. However, dependant on the wettability of the material, under this movement, the droplet could produce a film of water along the length of the material surface, which will result in a decrease in the flashover voltage, as discussed in [106]. Linking this with the surface manipulation discussed in Section 2.6.3, the authors of [115] show that surface roughness has an effect on the contact angle, depending upon how hydrophobic or hydrophilic the material is. The authors showed that, if the material surface is hydrophobic, it will be even more hydrophobic after treatment to roughen the surface. If the material surface is hydrophilic, it will be even more hydrophilic after treatment to roughen the surface. This result is in line with Wenzel's equation (2.61) [116], which shows that surface roughness treatment will only amplify the surface wettability of a certain material.

$$cos\theta_w = R_a cos\theta \tag{2.61}$$

In equation (2.61), θ_w and θ are the water contact angles of the rough and smooth surfaces of the material, respectively, and R_a is the surface roughness of the material. The contact angle of water droplets on a spacer surface is used to determine whether the material is hydrophobic or hydrophilic and it is commonly known that a droplet with a contact angle of >90° indicates a hydrophobic surface, while a contact angle of <90° indicates a hydrophilic surface [117].

Generally, when regarding surface flashover, studies on vacuum systems are common, due to the probability of the occurrence of flashover increasing, due to the desorption of gas from the dielectric surface. When testing insulating systems in pressurised gases, however, there are other mechanisms that result in insulation failure, as shown in the review, [118]. Considering all the mechanisms discussed in Sections 2.3 and

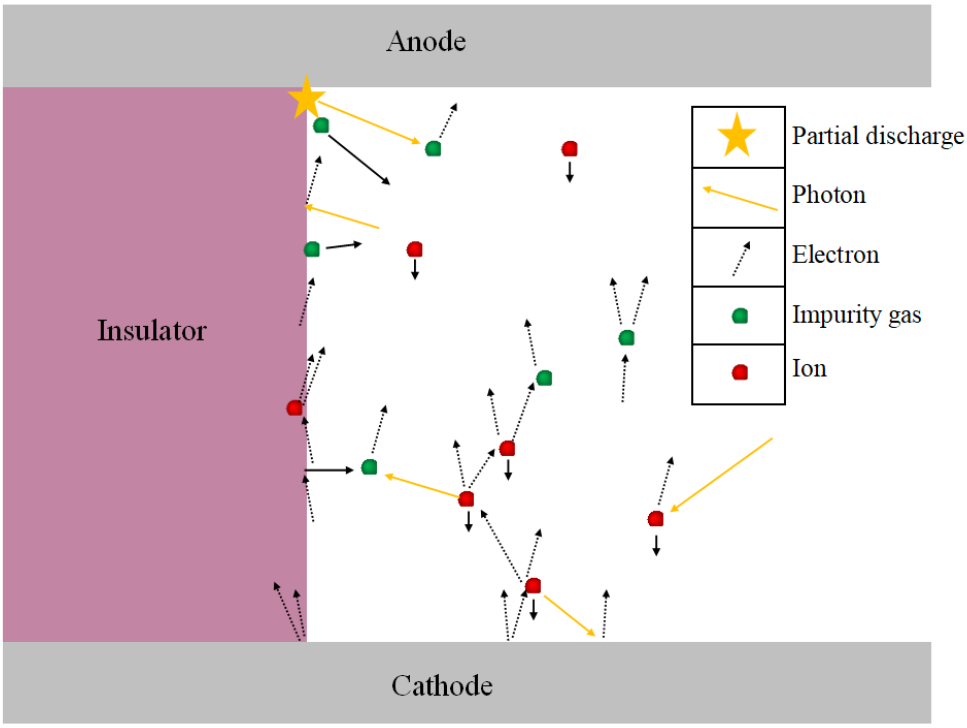

Figure 2.29 - Different processes of surface flashover in compressed gases, modified from [119]

2.6, summarising all of the key process involved in the flashover of a solid in compressed gases, Figure 2.29 shows some of the key processes that play an important role in the flashover of solid insulators in gases, [119].

Surface charging of the dielectric surface is dominant in driving the flashover of compressed air-solid interfaces. This surface charge accumulation can be due to free electrons impacting the surface of the material and being adsorbed, or due to charge from the spacer itself, whether intrinsic to the material or on the surface [120].

The effect of surface charging on the flashover voltage of an insulation system is discussed in [121]. The authors found that, as the pressure inside the test apparatus was changed, the charge density on the surface of the dielectric changed. In SF_6, the authors observed that as the pressure was increased, the surface charge density was increased.

In terms of free electron sources in compressed insulation systems [122], these include –

- Background radiation natural ionisation
- Secondary electron emission
- Field emission from electrons
- Partial discharges in the gas

These sources of free electrons have already been discussed, in Section 2.6. What is important when working with compressed gas insulation systems is the potential for gas breakdown away from the spacer surface itself, following the mechanisms discussed in Section 2.3. Work in [123] has been completed, characterising the behaviour of streamer discharges near dielectric surfaces. Positive discharges were found to move away from the dielectric surface, with the authors concluding that this was due to the abundance of charge carriers in the gas, generated by photoionisation, enabling the streamer to propagate following the field lines. In [124], the author found that when a streamer is propagating close to the surface of a dielectric, the level of photoionisation which would normally proceed within an open gas gap will be reduced, effectively being blocked at the side of the streamer head closest to the solid dielectric. If the dielectric surface were negatively charged, however, then the surface could provide a source of free electrons.

In [125] and [126], the authors have simulated both positive and negative streamers, analysing their level of attraction to the surface of a dielectric during energisation. The authors concluded that, when comparing the propagation of positive and negative streamers, at short distances to the dielectric, streamers of both polarities will be attracted to the surface of the spacer. When the permittivity of the material was changed, this slowed down the propagation of negative surface streamers. Also, in [125], as the initiation point which was seeded further away from the triple junction point, the time taken for the positive streamer to come in contact with the dielectric increased. Also, differences in the velocity of the streamers were also evident, travelling 10 mm in 4 ns for bulk gas breakdown, increasing to 10 mm in 20 ns for surface flashover, when initiated 1 mm from the dielectric.

2.6.4. Conclusions

From the literature review important aspects have been identified that have been taken forward into the design of the study, and the effect each has on the flashover voltage of the insulation system, as well as the synergistic effect of multiple factors. Therefore, the following aspects have been included –

- Effect of Insulator Material
- Effect of Material Surface
- Effect of Triple Junction Point Angle
- Effect of Humidity
- Effect of Pressure
- Effect of Polarity

The following Chapter III will discuss these aspects and the design and implementation of these systems, building a foundation for the experimental results presented and discussed in Chapters IV, V and VI.

The principles of pulsed power systems have been discussed in terms of energy storage methods. The fundamentals of the breakdown of gases, solids, and gas-solid interfaces have also been outlined. Special consideration was given to the breakdown mechanisms in gases and across gas-solid interfaces, due to the low probability of bulk solid breakdown, due to the dimensions of the solid samples and magnitude of the test voltages. Within each section, historical and recent references were discussed, relevant to the scope of this thesis.

This thesis will consist of flashover voltage data for air-solid interfaces with varying solid material, surface manipulation, humidity, pressure and impulse polarity, providing new data and associated discussion, relevant to the pulsed power industry. Under the fast *dV/dt* impulsive voltages used in this thesis, the synergistic effect of physical and environmental parameters on the breakdown/flashover performance of the system will be discussed. Therefore, this work will provide a useful source of information within the pulsed power industry, for scientists and engineers involved in the design process of insulating mechanical supports for various industrial systems.

2.7. CHAPTER II REFERENCES

[1] Lin, Tianyu, Yongpeng Zhang, Zhijian Lu, Zhengwen Wang, Peng Wei, Chengying Liu, and Lanjun Yang. 2021. "Dielectric Surface Flashover under Long-Term Repetitive Microsecond Pulses in Compressed Gas Environment" *Materials* 14, no. 12: 3343. https://doi.org/10.3390/ma14123343

[2] Liang Zhao, Jian Cang Sun, *and* Chun Liang Liu, "Review of developments on polymers' breakdown characteristics and mechanisms on a nanosecond time scale", AIP Advances 10, 035206 (2020) https://doi.org/10.1063/1.5110273

[3] J. C. Martin, "THE PRE-HISTORY OF PULSED POWER," in IEE Colloquium on Pulsed Power, 1995

[4] G. A. Mesyats, PULSED POWER. Springer, 2005.

[5] Jane Lehr and Pralhad Ron – Foundations of Pulsed Power Technology, IEEE PRESSS, Wiley, 2017

[6] H. Bluhm, Pulsed Power Systems. Springer Berlin Heidelberg, 2006

[7] H. W. Lee, S. K. Kang, S. K. Kwon, I. H. Won, H. C. Kwon, H. Y. Kim, J. K. Lee, and H. W. Lee, "Enhancement of microwave plasma characteristics for biomedical applications using pulse modulation method," in *IEEE Conference on Plasma Science*, 2013, pp. 312–315.

[8] S. R. Rajulapati, F. A. Husain, S. B. Ananthapadmanabha, K. H. Schoenbach, and S. Xiao, "Nanosecond Biphasic Pulse Generators for Biomedical Applications," in *IEEE Conference on Plasma Science*, 2013, pp. 593–596.

[9] T. Masuoka, T. Kawakami, T. Kiyoshima, C. Asada, Y. Nakamura, K. Teranishi, and N. Shimomura, "Effect of Pulsed Discharges on Mycelium Growth of Sparassis Crispa," in *IEEE Pulsed Power Conference*, 2015, pp. 67–71.

[10] V. Tran, T. Park, H. Choi, and J. Choi, "High Efficiency and Reliability Pulsed Power System for Medical Lasers With the Digital Controller" Ii . *Circuit Descriptions and Basic*," pp. 223–228, 2015.

[11] S. Matsubara, A. Nakagawa, S. Kuniyasu, K. Teranishi, Y. Uto, and N. Shimomura, 266“Investigation of effect of applied nanosecond pulsed electric fields on tumor,” *Dig. Tech. Pap. Int. Pulsed Power Conf.*, vol. 2015–Octob, pp. 374–378, 2015

[12] H. Akiyama, T. Sakugawa, T. Namihira, K. Takaki, Y. Minamitani, and N. Shimomura, “Industrial applications of pulsed power technology,” *IEEE Trans. Dielectr. Electr. Insul.*, vol. 14, no. 5, pp. 1051–1064, 2007.

[13] M. P. Wilson, L. Balmer, M. J. Given, S. J. MacGregor, and I. V. Timoshkin, “Optimization of the spark gap parameters for high power ultrasound applications,” *Conf. Rec. Int. Power Modul. Symp. High Volt.* Work., pp. 306–309, 2006.

[14] I. V. Timoshkin, J. W. Mackersie, and S. J. MacGregor, “Plasma channel miniature hole drilling technology,” *IEEE Trans. Plasma Sci.*, vol. 32, no. 5 I, pp. 2055–2061, 2004.

[15] S. Qin, I. V. Timoshkin, M. MacLean, M. P. Wilson, S. J. MacGregor, M. J. Given, J. G. Anderson, and T. Wang, “Pulsed electric field treatment of microalgae: Inactivation tendencies and energy consumption,” *IEEE Trans. Plasma Sci.*, vol. 42, no. 10, pp. 3191–3196, 2014.

[16] M. Zhang *et al.*, "Design of High Voltage Pulsed Power Supply for HFRC," in *IEEE Transactions on Plasma Science*, vol. 48, no. 6, pp. 1688-1692, June 2020, doi: 10.1109/TPS.2020.2987038.

[17] J. Kwak *et al.*, "KSTAR Status and Upgrade Plan Toward Fusion Reactor," in *IEEE Transactions on Plasma Science*, vol. 48, no. 6, pp. 1388-1395, June 2020, doi: 10.1109/TPS.2020.2964776

[18] Y. Lv *et al.*, "Optimization of the Pulsed High-Field Coil in a Magnetic Trap Type Plasma Compression Device," in *IEEE Transactions on Applied Superconductivity*, vol. 30, no. 4, pp. 1-5, June 2020, Art no. 4201605, doi: 10.1109/TASC.2020.2968261

[19] T. A. Mehlhorn, "Pulsed Power as a Science: Predictive Simulations for Beams, Z-Pinches, and Other Applications," in *IEEE Transactions on Plasma Science*, vol. 48, no. 4, pp. 768-791, April 2020, doi: 10.1109/TPS.2020.2967648.

[20] A. Guenther, M. Kristiansen, and T. Martin, “Opening switches,” in Advances in pulsed power technology: *Opening Switches, New York: Plenum Press*, 1987, p. 7

[21] J. R. Macdonald, M. A. Schneider, J. B. Ennis, F. W. Macdougall, and X. H. Yang, “High Energy Density Capacitors,” in *IEEE Electrical Insulation Conference*, 2009, no. June, pp. 306–309.

[22] Mirshamsi, Ebrahim - ‘Performance of opening and closing switches for pulsed-power networks’. Loughborough University. 1996, PhD Thesis. https://hdl.handle.net/2134/35586

[23] Wang, Ge, Lu, Zhilun, Li, Yong, Li, Linhao, Ji, Hongfen, Feteira, Antonio, Zhou, Di, Wang, Dawei, Zhang, Shujun, Reaney, Ian M, ‘Electro ceramics for High-Energy Density Capacitors: Current Status and Future Perspectives’, *American Chemical Society, Chemical Reviews*, VL - 121, IS - 10, 2021

[24] T. R. Jow *et al*., "Pulsed power capacitor development and outlook," *2015 IEEE Pulsed Power Conference (PPC)*, Austin, TX, 2015, pp. 1-7.

[25] R.A. Cooper, J.B. Ennis, and D.L. Smith, “ZR Marx Capacitor Life Test and Production Statistics”. *Proceedings of the IEEE International Pulsed Power Conference*, 2005.

[26] A. H. Bushnell, “Interfacing pulsed power systems to switching power supplies,” Proc.2002 *IEEE International Power Modulator Conference*, pp. 290-292, 2002.

[27] E. Marx, Deutsches Reichpatent No. 455 933,1923.

[28] R.A. Fitch, Marx-and Marx-Like High Voltage Generators. *IEEETrans.Nucl.Sci.*, Vol. 18, No. 4, pp. 190–198, 1971.

[29] G.W. Swift, Charging Time of a High Voltage Impulse Generator. *IEEE Electron. Lett.*, Vol. 5, No. 21, p. 534, 1969.

[30] G.A. Mesyats, *Pulsed Power*, Kluwer Academic/Plenum Publishers, 2005.

[31] F. Heilbronner, “Firing of multistage impulse generators,” Elektrotech Z Ausg A, vol. 92 (6), pp. 372-376, 1971.

[32] D. Kind, and K. Feser, “Fundamental principles of high-voltage test techniques,” in *High Voltage Test Techniques*, 2nd ed. London: Newnes, 2001, ch. 1, pp. 1-109.

[33] R.A. Cooper, J.B. Ennis, W.J. Gratza, R. Miller, S.K. Lam, and P.S. Sincerny, “100 kV capacitor development for fast Marx generators,” Proc. 14th *IEEE International Pulsed Power Conference*, vol. 1, pp. 530-533, 2003.

[34] A. S. Yudin, S. S. Martemyanov, A. A. Bukharkin, I. V. Bugaev and E. G. Krastelev, "Triggered Spark Gap Switch with Gas Circulation for Repetitively Operated Multistage Marx Generator," *2018 20th International Symposium on High-Current Electronics (ISHCE)*, Tomsk, 2018, pp. 166-169

[35] A. A. Fridman, L.A. Kennedy, “Plasma physics and engineering”, New York: Taylor & Francis, 2004.

[36] Michael Keidar and Isak I. Beilis “Plasma Engineering, Applications from Aerospace to Bio- and Nanotechnology”, Chapter 1 – Pages 1 – 78, Plasma Concepts *Elselvier* 2013 ISBN:978-0-12-385977-8

[37] M Abdel-Salam H Anis, A El-Morshedy, R Radwan 'High Voltage Engineering' [Book Section] // High Voltage Engineering. - NY: Marcel Dekker, 2010. - Vols. 149-172 'The corona discharge'.

[38] Ravindra Arora, Wolfgang Mosch - Field Dependant Behaviours of Air and Other Gaseous Dielectrics" *Chapter 3 High Voltage and Electrical Insulation Engineering* (IEEE) Wiley pages 69 - 168

[39] M Abdel-Salam H Anis, A El-Morshedy, R Radwan High Voltage Engineering 'Ionization and deionization processes in gases'. [Book Section] // High Voltage Engineering. - [s.l.] : Marcel Dekker, 2010. - Vols. 81-103

[40] E. Kuffel, W. S. Zaengl, and J. Kuffel, High Voltage Engineering: Fundamentals, Newnes, New York, NY, 2000

[41] Nasser, Essam, Fundamentals of Gaseous Electronics. Wiley-Interscience, New York, NY, 1971.

[42] J. M. Meek, J. D. Craggs - ‘Electrical breakdown of gases’ - Chichester, New York : Wiley series in plasma physics, 1978. - Vol. chapter 7.

[43] M Abdel-Salam H Anis, A El-Morshedy, R Radwan High Voltage Engineering 'Electrical breakdown of gases'. [Book Section] // High Voltage Engineering. - [s.l.] : Marcel Dekeer, 2010. - Vols. 115

[44] Andreas Kuchler “High Voltage Engineering, Fundamentals Technology Applications”, Springer Vieweg Chapter 3 – Electric Strength page 141 – 217 2018,

[45] Y.P. Raizer, Gas Discharge Physics, Springer-Verlag, New York, NY, p. 71, 1991.

[46] F.Paschen,Uber die zum funkenu bergangin Luft,Wasserstoff und Kohlensaure bei verschiedenen Druckeneforderliche Potential differenz. *Ann. Phys .Chem.* ,Vol.37, p.69,1889

[47] M S Naidu, V Kamaraju, “High Voltage Engineering” McGraw Hill Education (India) Private Limited ISBN-13: 978-1-25-906289-6, 2013 Chapter 2. conduction and breakdown in gases pages

[48] Dmitry Levko, Robert R. Arslanbekov, Vladimir I. Kolobov; Modified Paschen curves for pulsed breakdown. *Physics of Plasmas* 1 June 2019; 26 (6): 064502. https://doi.org/10.1063/1.5108732]

[49] L. Babich and T. V. Loĭko, "Generalized Paschen’s Law for Overvoltage Conditions," in *IEEE Transactions on Plasma Science*, vol. 44, no. 12, pp. 3243-3248, Dec. 2016, doi: 10.1109/TPS.2016.2629022.

[50] J.M.Meek and J.D.Craggs, *Electrical Breakdown of Gases*, Oxford Press, p.266, 1953.

[51] Briels T M P, Kos J, Winands G J J, van Veldhuizen E M andEbert U 2008 Positive and negative streamers in ambient air:measuring diameter, velocity and dissipated energyJ. Phys.D: Appl. Phys.41234004

[52] Alejandro Luque and Valeria Ratushnaya and Ute Ebert “Positive and negative streamers in ambient air: modelling evolution and velocities” *Journal of Physics D: Applied Physics* 2008 10.1088/0022-3727/41/23/234005

[53] Tarasenko, V.F., Naidis, G.V., Beloplotov, D.V. *et al.* Measuring and Modeling Streamer Velocity at an Air Discharge in a Highly Inhomogeneous Electric Field. *Plasma Phys. Rep.* **46,** 320–327 (2020). https://doi.org/10.1134/S1063780X20030113

[54] Asif Iqbal[4,1], Daniel Wozniak[4,2,3], Md Ziaur Rahman[2,3], Sneha Banerjee[5,1], John Verboncoeur[1], Peng Zhang[6,1] and Chunqi Jiang[6,2,3] Influence of discharge polarity on streamer breakdown criterion of ambient air in a non-uniform electric field' *Journal of Physics D: Applied Physics*, Volume 56, Number 3, December 2022

[55] Sadaoui, F. and Abderrahmane Beroual. "Influence of polarity on breakdown voltage of gases in divergent electric field under lightning impulse voltages." 2012 *International Conference on High Voltage Engineering and Application (*2012): 496-499.

[56] P. Chowdhuri, A. K. Mishra, P. M. Martin and B. W. McConnell, "The effects of nonstandard lightning voltage waveshapes on the impulse strength of short air gaps," in *IEEE Transactions on Power Delivery*, vol. 9, no. 4, pp. 1991-1999, Oct. 1994, doi: 10.1109/61.329531.]

[57] Beloplotov, Dmitry & Tarasenko, Victor & Lomaev, Mikhail & Sorokin, Dmitry. (2015). Inverted Polarity Effect at the Subnanosecond High-Voltage Breakdown of Air. *IEEE Transactions on Plasma Science*. 43. 1-7. 10.1109/TPS.2015.2480872.

[58] A. Verhaart and P. C. T. Van der Laan, "The influence of water vapor on avalanches in air", *J. Appl. Phys.*, Vol. 55, pp. 3286-3292, 1984

[59] KUFFEL, E.: 'Electron Attachment Coefficients in Oxygen, Dry Air, Humid Air and Water Vapour', *Proceedings of the Physical Society*, 1959, 74, p. 29

[60] L. Fouad, S. Elhazek, "Effect of humidity on positive corona discharge in a three electrode system", *Journal of Electrostatics*, Volume 35, Issue 1, 1995, Pages 21-30,

[61] Li, Bingxu & Li, Xingwen & Fu, Mingli & Zhuo, Ran & Wang, Dibo. (2018). Effect of humidity on dielectric breakdown properties of air considering ion kinetics. *Journal of Physics D*: Applied Physics. 51. 10.1088/1361-6463/aad5b9.

[62] Abdel-Salam, M “Influence of humidity on charge density and electric field in electrostatic precipitators” - *Journal of Physics D: Applied Physics* – 1992 - IOP Publishing SP - 1318-1322 IS - 9 VL - 25

[63] Loeb L B “Electrical coronas: their basic physical mechanisms”– Berkerley CA University of California press, 1965

[64] D. Rodriguez, R. S. Gorur and P. M. Hansen, "Effect of humidity on the breakdown characteristics of air in uniform field for the very low frequency (VLF) band," in *IEEE Transactions on Dielectrics and Electrical Insulation*, vol. 16, no. 5, pp. 1397-1403, October 2009, doi: 10.1109/TDEI.2009.5293953

[65] G. A. Eiceman, and Z. Karpas, Ion Mobility Spectrometry, CRC Press, Boca Raton, FL, Ch. 2, 3, 2005.

[66] A Brisset *et al* “Experimental study of the effect of water vapour on dynamics of a high electric field non-equilibrium diffuse discharge in air” 2021 *J. Phys. D: Appl. Phys.* **54** 215204 10.1088/1361-6463/abe81e

[67] Niu, H. & Xu, T. & Zhuang, X. & Yi, Z. & Liu, Y.. (2017). Analysis on dramatic decline of air gap breakdown voltage in the fog-haze weather. *Gaoya Dianqi/High Voltage Apparatus*. 53. 181-185 and 191. 10.13296/j.1001-1609.hva.2017.01.030.

[68] Niu, R. Guo, T. Xu, and J. Xu, ‘‘Research on weather condition of significant decline of air gap breakdown voltage,’’ inProc. IEEE 15th Int. Conf.Environ. Electr. Eng. (EEEIC), Rome, Italy, Jun. 2015, pp. 1725–1729.

[69] F. Zhou, Y. Ding, S. Wang, X. Yao and F. Lv, "Study on the influence of rainfall on the electric field distribution and switching impulse voltage of large-size sphere–plane gap," in *The Journal of Engineering*, vol. 2019, no. 16, pp. 2748-2752, 3 2019, doi: 10.1049/joe.2018.8535.

[70] IEC 60060-1; High-voltage test techniques – Part 1: General definitions and test requirements

[71] Guan, L. Wang, B. Yang, X. Liang, and Z. Li, ‘‘Electric field analysis of water drop corona,’’ *IEEE Trans. Power Del.*, vol. 20, no. 2, pp. 964–969,Apr. 2005, doi: 10.1109/TPWRD.2004.837672.

[72] M. G. Hogg, I. V. Timoshkin, S. J. MacGregor, M. P. Wilson, M. J. Given and T. Wang, "Electrical breakdown of short non-uniform air gaps," *2013 19th IEEE Pulsed Power Conference (PPC)*, San Francisco, CA, 2013, pp. 1-4, doi: 10.1109/PPC.2013.6627482.

[73] D.L. Pulfrey, “The electrical breakdown of solid dielectrics in non-uniform fields,” *J. Phys. D: Appl. Phys*., vol. 5, pp. 647-655, 1972.

[74] W. Schottky, “Cold and hot electron discharges,” *Z. Phys*., vol. 14 (2), pp. 63-106, 1923.

[75] R.H. Fowler, and L. Nordheim, “Electron emission in intense electric fields,” Proc. R. Soc. Lond. A, vol. 119, pp. 173-181, 1928

[76] Naidu, Motukuru S., and V. Kamaraju. *High voltage engineering*. Tata McGraw Hill, 2013. Chapter 4, Breakdown in Solid Dielectrics

[77] N. L. Dao, P. L. Lewin, I. L. Hosier and S. G. Swingler, "A comparison between LDPE and HDPE cable insulation properties following lightning impulse ageing," *2010 10th IEEE International Conference on Solid Dielectrics*, Potsdam, 2010, pp. 1-4, doi: 10.1109/ICSD.2010.5567944.

[78] T. Niwa, M. Hatada, H. Miyata and T. Takahashi, "Studies on the improvement of breakdown strength of polyolefins," in *IEEE Transactions on Electrical Insulation*, vol. 28, no. 1, pp. 30-34, Feb. 1993, doi: 10.1109/14.192237.

[79] L. Rogers *et al*, “High Voltage Insulation and Gas Absorption of Polymers in High Pressure Argon and Xenon Gases”, 2018 *JINST* 13 P10002 [arXiv:1804.04116].

[80] Dabbak, Sameh & Illias, Hazlee & Ang, Bee & Abdul Latiff, Nurul Ain & Makmud, Mohamad. “Electrical Properties of Polyethylene/Polypropylene Compounds for High-Voltage Insulation”. *Energies.* 11. 1448. 2018 10.3390/en11061448.

[81] E. Kuffel, W.S. Zaengl, and J. Kuffel, “Breakdown in solid and liquid dielectrics,” *High Voltage Engineering: Fundamentals*, 2nd ed., Newnes, 2000, ch. 6, pp. 367-394.

[82] T. S. Sudarshan and R. A. Dougal, "Mechanisms of Surface Flashover Along Solid Dielectrics in Compressed Gases: a Review," in *IEEE Transactions on Electrical Insulation*, vol. EI-21, no. 5, pp. 727-746, Oct. 1986.

[83] D. K. Davies, "Charge generation on dielectric surfaces," *Brit. J. Appl. Phys*., Ser. 2, Vol. 2, 1969.

[84] H. Miller, "Surface Flashover of Insulators," *IEEE Transactions on Electrical Insulation*, Vol. 24, No. 5, pp. 765-786, October 1989.

[85] E. R. B. Adamson, "Secondary Electron Emission Coefficient from Lexan: Low-Energy Crossover," Dissertation for the Degree of Doctor of Philosophy in Physics, Texas Tech University, Lubbock, Texas, 1993

[86] Dionne, G. F., "Origin of Secondary-Electron-Emission Yield-Curve Parameters," *J. Appl. Phvs*.. Vol. 46, No. 8, August 1975, pp. 3347-3351.

[87] F. Hegeler, "Dielectric Surface Flashover in a Simulated Low Earth Orbit Environment," Dissertation for the Degree of Doctor of Philosophy in Electrical Engineering, Texas Tech University, Lubbock, Texas, 1995

[88] N. Matsuoka, Y. Fuchi, M. Kozako and M. Hikita, "Effect of permittivity variation on surface flashover of GIS epoxy spacer model in SF6 gas," *2016 IEEE International Conference on Dielectrics (ICD)*, Montpellier, 2016, pp. 96-99.

[89] D. L. Schweickart, H. Kirkici, L. C. Walko and W. G. Dunbar, "Insulation and dielectric breakdown design considerations in sub-atmospheric environments," *2007 16th IEEE International Pulsed Power Conference*, Albuquerque, NM, 2007, pp. 1661-1664.

[90] M.R. Wertheimer, L. Paquin, H.P. Schreiber, and S.A. Boggs, "Dielectric permittivity, conductivity, and breakdown characteristics of polymer-mica composites*," IEEE Trans. Electr. Insul*., vol. EI-12 (2), pp. 137-141, 1977.

[91] I.V. Timoshkin, S.J. MacGregor, R.A. Fouracre, B.H. Crichton, and J.G. Anderson, "Transient electrical field across cellular membranes: pulsed electric field treatment of microbial cells*," J. Phys. D: Appl. Phys*., vol. 39 (3), pp. 596-603, 2006.

[92] J. D. Cross, T. S. Sudarshan, "The Effect of Cuprous Oxide Coatings on Surface Flashover of Dielectric Spacers in Vacuum", *IEEE Trans. Electr. Insul.*, vol. 9, pp. 146-150, 1974

[93] H. C. Miller, E. J. Furno, "The Effect of Mn/Ti Surface Treatment on Voltage-Holdoff Performance of Alumina Insulators in Vacuum", *J. Appl. Phys.*, vol. 49, pp. 5461-5420, 1978.

[94] R. A. Anderson, "Time-Resolved Measurements of Surface Flashover of Conical Insulators", *1975 Annual Report Conf. on Electr. Insul. and Dielectr. Phen National Academy of Sciences*, 1978.

[95] H. H. Zhong, H. C. Karner and M. Gollor, "Time characteristics of fast pulsed flashover in vacuum," *[1991] Proceedings of the 3rd International Conference on Properties and Applications of Dielectric Materials*, Tokyo, Japan, 1991, pp. 292-295 vol.1.

[96] A. Zhabin, A. S. d. Ferron, L. Ariztia, M. Rivaletto, B. M. Novac and L. Pecastaing, "Determination of Breakdown Voltage Along the Surface of a Cylindrical Insulator," in *IEEE Transactions on Dielectrics and Electrical Insulation*, vol. 29, no. 1, pp. 327-333, Feb. 2022, doi: 10.1109/TDEI.2022.3148469

[97] Y. Qin *et al*., "A study on flashover characteristics of supporting insulators in SF6 under lightning impulse," *2015 IEEE 11th International Conference on the Properties and Applications of Dielectric Materials (ICPADM)*, Sydney, NSW, 2015, pp. 604-607.

[98] J. D. Smith and L. L. Hatfield, "The effects of surface roughness on the surface flashover voltage of lucite, lexan, and celcon," *7th Pulsed Power Conference*, Monterey, CA, USA, 1989, pp. 824-827

[99] Streamer propagation along a profiled dielectric surface Plasma Sources Science and Technology, Meyer, H K H, Marskar, R, Gjemdal, H and Mauseth, F, 2020, *IOP Publishing*, Issue 11, Volume 29

[100] H. K. Meyer, R. Marskar, H. Osberg and F. Mauseth, "Surface Flashover over a Micro-Profiled Cylinder in Air," in *IEEE Transactions on Dielectrics and Electrical Insulation*, doi: 10.1109/TDEI.2023.3277413

[101] Zhenyu Zhan, Qizhe Zhang, Fangcheng Lü, Yan Liu, Wei Liu, Zhibing Li, Qing Xie; Effect of the surface roughness of epoxy resin on its creeping flashover characteristics in C_4F_7N-CO_2 gas mixtures. *AIP Advances* 1 April 2019; 9 (4): 045129. https://doi.org/10.1063/1.5095720

[102] T. Takuma, "Field behaviour at a triple junction in composite dielectric arrangements," in *IEEE Transactions on Electrical Insulation*, vol. 26, no. 3, pp. 500-509, June 1991.

[103] T. Takuma, T. Kouno and H. Matsuda, "Field Be- havior near Singular Points in Composite Dielectric Arrangements", *IEEE Trans. Elect. Insul*., Vol. 13, pp. 426-435, 1978.

[104] J. Song, J. Kim, B. Seok and Y. Choi, "Evaluation of discharge characteristics on the triple junction for development of the Gas-Insulated Switchgear," *2012 15th International Conference on Electrical Machines and Systems (ICEMS)*, Sapporo, 2012, pp. 1-5.

[105] K. P. Morales, J. T. Krile, A. A. Neuber and H. G. Krompholz, "Pulsed Dielectric Surface Flashover at Atmospheric Conditions," *2005 IEEE Pulsed Power Conference*, Monterey, CA, 2005, pp. 1147-1150

[106] J. T. Krile, A. A. Neuber, J. C. Dickens and H. G. Krompholz, "DC flashover of a dielectric surface in atmospheric conditions," in *IEEE Transactions on Plasma Science*, vol. 32, no. 5, pp. 1828-1834, Oct. 2004.

[107] D. E. Gourgoulis, P. N. Mikropoulos, C. A. Stassinopoulos and C. G. Yakinthos, "Effects of negative DC pre-stressing on positive impulse breakdown characteristics of conductor-rod gaps," in *IEE Proceedings - Science, Measurement and Technology*, vol. 152, no. 4, pp. 155-160, 8 July 2005.

[108] A Beroual and I Fofana 'Positive discharges in long air gaps', *IOP publishing* 2016

[109] Allen, N.L., and Dring, G.: ‘Effect of humidity on the properties of corona in a rod-plane gap under positive impulse voltages’ ,*Proc. R. Soc. Lond. A, Math. Phys. Eng. Sci.*, 1984,A396,pp. 281–295

[110] Davies, A.J., Dutton, J., Turri, R., and Waters, R.T.: ‘The effect of humidity on space charge growth in short air gaps’. *Proc. 5th Int.Symp. on Gaseous Dielectrics*, Paper 58, Knoxville, USA, 1987

[111] T. Kondo, R. Ozaki and K. Kadowaki, "Effect of superposed repetitive pulses onto DC voltage on discharge extension into fog water produced by electrospray," *2017 International Symposium on Electrical Insulating Materials (ISEIM)*, Toyohashi, 2017, pp. 390-393.

[112] A. Krivda and D. Birtwhistle, "Breakdown between water drops on wet polymer surfaces," *2001 Annual Report Conference on Electrical Insulation and Dielectric Phenomena (Cat. No.01CH37225)*, Kitchener, Ontario, Canada, 2001, pp. 572-580.

[113] W. Pfeiffer and K. Ermeler, "Influence of humidity exposure time on dielectric properties of insulation material surfaces," *1999 Annual Report Conference on Electrical Insulation and Dielectric Phenomena (Cat. No.99CH36319)*, Austin, TX, USA, 1999, pp. 492-495 vol.2.

[114] B. K. Gautam, Y. Mizuno, G. Matsubayashi, K. Sakanishi, T. Kawaguchi and R. Matsuoka, "Effect of Wetting Conditions on The Contamination Flashover Voltages of Polymer Insulators," *2006 IEEE 8th International Conference on Properties & applications of Dielectric Materials*, Bali, 2006,

[115] Jianyi Xue, Han Wang, Junhong Chen, Kefeng Li, Yanqin Liu, Baipeng Song, Junbo Deng, *and* Guanjun Zhang "Effects of surface roughness on surface charge accumulation characteristics and surface flashover performance of alumina-filled epoxy resin spacers”- *Journal of Applied Physics* VL - 124, IS - 8 - American Institute of Physics

[116] R. N. Wenzel,Ind. Eng. Chem.28, 988–994 (1936)],

[117] Boinovich, L & Emelyanenko, Alexandre. “Hydrophobic materials and coatings: Principles of design, properties and applications”. *Russian Chemical Reviews*. 77. 583 2008

[118] T. S. Sudarshan and R. A. Dougal, "Mechanisms of Surface Flashover Along Solid Dielectrics in Compressed Gases: a Review," in *IEEE Transactions on Electrical Insulation*, vol. EI-21, no. 5, pp. 727-746, Oct. 1986, doi: 10.1109/TEI.1986.348922.

[119] Cookson, Alan H.: 'Review of high-voltage gas breakdown and insulators in compressed gas', IEE Proceedings A (*Physical Science, Measurement and Instrumentation, Management and Education, Reviews*), 1981, 128, (4), p. 303-312, DOI: 10.1049/ip-a-1.1981.0045 IET Digital Library, https://digital-library.theiet.org/content/journals/10.1049/ip-a-1.1981.0045

[120] C. M. Cooke, “Charging of insulator surfaces by ionization and transport in gases,” *IEEE Trans. Electr. Insul.*, vol. El-17, no. 2, pp. 172–178, Apr. 1982

[121] Li, Shengtao & Huang, Yin & Min, Daomin & Qu, Guanghao & Niu, Huan & Li, Zhen & Wang, Weiwang & Li, Jianying & Liu, Wenfeng. (2019*). Synergic effect of adsorbed gas and charging on surface flashover*. Scientific Reports. 9. 5464. 10.1038/s41598-019-41961-0.

[122] I. A. Bean, C. S. Adams and T. E. Weber, "HVDC Surface Flashover in Compressed Air for Various Dielectrics," in *IEEE Transactions on Dielectrics and Electrical Insulation*, vol. 27, no. 6, pp. 1982-1988, December 2020, doi: 10.1109/TDEI.2020.008981.

[123] Dubinova A A 2016 Modeling of streamer discharges near dielectrics PhD Thesis Eindhoven: TU Eindhoven oCLC: 956923350

[124] Simulations and Measurements of Streamer discharges near Dielectrics Sigurd Gard Midttun, Norwegian University of Science and Technology 2017 MSc

[125] Xiaoran, Li & Sun, Anbang & Zhang, Guanjun & Teunissen, Jannis. “A computational study of positive streamers interacting with dielectrics.” *Plasma Sources Science and Technology* VL 29 No 6, 2020

[126] X. Li, A. Sun and J. Teunissen, "A computational study of negative surface discharges: Characteristics of surface streamers and surface charges," in *IEEE Transactions on Dielectrics and Electrical Insulation*, vol. 27, no. 4, pp. 1178-1186, Aug. 2020, doi: 10.1109/TDEI.2020.008880.

3. CHAPTER III

SYSTEMS AND METHODOLOGY

3.1. INTRODUCTION

The equipment and different procedures used in the experimental work in this thesis, and how they relate to the overall attainment of results, are described in this chapter. The main discussion points included within this chapter are as follows –

- Impulse generator information, as well as other equipment used in the generation of high voltage impulses.
- Test-cell arrangements and characteristics
- Gas and solid dielectrics information
- Electrostatic simulation of utilised test-cell
- Gas handling in Marx generator control and test cell processes
- Measurement equipment used for analysis of resultant waveforms and flashover information.
- Statistical analysis methods to extract probability information for flashover/breakdown datasets.
- Data representation

Overall, this will inform on the physical equipment, testing standards and statistical analysis used in the generation of data in Chapters IV, V and VI.

3.2. IMPULSE GENERATION

In Section 2.2, Marx generator technology was introduced and discussed as the ideal method of voltage generation in this thesis. In order to achieve the impulse voltages to test the multiple insulation systems, a 10-stage Marx Generator was utilised. The air-insulated Marx generator was operated in the single-shot regime and was of inverting polarity. The Marx generator used within this study is shown in Figure 3.1, which shows the 10-stage system used for voltage multiplication. This Marx generator

was used to produce voltages within this work of up 300 kV, with a wave-shape of 100/700 ns, to replicate the fast *dV/dt* conditions of a pulsed power system.

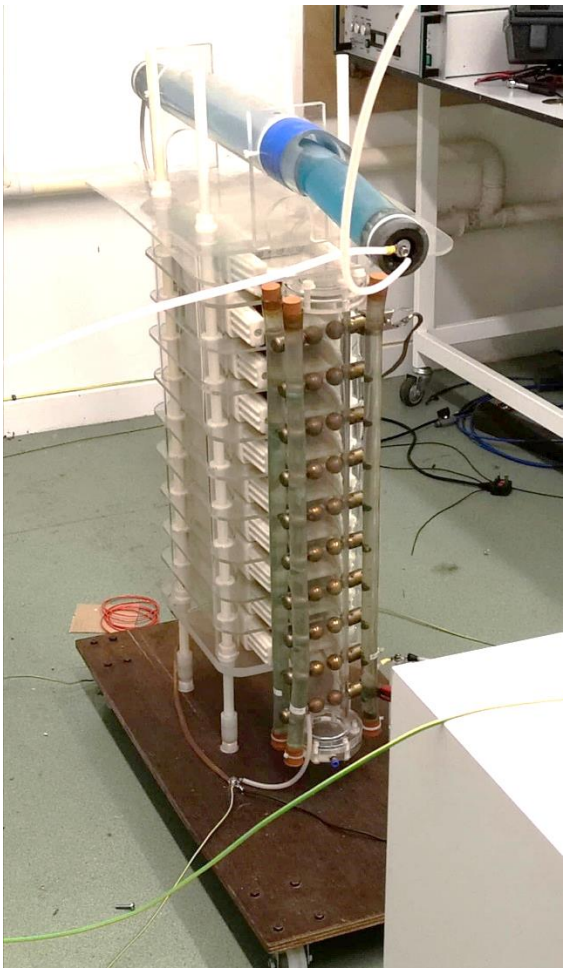

Figure 3.1 - 10-stage Marx Generator, each capacitive stage can be seen here with the output (front) wave-shaping resistor

The 10-stage Marx generator and charging equipment is made up of the following components –

- 100 kV, 2.5 mA, Glassman High Voltage DC Supply (Glassman Inc, USA)

The Glassman HVDC supply has built-in voltage and current meters allowing the charging of the capacitors to be monitored before triggering. The DC charging voltage was also monitored using a 1000:1 Testec HVP-40 HV probe and DMM.

- 1 MΩ Charging resistor

Charging resistor made up of 100 (Meggit, UK) 10 kΩ ceramic-cased wire wound resistors connected in series.

- 80 nF, Single Sided S-type Capacitors (Maxwell Inc, USA)

For the 10-stage Marx generator set up this equated to a nominal erected capacitance of 8 nF.

- Stage resistances of 60 kΩ

These resistances were achieved by submerging spherical bronze phosphor electrodes in a PVC pipe filled with Copper-Sulphate ($CuSO_4$) solution as illustrated in Figure 3.1 and 3.3a. These electrodes were set to equal distances in order to achieve resistance matching. Also, 2 kΩ discharge resistors are also connected between alternate stages of the spark column shown in Figure 3.1 and 3.2.

- 10-stage spark column

The 25 mm bronze phosphor electrodes were housed within an air-insulated Perspex column, which is shown in Figure 3.1 and 3.3a. This setup allows the Marx generator to be triggered by reducing the air pressure within the column, triggering the closure of all 10 sphere gaps and generating the output voltage impulse, as shown in Figure 3.3b. The triggering of the Marx is further discussed in Section 3.5.1, where the gas handling relating to the Marx generator control is discussed. The gap between each pair of phosphor-bronze electrodes housed within the air-insulated spark column is 10 mm.

During testing, the Marx generator was charged by either a positive or negative polarity DC voltage, resulting in output negative and positive impulses, respectively (inverting Marx), as discussed in Section 2.2.1. Both polarities were tested to investigate any polarity effect during testing under different environmental conditions - this is further discussed in Section 3.4.4.

The Marx generator circuit is shown in Figure 3.2, where each component can be clearly identified. A sketch showing the layout of the spark gaps in Figure 3.3a is presented alongside a photograph of the (closed) spark gaps in the physical system in Figure 3.3b. The capacitors seen in Figure 3.1, and shown in the Marx circuit in Figure

3.2, are rated at 70 kV in air – and up to 100 kV when immersed in insulating oil or a pressurised gas – the distance between the external spark-column electrodes limited the DC charging voltage that could be applied to the system to <50 kV, yielding a maximum nominal output voltage in the region of 500 kV.

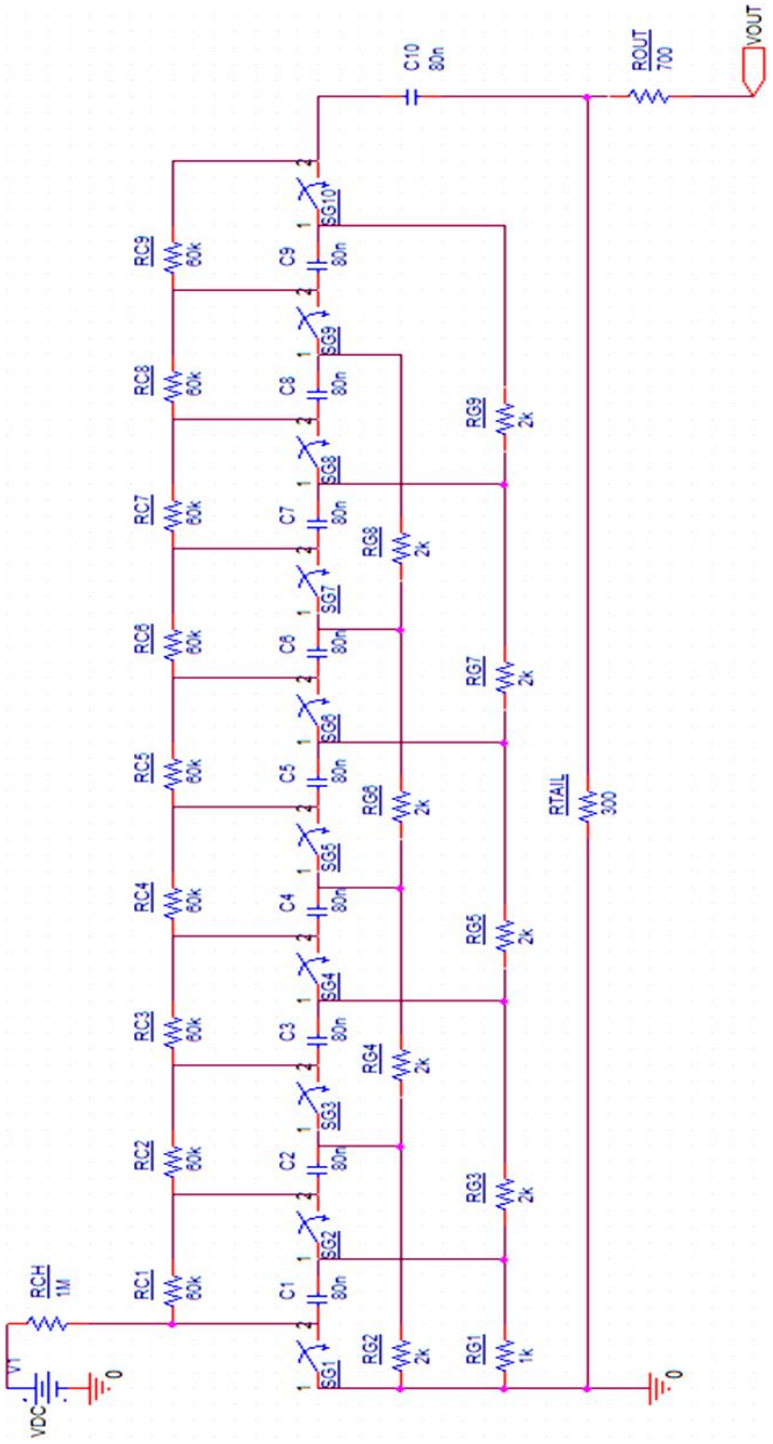

Figure 3.2 - Circuit schematic of 10-stage Marx Generator showing all components and values

a) b)

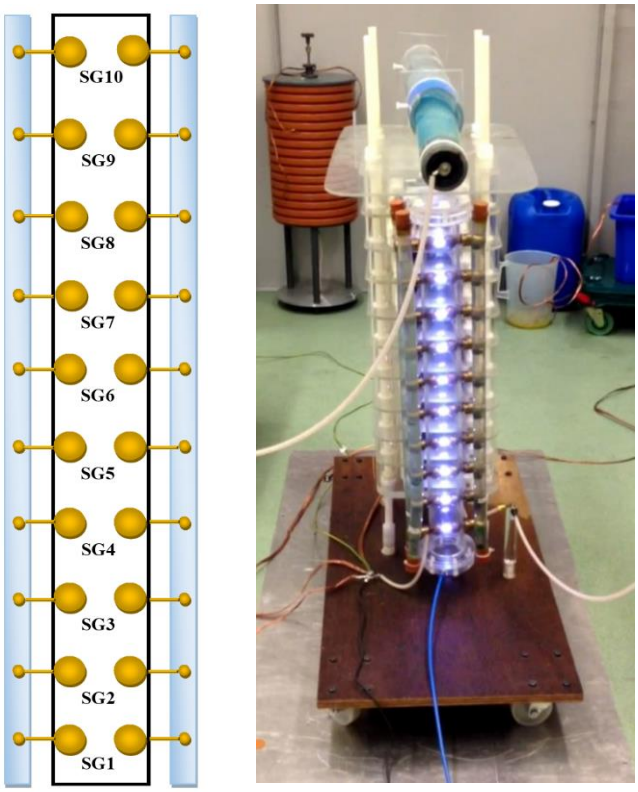

Figure 3.3 - a) Illustration of spark column showing each of the 10-spark gap switches and b) Marx generator with 10 spark gaps triggered, closing SG1 – SG10, connecting the capacitors in series and multiplying the charging voltage.

The spark gaps are triggered by depressurisation of the spark column, which is illustrated in Figure 3.3, and further discussed in Section 3.5.1. During the discharge process, the ultraviolet (UV) light which is generated from the breakdown of each spark gap can provide initiatory electrons to other gaps in the column, minimising the statistical time lag associated with the breakdown of each gap. The discharge resistors (RG1-RG9) also aid the breakdown sequence by ensuring the existence of capacitive coupling between the stages, to assist in maximising the spark gap over-voltages following closure of the first gap [1].

As discussed in Section 2.2.1, one of the advantages of a Marx generator is the achievable variability in the output voltage wave-shape. In order to replicate the fast *dV/dt* of a pulsed power system, the output voltage wave-shape of 100/700 ns was chosen to keep the duration of the output pulse to the sub-μs level. In the configuration

depicted in Figure 3.2, a 300-Ω $CuSO_4$ wave-tail resistor (RTAIL in Figure 3.2) was connected in parallel with the load, controlling the fall-time to half-peak value and providing an alternative path to earth for the stored energy of the stages, should no breakdown occur in the test cell. The output impedance was 700 Ω, in the form of a second $CuSO_4$ (wave-front) resistor (ROUT in Figure 3.2). The output waveform generated is shown and discussed further in Section 3.6.2.

3.3. ENVIRONMENTAL TEST CELL

This section will provide details on the design on the test-cell, which was required for tests to be undertaken, while maintaining control of different environmental conditions. The scope of testing required a sealed chamber, whereby the internal humidity and pressure could be altered during the testing process, in order to investigate corresponding changes in the flashover performance of the insulation systems.

A customised test cell was designed and is shown in Figure 3.4. This consists of a sealed test chamber which houses the electrodes and dielectric spacer, and a humidity sensor in order to monitor the achieved relative humidity inside the test-cell.

a) b)

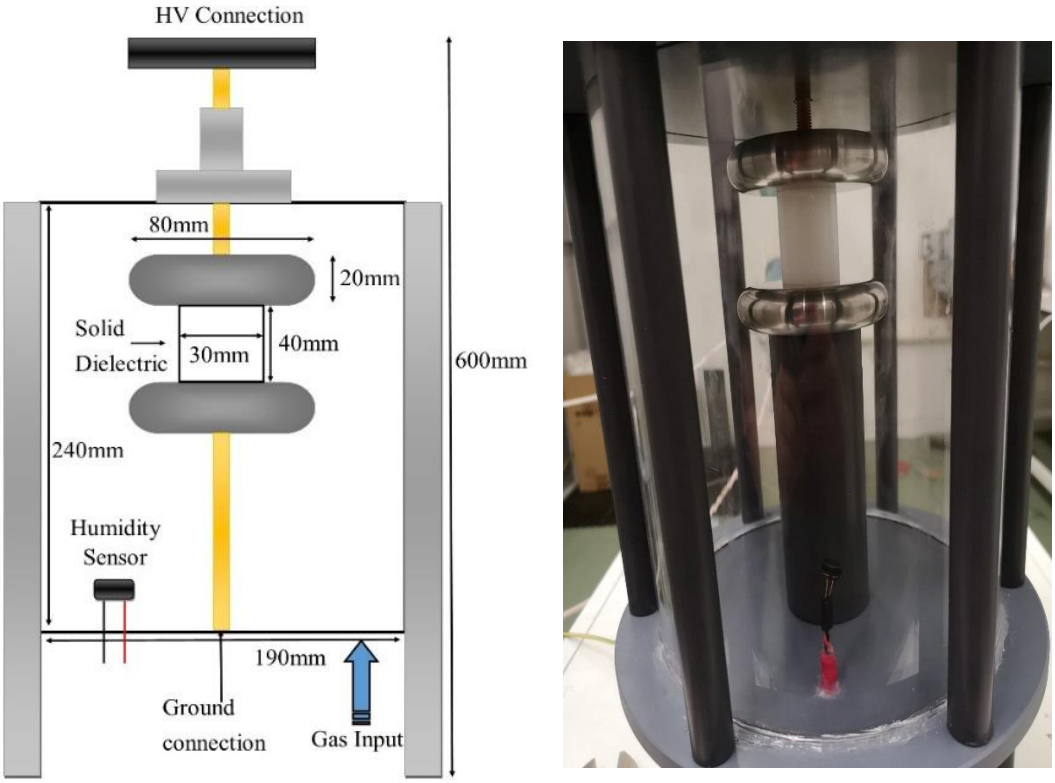

Figure 3.4 - Test cell used for testing within sub-optimal conditions. a) shows a schematic of the test cell including all dimensions and components b) shows the physical test cell, with the humidity sensor a safe distance away from the electrodes.

The test-cell was designed to have a large capacity, allowing the humidity sensor that is housed at the base of the test-cell to be located far from the high voltage electrical discharges across the inter-electrode gap.

The test-cell was designed with a plane-parallel electrode arrangement, as shown in Figure 3.4. This resulted in a quasi-uniform electric field distribution within the gap, as further discussed in Sections 3.4.4.

3.4. INSULATION SYSTEM DIELECTRICS AND MATERIAL CHARACTERISTICS

The insulation system was tested in two different configurations, without a solid spacer with just air dielectric between the electrodes, and with a solid spacer bridging the gap between the electrodes.

3.4.1. Gaseous Dielectric

The gaseous dielectric used within the insulation system was BOC Zero Grade dry air [2]. The water content of the air was typically <5 ppm as received but was measured consistently to have relative humidity of <10% RH. In subsequent tests, moisture was added to the air to produce air with ~50% RH and >90% RH, following the procedure outlined in Section 3.5.2, where air was passed through a water bath with an ultrasonic humidifier.

3.4.2. Electrode Material

The electrodes which were used in the insulation system shown in Figure 3.4 were made of stainless steel, polished to a mirror finish. Within the design of the test cell, these were easily able to be removed in order to be polished prior to subsequent tests. The electrodes were rounded at the edges in order to minimise the electric field strength at this region, which is further discussed with the aid of simulation work in Section 3.4.4.1. This geometry was chosen over Rogowski profile electrodes for ease of machining, particularly were the assembly to be scaled-up, and to replicate the conditions found in practical systems. The electrodes were setup up parallel to each other with a 40 mm gap, as shown in Figure 3.4.

3.4.3. Solid Dielectrics

To complete the insulation system, solid insulating spacers were added between the parallel-plane electrodes. The solid dielectrics used within this thesis were High Density Polyethylene (HDPE), Polyetherimide (Ultem) and Polyoxymethylene (Derlin)). These materials were selected, as they are easily machinable, which was important as clear indentation are to be subjected to the spacer surface as discussed in Section 3.4.3.2. Additionally, these materials having varied electrical characteristics in terms of permittivity of material and different water absorption properties, which prompted the testing of the hydrophobic or hydrophilic properties of the materials,

with information on this process discussed in this section. As these materials exhibited varying characteristics, they were chosen material for this study. Relevant properties of these materials are listed in Table 3.1.

Table 3.1 - Solid dielectric properties

Material	Relative Permittivity	Water absorption (% at saturation in water at 23 °C)	Volume resistivity (Ωcm)	Surface resistivity (Ω)
HDPE [3]	2.3	0.02	10^{15}	10^{13}
Polyetherimide [4]	3	1.35	10^{14}	10^{13}
Polyoxymethylene [5]	3.8	0.8	10^{14}	10^{13}

Selection of the materials was dictated by the changing properties of each induvial material as outlined in Table 3.1. It was assumed that the varying relative permittivity of the materials, along with the varying water absorption (due to testing in humid air) would provide differences in flashover behaviour.

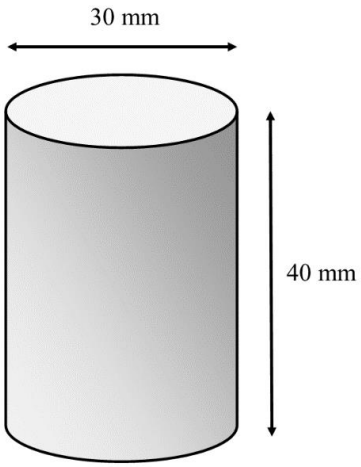

Figure 3.5 – Spacer illustration, showing dimensions.

As shown in Figure 3.5, throughout testing, the spacers were kept a constant size of 30 mm in diameter and 40 mm in length. The reasoning behind the size of the spacer used was to achieve 100s kV in breakdown/flashover voltage and the diameter was chosen so that the spacer is situated within the uniform field distribution within the parallel plane setup, as shown and discussed in Section 3.4.4. Two types of surface

finish were investigated, in order to determine if the breakdown/flashover voltage could be increased by modification of the spacer surface alone. The two surface finishes used were a ‘smooth’, machined surface finish, and a novel ‘knurled’ surface finish. The characteristics of the spacer surfaces will be discussed in Sections 3.4.3.1 and 3.4.3.2.

The way in which materials behave in a high-humidity environment has an effect on the flashover strength, as outlined in [6], in terms the hydrophobicity of the material. In order to quantify the hydrophobicity or the hydrophilicity of the materials tested, an experiment was completed in order to characterise the materials. Using single droplet analysis, which is used in standard [7], a single distilled water droplet was added to the surface of smooth machined samples of all three materials in the form of one 20 µl droplet, in order to measure the angle of contact between each droplet and the respective material. Figure 3.6 shows the differences in the water droplets observed on each material, with contact angles and dimensions detailed. The water droplet used in the analysis was from the same water that was used to create the ~50% RH and >90% RH environments throughout the testing phase.

According to [7], the liquid droplets were analysed by measuring the droplet height and width, to measure the angle of contact on the insulator surface by using equation (3.1).

$$\theta = 2 \cdot \arctan\left(\frac{H}{R}\right) \tag{3.1}$$

Where:

θ = contact angle

H = height of droplet

R = half droplets width

An example of each droplet is shown in Figure 3.6. This test was conducted using a pipette, depositing a single 20 µl droplet of distilled water, in order to assess the hydrophobic/hydrophilic nature of the materials.

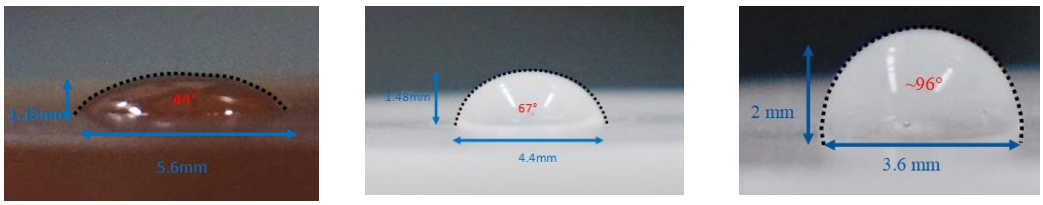

(a) (b) (c)

Figure 3.6 – Example water contact angles for samples of a) Polyetherimide b) Polyoxymethylene and c) HDPE

From Figures 3.6a, 3.6b and 3.6c, it is evident that the materials show different behaviour in terms of angular distribution of a single water droplet. In accordance with [7], this process was completed 10 times for each material, and the average results of the 10 tests are shown in Figure 3.7, along with the 1σ standard deviation (error bars).

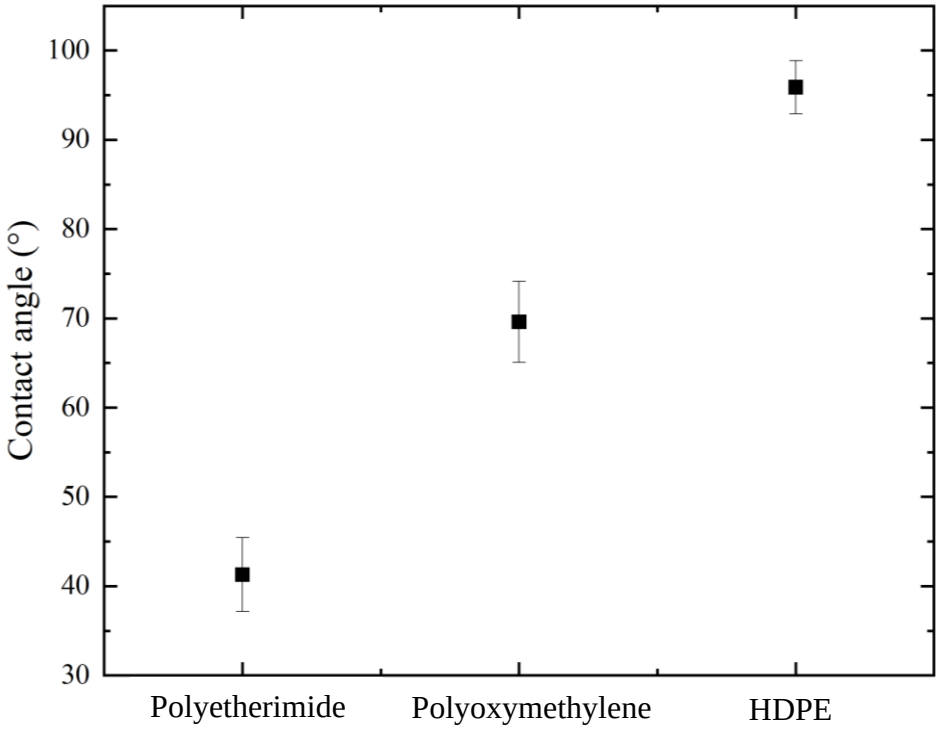

Figure 3.7 - Water contact angle of each material, each point shows the average of 10 tests with the error bars representing ±1σ

Due to the large angle of contact of ~96°, HDPE is hydrophobic (>90° contact angle) - with similar results are reported in [8]. For Polyoxymethylene, the water contact angle was measured at ~70°, with similar to values obtained in [9]. The contact angle for Polyetherimide was ~40°, with similar to contact angles measured in [10]. Both Polyoxymethylene and Polyetherimide are considered to be hydrophilic materials, given the angles of contact <90°, [8].

This information is important in Chapters V and VI, when discussing the high humidity performance of the solid insulation systems, as the presence of water droplets on the spacers can cause increases in the local electric field strength along the insulator surface [11].

Sections 3.4.3.1 and 3.4.3.2 will introduce both types of material surface finish which were applied to the solid materials.

3.4.3.1. Smooth Machined Surface Dielectric

Firstly, samples of the materials were subjected to a smooth (machined) surface finish, where the materials were machined to the required size, as shown in Figure 3.8. This will enable the changing surface subjected to the materials in Section 3.4.3.2 to be tested in comparison with a smooth reference surface.

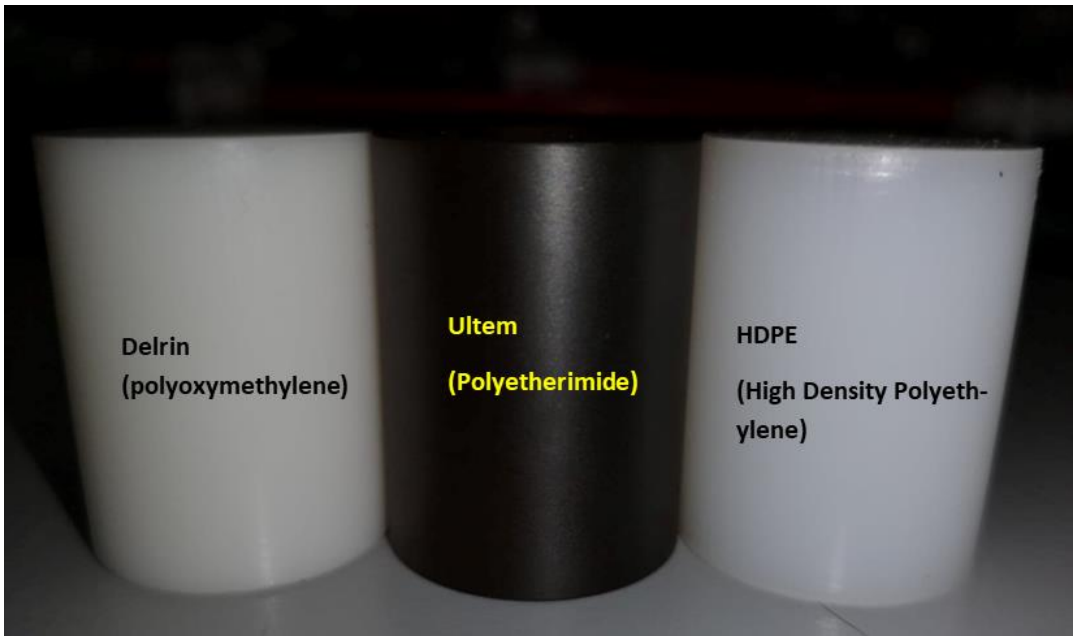

Figure 3.8 - Solid Polyoxymethylene, Polyetherimide and HDPE dielectric materials with smooth (machined) surfaces

3.4.3.2. Surface Modified 'Knurled' Surface Dielectric

Samples of the materials were also subjected to a novel knurled surface finish, as shown in Figure 3.9. Knurling is a turning method through which patterns can be indented onto the surface of a material. This is commonly used on metals, but this

method has been adopted as an alternative to surface roughening in this work, with a view to increasing the breakdown voltage, without resorting to increasing the length of the solid insulator. Other surface modification techniques were considered, for example looking at ring topologies across the surface with different angles referenced to the spacer surface, but these proved unsuitable as the topologies were too complex to produce within a reasonable timeframe whereas, the knurling method has an advantage of being a very quick, cheap and consistent way of modifying a materials surface.

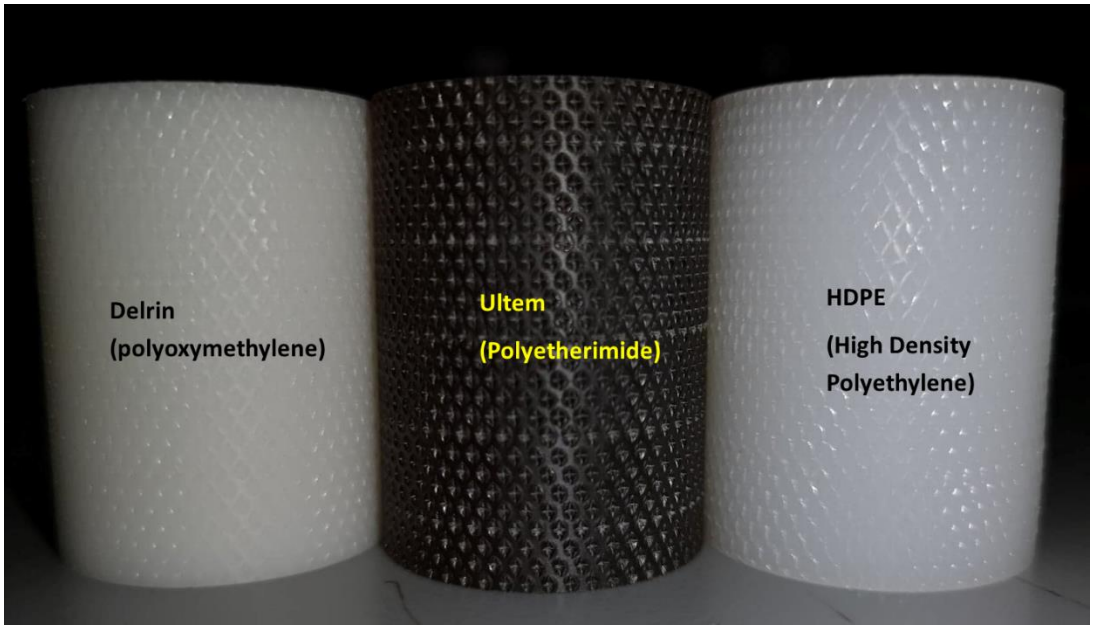

Figure 3.9 – Solid Polyoxymethylene, Polyetherimide and HDPE dielectric materials with knurled surfaces

During the knurling process, diamond-shaped indentations are rolled onto the surface of the spacer materials. This can be seen as a potential alternative to commonly used methods for adding surface deviations to materials, such as surface roughening using grit papers. The knurling method can be seen to be a more intrusive method than adding surface roughness using sandpapers, which modifies the surface without changing the overall shape of the spacer and potentially altering mechanical properties. The addition of the knurled surface is detailed more clearly in Figure 3.10a, where the indentations are shown and numbered, as well as a cross-section showing the measurements in terms of knurling depth and space between indentations. It can be seen that 14, 0.5 mm indentations are added to the 40 mm long surface. The distance

between each indentation 'from trough to trough' was ~2.85 mm. The angle of knurl on the samples used in this work was ~30°, as shown in Figure 3.10b.

The use of the knurling method can modify the angle of contact between the spacer and the electrode, which can either increase or decrease the electric field at the triple junction point (discussed in Section 2.6.3.2). The cross-section in Figure 3.10a was simulated in order to show the effect of the knurling process on the electric field strength at the triple junction point. This effect could result in a higher probability of surface flashover, with contact smaller TJP contact angles created. Conversely, however, this could decrease the field strength if the angle of contact is increased, as discussed in Section 2.6.3. The effect of these triple junction point angles on the electric field distribution, in relation to Figure 3.10a, have been simulated in Section 3.4.4.

a)

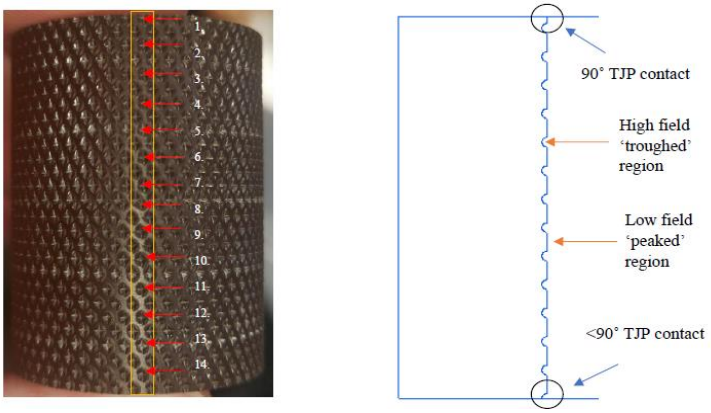

b)

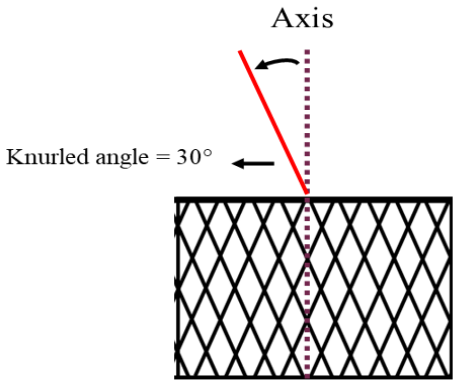

Figure 3.10 - a) Illustration of a knurled Polyetherimide surface, showing the number of indentations over the surface of the dielectric with a cross-section showing information on the triple junction point contact angle over the surface of the material b) illustration of the indentations on the surface, helix angle = 30°

3.4.3.3. Sample preparation

In order to ensure consistency in the sample testing, the following preparation was undertaken for each spacer before testing. Using non-powdered disposable gloves, each material was cleaned with ethanol, in order to remove any surface residue from the machining processes, the samples were then dried in a furnace at 60 °C for 1 hour prior to testing. Each test sequence consisted of 20 breakdown events. After a test sequence had been completed the spacer was replaced in order to minimise the effects of degradation.

3.4.4. Simulation of Test Cell under Various Conditions

This section will inform on the different physical and environmental situations of the test cell in terms of testing an open gas gap, and gaps bridged by an insulating spacer, with smooth and knurled surface finishes. The influence of increasing the relative humidity, due to the resultant formation of water droplets, on the electric field distribution was investigated. The simulations were completed in axisymmetric electrostatic mode. Figure 3.11 shows a representation of the boundary conditions used in the electrostatic simulations, using Quickfield. The test-cell is housed within a Faraday-caged lab, therefore, to identify the effect of this, a boundary condition of $V = 0$ was applied to the boundaries of the simulation space, as in [12] and [13]. This was to monitor the effect of the grounded electrode on the electric field distribution. The effect of grounded areas has been shown in [14], where higher field regions are evident at the HV electrode, creating an asymmetrical electric field distribution, when only one electrode is energised, irrespective of the geometrically-symmetrical nature of the electrodes used. Each of these simulations has 100 kV applied to the (upper) HV electrode, and the lower electrode is grounded.

As these simulations were conducted with axisymmetric rotational symmetry, the simulation for knurled surface topologies does not fully represent the physical representation of samples with knurled surfaces. This is a limitation of the using this model.

The resulting field distribution is shown in Figure 3.12, where a high field region can be seen at the rounded edges of the HV electrode. What is also evident from Figure 3.12, is that the field distribution in the gap is also asymmetrical; this is due to the ratio of inter-electrode gap distance to electrode radius. The effect of this ratio will be discussed in Chapter IV, where open air gaps have been tested and characterised. The effect of these boundary conditions is evident, where the electric field strength is almost double at the edge of the HV electrode in comparison to that at the edge of the grounded electrode. As this asymmetry exists within the inter-electrode gap, both voltage polarities were tested.

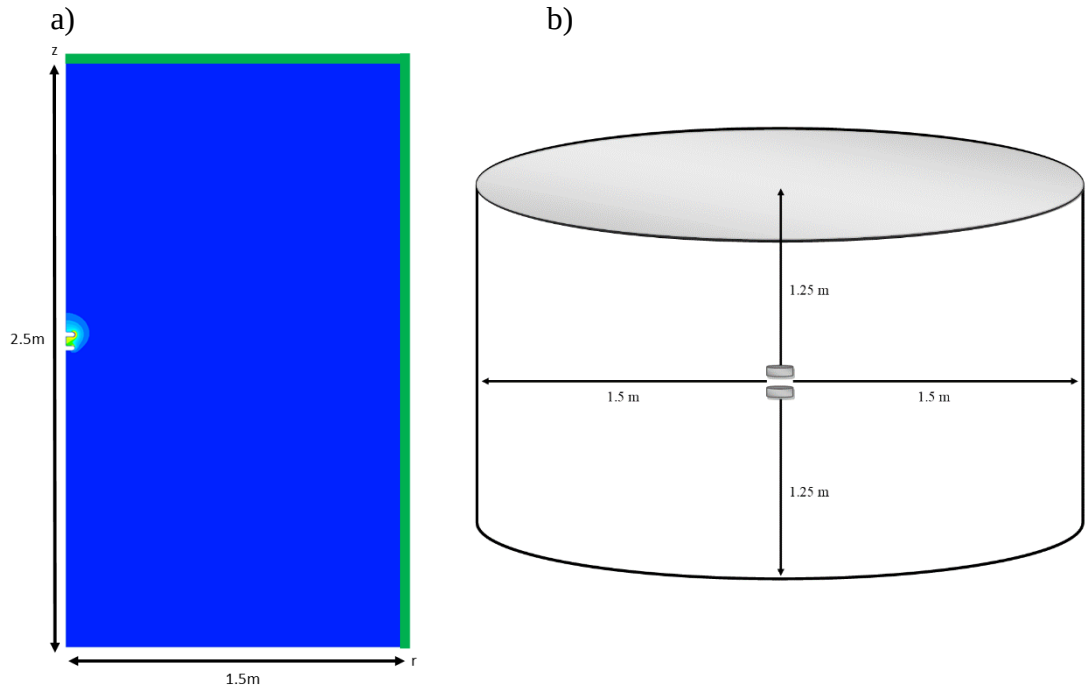

Figure 3.11 - Boundary condition in terms of distance to grounded areas of the laboratory. a) shows the distance to the grounded ceiling and walls on a 2D plane b) Shows the axisymmetric representation of distances, after simulation has rotated around the z-axis.

3.4.4.1. No spacer

The no spacer simulation focuses on the high field regions at the HV electrode edge. As discussed previously, this is particularly important as an asymmetric field distribution in the geometrically symmetrical gap warrants tests with both voltage polarities to be conducted. Figure 3.12 shows the field distribution across the gap.

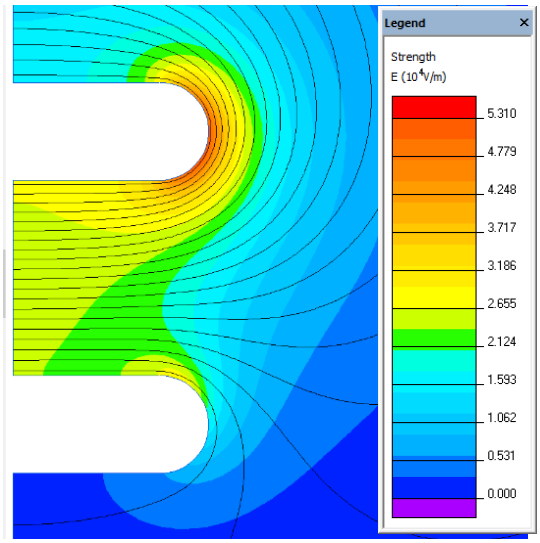

Figure 3.12 - Electrostatic field simulation colour map showing the electric field strengths across the inter-electrode gap; note the asymmetry at the rounded edges of the electrodes.

From this simulation, it is clear that an asymmetrical field is occurring, with the electric field strength being 87% higher at the HV electrode compared to the ground electrode. This effect has also been shown in similar studies in [12], [13] and [14], where using similar boundary conditions has also resulted in an asymmetrical field distribution.

3.4.4.2. Solid with Smooth Surface Finish

Figure 3.13 shows a colourmap of the electric field distribution with a solid between the electrodes. In this simulation, Polyetherimide was used, with a relative permittivity of 3; this was kept consistent throughout all material simulations in Figure 3.13 and 3.14.

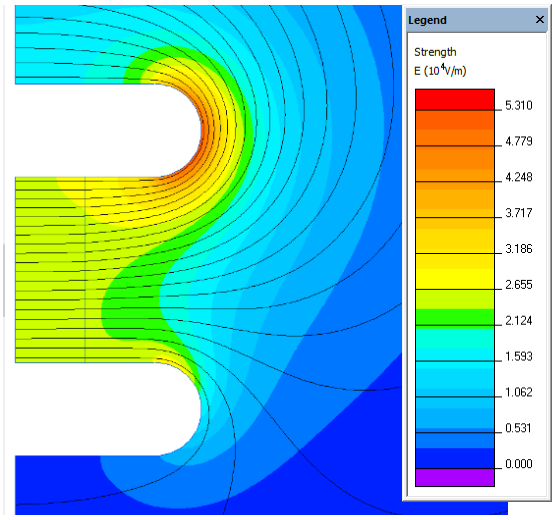

Figure 3.13 - Electrostatic field simulation colour map showing the electric field strengths across the inter-electrode gap across a smooth material surface (Polyetherimide) - 100 kV is applied to the upper electrode and the lower electrode is grounded

It can be seen that there is a slight increase in the electric field at the HV electrode triple junction point, compared to the ground electrode triple junction point. When comparing the field strength to the fields found at the electrode edges in Figure 3.12 (no spacer), however, the resultant field strength is much lower at the triple junction point. When the point of contact (between the HV electrode and spacer surfaces) has an angle of 90º, the electric field strength at the triple junction point is 48% weaker than that at the rounded edge of the electrode.

3.4.4.3. Solid with Knurled Surface Finish

Figure 3.14 shows the field distribution when a solid (Polyetherimide) spacer with a knurled surface finish is included between the electrodes. What is particularly important regarding the field distribution across the knurled surface is that there will be different angles at the point of contact between the HV electrode and the solid, whereby the knurled section (peak or trough) that makes contact with the electrode dictates the field strength at that point. As shown in Figure 3.14, the field within the knurled sections (troughs) is higher than that at the peaks. However, due to the limitation of the electrostatic simulation software, this model will result in a uniformly placed indentations as the simulation is axially symmetric, so therefore doesn't show the exact 3D representation of the knurled as shown in Figures 3.10b.

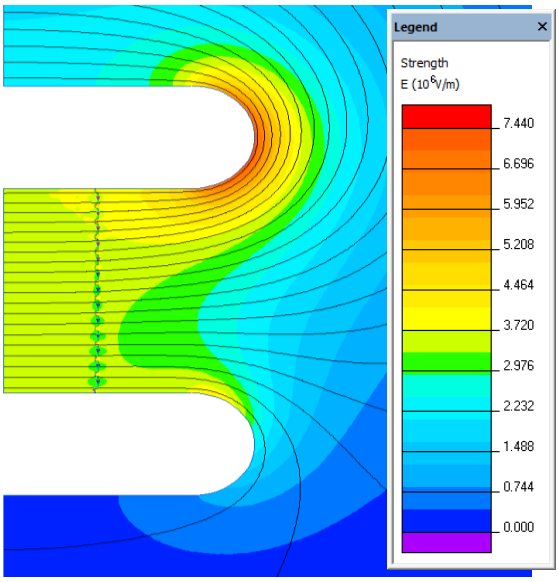

Figure 3.14 - Electrostatic field simulation colour map showing the electric field strengths across the inter-electrode gap with a knurled dielectric spacer (Polyetherimide) - 100 kV is applied to the upper electrode and the lower electrode is grounded

Within Figure 3.14, the field strength can be seen to be much higher in the trough areas on the dielectric surface, which was also reported by the authors of [15]. The electric field strength at the troughs is higher than that at the electrode edges. As shown from Figure 3.14, in this example also the TJP angle has been simulated within a troughed region, and due to the knurled surfaces this angle can vary, therefore, in order to understand the electric field strength in relation to the electric field at the outside of the electrodes, Figure 3.15 gives the field strength at the triple junction point (TJP)

with respect to TJP angle (angle between HV electrode surface and solid spacer surface), as a percentage of the field recorded at the electrode edges. The angle of the TJP has a large effect on the field strength, where at 90° angle the field strength is 48% lower than that at the rounded HV electrode edge, whereas reduction of the contact angle through knurling was shown to increase the electric field intensity at the TJP, referenced to that at the electrode edges, as seen in Figure 3.15.

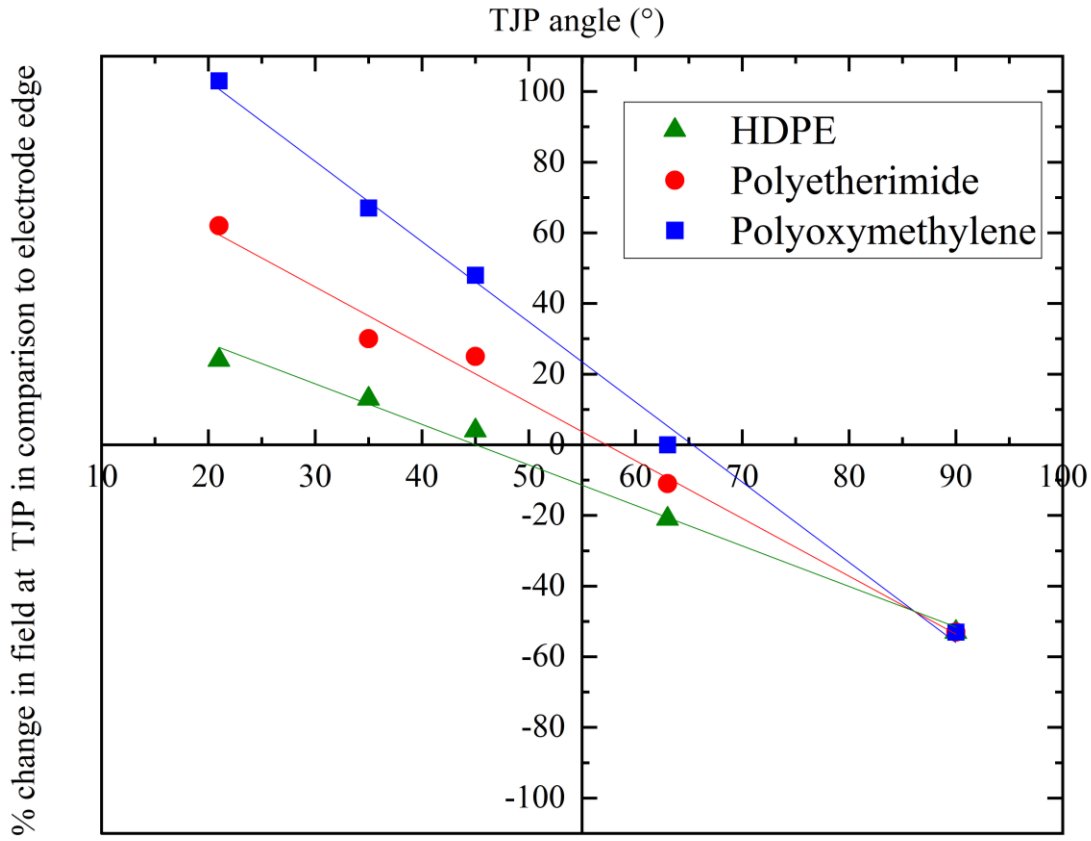

Figure 3.15. Percentage change of TJP electric field strength compared to field at electrode edge at TJP angles of 21°, 35°, 45°, 63° and 90°.

In Figure 3.15, the maximum field strength was measured at the TJP with a 0.5 mm depth (depth of knurl) at angles of 21°, 35°, 45°, 63° and 90°. This value was then compared to the maximum field strength found at the electrode edge in Figure 3.12, in order to find the percentage difference between these fields. As expected, as the TJP angle decreased, the field increased. Ultimately, using an iterative approach in additional electrostatic field simulations, the threshold contact angles at which the field at the triple junction point would exceed that at the rounded electrode edge were 50° for a knurled HDPE surface, 56° for a knurled Polyetherimide surface, and 63° for

a knurled Polyoxymethylene surface. This change in electric field magnitude at the TJP dependant on contact angle may have an effect on the discharge initiating point, this will be discussed through Sections 6.4 and 6.5.

3.5. GAS HANDLING

This section will contain all relevant information regarding the gas handling systems and processes used throughout the practical testing phase.

3.5.1. Marx Generator Control

In order to control the 10-stage Marx generator, a gas system was implemented to control the switching of the 10 spark gap switches, housed within a pressurised chamber as discussed in Section 3.3. When the pressure of the gas in the spark column is decreased (the *pd* product decreases), the breakdown voltage of the gas gaps will also decrease. The triggering control system consists of a rotary vacuum pump and an air compressor, connected to the spark column through a manifold and pressure gauge, as shown in Figure 3.16, as well as an exhaust. The pressure of the gas within the spark column can be increased to increase the achieved hold-off voltage of the sphere gap, thereby increasing the Marx generators potential output voltage. The vacuum pump is subsequently connected in order to reduce the pressure in the spark column, which ultimately triggers the Marx generator. Figure 3.17 shows the gas pressure required for each level of charging (hold-off) voltage. Note that for safe operation of the Marx generator, the spark column was always pressurised to 0.4 bar gauge over the self-breakdown voltage, to avoid accidental self-triggering.

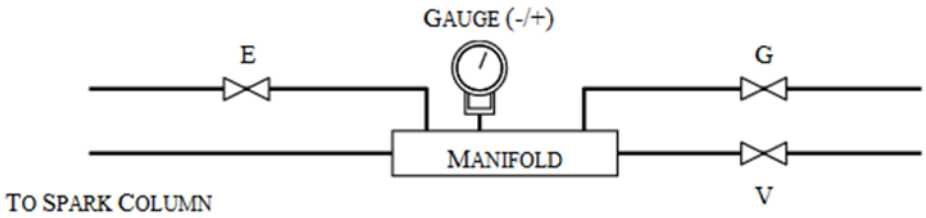

Figure 3.16 - Diagram of the gas control board for triggering of the Marx Generator, where E is the exhaust to atmospheric pressure, G in the gas supply connection and V is the vacuum pump connection

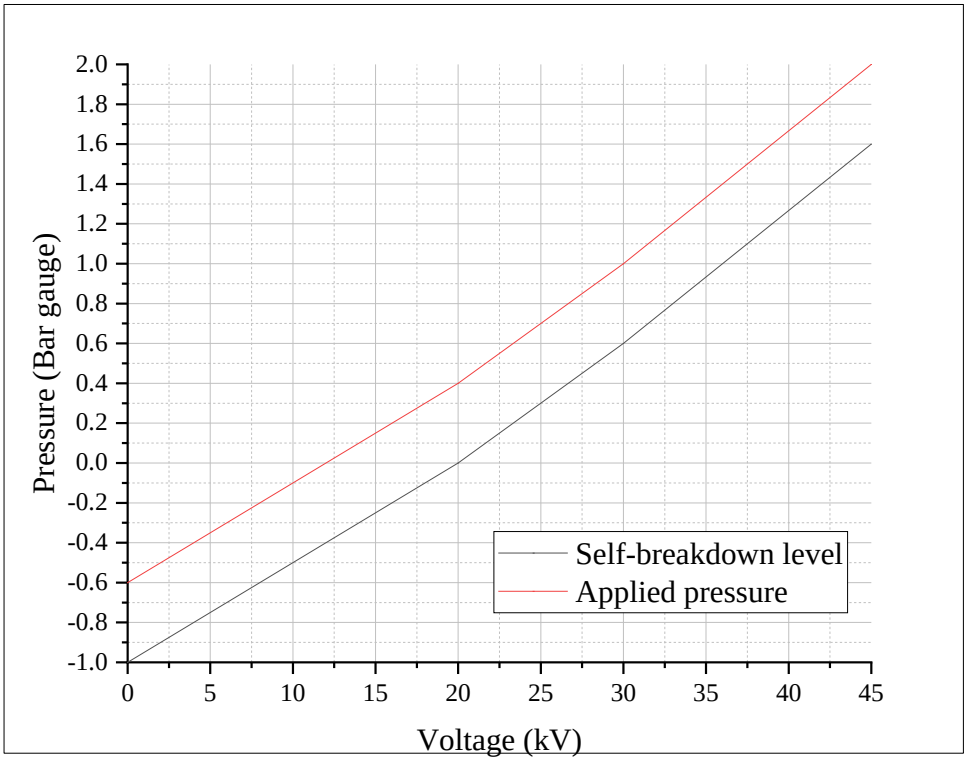

Figure 3.17 - Gauge pressure versus self-breakdown voltage for spark column. The red curve represents the initial gas pressure before charging of the impulse generator stages, with the minimum pressure corresponding to the points on the red line, at least 0.4 bar above the self-breakdown pressure (black curve). Modified from work completed in [16]

3.5.2. Humidity and Pressure Control in Test Cell

As the dielectrics were to be tested under different environmental conditions, the test cell was designed to accommodate the required changes in pressure and humidity. Therefore, a sealed cylindrical test cell was created in order to hold the pressures of -0.5, 0 and 0.5 bar gauge. A 5 mm thick Perspex cylinder was used for the main body of the test cell, with PVC flanges at the top and bottom (as shown in Figure 3.4). The pressure line for the test-cell is fed through a gas board with an analogue meter indicating the gas pressure within the test-cell. This connection is shown in Figure 3.18, which also shows the dry and wet lines used for generating different levels of relative humidity within the test cell.

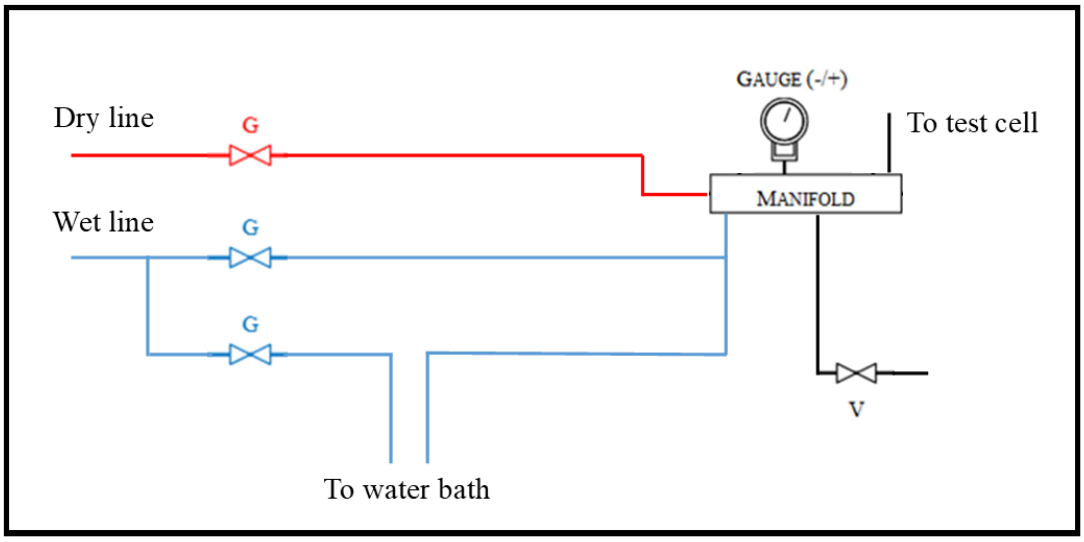

Figure 3.18 - Diagram of gas control board for test-cell, where G is the gas supply connection to either the dry (red) line or the wet (blue) line and V is the vacuum pump connection.

The humidity levels used in this work were <10% RH, ~50% RH and >90% RH. The gas bottle was only ever opened when connected to the 'dry line' or the 'wet line' (not both simultaneously) shown in Figure 3.16. To achieve <10% RH, the dry line was used in order to input gas straight from the gas bottle itself. The achievement of ~50% RH was by connecting the gas bottle to the wet line, and using both isolating valves, mixing the air from two inputs, one straight from the gas bottle, and one connected via a water bath and ultrasonic humidifier. By mixing the feeds from these lines and monitoring the RH, ~50% RH was achieved prior to testing. For >90% RH, air from the gas bottle was passed directly through the water bath, achieving the high humidity (>90% RH) environment, again monitored by the circuit as described below.

The water used throughout the full study was distilled water, the water bath consisted of a 5 mm Perspex surround and PVC flanges top and bottom. An ultrasonic humidifier was submerged within the water in order to create the high humidity during testing. In order to minimise contamination within the water, the Perspex/PVC water bath was taken and filled directly from the distilled water source.

To monitor the humidity inside the test cell, a sensor was implemented into the design, as shown in Figure 3.19, from [17]. The TE Connectivity HS1101LF sensor was housed within the test cell itself (see Figure 3.4b), to provide the achieved RH of the air within the test cell.

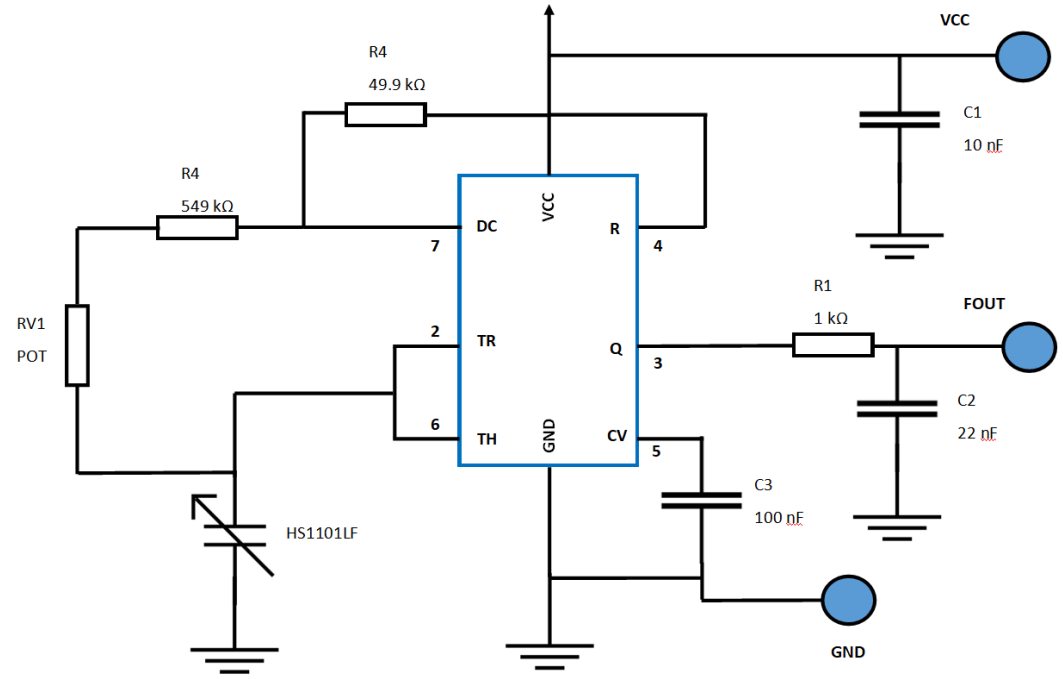

Figure 3.19 – 555 timer frequency output circuit modified from [17]

The values of the components used in the 555-timer circuit are shown in Figure 3.19. This circuit enabled the RH to be related to the output frequency. This circuit is the typical astable design for a 555 timer. The TE Connectivity HS1101LF, used as a variable capacitor, is connected to the TRIG and THRES pins. Pin 7 is used as a short circuit pin for resistor R4. The HS1101LF equivalent capacitor is charged through R22 and R4 to the threshold voltage (approximately 0.67 Vcc), and discharged through R22 only to the trigger level (approximately 0.33 Vcc), since R4 is shorted to ground by pin 7. Since the charging and discharging paths of the sensor run through different resistors, R22 and R4, the duty cycle is determined by equations 3.2 – 3.5: [17]

$$t_{high} = C_{@\%RH} * (R22 + R4) * \ln(2) \quad (3.2)$$

$$t_{low} = C_{@\%RH} * R22 * \ln(2) \quad (3.3)$$

$$F = \frac{1}{t_{high} + t_{low}} \quad (3.4)$$

$$Output\ duty\ cycle = t_{high} * F \quad (3.5)$$

To provide an output duty cycle close to 50%, R4 should be very low compared to R22 [17]. The HS1101LF relative humidity sensor has an accuracy of ±2% RH.

The output of the sensor circuit was connected to a separate Rohde and Schwarz HMO2024 oscilloscope, in order to monitor and set the RH of the system before each test was conducted. The additional capacitance from the connecting wires from the sensor within the test-cell in the laboratory to the circuit housed within the diagnostics part of the lab was taken into account by using equations 3.2 – 3.5. These calculated capacitances were used to set the signal frequencies corresponding to the three humidity levels used in this work, as listed in Table 3.2. These values were calibrated with a Testo 608-H2 Thermohydrometer [18], with an operation range from 2% - 98% RH and a ETI6100 Thermohydrometer, with an operation range of 0% - 100% RH, in order to ensure the achieved humidity levels were consistent and accurate.

Table 3.2 - Capacitance and output frequency of the 555-timer circuit from the system tested within the lab

Relative Humidity	Capacitance	Accepted Frequencies
<10%	195.7 – 199.4 pF	6.3 – 6.42 kHz
50 ±5%	209.4 – 212.2 pF	5.92 - 6 kHz
>90%	223.6 – 226.8 pF	5.54 - 5.62 kHz

An example of the output waveform from the circuit in Figure 3.19 is shown in Figure 3.20, for ~50% RH.

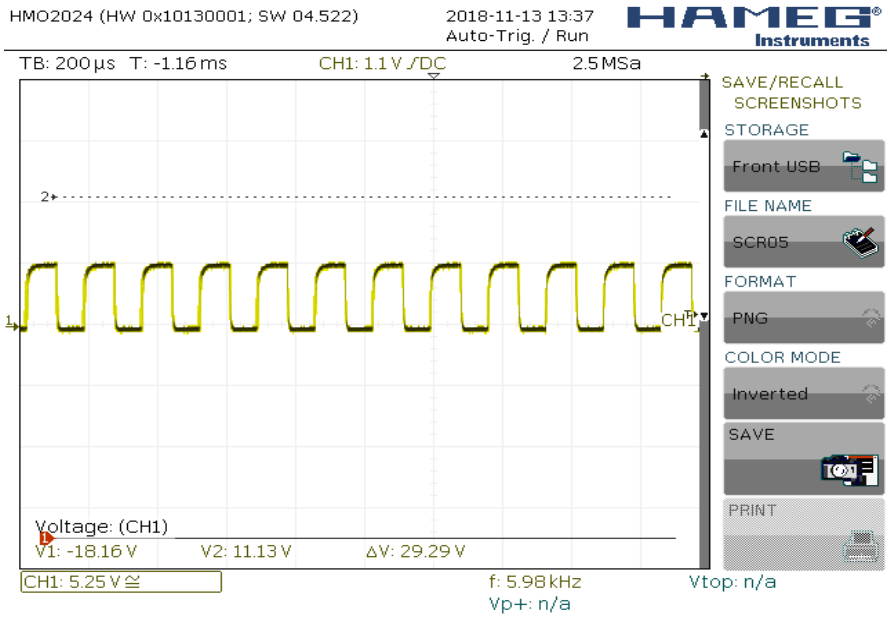

Figure 3.20 - Output waveform of the 555-timer circuit showing 5.98 kHz signal, corresponding to ~50% RH

In order to provide protection to the humidity measurement system under high voltage breakdown, the connecting wires to the frequency response circuit were then disconnected during the testing process, once the desired humidity level had been set and verified. After completion of each test, the chamber was evacuated and refilled with gas, and the buffer circuit was reconnected to monitor and set the RH.

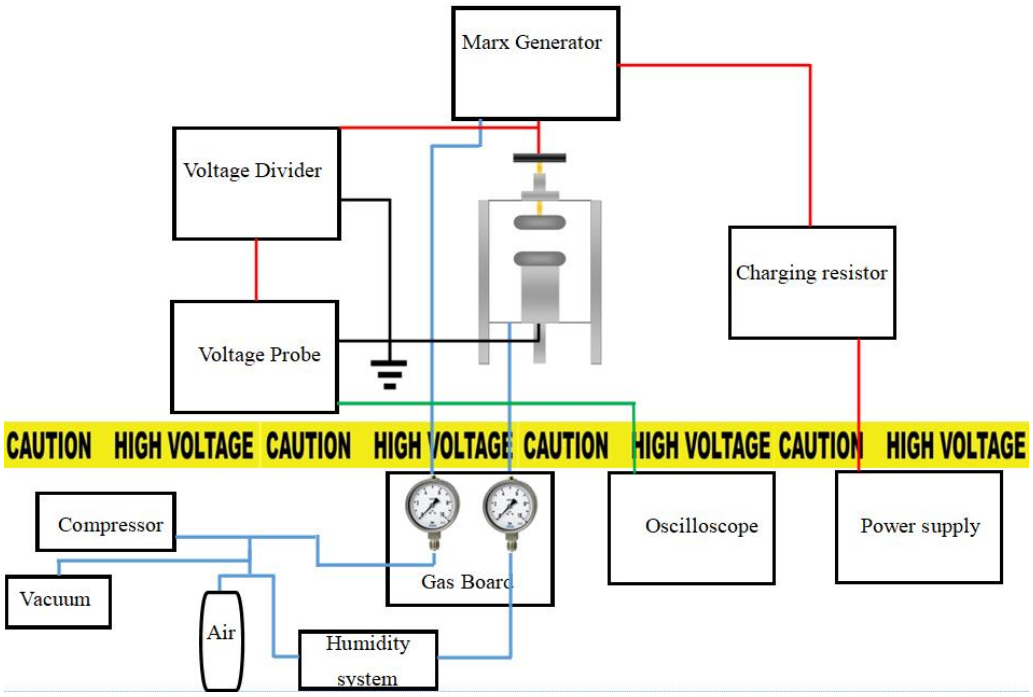

Figure 3.21 – Overall architecture of the experimental system, separated into diagnostics and control section (lower part of figure) and HV section of lab (upper part of figure)

Combining the sub-systems presented in Sections 3.5.1 and 3.5.2, the overall architecture of the experimental system is show in Figure 3.21, where the equipment in the high voltage and diagnostics sections of the lab can be differentiated.

3.6. HV GENERATION, MEASUREMENT AND ANALYSIS

The diagnostics equipment is introduced herein, as well as the wave-shaping circuitry of the 10-stage Marx Generator. The testing standards adhered to are also introduced, as well as information on the statistics used in analysis of the flashover/breakdown voltage data.

3.6.1. Diagnostics Equipment

The output of the Marx generator was connected to the test cell and a voltage divider in parallel. A 1000:1 Tektronix P6015A HV probe was connected to the tap-off point of an 8:1 $CuSO_4$, 2 kΩ resistive voltage divider, and through to a Tektronix MDO3012 oscilloscope for analysis of the resulting waveforms. The voltage divider is 700 mm in length and has an inner diameter of 50 mm. The tap-off point is situated 70 mm from the earth plate. An illustration of the voltage divider is provided in Figure 3.22.

The voltage divider is formed from 50-mm diameter PVC tubing, filled with aqueous $CuSO_4$ solution of the required resistivity to yield an input impedance of 2 kΩ. A bronze-phosphor sphere of diameter 25 mm formed the high-voltage electrode; a short length of M6 screwed rod was used to connect this internal sphere to the external circuit via a PVC feedthrough. A 19-mm diameter bronze-phosphor sphere was used to cover the sharp edges of the threaded connection externally, in order to prevent high field regions forming and resulting in unwanted breakdown. The earth electrode was formed from a 40-mm long section of 50-mm diameter brass rod, connected to a 250-mm diameter aluminium plate of thickness 3 mm. The tap-off point consisted of an internal bronze-phosphor sphere of diameter 10 mm, fed through the side wall of the vessel by M3 screwed rod, and covered externally by a second 10-mm diameter bronze-phosphor sphere.

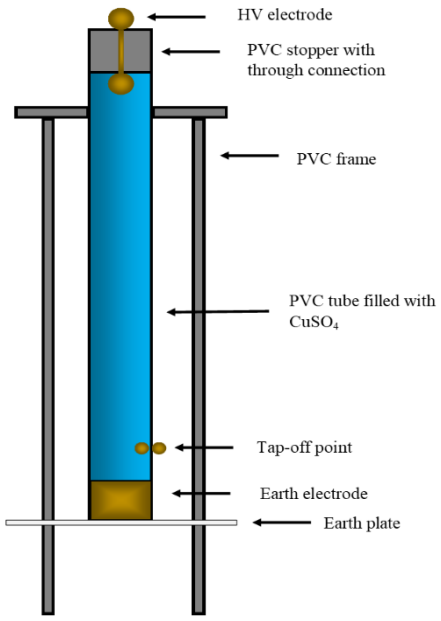

Figure 3.22 – Cross section diagram of Samtech DE(LRP)-02 voltage divider

The structure was supported by three cylindrical PVC legs underneath the earth plate, and by a PVC support frame consisting of a 250-mm diameter disc with a central clearance hole for the divider, and three 650-mm long sections of 20-mm diameter rod between this disc and the earth plate. The PVC support legs were 130 mm long and 25 mm in diameter.

The response time of the divider was calculated by estimating the stray capacitance and inductance of the voltage divider using [19]. But for a vertical divider, the C_0 is in the range of 12-20 pF, [16]. To determine if the voltage divider has a fast enough response to the output impulse rise time of t_r = 100 ns when R = 2 kΩ, equations 3.6 and 3.7 must be satisfied, [20].

$$\frac{L_0}{R} < \frac{t_r}{20} \tag{3.6}$$

$$0.23 C_0 R < t_r \tag{3.7}$$

As the calculated values satisfy these equations, then the voltage divider in Figure 3.22 is of a good design for measuring output impulses with a rise time of 100 ns. Under this arrangement, the maximum accepted values of stray capacitance and inductance for t_r = 100 ns with R = 2 kΩ, are C_{max} ~210 pF and L_{max} ~10 μH.

The theoretical response time of 5 ns for the system was found using equation 3.8, [21].

$$T = \frac{C_0 R}{6} \tag{3.8}$$

The voltage divider was calibrated at low voltages (40 kV peak), by measuring the voltage at the input of the divider and comparing this with the voltage at the tap-off point, for the same applied charging voltage. This calibration procedure was conducted after every 20 shots, in order to monitor if any changes in division ratio occurred. A consistent division ratio of ~8:1 was found over all of the testing programme.

For voltage measurement during testing, a Tektronix (USA) P6015A high-voltage probe (1,000:1 division ratio) was connected between the tap-off point on the voltage

divider and ground, such that the total division ratio was ~8,000:1. The Tektronix probe has a peak impulse voltage measurement capability of 40 kV when used standalone, and 320 kV when connected to the tap-off point on the liquid-resistive divider. The nominal bandwidth of the Tektronix probe is 75 MHz. High voltage waveforms were viewed and recorded with a Tektronix (USA) MDO 3012 digital oscilloscope, with a bandwidth of 100 MHz and a sampling rate of 2.5 GS/s.

3.6.2. Wave-shaping of 10-stage Marx Generator Output

Figure 3.23 shows a circuit diagram of the connections from the output of the Marx generator, connected to the test cell and the monitoring station where the data was recorded.

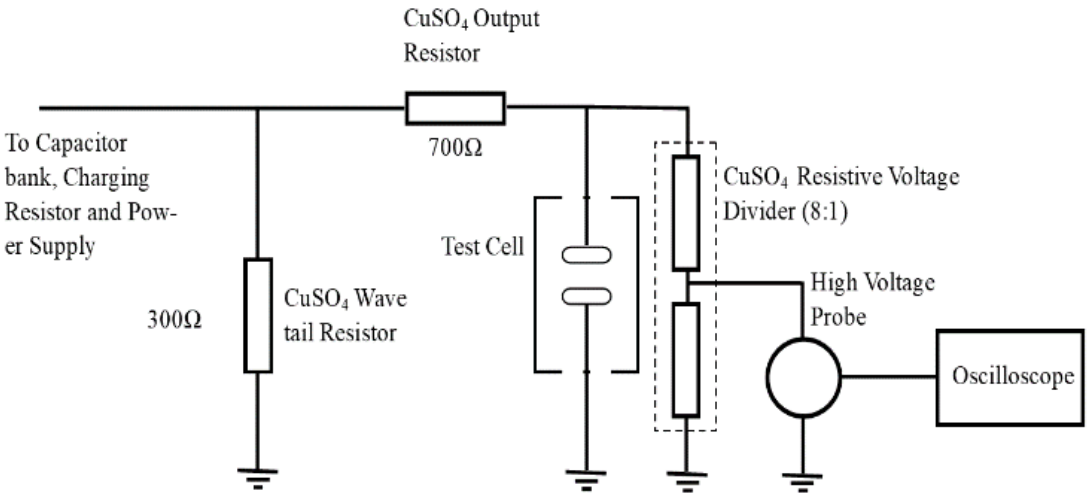

Figure 3.23 - Schematic diagram showing the output and measurement circuit used with the 100/700 ns output Marx generator used throughout the study

Figure 3.24 shows the resulting (positive) 100/700 ns output voltage waveform (no breakdown).

a) b)

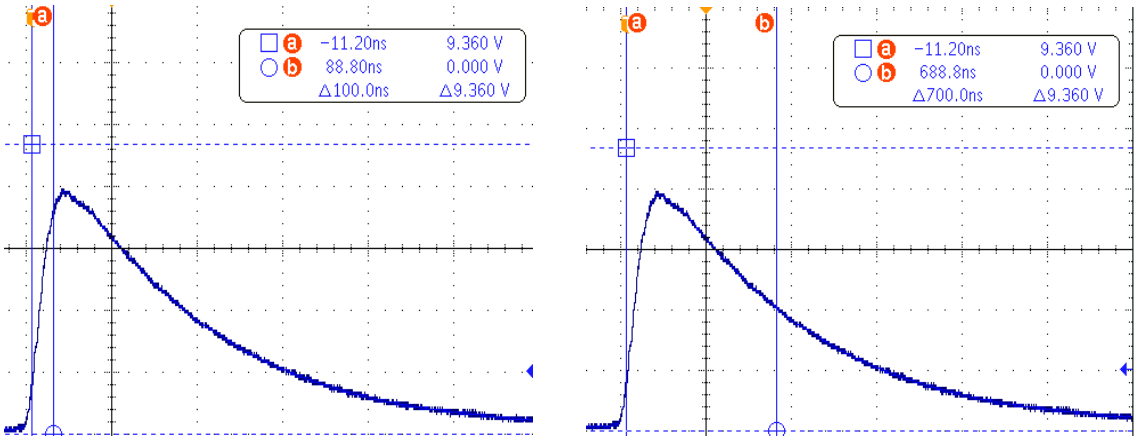

Figure 3.24 - Output waveform showing a) the 100 ns (10% - 90%) rise time and b) The time to half value of 700 ns; where no breakdown is recorded (no voltage collapse)

3.6.3. Output Measurement

In terms of reading output voltage waveforms, Figure 3.25 shows a flashover/breakdown occurrence for a positive-polarity impulse. Once a breakdown or flashover event occurred, the peak applied voltage and time to breakdown were recorded for each event.

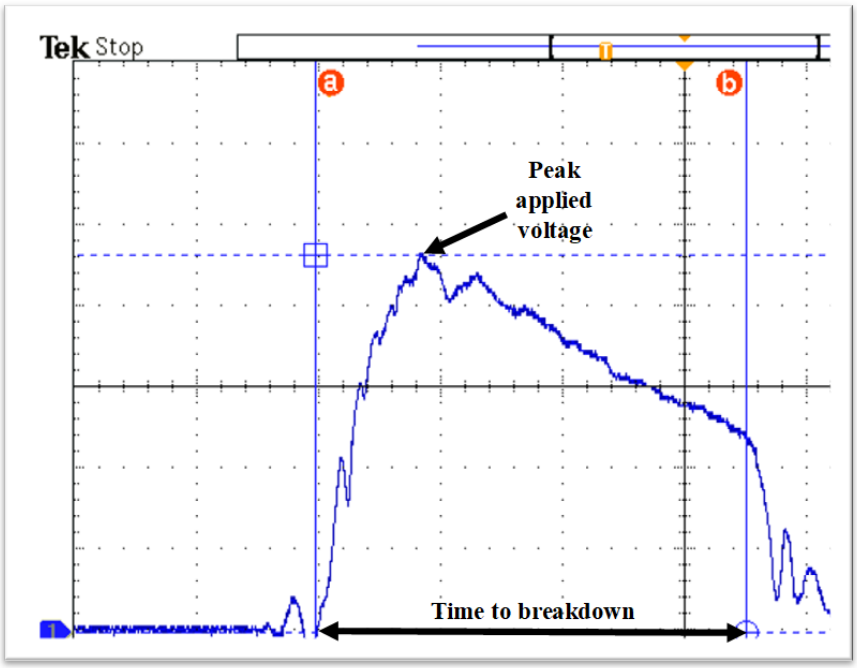

Figure 3.25 - Example of an output breakdown voltage waveform where the peak applied voltage and the time to breakdown were extracted from the output waveform. This output was measured during testing of a Polyoxymethylene sample with a knurled surface finish, at 0 bar gauge pressure and under >90% RH. The peak applied voltage recorded was 76.3 kV, and the time to breakdown was 548 ns

3.6.4. ASTM D3426-97 'step-up' testing procedure

The testing procedure implemented was a 'step up' method, as included in the ASTM D3426-97 standard [22]. The voltage level initially applied was set to provide a low probability of flashover, before the charging voltage was increased in iterations of 300 V, monitored using a DMM, via a 1000:1 Testec HVP-40 HV probe. Once a flashover event was initiated from one of the three tests at each level, the resulting waveform was inspected, and the flashover voltage (peak applied voltage) and the time to breakdown was recorded. Once the test cell was evacuated and refilled with gas, the output voltage was then decreased back to a level with a low probability of breakdown, and the process repeated until the occurrence of another flashover event. Two, clear withstand levels were always observed before a valid breakdown voltage was recorded. The step-up testing procedure has been illustrated in Figure 3.26, showing at least two legal breakdown events with respect to time and voltage application (5th and 4th stage breakdown).

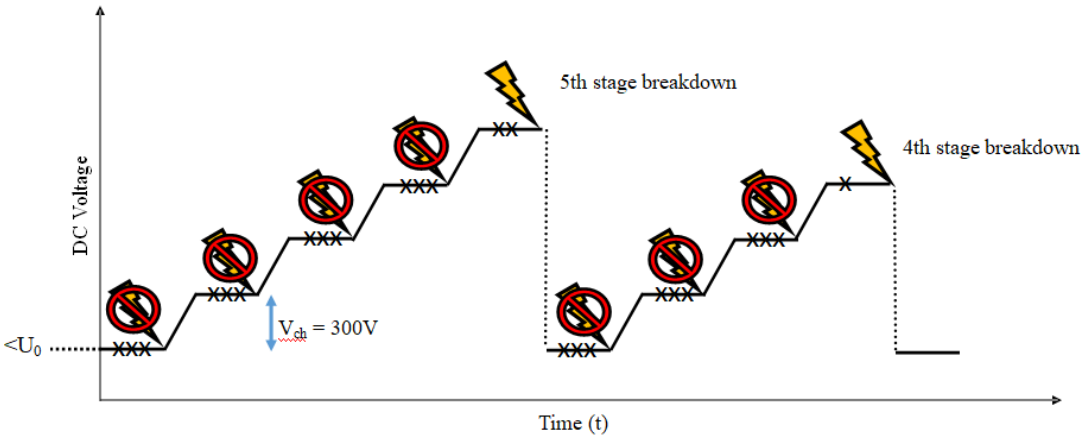

Figure 3.26 – Step-up testing procedure illustration, showing two legal breakdown/flashover voltage occurrences in accordance with ASTM D3426-97

This process was conducted N = 20 times for each set of test conditions, in order to achieve 20 breakdown voltage results for each set of experimental conditions.

3.7. Error and Uncertainty

Errors and uncertainties can have a substantial impact on the accuracy of measurements. Factors such as the condition of the measuring instrument, the stability

of the item being measured, difficulties in the measurement process, calibration uncertainties, operator proficiency or reaction time, sampling issues, and environmental conditions, all have the potential to contribute to measurement errors and uncertainties [23].

To enhance the accuracy of measurements, it is crucial to identify and minimise sources of uncertainty. This can be achieved by employing calibrated instruments, ensuring stable conditions throughout the measurement process, employing appropriate sampling techniques, and providing training to operators to reduce their influence on the measurements.

In certain situations, it may be necessary to conduct multiple measurements to decrease the impact of uncertainties on the overall accuracy. Furthermore, statistical analysis techniques can be used to quantify the uncertainty related to the measurements and to estimate the overall accuracy of the results.

Measuring short-duration transient events, such as those with durations ranging from nanoseconds (ns) to microseconds (μs), poses numerous challenges. The most significant challenge is ensuring that the measuring system is capable of accurately capturing rapidly-changing signals. This requires careful consideration of two critical factors, namely, the rise time or bandwidth of the equipment, and the sampling rate of the oscilloscope used to capture the waveforms.

The measuring system's bandwidth (BW) is defined as the frequency range over which the measured signal is attenuated by ≤3 dB, indicating that the captured signal voltage is at least 70% of the maximum voltage measured. The rise time, τ_r, is a measure of how fast the signal changes and is related to the bandwidth of the measuring system through equation 3.9. Thus, both the bandwidth and the rise time are crucial factors that affect the capability of the measuring system to capture short-duration transient events.

$$\tau_r = \frac{0.35}{BW} \qquad 3.9$$

To ensure accurate measurements of short-duration transient events, it is generally recommended that the rise time of the measuring equipment be 3 to 5 times shorter than the rise time of the signal being measured, [24].

Table 3.3 presents a detailed summary of the equipment used in the tests and their corresponding rise time and bandwidth characteristics. The bandwidth values listed in the table were obtained directly from the manufacturers.

Notably, the Tektronix high voltage probe has the lowest bandwidth of 75 MHz, with the fastest response time of approximately 5 ns. As such, the acquisition of flashover characteristics related to higher frequencies is limited by the lowest bandwidth value of the measuring equipment. This highlights the importance of selecting equipment with appropriate bandwidth and response time characteristics, to ensure accurate and reliable measurements of short-duration transient events.

Table 3.3 - Test equipment rise time and bandwidth.

Equipment	Bandwidth (MHz)	Rise Time (ns)
Tektronix MDO3012 Oscilloscope (sampling rate 2.5 GS/s)	100	3.5
Rhode and Schwartz HMO2024 (sampling rate 2 GS/s)	200	1.75
Tektronix high voltage probe P6015A	75	4.7
8-1 Resistive voltage divider	70	5

3.8. LABORATORY SETUP

This section provides information on the laboratory setup used to execute the practical work, where Figure 3.27 shows the diagnostics part of the lab and Figure 3.28 shows the HV testing section of the lab, which are isolated from each other as shown by the physical partition in Figure 3.27 (and illustrated in Figure 3.21).

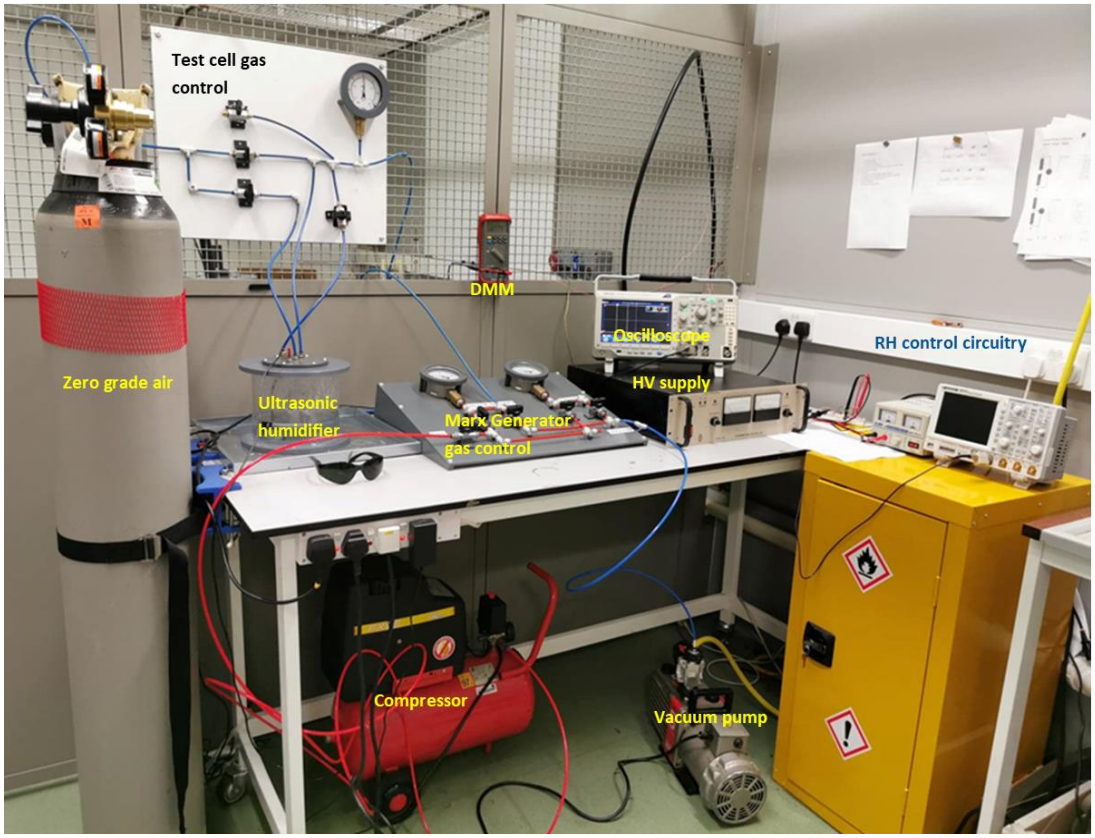

Figure 3.27 - Diagnostics section of the laboratory showing all diagnostics equipment and gas connections with physical partition isolating from the HV section of lab

In Figure 3.27, each part of the diagnostics and control section of the lab is identified, including:

- the gas control equipment to affect triggering of the spark column of the Marx generator, as well as to set the pressure and humidity inside the test cell.
- The oscilloscope and circuitry used to monitor the relative humidity of the air in the test cell.
- The HV supply, along with the DMM used to display the DC charging voltage, being fed from a Testec HVP 40 kV DC probe monitoring this charging voltage.
- The oscilloscope used to monitor the output voltage waveforms from the Marx generator, showing either a withstand or breakdown/flashover event, as outlined in Figures 3.24 and 3.25, respectively.

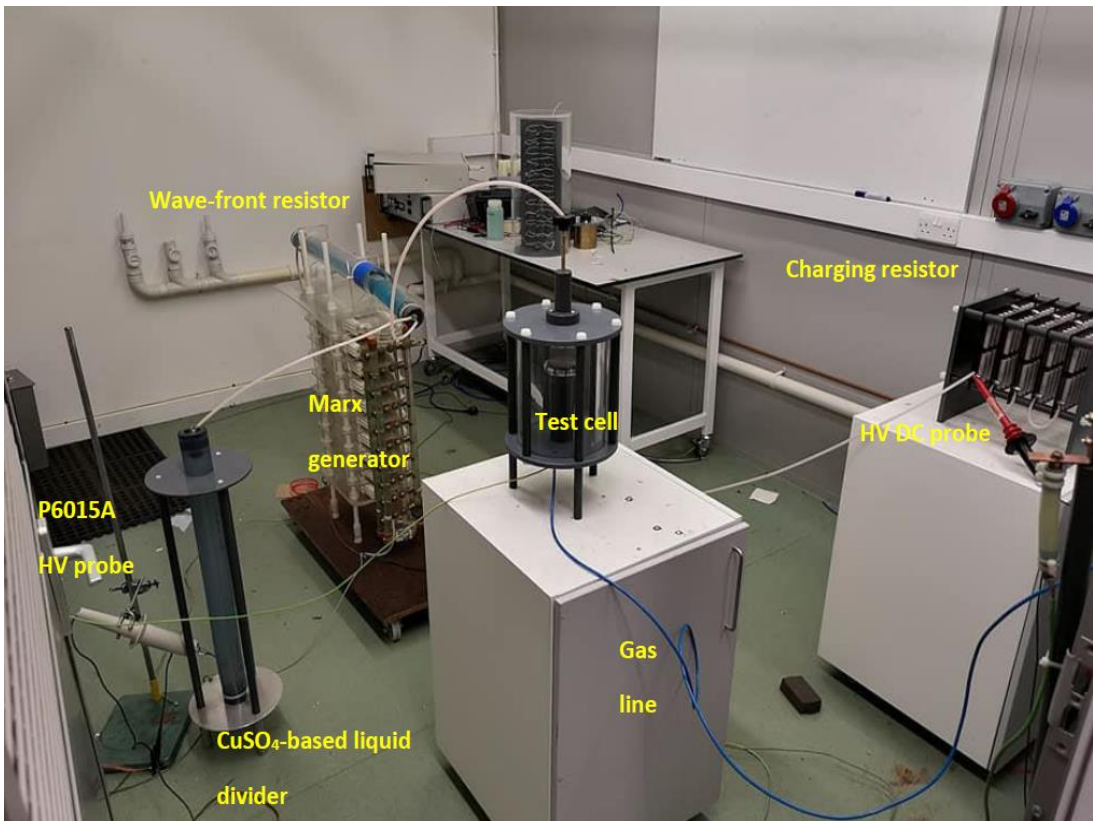

Figure 3.28 - HV section of lab with all the equipment connected to test the insulation system within the test cell

The connections of the experimental setup, in Figure 3.28, consist of the HV supply which is connected to the charging resistor shown on the right. The 10 stage Marx generator is used as the pulsed power source in this experimental set up. The Marx generator was charged by a 100 kV HVDC power supply (shown in Figure 3.27) through a 1 MΩ charging resistor.

At the output side of the charging resistor, a Testec HVP 40 DC voltage probe (40 kV DC) is connected to monitor the charging voltage, which is displayed on a digital multi-meter in the diagnostic area of the laboratory (shown in Figure 3.27).

Two aqueous $CuSO_4$ resistors were used to tailor the rise and fall time of the output HV impulses. A 300 Ω wave-tail resistor was connected in parallel with the load, and a 700 Ω wave-front resistor was located on the top of the Marx generator. This Marx topology produces ~100/700 ns HV impulses.

The output of the Marx generator was connected to the HV electrode of the test cell, as well as to a liquid resistive voltage divider (2 kΩ), with a Tektronix P6015A HV

probe (40 kV peak voltage, 75 MHz nominal bandwidth, 1000:1 division ratio) connected to a tap-off point on the divider to analyse the waveforms using a MDO3012 digitising oscilloscope (100 MHz bandwidth, 2.5 GS/s sampling rate).

3.9. STATISTICAL ANALYSIS METHODS

Understanding of the influence of experimental conditions on the breakdown voltage of composite insulation is important to facilitate optimal design of high voltage systems. This includes ensuring that the statistical analysis performed on breakdown voltage data is relevant, in providing extra information on the failure voltages, mainly the enlargement process when the number of points within data sets is limited. Therefore, in order to investigate the applicability of statistical techniques in aiding to elucidate further detail about the breakdown process, two statistical methods were applied and analysed, in order to find the most suitable to be applied to the data generated during a specific set of breakdown tests. Both 2-parameter Weibull and 3-parameter Weibull fittings are discussed herein, as applied to the authors' experimental data on the flashover voltages across air-solid interfaces, subjected to impulse voltages. Fitting the 2-parameter Weibull and 3-paramter Weibull distributions to breakdown voltage data obtained for each set of test conditions allowed for the relative quality of fit of each to be directly compared. The Kolmogorov-Smirnov (K-S) test was used to compare the maximum distance between the experimental data and the theoretical cumulative distribution function (CDF), and evaluate the goodness of the fit thus identifying the most accurate method of statistical analysis for a given dataset.

3.9.1. Introduction

This section will provide information on the statistical analysis methods used in characterising the distribution of the flashover voltages for each set of test conditions. This will focus mainly on the Weibull distribution, as this is a widely used statistical analysis process used within high voltage engineering [25-30], as well as prevalent in other areas of research [31-32]. The 2-parameter Weibull distribution has been used mainly to find the scale and shape parameters from each breakdown/flashover dataset,

however, the 3-parameter Weibull distribution has also been investigated, to estimate the γ value for the breakdown/flashover voltage where the probability of a breakdown/flashover event occurring is 0. This information will assist in the choice of data representation in this thesis, which is discussed in Section 3.10. Therefore, it is imperative to further understand the statistics of the data, and how this will relate to the overall results of the data shared. The Weibull distribution defines the probability connected with continuous data, much like the normal distribution does. However, it can also model skewed data, unlike the normal distribution. In fact, because of its versatility, it can model data that is skewed both left and right, [33].

This section will describe the selection of each statistical analysis method in terms of goodness of fit, as well as the particulars of the selected statistical analysis method and its findings.

3.9.2. 2-parameter and 3-parameter Weibull distributions

Both 2-parameter and 3-parameter Weibull statistical analysis was performed on all breakdown data, in order to characterise the trends. In this work, V is the peak applied voltage that was found to induce flashover. Using the 2-parameter (3.12) and the 3-parameter Weibull distribution (3.14) [34], two or three different parameters characterizing the distribution are found per dataset. The first parameter, α (kV), defines the offset voltage, (V), where the probability of breakdown is 63.2%, $V_{63.2} = \alpha$. The second parameter, β, is used to control the skewness and the kurtosis of the distribution and is found from the gradient of the distribution, which will ultimately give information on how sensitive the specific insulation system is to a change in applied voltage. Lastly, using the 3-parameter Weibull distribution, the voltage associated with 0% probability of failure (γ) was found for each of the sets of test parameters. For each 20-datapoint test, using equation 3.10, the 0.01% probability of breakdown/flashover (1 failure in 10,000 shots) was calculated from the CDF, thereby enabling comparison with the γ values found from the 3-parameter distribution.
The 2-parameter Weibull distribution is defined in equation 3.10.

$$F(V) = 1 - exp\left[-\left(\frac{V}{\alpha}\right)^{\beta}\right] \tag{3.10}$$

Equation 3.10 characterises the cumulative probability of failure and gives a distribution in terms of flashover voltage with respect to probability of failure occurring. In order to form probability plots to compare the behaviour of the different gas-solid (or gas only) gaps, the CDF from equation 3.10 is converted into the linear form shown in equation 3.11:

$$\ln\left[\ln\frac{1}{1-F(V)}\right] = \beta\ln(V) - \beta\ln(\alpha) \tag{3.11}$$

In order to understand the difference between 2-parameter and 3-parameter Weibull distributions, a linear regression technique was used in order to determine the γ value where the R value was maximum when $\gamma \neq 0$, enabling a 3-parameter Weibull distribution to then be used, as shown in equation 3.12.

$$F(V) = 1 - exp\left[-\left(\frac{V-\gamma}{\alpha}\right)^{\beta}\right] \tag{3.12}$$

Equation 3.13 shows the 3-paremeter Weibull distribution in equation 3.12 in linear form, for completeness' sake.

$$\ln\left[\ln\frac{1}{1-F(V)}\right] = \beta\ln(V-\gamma) - \beta\ln(\alpha) \tag{3.13}$$

In order to produce the Weibull plots which are discussed in this chapter and are shown throughout Chapters IV, V and VI the following procedure was followed:

1. The 20 applied voltages which resulted in breakdown/flashover were sorted into ascending numerical order.
2. These voltages were then assigned rank numbers, where the lowest voltage was assigned rank 1 and the highest voltage was assigned rank 20.
3. In order to estimate the unreliability, *F*(*V*), this was defined using Bernard's approximation of median ranks, [35], using equation 3.14:

$$\text{Median ranks} = \frac{(i-0.3)}{(n+0.4)} \tag{3.14}$$

where *i* represents the rank order in terms of breakdown voltage as discussed in point 2, and *n* represents the numbers of values within the dataset, *n = 20.*

4. Equation 3.10 or 3.12, as appropriate, was then used, dependent upon if a 2-parameter or 3-parameter Weibull distribution was being fitted.
5. The *x*-axis values were assigned either ln(V) or ln($V-\gamma$), dependent upon use of the 2-parameter or 3-parameter Weibull distribution.
6. In order to determine the optimal values of β, linear regression was used in order to find the gradient of the straight lines, and therefore the values of β. α is found from $\alpha = \exp - \left(\frac{c}{\beta}\right)$, [36]; a graphical representation is shown in Figure 3.29.
7. Using these α and β values, the 2-parameter Weibull CDF was determined.

Using equation 3.10, the 0.01% probability of failure was found from the sigmoidal CDF as this is a common failure rate used in pulsed power systems when commissioning new or modifying existing equipment. After these steps were completed, the α and β values were extracted from the plots, as shown in an example for a knurled Polyetherimide spacer tested with positive polarity at 0.5 bar gauge and >90% RH in Figure 3.29. A CDF from the values extracted from Figure 3.29 is shown in Figure 3.30 based on α, β and $V_{0.01}$, values.

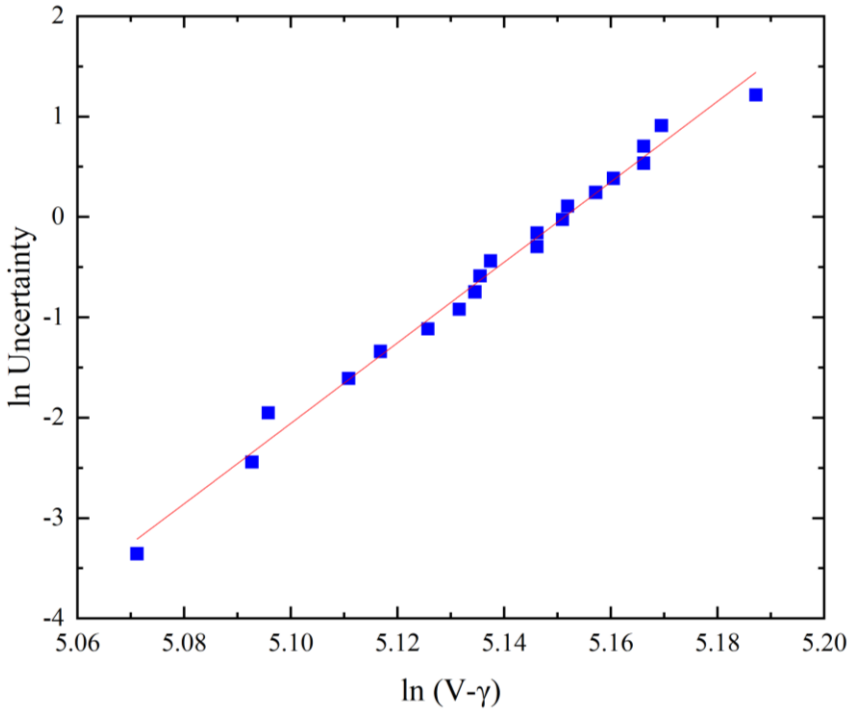

Figure 3.29 - Weibull plot of peak applied voltage data of a knurled Polyetherimide spacer tested at 0.5 bar gauge and >90% RH, under positive polarity impulses, fitted with the 2-paraneter Weibull distribution with $\gamma = 0$.

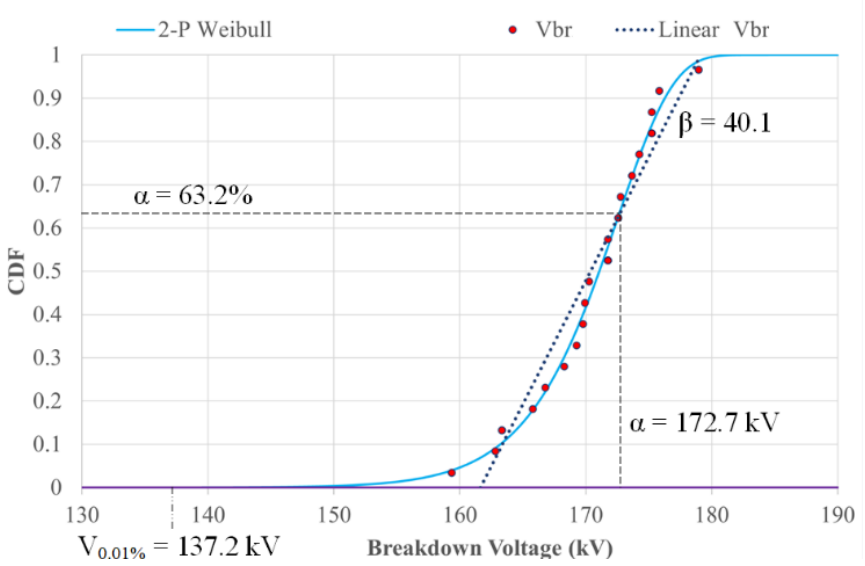

Figure 3.30 - Resultant CDF from the values extracted from the Weibull plot process from Figure 3.29 and the calculated $V_{0.01}$ values.

Figure 3.30 shows an example distribution from the results for a knurled Polyetherimide spacer, tested at 0.5 bar gauge and >90% RH, under positive polarity. The calculated values from Figure 3.30 were α = 172.7 kV and β = 40.1. These values were then used to produce a CDF, from which the value of $V_{0.01}$ was calculated, and found to be 137.2 kV, shown approximately on Figure 3.30.

In a separate example, for an open-air gap at ~50% RH and 0.5 bar gauge pressure, under positive impulses in order to define the associated 3-parameter Weibull distributions, to find the approximate γ value, to enable the 3-parameter Weibull distributions to be plotted. This was done by associating the γ value with the correlation coefficient, *R*, concluding on the γ value yielding the best linear fit. This process was conducted by allowing multiple values for γ to be entered, therefore the relationship between the two parameters could be monitored and graphed. The *R* value was calculated by using the Pearson product-moment correlation coefficient for two sets of values, *X* and *Y*, represented by $\ln(V-\gamma)$ and $\ln\left(-\ln\left(1-F(V)\right)\right.$ respectively, from Figures 3.31 and 3.32, and given by equation 3.15, where $\bar{X}$ and $\bar{Y}$ are the sample means of the two arrays of values.

$$R = \frac{\sum(X-\bar{X})(Y-\bar{Y})}{\sqrt{\sum(X-\bar{X})^2 \sum(Y-\bar{Y})^2}} \tag{3.15}$$

Therefore, when the correlation coefficient (*R*) is maximum, the corresponding value of γ used to find this maximum value of *R* can be approximated as the location parameter (γ) value. This follows a similar method to that in [37], maximising the correlation coefficient in order to approximate a γ value.

Figure 3.33 shows the distribution generated for the 3-parameter Weibull distribution, found by estimating γ from the maximum correlation coefficient, using equation 3.15. It can be seen that the maximum correlation coefficient of 99.15% was found when γ = 161.6 kV, whereas the correlation coefficient had a value of 91.68% at γ = 0. In terms of linear regression, a better fit is found when γ = 161.6, (Figure 3.32), compared to when γ = 0 (Figure 3.31), culminating in an increase in the *R* value of ~8% between the distributions, when moving from γ = 0 to γ = 161.6. The values found using this process for each test iteration were used in order to generate the 2-parameter and 3-parameter Weibull CDFs.

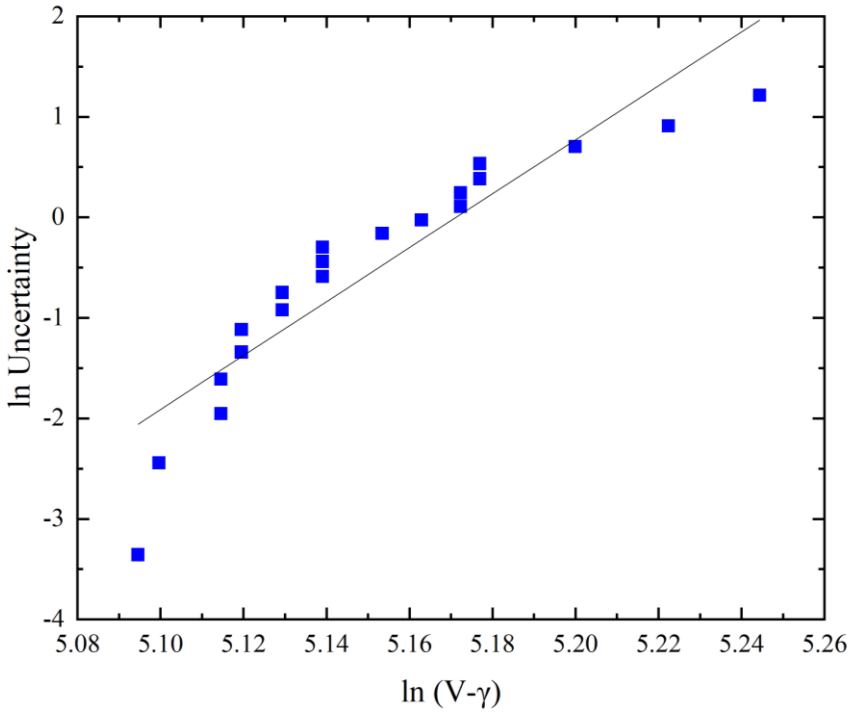

Figure 3.31 - Linear relationship between γ = 0 and R = 91.68% from a 2-parameter Weibull distribution or an open-air gap at ~50% RH and 0.5 bar gauge pressure, under positive impulses.

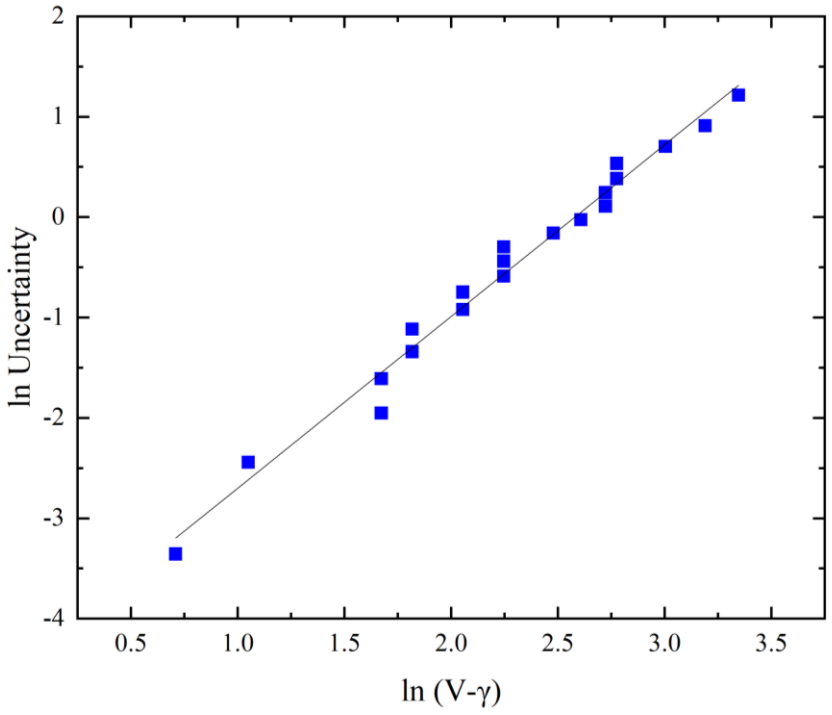

Figure 3.32 - Linear relationship between γ = 161.6 and R = 99.15% from a 3-parameter Weibull distribution for an open-air gap at ~50% RH and 0.5 bar gauge pressure, under positive impulses.

Finally, once the α, β and γ values were found for each dataset, these values were then transferred over to a probability/voltage plot for ease of comparison between different tests. All of the above analysis was conducted using Microsoft Excel.

Following comparison of values extracted from corresponding 2-parameter and 3-parameter Weibull distributions, the 2-parameter distribution was chosen to be applied to all of the results generated in the study, used to define a low, but non-zero, probability of breakdown or flashover of the insulation systems. As shown in Figure 3.33, it was intitally found that when increasing the γ value of the system, the Pearson (R) coefficient was seen to increase. An example is shown in Figure 3.33, for breakdown of an open-air gap at ~50% RH and 0.5 bar gauge pressure, under positive impulses.

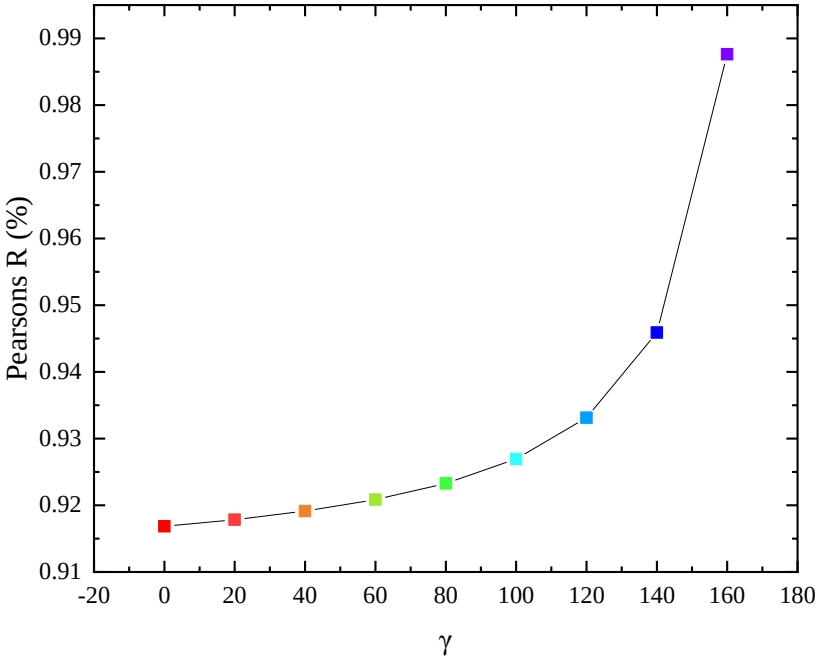

Figure 3.33 - The relation of the Pearson coefficient, R, to increasing location parameter, γ, showing R increasing from 91.7% at γ = 0, to 99.2% at γ = 161.6

From plotting the gamma values against the Pearson coefficient, R, it was shown that increasing the gamma value results in a more linear behaviour, as shown in Figure 3.34. As γ increased, it was found that the spread in values fits the linear approximation better γ = 161.6, in comparison to when γ = 0. This is particularly interesting, as the difference in the V-γ values at γ = 0, hides the fact that the distribution does not fit the

linear approximation as well, this is shown from these two examples measured individually in Figures 3.31 and 3.32 for γ = 0 and γ = 161.6 respectively.

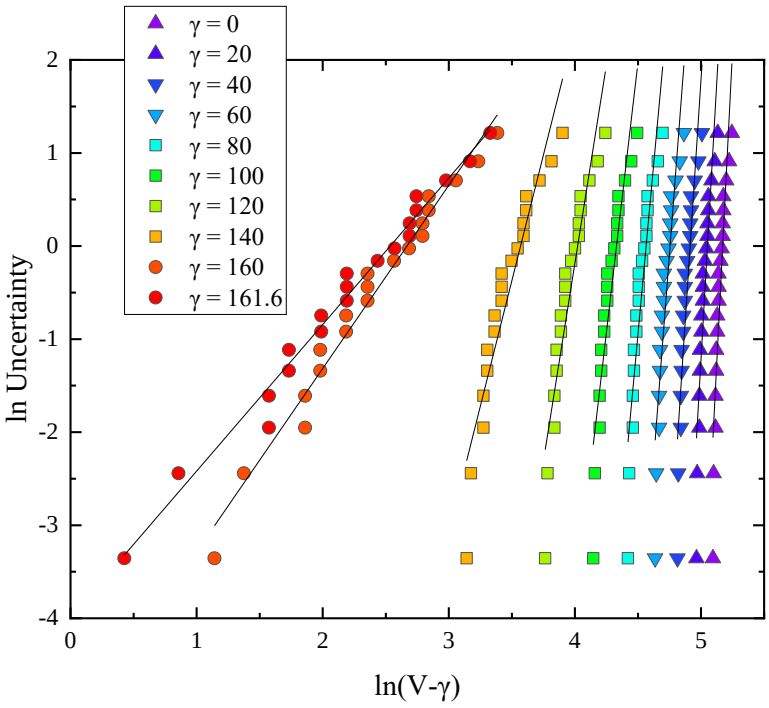

Figure 3.34 – Data points in an open gap arrangement for tests at ~50% RH and 0.5 bar gauge, under positive energisation - it is apparent that with increasing gamma, the behaviour fits the linear distribution

From each system tested, by adjusting γ from 0 to 160 in iterations of 20, with γ = 161.6 finally added as the maximum value, each value of α and β was found at each respective iteration. Figure 3.35 shows the CDFs of each iteration with varying shape. As shown, the α value remains consistent due to the linear shift of the γ value where:

$$\alpha = \alpha_{new} + \gamma \tag{3.16}$$

Where each synthetic CDF intersects irrespective of the γ value at 0.632 (α). However, for the β terms, these do not remain consistent as the distribution must cross the x-axis at γ, so therefore to keep a constant α value, β must change, as shown in Figure 3.35, where the β value decreases from 26.84 at γ = 0, to 1.58 at γ = 161.6, where the maximum Pearson coefficient is found (99.2%).

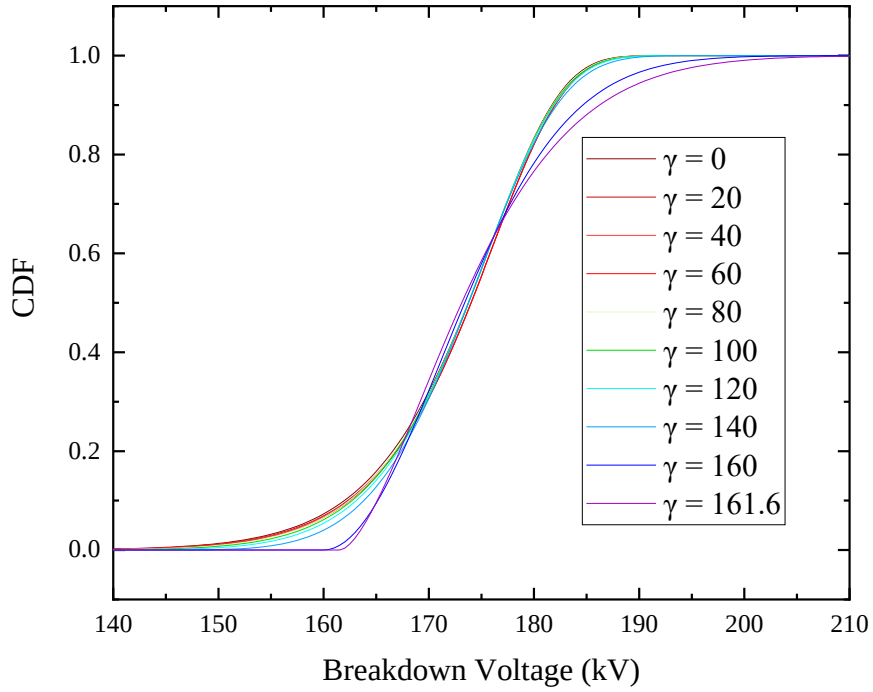

Figure 3.35 - Cumulative distribution function of the same data set with varying γ, showing the change in the shape of each function.

So, from this dataset, due to the linear regression technique used, the V_0 (0% probability voltage value) is shown to occur at 161.6 kV. So, from the definition of γ, this means that below this level of applied voltage (161.6 kV), the probability of failure is zero, and no failure events will take place below this value. This conclusion begins to be problematic when considering the breakdown voltages associated with these two statistical analysis methods, as in Figure 3.36.

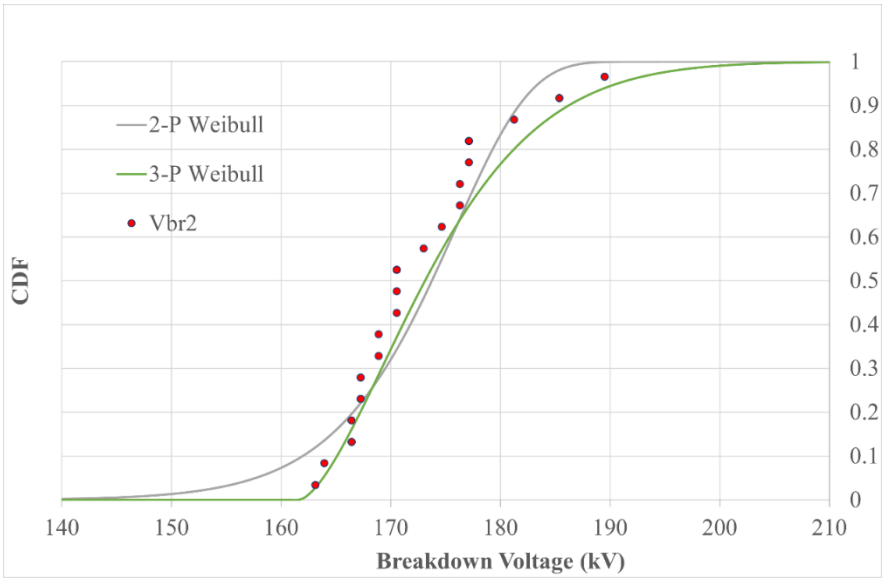

Figure 3.36 – 2 parameter and 3-parameter Weibull distribution fit against the measured flashover values of the data set

Although the 3-parameter Weibull distribution is shown to provide the best fit to the data, the implied 0% probability value is shown to reside only ~2 kV below the lowest measured breakdown voltage. Using the 2-parameter Weibull distribution, where $\gamma = 0$, calculations can be made in order to approximate the applied voltage associated with a very low probability of failure from the CDF.

On this basis, conservatively, when calculating low probabilities, it was decided that the 2-parameter Weibull distribution would be used, with a calculated value of $V_{0.01}$ providing a probability of failure of 1 in 10,000 shots, information of practical significance to system designers, where a consistent $\gamma = 0$ value has been used in order to directly compare the α and β values, from the each dataset.

3.9.3. Kolmogorov-Smirnov Test

In order to investigate the applicability of statistical techniques in aiding to elucidate further detail about the breakdown process, multiple statistical methods were applied and analysed, in order to validate the conclusion that the 2-parameter Weibull distribution be used to represent all experimental data generated in this thesis. Therefore, 2-parameter Weibull fittings are discussed herein, as applied to all experimental data on the breakdown and flashover voltages in this thesis. The 2-parameter Weibull cumulative distribution functions (CDF) were plotted, to enable

extraction of the specific fitting parameters associated with each distribution. The CDF for each statistical method has been plotted alongside the empirical cumulative distribution function (ECDF), found from the flashover voltages recorded during experimental testing. The distribution of best fit was then analysed by using the Kolmogorov-Smirnov (K-S) test, in order to determine the CDF that best represented the ECDF, which is a widely used goodness of fit test [38]. These theoretical CDFs were plotted alongside the practical ECDFs, and the K-S test was used to determine the optimum coefficient of determination (COD) between the various distribution models. The COD test used in this paper is the Kolmogorov-Smirnov (K-S) test statistic, described in [39], which determines the best fit by the greatest vertical distance which results from the plotting of the empirical and theoretical CDFs. The rejection of the null hypothesis is achieved when the K-S test statistic is greater than the critical value. The critical value used in this paper, at a *p*-value of 0.05, is 0.2941, which refers to the 95% confidence interval, taken from [40]. The K-S statistic can be written as in equation 3.17:

$$D_n = \max_x \left| F_{exp}(x) - F_{obs}(x) \right| \tag{3.17}$$

where D_n is the Kolmogorov-Smirnov statistic, F_{exp} is the cumulative distribution function associated with the null hypothesis, and F_{obs} is the empirical distribution from the data gathered from testing. Shown in Figure 3.37 is an illustrative example of how equation 3.17 relates to the practical examples associated with the CDF and ECDF, where the maximum distance from the ECDF (in blue) to the CDF (in red), represented by the arrow, allows D_n to be determined. The significance of this value is that it allows the largest distance that the ECDF diverges from the CDF to be determined. By plotting multiple distributions, and analysing multiple K-S critical values, the specific tested distribution (in this case 2-Parameter Weibull analysis) can be tested in terms of applicability of representation of each data set. From using these specific functions in relation to the distribution models used, theoretical CDF data can be plotted for the 2-parameter Weibull.

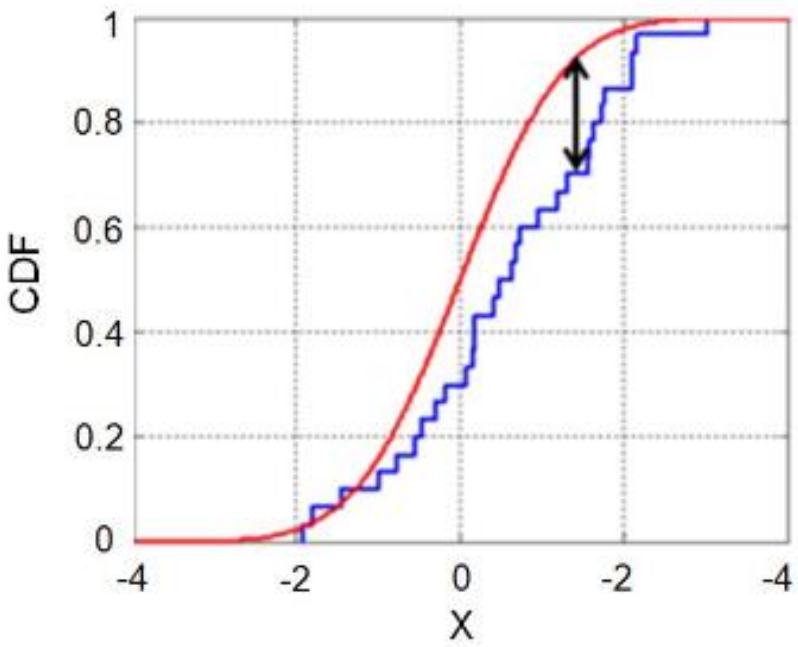

Figure 3.37 - Illustrative example of K-S test, with maximum deviation shown from the black arrow between the CDF in red and ECDF in blue

From the analysis conducted, information has been generated on the distribution of fit of the 2-parameter Weibull distributions, applied to the authors' empirical data on the breakdown/flashover voltages and times to breakdown/flashover associated with impulsive breakdown of solid-air interfaces. Each 2-Parameter Weibull distribution tested were able to represent each of the datasets tested in this thesis, due to distance values, D_n, being lower than the corresponding critical value used in this paper, at a *p*-value of 0.05, which is a value of 0.2941 for 20 data points.

Therefore, it was concluded that in order to further analyse the data in terms of probability and sensitivity of breakdown/flashover, the 2-Parameter Weibull analysis was chosen in order to compare the probability of breakdown and flashover voltages under the various test environments.

3.10. DATA REPRESENTATION

The obtained breakdown voltage values, V_i, were used to calculate the V_{50} flashover voltages. As Weibull analysis has been used in this thesis to further understand the insulation system performance, the CDF was firstly found for each system, which

corresponds to equation 3.18. The V_{50} values are equivalent to the median of the Weibull distribution for each data set.

$$V_{50} = \ln(0.5)^{\frac{1}{\beta}} * \alpha \tag{3.18}$$

Therefore, the flashover/breakdown voltage can be found for each insulation system. This enables the optimum insulation system to be found for each of the sets of test conditions, where the V_{50} values can be compared of each system.

Once the median value (50%) flashover value for each data set has been found, the probability density function (PDF) associated with the CDF is plotted, as shown in Figure 3.38a and 3.38b, using the α and β values calculated from the process outlined in Section 3.9.2. The PDF of this distribution is given by equation 3.19:

$$f(V) = \frac{\beta}{\alpha}\left(\frac{V}{\alpha}\right)^{\beta-1} e^{-\left(\frac{V}{\alpha}\right)^{\beta}} \tag{3.19}$$

and the corresponding CDF is given by equation 3.12.

The 20 breakdown voltage values obtained for each set of test conditions were used in the statistical analysis, performed using Microsoft Excel software. To find the α and β values of the 2-parameter Weibull distribution for each dataset, equation 3.10 was linearised to the form in equation 3.11 , and $\ln\left[-ln\left(1-F(V)\right)\right]$ versus $\ln(V)$ was plotted. The shape and scale parameters were then calculated, where β was found from the gradient of the straight line, and $\alpha = e^{-\left(\frac{c}{\beta}\right)}$, where c is the intercept value. The obtained α and β values were used to plot synthetic PDFs using equation 3.19 for each set of experimental data. The V_{50} breakdown/flashover initiation voltage, which is defined as the median voltage value of the CDF, in equation 3.18, was obtained for each series of tests.

For each test, to show the spread in the obtained flashover voltage values, the voltage interval where ~95.4% of data-points reside (95.4% voltage spread interval) was determined using equation 3.19, by identifying the point of intersection of this PDF with the negative skewness. By identifying the 2.3% and 97.7% probability values on the generated synthetic CDF, the end points of these voltage intervals are presented as

asymmetrical error bars for each V_{50} value. This process exemplifies a spread of data to 2σ.

The versatility of the Weibull distribution allows for skewness and kurtosis to be factored into a distribution when analysing data where error bars are not symmetrical, different to other statistical analysis methods, for example the gaussian distribution found from the normal distribution. As the Weibull distribution results in a skewed distribution, as shown in Figures 3.38a and 3.38b, this gives extra information on the failure rate of the insulation system.

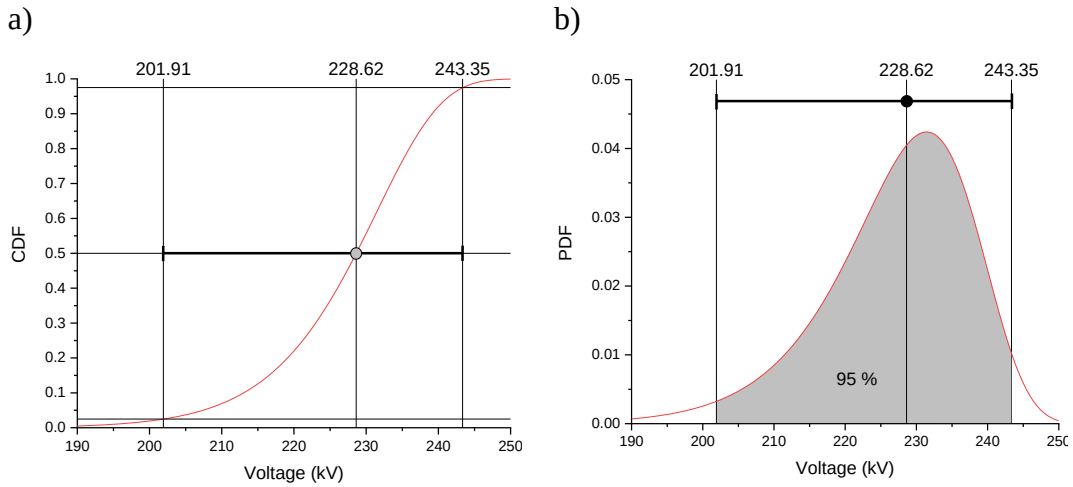

Figure 3.38 – Example of a 2-parameter a) cumulative distribution function (CDF), showing where the 2.3% and 97.7% probability values intersect with the CDF and b) an asymmetrical probability density function (PDF), where the ~95.4% area has been outlined from the error bars at each side of the median (50% probability) value.

For each test, the error bars were found by measuring where ~95.4% of data points reside, by identifying the point of intersection of the CDF and the probability values at 2.3% and 97.7% This process shows that the asymmetrical error bars can be used to represent the negative skewness of the 2-parameter Weibull distribution, as shown from the PDF, showing the ~95.4% area for each distribution, as shown in Figure 3.39a and 3.39b. The solid vertical lines of each PDF represent the V_{50} (median) value (equation 3.18), and the dashed lines represent the locations of the upper and lower error bars - in this particular arrangement, the lower error bar is 88% larger than the upper error bar.

The discussion of the results throughout this thesis puts emphasis on the comparison of these skewed error bars of each compared test, where two or more datasets can be compared. As shown in Figure 3.39a, if the error bars do not overlap, the distributions

are shown to be independent of one another, and the areas of each distribution where ~95.4% of datapoints reside do not overlap. However, if the error bars do overlap, an area of overlap is created between the two PDFs, as shown in Figure 3.39b, indicating that the distributions are not independent.

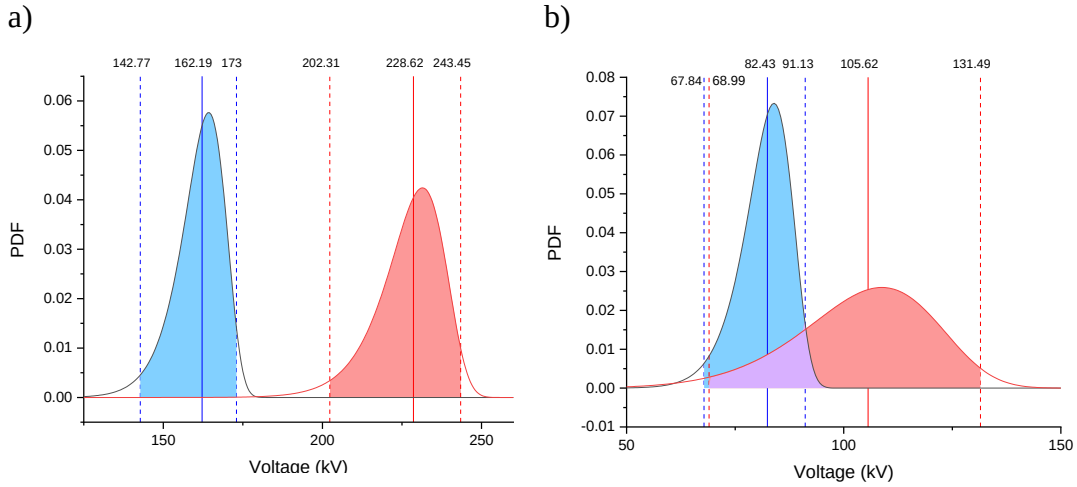

Figure 3.39 – Comparison of two datasets when the error bars a) do not overlap, showing independence and b) when the error bars do overlap, showing that the distributions are not independent.

This method of data visualisation has been used throughout this thesis, showing the V_{50} (median) values where the 50% probability of failure has been calculated and determined from each CDF. In all cases, the error bars have been set to contain ~95.4% of datapoints measured directly from the CDF, with the skewness shown from the PDF of each data set.

3.11. CHAPTER III REFERENCES

[1] J.C. Martin, “High voltage design considerations,” in J.C. Martin on Pulsed Power, vol. 3, T.H. Martin, Ed., A.H. Guenther, Ed., and M. Kristiansen, Ed. New York and London: Plenum Press, 1996, ch. 12, pp. 489-501.

[2] BOC Air Zero Grade [online] Available: https://www.boconline.co.uk/en/images/air-zero-grade-factsheet_tcm410-450352.pdf Accessed 13th August 2023

[3] HDPE data sheet, [Online]. Available: https://plastim.co.uk/wp-content/uploads/2019/07/HDPE-PE-300-Technical-Data-Sheet.pdf Accessed: August 15th, 2023.

[4] Ultem (Polyetherimide) Data Sheet, [Online]. Available: https://www.plasticstockist.com/downloads/datasheets/pei1000.pdf Accessed: August 13th 2023

[5] Delrin (Polyoxymethylene) Data Sheet, [Online]. Available: https://www.theplasticshop.co.uk/plastic_technical_data_sheets/delrin_acetal_homopolymer_technical_data_sheet.pdf Accessed: August 13th 2023

[6] A. Krivda and D. Birtwhistle, "Breakdown between water drops on wet polymer surfaces," 2001 Annual Report *Conference on Electrical Insulation and Dielectric Phenomena* (Cat. No.01CH37225), Kitchener, Ontario, Canada, 2001, pp. 572-580.

[7] ASTM Standard D5946, 2017, Standard Test Method for Corona-Treated Polymer Films Using Water Contact Angle Measurements *ASTM International*, DOI: 10.1520/D5946-17, www.astm.org.

[8] Tyubaeva PM, Tyubaev MA, Podmasterev VV, Bolshakova AV, Arzhakova OV. “Hydrophilization of Hydrophobic Mesoporous High-Density Polyethylene Membranes via Ozonation.” *Membranes* (Basel). 2022 Jul 26;12(8):733. doi: 10.3390/membranes12080733. PMID: 35893451; PMCID: PMC9330096.

[9] Bannwarth, Markus B, Klein, Rebecca, Kurch, Sven, Frey, Holger, Landfester, Katharina, Wurm, Frederik R “Processing and adjusting the hydrophilicity of

poly(oxymethylene) (co)polymers: nanoparticle preparation and film formation”,., 2016, *Polymer Chemistry* VL - 7 IS - 1 The Royal Society of Chemistry

[10] Isloor, Arun & Hebbar, Raghavendra & Ismail, Ahmad. (2014). Preparation of antifouling Polyetherimide / hydrolysed PIAM blend nanofiltration membranes for salt rejection applications. *RSC Adv*.. 4. 10.1039/C4RA05791K

[11] Zhicheng Guan, Liming Wang, Bo Yang, Xidong Liang and Zhi Li, "Electric field analysis of water drop corona," in *IEEE Transactions on Power Delivery*, vol. 20, no. 2, pp. 964-969, April 2005, doi: 10.1109/TPWRD.2004.837672

[12] Leandros A. Maglaras, Athanasios L. Maglaras, Frangiskos V. Topalis, “The influence of the Effect of Grounding and Corona Current on the Field Strength the Corona Onset and the Breakdown Voltage of Small Air Gaps”, *WSEAS TRANSACTIONS on POWER*, vol 3 no 1 pp. 103-108 Jan 2008

[13] A. Maglaras and F. V. Topalis, "Influence of ground and corona currents on dielectric behavior of small air gaps," in *IEEE Transactions on Dielectrics and Electrical Insulation*, vol. 16, no. 1, pp. 32-41, February 2009, doi: 10.1109/TDEI.2009.4784549.

[14] Ravinda Arora, Wolfgang Mosc “High Voltage and Electrical Insulation Engineering”, Section 2.3.1.1. The effects of grounding on field configuration, Page 19

[15] A. S. Pillai, R. Hackam and P. H. Alexander, "Influence of Radius of Curvature, Contact Angle and Material of Solid Insulator on the Electric Field in Vacuum (and Gaseous) Gaps," in *IEEE Transactions on Electrical Insulation*, vol. EI-18, no. 1, pp. 11-22, Feb. 1983, doi: 10.1109/TEI.1983.298577.

[16] Wilson, Mark Peter., and University of Strathclyde. Dept. of Electronic Electrical Engineering. Impulse Breakdown of Liquid-solid Interfaces (2011), Page 63.

[17] HS1101LF – Relative Humidity Sensor Data sheet [online] - https://docs.rs-online.com/9d2c/0900766b8142cdcd.pdf Accessed: August 13th 2023

[18] Testo 608 – H2 Thermal hygrometer Data sheet, [online] https://static-int.testo.com/media/40/ea/e2780e80243b/testo-608-Data-sheet.pdf Accessed: August 13th 2023

[19] Jinliang, “A resistance divider for measurement of high voltage pulse with nanosecond response time,” *High-Voltage Eng*., vol. 22, no. 4,pp. 65–67, 1996

[20] Y. Liu, F. Lin, G. Hu and M. Zhang, "Design and Performance of a Resistive-Divider System for Measuring Fast HV Impulse," in *IEEE Transactions on Instrumentation and Measurement*, vol. 60, no. 3, pp. 996-1002, March 2011, doi: 10.1109/TIM.2010.2064410.

[21] D. Kind, and K. Feser, “Fundamental principles of high-voltage test techniques,” in *High Voltage Test Techniques*, 2nd ed. London: Newnes, 2001, ch. 1, pp. 1-109.

[22] ASTM International Standard Test Method for Dielectric Breakdown Voltage and Dielectric Strength of Solid Electrical Insulating Materials Using Impulse Waves, Standard D3426-97, *ASTM International*, West Conshohocken, PA, USA, 1997, doi: 10.1520/D3426-97.

[23] S. Bell, Measurement Good Practice Guide No.11: A Beginner's Guide to Uncertainty of Measurement, *National Physical Laboratory* Teddington Middlesex, UK, 1999.

[24] Understanding Oscilloscope Bandwidth, Rise Time and Signal Fidelity, Tektronix, [online] *Technical Brief*, https://people.ece.ubc.ca/robertor/Links_files/Files/TEK-Understanding-Scope-BW-tr-Fidelity.pdf Accessed: August 13th 2023

[25] M. J. Given et al., "Modifications to the von Laue statistical distribution of the times to breakdown at a polymer-oil interface," in *IEEE Transactions on Dielectrics and Electrical Insulation*, vol. 24, no. 4, pp. 2115-2122, 2017.

[26] M. P. Wilson et al., "Impulse-driven Surface Breakdown Data: A Weibull Statistical Analysis," in *IEEE Transactions on Plasma Science*, vol. 40, no. 10, pp. 2449-2456, Oct. 2012, doi: 10.1109/TPS.2011.2181172.

[27] W. Yuan et al., "Weibull statistical analysis of size effects on the impulse breakdown strength in transformer oil," 2017 *IEEE 19th International Conference on Dielectric Liquids* (ICDL), 2017, pp. 1-4, doi: 10.1109/ICDL.2017.8124618.

[28] Q. Wang, L. Hao, Y. Gao, J. Zhao and Y. Wang, "Probability distribution model of DC basin insulator flashover," 2020 *IEEE International Conference on High Voltage Engineering and Application* (ICHVE), 2020, pp. 1-4, doi: 10.1109/ICHVE49031.2020.9279493.

[29] Ahmad, Mohd; Bashir, Nouruddeen; Ahmad, Hussein; M. Piah, M. Afendi; Abdul-Malek, Zulkurnain; Yusof, Fadhilah, "Statistical Analysis of Electrical Tree Inception Voltage, Breakdown Voltage and Tree Breakdown Time Data of Unsaturated Polyester Resin", *Journal of Electrical Engineering and Technology* 2013/07/01, 840, 849 810.5370/JEET.2013.8.4.840

[30] Wu, Jiang & Zhang, Bo & Li, Tianjiao & Du, Yan & Cao, Wen & Yang, Hao. "Effect of Trap Regulation on Vacuum DC Surface Flashover Characteristics of Nano-ZnO/PI Film". *Polymers.* 2022 14. 3605. 10.3390/polym14173605

[31] Langat, P.K.; Kumar, L.; Koech, R. Identification of the Most Suitable Probability Distribution Models for Maximum, Minimum, and Mean Streamflow. *Water* **2019**, *11*, 734. https://doi.org/10.3390/w11040734

[32] K. Tamaki et al., "Comparative study on feature descriptors for brain image analysis," 2014 *Joint 7th International Conference on Soft Computing and Intelligent Systems (SCIS) and 15th International Symposium on Advanced Intelligent Systems* (ISIS), Kitakyushu, 2014, pp. 679-682.

[33] Chakravarti, I.M.; Laha, R.G.; Roy, J. "Handbook of Methods of Applied Statistics"; *Wiley Series in Probability and Mathematical Statistics* (USA) eng;Wiley: Hoboken, NJ, USA, 1967.

[34] W. Weibull, "Statistical distribution function of wide applicability," *Am. Soc. Mech. Engrs*. – Trans. (J. Applied Mechanics), vol. 18 (3), pp. 293-297, 1951.

[35] A. Bernard and E. C. Bos-Levenbach, Hetuitzetten van waarnemingen op waarschijnlijkheids-papers, Stat. Neerl., 7, 1953, 163-173.

[36] "IEC/IEEE Guide for the Statistical Analysis of Electrical Insulation Breakdown Data (Adoption of IEEE Std 930-2004)," in *IEC 62539 First Edition 2007-07 IEEE 930* , vol., no., pp.1-53, 2007, doi: 10.1109/IEEESTD.2007.4288250.

[37] Park, Chanseok – "A Note on the Existence of the Location Parameter Estimate of the Three-Parameter Weibull Model Using the Weibull Plot" *Mathematical Problems in Engineering* 2018/10/09 DOI - 10.1155/2018/6056975

[38] Demir, M. and Celâl Korasli. "Statistical approach for determining impulse breakdown voltage distribution under DC sweep voltage." *Turkish Journal of Electrical Engineering and Computer Sciences* 22 (2014): 12-24

[39] Frank, J., Massey. (1951). "The Kolmogorov-Smirnov Test for Goodness of Fit. Journal of the American Statistical Association", 46(253):68-78. doi: 10.2307/2280095

[40] L.H. Miller, "Tables of Percentage Points of Kolmogorov Statistics,"*JASA*,51, 1956, 111–12

4. CHAPTER IV

NO SPACER (OPEN GAP) BREAKDOWN

4.1. INTRODUCTION

Chapter IV presents experimental data gathered for open air gaps, with no solid spacer bridging the electrodes ('no spacer' tests), and with regards to the changing environmental parameters of pressure and humidity, achieved using the test cell outlined in Chapter III. This data provides baseline reference values, enabling comparison with the breakdown characteristics of insulation systems bridged with solid dielectrics with smooth and knurled surfaces in Chapters V and VI, respectively.

The understanding environmental conditions on the breakdown voltage of an air insulated system is a common study. In terms of different tested humidities, research groups have recorded both decreases and increases in breakdown voltage with increasing humidity in the system.

In [1], a high humidity, >80% RH, is stated to result in a decrease in the breakdown voltage as the discharges within the system becomes irregular resulting in a fluctuation of results throughout testing. In highly humid environments, the accumulation of water droplets can also have an adverse effect on the breakdown voltage of system, a potential reason for this could be due to the high-field regions caused by water droplets forming on the electrodes as reported in [2]. In practical systems, the effect of high humidity was seen to decrease the breakdown strength of an air insulated system as shown in [3] and [4]. Conversely, the effect of humidity has also been shown to have no impact or to increase the breakdown voltage This is seen in [5], where no change in breakdown voltage was found for lightning impulses for humid air, with moisture content ranging from 300 ppm to 1500 ppm. Additionally, in [6] and [7], there was a general breakdown voltage increase of 5% - 10% with increasing moisture content, and also seen in [8], where the average breakdown voltage of an air gap was found to increase slightly with increasing humidity, from 9.8 g/m^3 to 20.7 g/m^3. It is also shown that the in terms of polarity breakdown the increase of humidity can have an effect on

the photoionisation processes, which are important in the positive-streamer breakdown mechanism, where high-energy photons are absorbed by water molecules at high levels of relative humidity [9] increasing the breakdown voltage.

The tests within this chapter will cover the full humidity spectrum at varying air pressures. The effects that these environmental conditions have on the breakdown voltage of an open-air gap pulsed power insulation systems will be discussed. Possible reasons for the changes observed are then discussed.

4.1.1. Experimental Method

Open air gaps were subjected to both positive and negative polarity 100/700 ns impulse voltages in the parallel-plane electrode arrangement introduced in Chapter III, with an interelectrode gap of 40 mm. The results in this section will be presented and discussed in terms of the effect of changing relative humidity (RH), with levels of <10% RH, ~50% RH and >90% RH, tested at pressures of −0.5 bar gauge, 0 bar gauge and 0.5 bar gauge.

As this section provides data that will be compared directly with that for composite air-solid insulation systems, a consistent number of 20 data-points was generated for each insulation system tested throughout this thesis. The V_{50} breakdown voltage from 20 tests, following the 'step up' method in the ASTM D3426-97 testing standard in Section 3.6.4, was found using Weibull statistical analysis for each set of test conditions. The asymmetrical error bars in the graphs represent the area which characterises the spread in the breakdown data where ~95.4% of data points reside, within each dataset's probability density function (PDF), and these values correspond to the points where the cumulative distribution function crosses the 2.3% and 97.7% probability lines, as discussed in Section 3.10. Using the same process, the t_{50} times to breakdown were also found for each insulation system tested.

To ensure consistency, the electrodes were inspected and polished after test sequences to remove surface pits that accumulated during the testing phase.

4.2. EXPERIMENTAL RESULTS

This section will provide the results of the open gap tests under changing environmental parameters (pressure and humidity), as well as both polarities of voltage impulse. Both breakdown voltage and time to breakdown were recorded for each breakdown event in the open gap arrangement, to facilitate comparison with the data for gas-solid insulation systems subjected to the same environments in Chapters V and VI.

4.2.1. Breakdown Voltage Results

In order to characterise the holdoff voltage of each open gap insulation system, the results herein show the difference in breakdown voltage with a consistent inter-electrode gap of 40 mm, in varying environmental conditions. The experimental results are presented separated by air pressure, followed by a discussion of these results in Section 4.3 in relation to polarity and humidity, and Section 4.4 in relation to polarity effect. Section 4.4.1 provides additional discussion on the polarity effect witnessed and on the effect that the environmental parameters have on the asymmetrical electrical performance of the system.

To frame the discussion in relation to the breakdown characteristics of the open gap, Weibull plots of the data are first presented. This enabled V_{50} to be calculated, and the generation of the error bars characterising the spread where ~95.4% of the data points reside, for each set of conditions. Breakdown voltages will be presented in relation to changing relative humidity at each tested pressure, which facilitates direct comparison with solid insulation systems in Chapters V and VI.

A 2-parameter Weibull plot of the breakdown data generated at -0.5, 0 bar and 0.5 bar gauge is presented in Figure 4.1, 4.2 and 4.3.

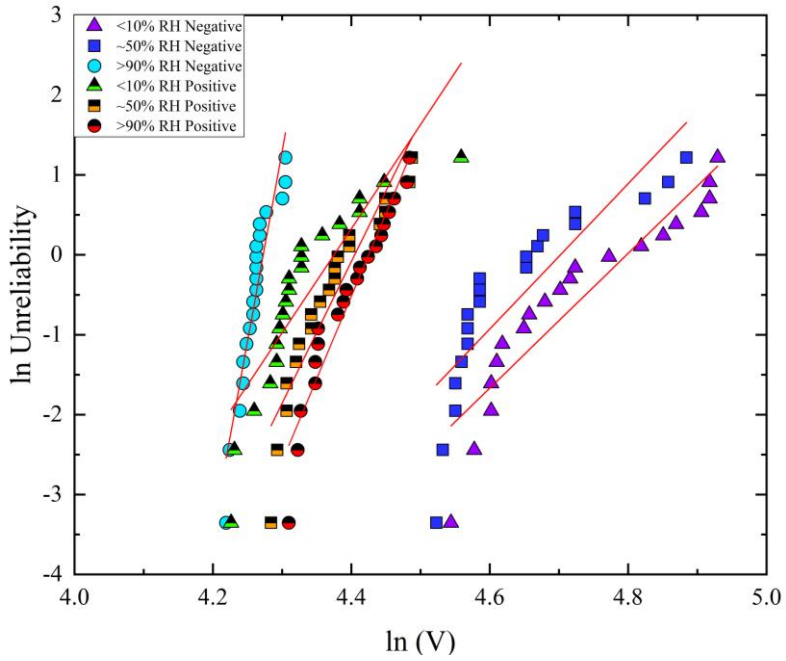

Figure 4.1 – Weibull plots and curve fits of breakdown voltage data for open gap breakdown results at -0.5 bar gauge.

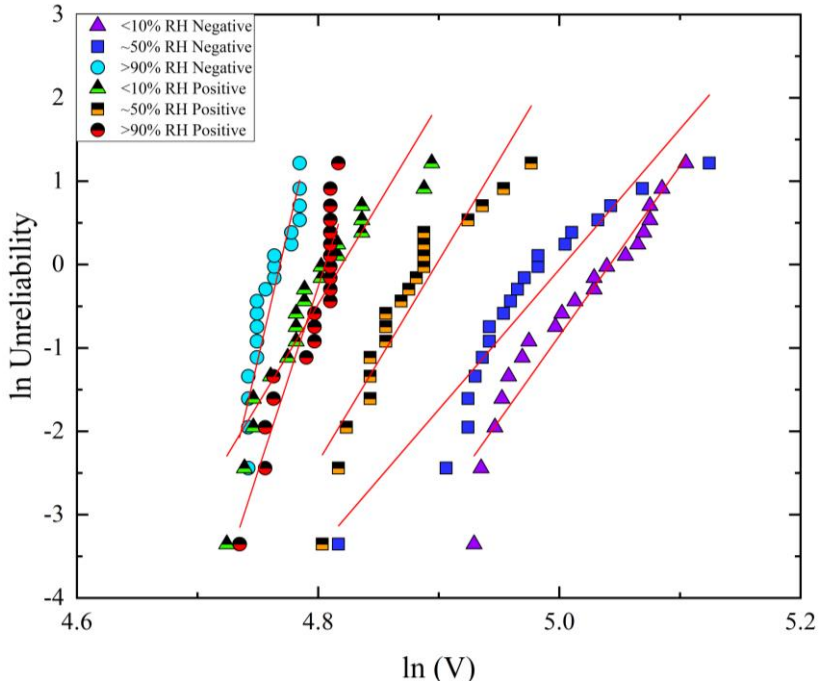

Figure 4.2 - Weibull plots and curve fits of breakdown voltage data for open gap breakdown results at 0 bar gauge.

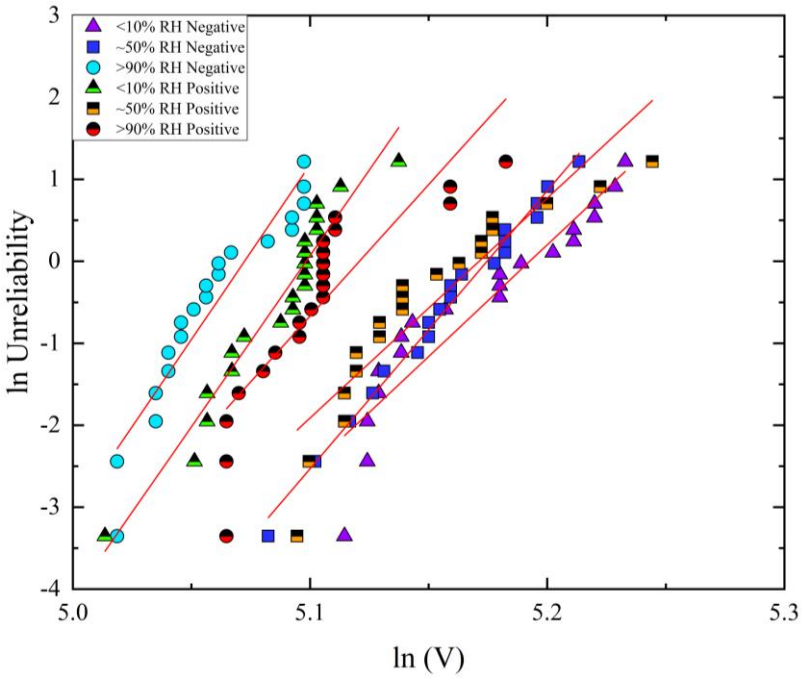

Figure 4.3 - Weibull plots and curve fits of breakdown voltage data for open gap breakdown results at 0.5 bar gauge.

As shown from Figure 4.1, at <10% RH, for both positive and negative polarity, the distributions show two distinct linear sections, suggesting that two different breakdown mechanisms are apparent. This could be an indication of electrode conditioning, where the breakdown voltages change in performance due to the surface of the electrode topology.

Analysing the Weibull distributions in Figure 4.1, 4.2 and 4.3, the V_{50} breakdown voltages and the spread (error bars) are shown in Figure 4.4a, 4.4b and 4.4c. Each bar represents the V_{50} from 20 impulsive breakdown voltages, and the error bars represent the 95.4% spread of the data.

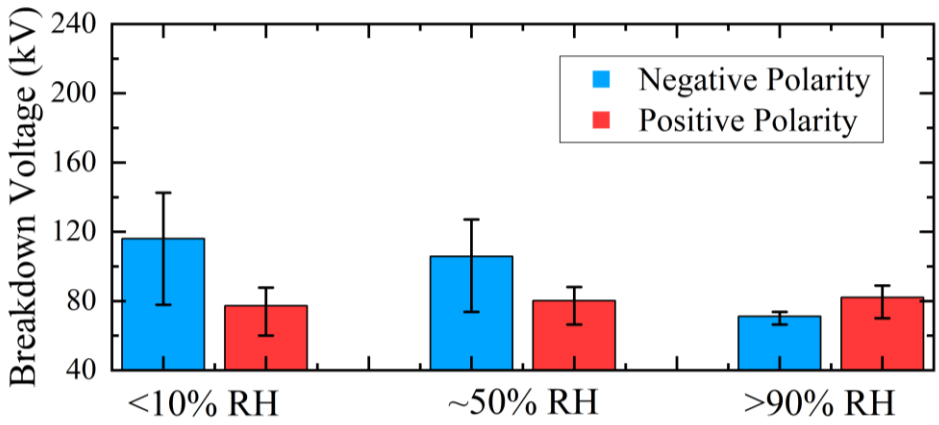

(a)

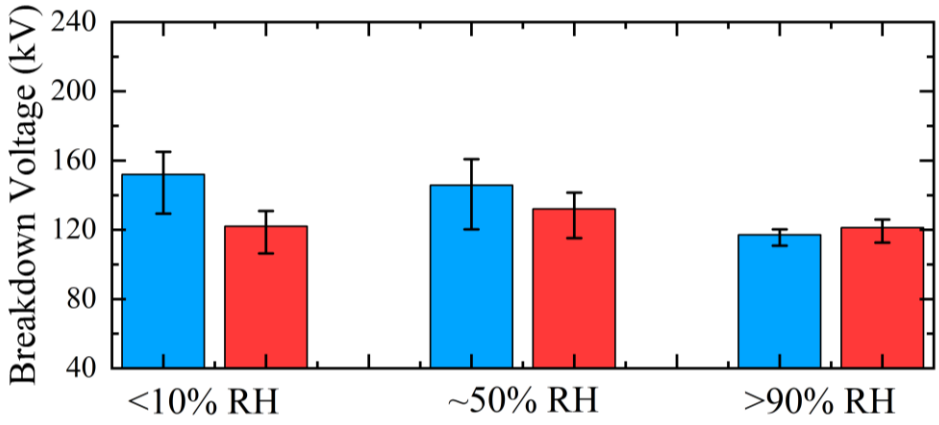

(b)

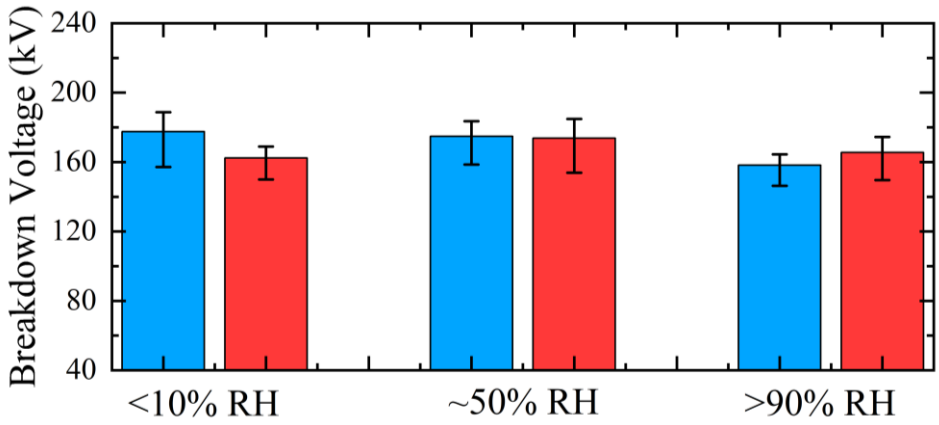

(c)

Figure 4.4 - Differences in negative and positive polarity breakdown voltages of open air gaps at (a)-0.5 bar gauge, (b) 0 bar gauge, and (c) 0.5 bar gauge. Each bar represents V_{50} from 20 breakdown voltages (median of the 2-parameter Weibull distribution), and the error bars characterise the spread in the breakdown data, where ~95.4% of data points reside.

What can be seen from Figure 4.4 is that as the pressure, humidity and polarity are changed, there are obvious changes in the breakdown characteristics of the insulation system.

For -0.5 bar gauge in Figure 4.4a, and focusing firstly on the change in polarity, for humidity levels of <10% RH and ~50% RH, the negative polarity voltages are higher than the positive polarity voltages, however, there are overlapping error bars at each pressure level. At >90% RH, there is a change in performance where the positive breakdown voltage increases over the negative breakdown voltage. Overall, this is due to the increasing humidity having an adverse effect on the negative breakdown voltage but having minimal effect on the positive polarity breakdown voltages. The highest V_{50} breakdown voltage at -0.5 bar gauge was recorded with a negative polarity impulse at <10% RH, being ~121 kV, and the minimum voltage was recorded at >90% RH with a negative polarity impulse, being ~76 kV.

What can be seen from the 0 bar gauge results in Figure 4.4b is that, again, in comparison to the results shown at -0.5 bar gauge, as the humidity and polarity are changed, there is a change in the breakdown characteristics of the insulation system. At both, <10% RH and ~50% RH, the nominal negative polarity voltages are higher than the positive polarity voltages, but with overlapping error bars. At >90% RH, the breakdown voltage is shown to be very close in value for negative and positive polarity, with positive being slightly higher. This shows very similar results to what was seen at -0.5 bar, but with smaller differences between each polarity showing the performance has become more symmetrical as the pressure has increased from -0.5 bar gauge to 0 bar gauge. The highest V_{50} at 0 bar gauge was recorded for negative polarity impulses at <10% RH, being ~155 kV, and the minimum V_{50} was recorded at >90% RH for negative polarity impulses, at ~117 kV.

What can be seen from the 0.5 bar gauge results in Figure 4.4c, is that as the humidity and polarity are changed, not only is there a change in the breakdown characteristics of the insulation system, but the trends are different. At <10% RH, the nominal negative polarity voltages are higher than the positive polarity voltages, at ~50% RH there is almost no difference in the nominal positive and negative breakdown voltages, and at >90% RH, there is a slightly higher positive polarity voltage than negative.

However, all above comparisons exhibit overlapping error bars. Again, as the pressure has increased generally the difference between positive and negative voltage has decreased, showing the pressure has a direct correlation to the witnessed polarity effect of the system. The highest V_{50} breakdown voltage at 0.5 bar gauge was recorded for negative polarity impulses at <10% RH, at ~180 kV, and the minimum voltage was recorded at >90% RH, also for negative polarity impulses, at ~160 kV.

Following application of the process outlined in Section 3.9 to all data sets generated in the testing phase, the values of α, β, V_{50} and $V_{0.01}$ are provided in Tables 4.1, 4.2 and 4.3. The value of α is closely related to the value of V_{50} and the value of β is related to the spread of the data with higher values indicating a narrower spread. What is important here is that the $V_{0.01}$ breakdown voltage value is directly related to the α and β values, where for higher β values, the $V_{0.01}$ value for a distribution will be closer to the α value.

Table 4.1 – α, β, V_{50} and $V_{0.01}$ values from the 2-paramter Weibull analysis for open gap tests at -0.5 bar gauge.

Pressure	**Humidity**	**Negative**				**Positive**			
		α (kV)	**β**	**V_{50} (kV)**	**$V_{0.01}$ (kV)**	**α (kV)**	**β**	**V_{50} (kV)**	**$V_{0.01}$ (kV)**
-0.5 bar gauge	<10% RH	121.2	8.4	116.1	40.7	79.4	13	77.2	39.2
	~50% RH	110.2	9.1	105.8	40	81.9	17.7	80.2	48.6
	>90% RH	71.7	47.5	71.2	59.1	83.5	20.7	82.1	53.5

Analysing the calculated 0.01% probability of failure values (1 failure in 10,000), in Table 4.1, looking at how the $V_{0.01}$ values, it can be seen is shown that, due to the increasing β value with increasing humidity that the calculated 0.01% probability of failure voltages generally increases with increasing humidity for both polarities.

Table 4.2 - α, β, V_{50} and $V_{0.01}$ values from the 2-paramter Weibull analysis for open gap tests at 0 bar gauge.

Pressure	**Humidity**	**Negative**				**Positive**			
		α (kV)	**β**	**V_{50} (kV)**	**$V_{0.01}$ (kV)**	**α (kV)**	**β**	**V_{50} (kV)**	**$V_{0.01}$ (kV)**
0 Bar gauge	<10% RH	154.8	20.4	152	98.5	123.9	24.1	122.1	84.5
	~50% RH	148.9	16.8	145.7	86.1	134	24.2	132	91.5
	>90% RH	117.7	62	117	101.5	122.2	44.5	121.2	99.4

Analysing the calculated 0.01% probability of failure values, for the 0 bar gauge results in Table 4.2, it is shown that for the $V_{0.01}$ values increasing humidity generally increases the breakdown voltage.

Table 4.3 – α, β, V_{50} and $V_{0.01}$ values from the 2-paramter Weibull analysis for open gap tests at 0.5 bar gauge.

Pressure	Humidity	Negative				Positive			
		α (kV)	β	V_{50} (kV)	$V_{0.01}$ (kV)	α (kV)	β	V_{50} (kV)	$V_{0.01}$ (kV)
0.5 Bar gauge	<10% RH	179.9	27.2	177.5	128.3	163.7	41.8	162.3	131.3
	~50% RH	176.7	33.9	174.8	134.7	176.1	26.8	173.7	125
	>90% RH	159.6	42.6	158.2	128.5	167.5	32.1	165.6	125.7

Analysing the calculated 0.01% probability of failure values, for the 0.5 bar gauge results in Table 4.3, it is shown that for the $V_{0.01}$ values, the increasing the humidity is shown to have no clear trend in the negative polarity breakdown voltage with the maximum occurring at ~50% RH. For positive polarity, a decrease is shown from the 0.01% probability of failure value with increasing humidity.

4.2.2. Volt/Time Breakdown Results

The time to breakdown gives extra information associated with the discharge process, potentially revealing how the discharge mechanism changes with the test conditions. This data is presented as volt-time graphs using the breakdown voltage values from Figures 4.4a, 4.4b and 4.4c, to enable the assessment of any trends in the breakdown behaviour of these systems. As breakdown occurred on the falling edge of the impulse, the error bars are large when graphing the 95.4% spread of data. The graphs are presented separated by energisation polarity.

In Figure 4.5 are the negative polarity volt-time graphs. The results show all negative polarity results at -0.5 bar gauge, 0 bar gauge and 0.5 bar gauge.

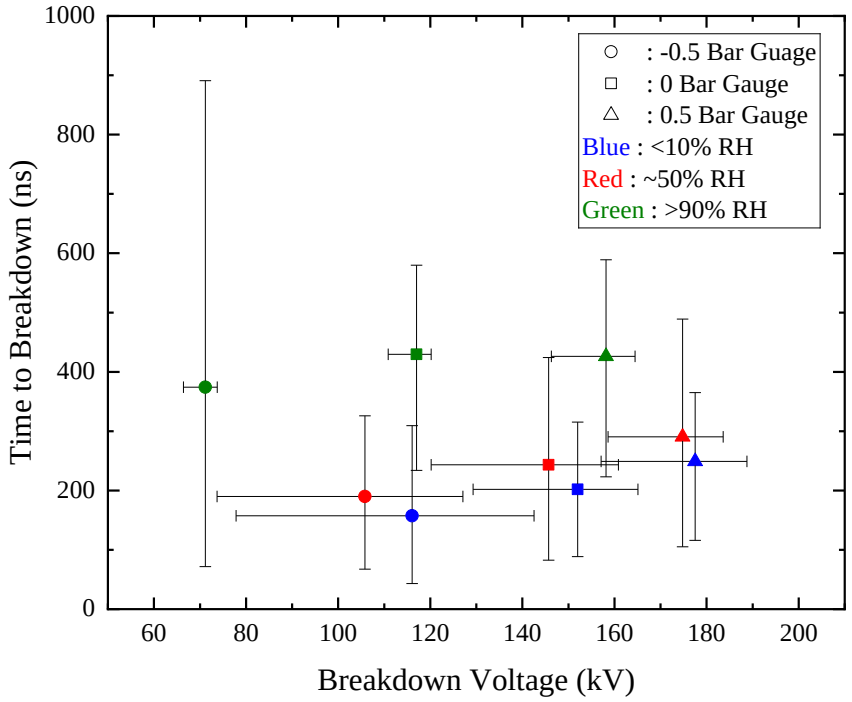

Figure 4.5 – Volt-time graph for negative polarity energisation

In Figure 4.5, the effect of humidity on the volt-time characteristics is clear. As the humidity is increased, the average time to breakdown values are shown to increase, due to the potential increase of the attachment coefficient with the elevated relative humidity, further discussed in Sections 2.4.4. and 4.3.1. What is also evident is that although the breakdown voltage increases with increasing pressure, the breakdown voltage and 95.4% spread of time to breakdown have a slight increase in time for each tested pressure at <10% RH, ~50% RH and >90% RH. This shows that at each specific breakdown voltage, these approximate values are the time required for the discharge process to lead to a full breakdown. Although the pressure is increasing, the time to breakdown stays fairly consistent due to the higher applied voltage. Numerical values are listed in Table AP2a for reference.

The positive polarity volt-time data are shown in Figure 4.6. From Figures 4.4a, 4.4b and 4.4c, it was shown that the positive breakdown voltages for each humidity at each specific pressure were more consistent than the negative polarity results, and this is reflected in the times to breakdown. What is evident is that, while there was a clear average increase in the time to breakdown with increasing relative humidity for

negative polarity, for positive polarity little effect of the humidity on the time to breakdown is seen, particularly at -0.5 bar gauge. As the pressure is increased to 0 bar gauge and to 0.5 gauge, the synergistic effect of the pressure and humidity is seen to result in an increase in the time to breakdown for similar breakdown voltages, where the added humidity hinders the positive streamer development, as discussed in Section 4.4.1, with breakdown occurring on the tail of the impulse.

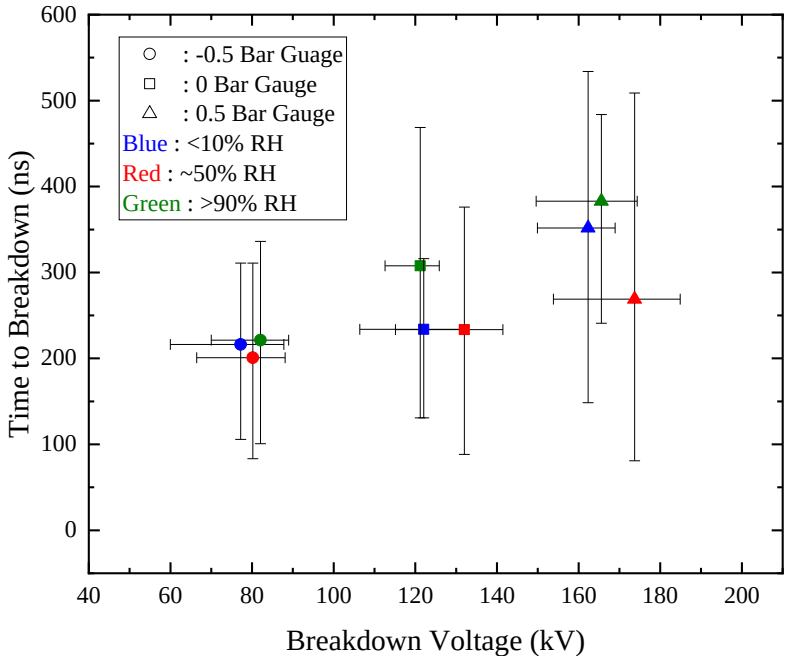

Figure 4.6 - Volt-time graphs for positive polarity energisation

The V_{50} and t_{50} values for positive energisation are presented in Table AP2b for reference.

4.3. Discussion of the Effect of Environmental Parameters on Breakdown Voltage

Due to the varying performance of the system, the effect of the environmental parameters and the impulse polarity on the breakdown voltage will now be discussed.

4.3.1. Effect of Humidity on the Breakdown Voltage

From Figures 4.4a, 4.4b and 4.4c, the breakdown voltages for each polarity show different trends in the breakdown voltage as the humidity is increased. For negative

polarity, an overall decreasing voltage is witnessed as the humidity is increased, particularly when increasing from ~50% RH to >90% RH. Whereas, for positive polarity, the breakdown voltages are very similar for all levels of humidity tested.

For negative polarity, increased humidity was also found to decrease the flashover strength of the air gap. Particularly at >90% RH, as the discharge voltage becomes irregular [1], a potential reason for this could be due to the high-field regions caused by water droplets forming on the electrodes as also witnessed in [2], which has manifested in a decrease in the negative breakdown voltage from 116.1 kV to 71.2 kV at <10% RH and >90% RH, respectively, at −0.5 bar gauge, 152 kV to 117 kV at 0 bar gauge and 177.5 kV to 158.2 kV at 0.5 bar gauge. This was also witnessed in [3] and [4], the effect of very high levels of humidity on the breakdown strength were reported also, where above 80% RH, the breakdown voltages were unpredictable in amplitude, similar to what was witnessed here for negative polarity breakdown at elevated humidity, culminating in a decrease in breakdown voltage.

For positive polarity, the effect of increasing humidity was minimal throughout the tests, with breakdown voltages of 77.2 kV at <10% RH, and 82.1 kV at >90% RH, at −0.5 bar gauge pressure, 122.1 kV to 121.5 kV at 0 bar gauge and 162.3 kV to 165.6 kV at 0.5 bar gauge. This minimal effect on the breakdown voltage with increasing humidity was also seen in [5].. The results in Figures 4.2, 4.4 and 4.6 for positive polarity generally follow what was found in [6] and [7] also, where there was a general breakdown voltage increase with increasing moisture content, which is similar to the trend observed here, particularly at -0.5 bar gauge. The slight increase in the positive polarity breakdown voltage at -0.5 bar gauge with increasing humidity was also seen in [8],.. This minimal effect/slight increase on positive polarity breakdown voltage with increasing humidity could be due to the aforementioned impact on photoionisation processes, which are important in the positive-streamer breakdown mechanism, [9], requiring an increase in applied voltage to cause breakdown at these higher levels of humidity, causing the positive polarity breakdown voltage to remain consistent at all levels of RH.

4.3.2. Effect of Pressure on the Breakdown Voltage

For all tested conditions in Figures 4.4a, 4.4b and 4.4c, increasing the pressure resulted in increased flashover voltage, as expected. As the gas pressure increases, the electron mean free path decreases, and the collision frequency increases. Electrons will gain less energy between collisions, which means that a higher applied field is required for free electrons to gain sufficient energy in order to cause an ionisation event [10], as was discussed in Section 2.3.1. This behaviour can also be visually seen from the Paschen curves discussed in Section 2.4.2, where at the right-hand side of the Paschen curve as the pressure increases, the breakdown voltage increases.

4.4. DISCUSSION OF POLARITY EFFECT OF BREAKDOWN VOLTAGE

From Figures 4.4a, 4.4b and 4.4c, there are clear differences in the breakdown characteristics for positive and negative polarity, with the magnitude of the difference between the two breakdown voltages changing as the environmental parameters change.

The polarity effect witnessed in symmetrical electrode setups was first reported by the authors of [11] and [12], who detail a polarity effect in symmetrical sphere gaps, with one electrode grounded, and provide discussion on potential reasons for the difference. At short gap spacings, the authors show similar breakdown voltage values between positive and negative energisation, where no difference in the breakdown voltage of the gap with respect to polarity is observed; this is due to the gap not being long enough, such that the effect of ground does not yet result in a field non-uniformity in the gap. The field distribution changes, however, as the gap length is increased. This effect is shown from the electric field distributions for the system used in the present study at 10 mm and 40 mm (inter-electrode distance used in this work), in Figure 4.7.

a) b)

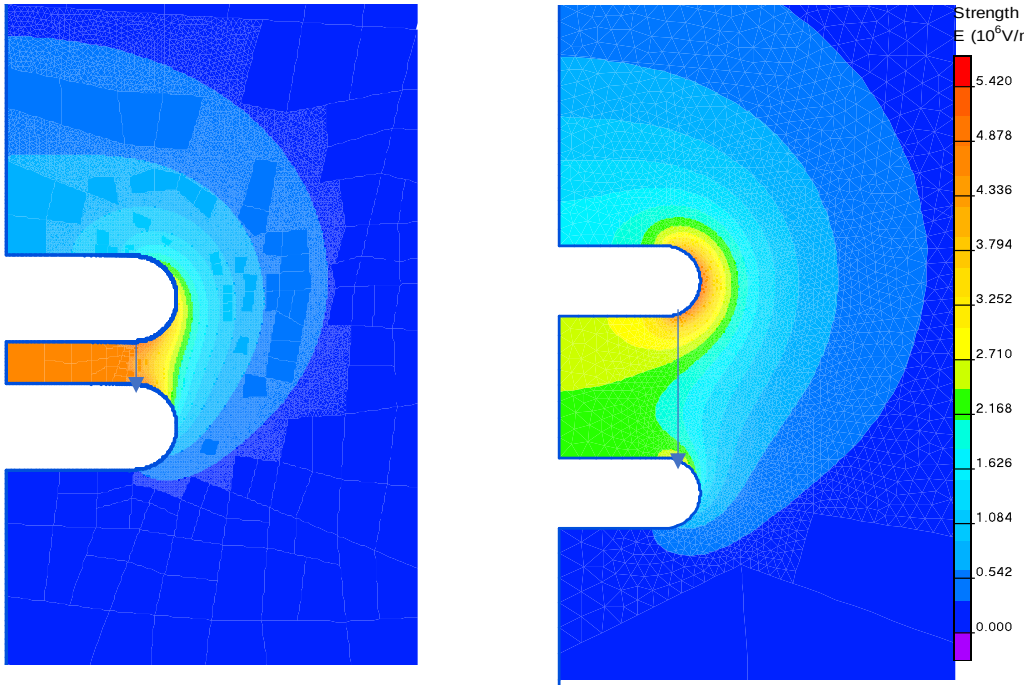

Figure 4.7 – Electric field distribution in a) 10 mm and b) 40 mm gap, with the separation distance shown to affect the field uniformity in the interelectrode gap. Vertical arrow shows contour line.

As shown in Figure 4.7, the effect of increasing distance between the electrodes has an effect on the asymmetry of the electric field simulation. This asymmetry is witnessed within sphere- sphere and parallel plane gaps in literature [13 – 22]. In order to understand the asymmetry which exists between the parallel plane electrode the electric field along the contours from Figure 4.7 are shown in Figure 4.8.

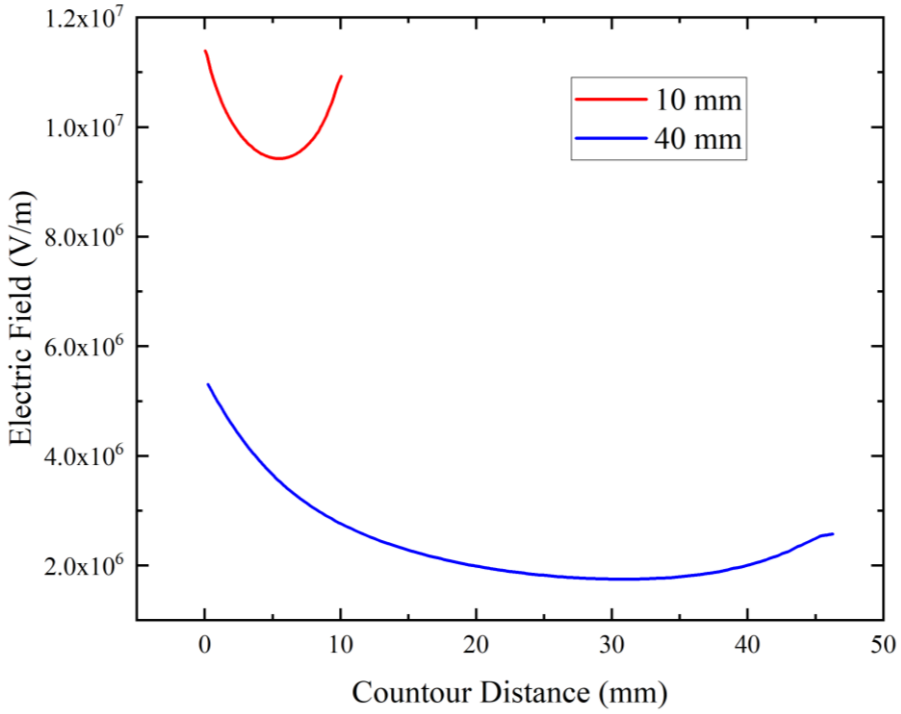

Figure 4.8 – Illustrative example of the electric field distribution in 10 mm and 40 mm gaps at the rounded edges of the electrodes following contours shown in Figure 4.7.

The asymmetry of the electric field distribution is shown to increase with increasing gap, with the HV electrode being 87% increase in comparison to the ground electrode for a 40 mm gap but only 27% increase for a 10 mm gap. As the working range of the insulation system is to increase into the 100s kV, a gap of 40 mm has been used so this field distribution must be taken into account.

As discussed previously, as the gap length is increased, the field non-uniformity increases, which has also been reported by authors who used a parallel-plane electrode setup as shown in [23]. The parallel-plane electrode system used in this thesis has a field uniformity factor of ~0.44, where the field at the HV electrode edge is ~2 times greater than the average field (E = V/d) in the 40 mm gap. Due to this field uniformity factor, an asymmetrical electric field distribution is produced, as shown in Figure 4.7b.

In the case of a non-uniform field distribution, the positive breakdown voltage is lower than the negative, due to electrons being absorbed by the positive HV electrode, leaving behind positive space charge in the gap. This positive space charge increases the effective ionisation zone, and adds to the HV electrode potential, leading to breakdown . For negative polarity, electrons are repelled by the HV electrode and are

subject to electron attachment due to the electronegativity of the gas, or the electrons are held by the positive space charge at the outer boundary of the ionised region, as discussed in Section 2.4.

From the illustrative examples of space charge under positive and negative polarity in Figure 4.9a and 4.9b, the resultant electric field distributions are shown in Figure 4.10a and 4.10b.

The effect of polarity on the breakdown voltages of non-uniform gas gaps is presented in [24] and [25]. When a positive polarity voltage is applied to the electrode topology from the current test cell arrangement, a non-uniform electrical field is established in the gap. Shown in Figure 4.10a is the electrical field strength in the inter-electrode gap. There are two different distributions shown - the dashed line is the electrical field distribution when there is no space charge, where the electrical field strength decreases as the distance increases; whereas the solid line shows the space-charge-modified electrical field distribution. The reason for this increase in electrical field strength at the anode is due to high electron mobility in a continuously increasing field. The positive electrode attracts electrons towards its surface, which, in turn, leaves behind positive space charge. The region between the positive electrode and the positive space charge has reduced local electrical field strength. Further into the gap, the field decreases towards the cathode. The space charge causes the field to strengthen until a point where the field starts to decrease due to the distance from the HV electrode, and the fact that the positive ions start to travel towards the cathode [22].

Discussion of the effect that polarity has on the breakdown voltage is given in [25]. In Figure 4.9, the distribution of space charge for positive applied voltage is shown, with positive ions and electrons depicted. When a positive voltage is applied, the initial electrons in the gas will accelerate towards the high voltage electrode and lead to an electron avalanche. As seen in Figure 4.9a, while positive ions briefly stay in the area around the rounded area of the plane parallel electrode due to their low mobility, electrons in the electron avalanche swiftly penetrate the electrode, as depicted by the arrows at the electrode surface in Figure 4.9a. Around the electrode, a significant number of positive ions gather and create the space-charge electric fields EPI and EPII. The direction of EPI is opposite to that of the external electric field *E*, which weakens

the field strength at this area, as can be seen from the electric field distribution in Figure 4.10a. This weakens the ionisation around the electrodes and suppresses streamer corona formation, resulting in a higher corona onset voltage. However, it should also be noted that the electric field strength in region II of Figure 4.9a is enhanced by EPII. If the applied voltage rises enough to trigger a self-sustaining discharge, the streamer channel can easily extend to the earth electrode and lead to gap breakdown.

Figures 4.9b and 4.10b show the process when a negative polarity is applied to the plane-parallel HV electrode. As seen, the positive ions are attracted towards the cathode in region EN_I, which increase the electrode field at the cathode, whereas in region EN_{II} electrons are repelled away from the high voltage, negative-polarity electrode in region. These electrons travel towards the anode in a decreasing field. The electron avalanche stops at the boundary surface, where the net ionisation coefficient is 0, due to the non-uniformity of the field distribution. Due to electron attachment, these free electrons go on to form negative ions [26], [27]. This has an effect on the overall field distribution seen in Figure 4.10b, which shows the overall field with and without space charge. It is this space charge which determines the increase in field near the cathode, and reduction in field at the anode. Within this geometry, a space charge ‘cathode sheath’ is formed a distance away from the HV electrode, which ultimately weakens the field at this point due to the high velocity of electrons being repelled from the anode - this weakened field then stops an avalanche taking place.

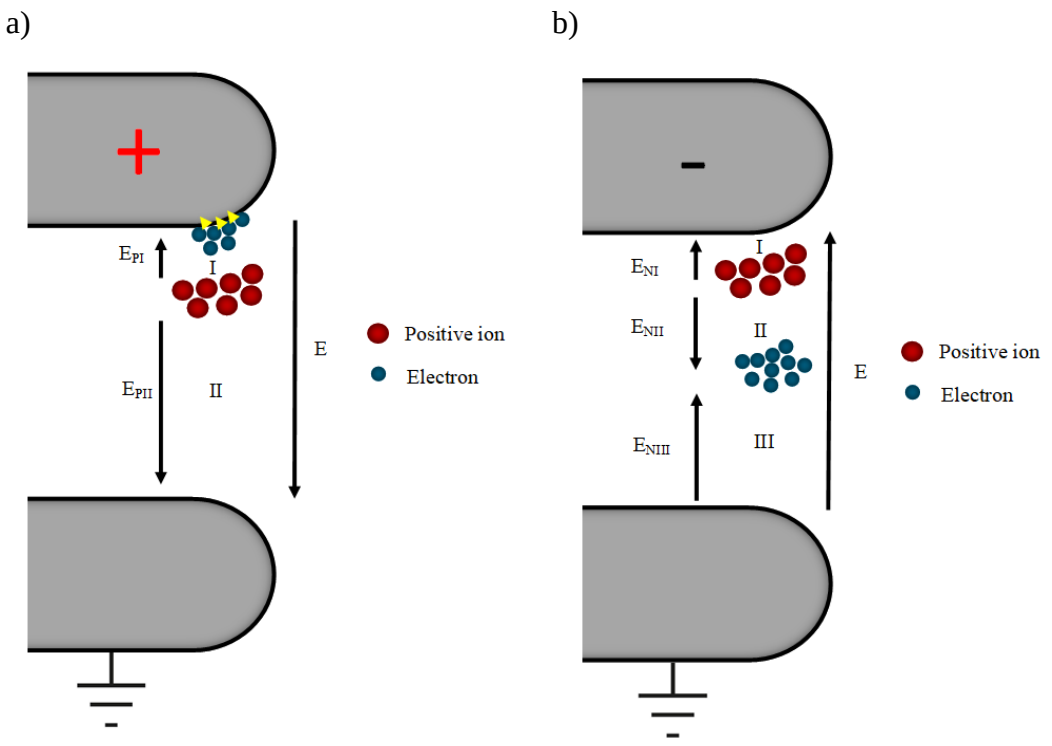

Figure 4.9 – Distribution of space charge in a) positive polarity and b) negative polarity electrode gap, modified from [21], for the plane-parallel electrode arrangement used in this thesis

As time progresses, positive space charge moves towards the cathode, which in turn increases the local electrical field strength [25]. Over time and with increasing applied potential, the negative space charge starts to disperse, making electron avalanches possible and leading to electrical breakdown. As a result, negative polarity breakdown voltages are higher than those for positive polarity in electronegative gases.

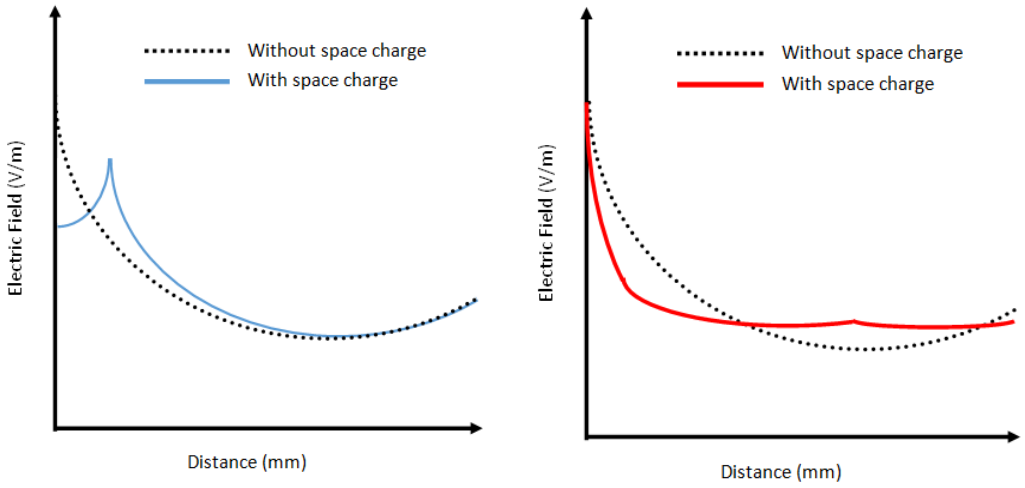

Figure 4.10 –Illustrative example of the field distribution of a) positive polarity and b) negative polarity with and without space charge

The effect of environmental parameters is now to be discussed in relation to the polarity effect discussed in Section 4.4.

4.4.1. Effect of Changing Environmental Parameters

It can be seen from Figures 4.4a, 4.4b and 4.4c that, as the environmental parameters are changed, the differences between the positive and negative breakdown voltages presented and discussed in Section 4.4.1 changed in magnitude. Overall, as the pressure was increased, the insulation system behaved more symmetrically. The same general behaviour was also witnessed as the humidity was increased. This section will discuss these points and give potential reasons for the changing polarity effects.

4.4.1.1. Effect of Pressure

From Figures 4.4a, 4.4b and 4.4c, it is clear that changing the pressure has an effect on the electrical asymmetry of the system, where the higher the pressure, the more electrically symmetrical the system behaves. This effect is hypothesised as being due to the following phenomena. From the charge left behind in filaments by applied impulses that did not result in breakdown, in relation to the time taken between each impulse and the lifetime of charge carriers, the incomplete streamers that do not transition into the final breakdown channel may have an effect on the breakdown polarity effect as the pressure is increased. An example of visualisation of such streamers in the sphere-sphere topology (lightning impulsive breakdown of air) and corresponding current waveforms is shown in [28]. The symmetry between the positive and negative breakdown voltages, therefore, could be due to the intensity of the pre-breakdown streamers. In this chapter, the observed reduction in the difference between positive and negative voltages at the higher breakdown voltages measured at 0.5 bar in Figures 4.4a, 4.4b and 4.4c, in comparison to the wider differences at -0.5 and 0 bar gauge, could be a result of (nominally) equally intensive positive and negative streamers propagating in the inter-electrode gap, with positive and negative charge injected by these streamers. As pre-breakdown current waveforms were not measured in this work, no direct information on the pre-breakdown streamer activity has been recorded. Pressure has been shown to have an effect in other research, such

as in [23], whereas the pressure was increased from 0.345 bar to 1 bar (5 to 15 psi in [23]) the average breakdown voltage became more symmetrical at the higher pressure.

4.4.1.2. Effect of Humidity

Another change evident from Figures 4.4a, 4.4b and 4.4c, is the effect of humidity on the asymmetrical electrical performance of the system. Facilitating the following discussion, an electrostatic simulation of the field in the presence of a build-up of water droplets at the edge of the earthed electrode is shown in Figure 4.12. As the relative humidity of the air increases, the electrical behaviour of the system appears to increase in symmetry also, at each pressure level. The potential reason for this is explained in [2]. As the air humidity inside the system is increased with increasing pressure, water droplets form on the lower, horizontally-oriented, grounded electrode, situated in the vertically-aligned insulation system, due to gravity. This creates local high-field regions [2] at the grounded electrode, which affect the electric field distribution in the air gap as the electric field increases from the droplets, as shown in Figure 4.11b, creating a more symmetrical field distribution.

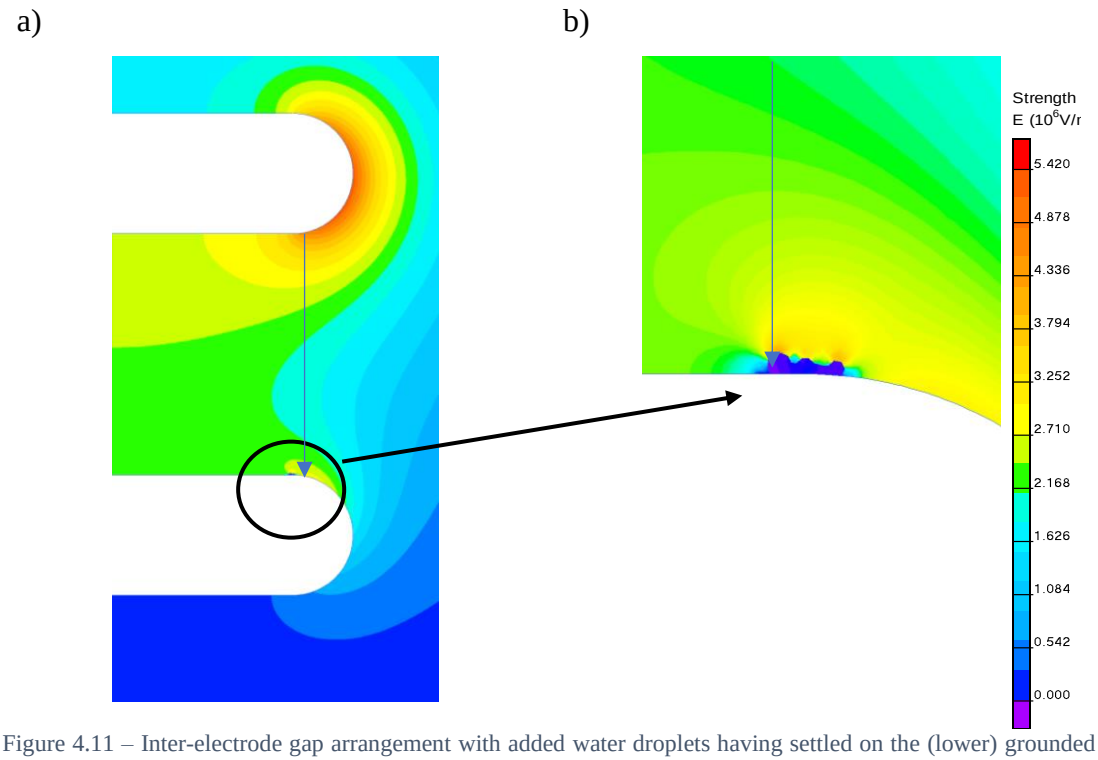

Figure 4.11 – Inter-electrode gap arrangement with added water droplets having settled on the (lower) grounded electrode in the vertically-aligned electrode system, affecting the electric field distribution in the gap, creating a high local field region at the droplets. Vertical arrow shows the contour. a) shows overview effect of droplet formation on electric field, and b) shows localised droplet effect on electric field

Comparing the electrostatic field simulation results from the results without water droplets on the earthed electrode is an electric field distribution as shown in Figure 4.12.

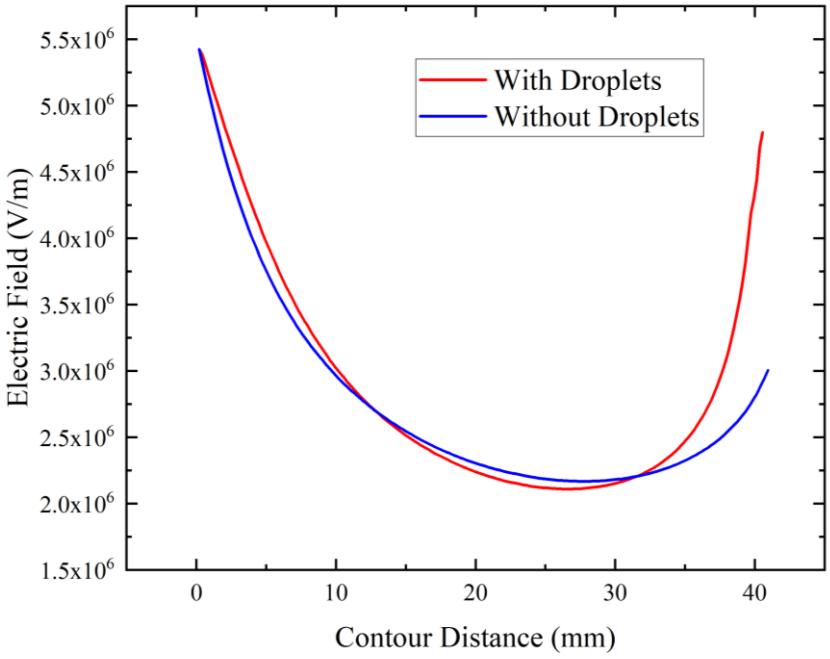

Figure 4.12 – Illustrative example of the electric field distribution with and without water droplets added on the surface of the earthed electrode.

Analysing Figures 4.4a, 4.4b and 4.4c, the change in performance is evident as the humidity is increased, for each level of pressure. This is particularly evident from the results at 0.5 bar gauge. At <10% RH, a higher negative breakdown voltage than positive is exhibited. When increasing the humidity to ~50% RH, there is no clear polarity effect in the breakdown voltages. Increasing the humidity further to >90% RH, the positive breakdown voltages appear to be higher than negative. However, for all these tests, there are overlapping error bars. When analysing the results at −0.5 bar gauge and 0 bar gauge, however, the performance of the electrode setup changes, where the differences in breakdown voltage with polarity become smaller, and therefore more symmetrical with increasing humidity, further supporting this hypothesis that increasing humidity results in a general increase in the electrical symmetry of the system.

4.5. CONCLUSIONS

In this chapter, the results of baseline testing of open-air gaps with both positive and negative polarity impulse voltages have been discussed, in environments of changing air pressure and humidity. Also, the asymmetrical electrical performance of the geometrically-symmetrical electrode arrangement for no-spacer tests has been explained, with a theoretical basis provided based on a focused literature review, and this basis being supported by the asymmetrical field distribution found from the simulation work completed through this chapter.

These results will provide an in-depth reference of the breakdown voltages to be compared with those for composite air-solid insulation systems detailed in Chapters V and VI. These results will also provide a baseline informing the discussion of the physical mechanisms responsible for breakdown in the air-solid gaps, in the context of the different discharge locations witnessed as the environmental parameters were varied.

4.6. CHAPTER IV REFERENCES

[1] High-Voltage Test Techniques—Part 1: General Definitions and Test Requirements, document EN 60060-1:2010.

[2] Guan, L. Wang, B. Yang, X. Liang, and Z. Li, ‘‘Electric field analysis of water drop corona,’’ *IEEE Trans. Power Del*., vol. 20, no. 2, pp. 964–969,Apr. 2005, doi: 10.1109/TPWRD.2004.837672.

[3] . Niu and T. Xu, ‘‘The relevance between dramatic declines of air gap breakdown voltage and fog-haze weather,’’ in *Proc. IEEE Region Conf.(TENCON)*, Nov. 2015, pp. 1–4

[4] H. Niu, R. Guo, T. Xu, and J. Xu, ‘‘Research on weather condition of significant decline of air gap breakdown voltage,’’ *in Proc. IEEE 15th Int. Conf. Environ. Electr. Eng. (EEEIC)*, Rome, Italy, Jun. 2015, pp. 1725–1729

[5] .-K. Seong, W.-J. Shin, J.-S. Hwang, J.-G. Lee, B.-W. Lee, K.-B. Seo, and D.-H. Jeong, ‘‘Effect of humidity and electrode roughness on the AC and impulse breakdown characteristics of dry-air,’’ in *Proc. IEEE Int. Conf. Condition Monitor. Diagnosis*, Sep. 2012, pp. 770–773.

[6] A. Davies and R. Turri, ‘‘Effect of humidity and gas density on switching impulse breakdown of short airgaps,’’ *Phys. Sci*., vol. 135, pp. 59–68,Jan. 1988.

[7] D. Rodriguez, R. Gorur, and P. Hansen, ‘‘Effect of humidity on the breakdown characteristics of air in uniform field for the very low frequency (VLF) band,’’ *IEEE Trans. Dielectr. Electr. Insul.*, vol. 16, no. 5,pp. 1397–1403, Oct. 2009, doi: 10.1109/TDEI.2009.5293953.

[8] . Lazaridis and P. Mikropoulos, ‘‘Positive impulse flashover along smooth cylindrical insulating surfaces under variable humidity,’’ *IEEE Trans. Dielectr. Electr. Insul.*, vol. 18, no. 3, pp. 745–754, Jun. 2011

[9] . Kuffel, ‘‘Electron attachment coefficients in oxygen, dry air, humid air and water vapour,’’ *Proc. Phys. Soc*., vol. 74, p. 297, Sep. 1959.

[10] . G. Christophorou and L. A. Pinnaduwage, ‘‘Basic physics of gaseous dielectrics,’’ *IEEE Trans. Electr. Insul*., vol. 25, no. 1, pp. 55–74, Feb. 1990.

[11] F. O. McMillan and E. C. Starr, "The Influence of Polarity on High-Voltage Discharges," in Transactions of the American Institute of Electrical Engineers, vol. 50, no. 1, pp. 23-33, March 1931, doi: 10.1109/T-AIEE.1931.5055733.

[12] F. O. McMillan, "Polarity Limits of the Sphere Gap," in Transactions of the American Institute of Electrical Engineers, vol. 58, no. 2, pp. 56-61, Feb. 1939, doi: 10.1109/T-AIEE.1939.5057923

[13] A. Pokryvailo, "Calculation of breakdown voltage of gas gaps with arbitrary geometry on examples of spheres and toroids," *2017 IEEE 21st International Conference on Pulsed Power (PPC)*, Brighton, UK, 2017, pp. 1-4, doi: 10.1109/PPC.2017.8291190.

[14] Qiu, Zhibin & Ruan, Jiangjun. “Electric Field Features and Its Application for Air Gap Breakdown Voltage Prediction.” inTechOpen 2018 10.5772/intechopen.72230.

[15] Z. Qiu and X. Wang, "A Feature Set for Structural Characterization of Sphere Gaps and the Breakdown Voltage Prediction by PSO-Optimized Support Vector Classifier," in *IEEE Access*, vol. 7, pp. 90964-90972, 2019, doi: 10.1109/ACCESS.2019.2927159.

[16] Leandros A. Maglaras, Athanasios L. Maglaras, Frangiskos V. Topalis, “The influence of the Effect of Grounding and Corona Current on the Field Strength the Corona Onset and the Breakdown Voltage of Small Air Gaps”, *WSEAS TRANSACTIONS on POWER*, vol 3 no 1 pp. 103-108 Jan 2008

[17] A. Maglaras and F. V. Topalis, "Influence of ground and corona currents on dielectric behavior of small air gaps," in *IEEE Transactions on Dielectrics and Electrical Insulation*, vol. 16, no. 1, pp. 32-41, February 2009, doi: 10.1109/TDEI.2009.4784549.

[18] A. Carrus, E. Cinieri, A. Fumi, and C. Mazzetti, ‘‘Short tail lightning impulse behaviour of medium voltage line insulation,’’ *IEEE Trans. Power Del.*, vol. 14, no. 1, pp. 218–226, Jan. 1999, doi: 10.1109/61.736725.

[19] E. Kuffel and M. Abdullah, ‘‘Corona and breakdown-voltage characteristics in sphere—Plane and rod—Rod gaps under impulse voltages of various wavefront durations,’’ *Proc. Inst. Electr. Eng.*, vol. 113, no. 6, pp. 1113–1119, Jun. 1966, doi: 10.1049/piee.1966.0182.

[20] Kuffel, Edmund and A. S. Husbands. “The influence of nearby earthed objects and of the polarity of the voltage on the direct-voltage breakdown of horizontal sphere-gaps.” *Proceedings of the IEE – Part A Power Engineering* vl. 108 is. 40 pp 308-314 (1961).

[21] Valavala, Madhu and Bhavya Kanchanapalli. *“*Measurement of Air Breakdown Voltage Using Standard Sphere Gap Method*.”* Department of Electrical Engineering National Institute of Technology, Rourkela Master Thesis *(*2020).

[22], Ravinda Arora, Wolfgang Mosc, “High Voltage and Electrical Insulation Engineering” Section 2.3.1.1. The effects of grounding on field configuration, Page 19

[23] Gandi, Vinod Kumar, Rishi Verma, Manoj Warrier, and Archana Sharma. 2022. "Effect of Electrode Profile and Polarity on Performance of Pressurized Sparkgap Switch" *Plasma* 5, no. 1: 130-145. https://doi.org/10.3390/plasma5010010

[24] Li, Longjie & Li, Jiangtao & Zhao, Zheng. (2020). Effect of switch parameters and polarity on the repetitive performance of a corona-stabilized switch viewed from behavior of space charge. *Physics of Plasmas*. 27. 10.1063/1.5138201.

[25] E Kuffel W S Kaengl 'Partial breakdown, corona discharges' *High Voltage Engineering* [Book Section] // High Voltage Engineering. - [s.l.] : 371-38 1984.

[26] P A Lawless K J Maclean, L E Sparks and G H Ramsey - 'Negative corona in wire-plate electrostatic precipitators, part I: Characteristics of individual tuft-corona discharges' [Journal]. - [s.l.] : *Journal of Electrostatics*, 1986. - Vol. 18 p 199 - 217.

[27] P A Lawless K J Maclean, L E Sparks, G H Ramsey 'Negative corona in wire-plate electrostatic precipitators, part II: calculation of electrical characteristics of contaminated discharge electrodes' [Journal]. - [s.l.] : *Journal of Electrostatics*, 1986. - Vol. 18. p 219 - 231.

[28] Current pulses caused by streamers in sphere-sphere electrode system" Journal of Physics: Conference Series 646 (2015) 012042 doi:10.1088/1742-6596/646/1/012042

5. CHAPTER V

SMOOTH MACHINED SURFACE DIELECTRIC FLASHOVER

5.1. INTRODUCTION

Chapter V will include data from flashover of dielectrics with smooth, machined surfaces, inserted into the parallel-plane electrode system characterised in Chapter IV. The sealed test cell allows for air-solid insulation systems to be tested under different environmental and physical conditions. The use of the same basic arrangement to that in Chapter IV will allow direct comparison of the breakdown characteristics of air-solid insulation systems with those of open-air gaps. The materials tested in this chapter were –

- High-Density Polyethylene (HDPE)
- Polyetherimide (Ultem)
- Polyoxymethylene (Delrin)

As in Chapter IV, the insulation systems were subject to changing environmental conditions of <10% RH, ~50% RH and >90% RH, and pressures of -0.5 bar gauge, 0 bar gauge and 0.5 bar gauge. Each insulation system was subjected to 100/700 ns impulse voltages, of both positive and negative polarity, using the step-up testing procedure to determine the breakdown/flashover voltage for each insulation system.

Overall, the results presented in this chapter will provide designers of pulsed-power systems with comparative data regarding -

- Which material will yield the highest flashover/breakdown voltage in various environmental conditions.
- Dependent upon material properties, how the discharge channel interacts with the spacer under different conditions.
- How the breakdown performance of each of the air-solid insulation systems compares to that of the open-air gap.

Experimental results are reported in [1], with surface flashover events characterised in air with varying humidity for PTFE, silicone rubber (SIR), nylon and glazed porcelain, with a rod-plane electrode topology, under positive impulse voltages. The authors observed that, as the absolute humidity increased from 5 g/m3 to 25 g/m3, the positive flashover voltage was seen to increase for both lightning impulse (LI) and switching impulse (SI) voltages. In [2], under a similar topology and negative polarity, it was observed that increasing the relative humidity (RH) resulted in the flashover strength decreasing. The flashover voltage was recorded at 10%, 30%, 60% and 90% RH, and decreased from 18 kV to 14 kV. In [3], the differences in the initiation and propagation of positive and negative streamers, resulting in flashover, are discussed. It was found that, under negative polarity, the plasma channel established at breakdown was seen to follow the surface of the material. Under positive polarity, however, the plasma channel at breakdown was seen to be repelled from the surface of the solid material and propagate through the bulk air. In [4], flashover of air gaps without solid spacers was characterised, under high humidity levels, up to and including 100% RH. Under these conditions, fog accumulation was found to have a detrimental effect on the breakdown strength of the air gap tested, especially for values of RH >80%. In [5], the effect of increasing water vapour content in SF_6 was investigated. The authors found that the increase of water content at a given pressure resulted in a decrease in the flashover strength of an epoxy-resin insulated system. It was also found that the presence of water for an extended period of time could result in chemical reactions occurring at the spacer surface, leading to reduced flashover initiation voltages.

As previous literature has informed, the effect of multiple environmental parameters has an effect on the flashover voltage of a system, this will be discussed in terms of environmental parameters in Section 5.3 and in Section 5.4, how this compares to the open gap analysis shown in Chapter IV.

5.2. EXPERIMENTAL RESULTS

The results in this section are based on sets of 20 tests at each polarity and set of environmental conditions using the ‘step up’ procedure from ASTM D3426-97, as

detailed in Section 3.6.4. The statistical analysis performed was identical to that in chapter 4 and the data is presented in the same manner.

These results will be further discussed in Section 5.3, where the effect of physical and environmental parameters will be discussed, and Section 5.4, in terms of discharge location, comparing the results here to those obtained in an open-air gap in Chapter IV., to facilitate comparative discussion of the breakdown mechanisms.

5.2.1. High-Density Polyethylene (HDPE)

Figure 5.1, 5.2 and 5.3 shows 2-parameter Weibull plots for HDPE samples tested at -0.5 bar gauge, 0 bar gauge and 0.5 bar gauge and at <10% RH, ~50% RH and >90% RH.

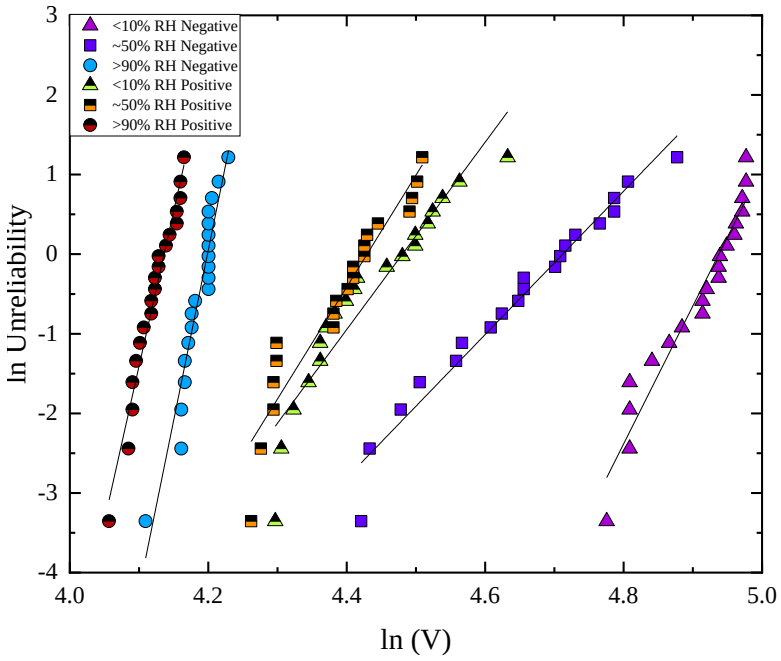

Figure 5.1. - Weibull plots and curve fits of breakdown voltage data for smooth HDPE surface at<10% RH, ~50% RH and >90% RH, all at -0.5 bar gauge

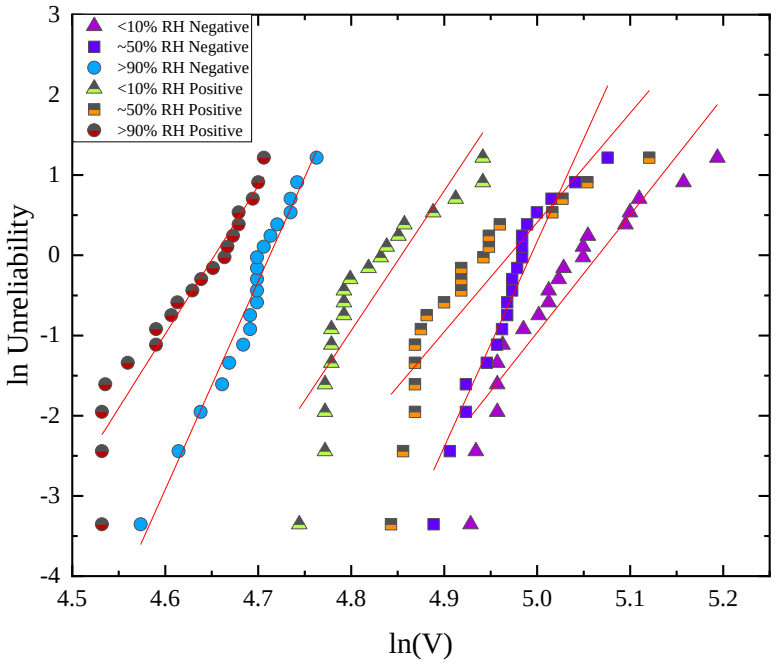

Figure 5.2 - Weibull plots and curve fits of breakdown voltage data for smooth HDPE surface at <10% RH, ~50% RH and >90% RH, all at 0 bar gauge

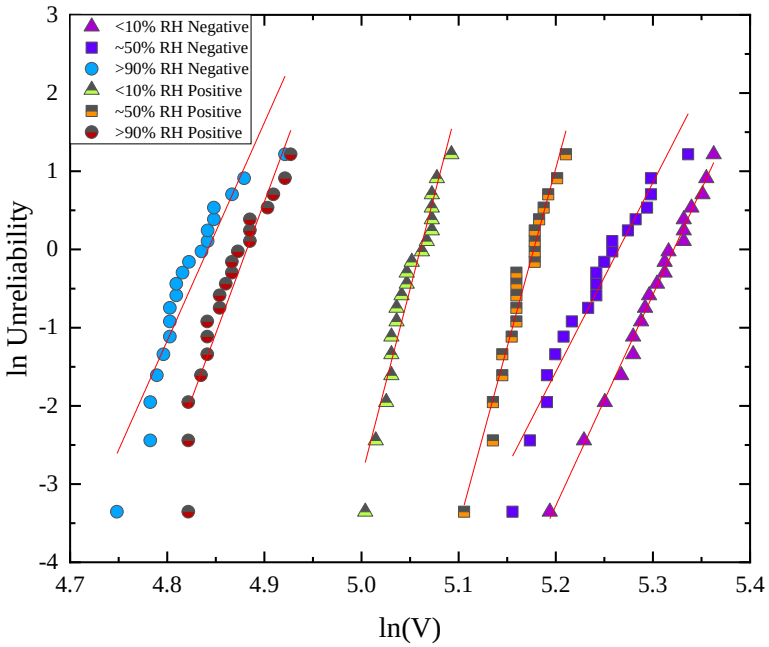

Figure 5.3 - Weibull plots and curve fits of breakdown voltage data for smooth HDPE surface at<10% RH, ~50% RH and >90% RH, all at 0.5 bar gauge

Analysing the Weibull distributions in Figure 5.1, 5.2 and 5.3, the V_{50} breakdown voltages and the spread (error bars) are shown in Figure 5.4a, 5.4b and 5.4c. Each bar represents the V_{50} from 20 impulsive breakdown voltages, and the error bars represent the 95.4% spread of the data.

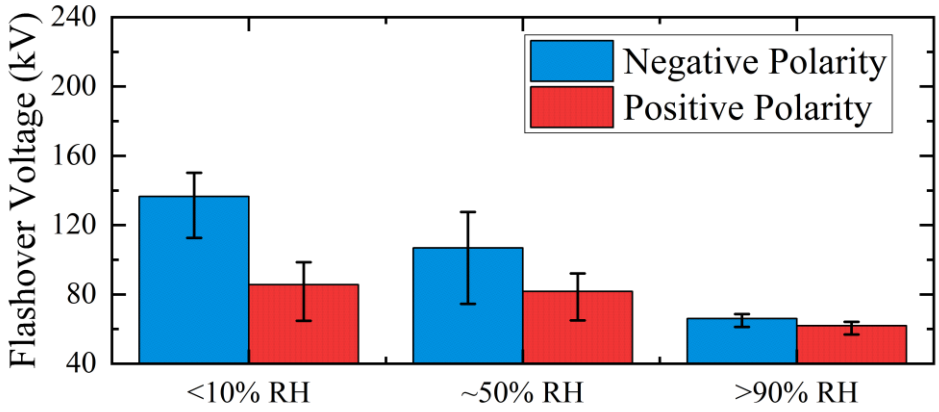

(a)

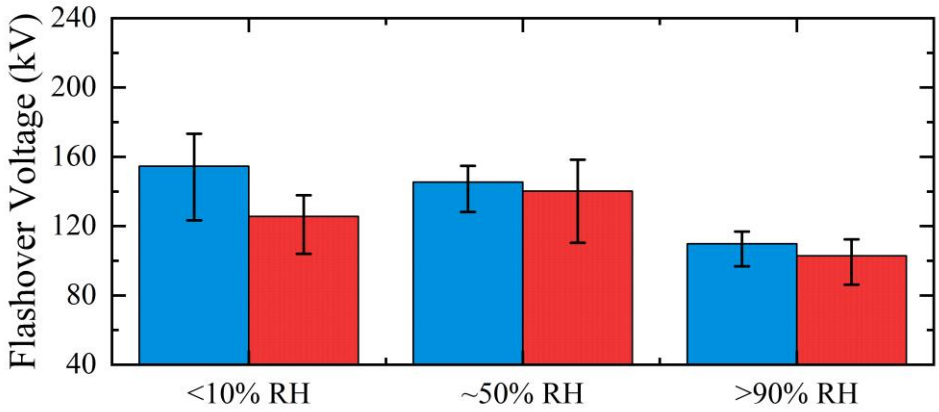

(b)

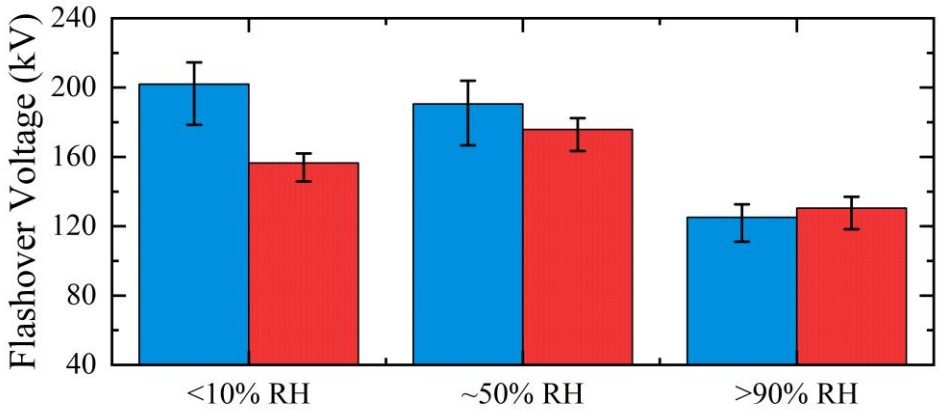

(c)

Figure 5.4 - Flashover voltages with a smooth, machined HDPE spacer at <10 % RH, ~50 % RH and >90% RH, under negative and positive polarity impulse voltages, at (a) -0.5 bar gauge, (b) 0 bar gauge and (c) 0.5 bar gauge. Each bar represents the average of 20 breakdown voltages and the errors bars show the 95.4% spread of data in relation to the 2-parameter Weibull distribution of each data set.

Figure 5.4a shows the HDPE insulation system results for changing humidity and polarity at a pressure of -0.5 bar gauge. As the humidity increases, the flashover voltage for both positive and negative polarity generally decreases. However, the difference between the positive polarity (lower) and negative polarity (higher) breakdown voltages decreases with increasing humidity. At <10% RH, the negative-polarity V_{50} is significantly higher than the positive, and the error bars do not overlap, indicating that the distributions are independent of one another (for 95.4% spread of data). As the RH is increased, the difference between negative and positive V_{50} values decreases significantly, resulting in overlapping error bars - this behaviour is evident from the ~50% RH and >90% RH results. Therefore, for an insulation system subjected to a humid environment, the breakdown behaviour becomes more electrically symmetrical. At >90% RH, the increased conductivity of the surface of the dielectric material leads to surface flashovers for both positive and negative polarity, creating a symmetrical electrical performance. The highest V_{50} breakdown voltage measured for HDPE at -0.5 bar gauge was under negative polarity, at <10% RH, with a flashover voltage of ~137 kV. The minimum flashover voltage measured in this arrangement was under positive polarity at >90% RH, with a flashover voltage of ~66 kV.

Figure 5.4b shows the HDPE insulation system results for changing humidity and polarity, at a constant pressure of 0 bar gauge. The negative V_{50} was always nominally higher than the positive value though the error bars overlap. The negative V_{50} decreases with increasing RH. However, for positive polarity, although the breakdown voltage at >90% RH is significantly lower than that at <10% RH, the highest V_{50} is exhibited at ~50% RH. Similar to the -0.5 bar gauge results, as the humidity is increased, the difference between the positive and negative V_{50} generally decreases. The difference between the negative and positive breakdown voltages at <10% RH and ~50% RH is less compared to that at -0.5 bar gauge (Figure 5.2), with the data gathered at >90% RH showing a similar difference. Again, as the air humidity is increased, the system exhibits a more electrically symmetrical performance. The highest V_{50} measured for HDPE at 0 bar gauge was under negative polarity at <10% RH, at ~155 kV. The minimum V_{50} flashover voltage was measured at ~100 kV, under positive polarity, in a >90% RH environment.

Figure 5.6 shows the HDPE insulation system results for changing humidity and polarity at a pressure of 0.5 bar gauge. For negative polarity, as also witnessed at -0.5 and 0 bar gauge, as the humidity increases there is a downward trend in V_{50}. For positive polarity, however, a similar behaviour to that observed at 0 bar gauge is witnessed - as the humidity is increased from <10% RH to ~50% RH, V_{50} is seen to increase, but again, as the humidity increases to >90% RH, V_{50} decreases.

At <10% RH, the negative-polarity V_{50} is again significantly higher than the positive, and the error bars do not overlap, indicating that the distributions are independent of one another (95.4% spread of data). As the RH is increased, the difference between negative and positive V_{50} values decreases significantly, resulting in overlapping error bars Again, as the insulation system is subjected to a more humid environment, the breakdown behaviour of the insulation system becomes more electrically symmetrical. With the increased conductivity of the surface of the dielectric at >90% RH leading to surface flashovers for both positive and negative polarity, creating a symmetrical electrical performance. The maximum V_{50} measured with a smooth HDPE spacer at 0.5 bar gauge was under negative polarity at <10% RH, with a flashover voltage of ~200 kV, and the minimum flashover voltage was measured at ~125 kV, under negative polarity and in a >90% RH environment.

Comparing the breakdown behaviour with HDPE spacers by RH level, at <10% RH, the negative V_{50} is greater than the positive, with no overlapping error bars for -0.5 bar gauge and 0.5 bar gauge, indicating significant difference from each other within a 95.4% spread of each distribution. At 0 bar gauge, although the negative breakdown voltage is higher than the positive, overlapping error bars are exhibited. At ~50% RH, the negative V_{50} is greater than the positive, but this comparison exhibits overlapping error bars for all tests. Finally, at >90% RH, the positive and negative V_{50} are much closer in magnitude, with overlapping error bars.

Further data highlighting the differences in the breakdown voltages of an insulation system bridged with a smooth HDPE spacer is shown in Table 5.1. The 2-parameter Weibull distribution parameters are shown, as well as the V_{50} and $V_{0.01}$ values obtained from the CDF of each data set.

Table 5.1 - Values of α, β and $V_{0.01}$ for smooth HDPE surfaces, for each set of environmental conditions and both polarities.

HDPE Smooth	**Pressure**	**Negative**				**Positive**			
		α (kV)	β	V_{50} (kV)	$V_{0.01}$ (kV)	α (kV)	β	V_{50} (kV)	$V_{0.01}$ (kV)
-0.5 bar gauge	<10% RH	139.4	17.3	136.5	81.9	88.3	11.8	85.6	40.3
	~50% RH	111.3	9	106.9	40	83.9	14.1	81.7	43.6
	>90% RH	66.6	42.8	66	53.7	62.6	38.9	62	49.4
0 bar gauge	<10% RH	158.5	14.7	154.6	84.6	128.2	17.4	125.6	75.6
	~50% RH	147.4	25.6	145.3	102.9	144	13.6	140.2	73.3
	>90% RH	111.3	26	109.8	78.1	104.9	18.5	102.9	63.7
0.5 bar gauge	<10% RH	204.7	27	201.9	145.5	157.7	48	156.5	130.2
	~50% RH	193.4	24.2	190.5	132.2	177.2	45.7	175.8	144.8
	>90% RH	126.7	27.9	125.1	91.1	131.9	33.7	130.5	100.3

With increasing pressure at <10% RH When comparing the calculated 0.01% probability of failure values (1 in 10,000 failures), increasing the pressure increases the value of $V_{0.01}$ for both positive and negative polarities. The values for negative polarity are significantly larger than for positive polarity.

In Table 5.1, for the -0.5 bar gauge results, the $V_{0.01}$ values, it's shown that, due to the generally increasing β value with increasing humidity that the calculated 0.01% probability of failure values (1 failure in 10,000), shows that the insulation follows no clear trend with negative polarity with the highest measured at <10% RH and the lowest measured at ~50% RH, where for positive polarity, with increasing humidity, there is an increase in the breakdown performance.

For the 0 bar gauge results in Table 5.1, it is shown that for the $V_{0.01}$ values, the increasing in humidity is also shown to follow no trend with negative polarity where the maximum breakdown voltage is measured at ~50% RH. For positive polarity, as the humidity increases, there is a decrease in the flashover voltage.

For the 0.5 bar gauge results in Table 5.1, it is shown that for the $V_{0.01}$ values, the increasing in humidity is shown to have a clear negative trend in the negative polarity breakdown voltage. For positive polarity, no trend is shown with the highest breakdown voltage being measured at ~50% RH.

5.2.2. Polyetherimide (Ultem)

Figure 5.5, 5.6 and 5.7 shows 2-parameter Weibull plots for Polyetherimide samples tested at -0.5 bar gauge, 0 bar gauge and 0.5 bar gauge and at <10% RH, ~50% RH and >90% RH.

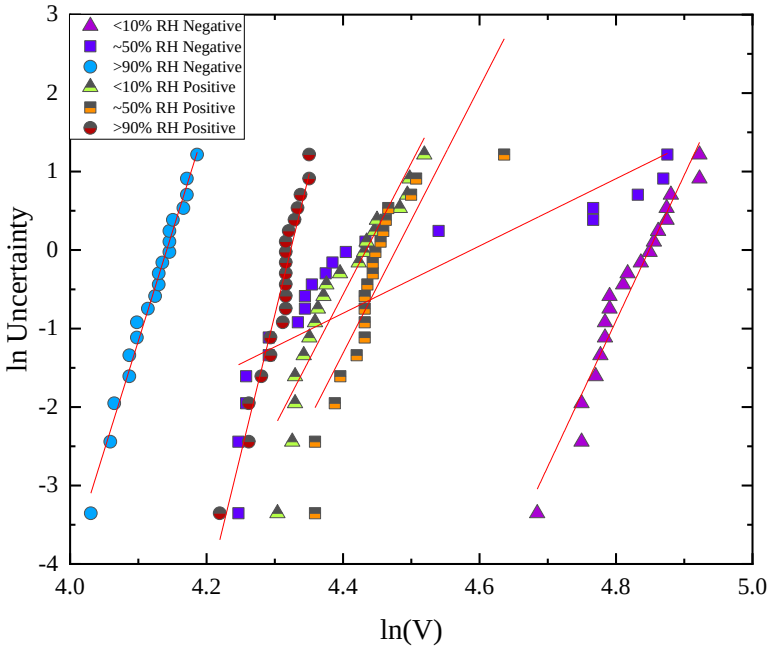

Figure 5.5 - Weibull plots and curve fits of breakdown voltage data for smooth Polyetherimide surface at <10% RH, ~50% RH and >90% RH, all at -0.5 bar gauge

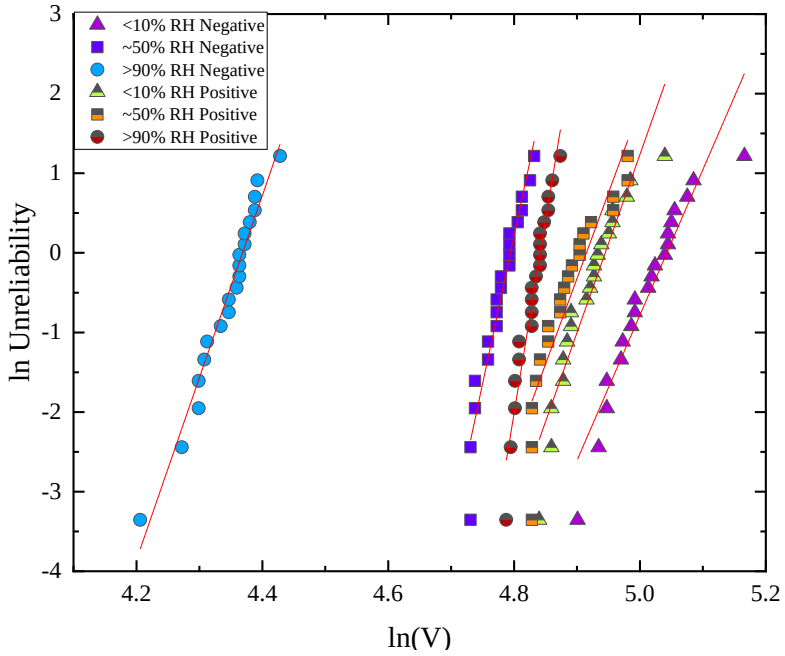

Figure 5.6 - Weibull plots and curve fits of breakdown voltage data for smooth Polyetherimide surface at <10% RH, ~50% RH and >90% RH, all at 0 bar gauge.

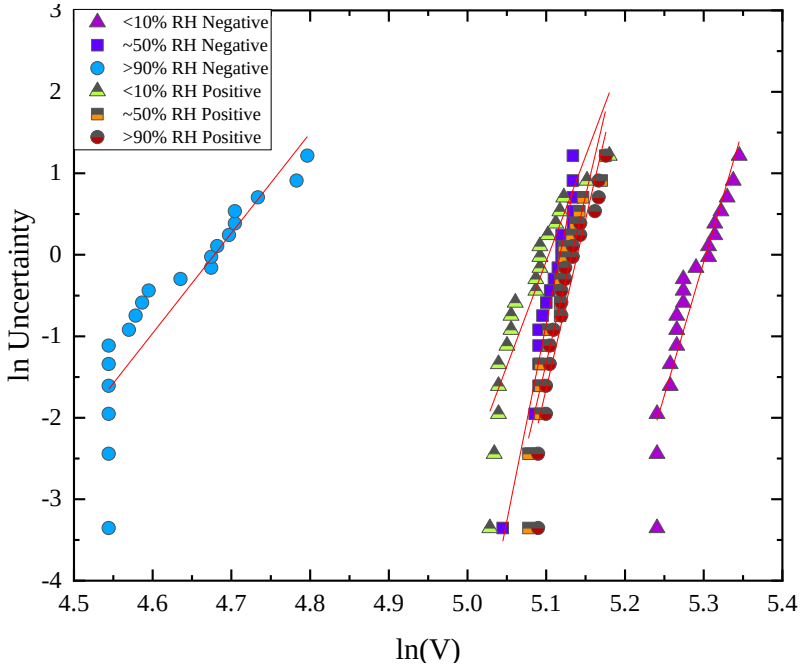

Figure 5.7 - Weibull plots and curve fits of breakdown voltage data for smooth Polyetherimide surface at <10% RH, ~50% RH and >90% RH, all at 0.5 bar gauge

Shown in Figures 5.5 and 5.7, distinct regions appear in specific distributions. In Figure 5.5, at ~50% RH, there at two distinct regions of discharge behaviour under negative polarity, indicating different discharge processes. As shown from a graph of

breakdown voltage vs breakdown number for this instance in Figure AP5b, the first five breakdown voltages were higher than those for the subsequent tests - this could be attributed to the change in breakdown performance of the insulation system, where bulk air breakdown and surface flashover events were recorded, as moisture accumulates within the test cell. This results in a large error bar recorded for this test condition.

Analysing each distribution, under negative polarity at >90% RH, there are two distinct regions of discharge behaviour, indicating different processes. As shown from the graph of breakdown voltage vs breakdown number for this instance in Figure AP5i, the first 10 breakdown voltages were higher than those for the subsequent tests - this could be attributed to the change in breakdown performance of the insulation system, where bulk air breakdown and surface flashover events were recorded, as moisture accumulates within the test cell.

When deriving the Weibull parameters from the data in Figures 5.5, 5.6 and 5.7, no censoring of data was conducted.

Analysing the Weibull distributions in Figure 5.5, 5.6 and 5.7, the V_{50} breakdown voltages and the spread (error bars) are shown in Figure 5.8a, 5.8b and 5.8c. Each bar represents the V_{50} from 20 impulsive breakdown voltages, and the error bars represent the 95.4% spread of the data. The conditioning observed from the distribution in Figure 5.5 and 5.7 discussed above resulted in large error bars in Figures 5.8a and 5.8c.

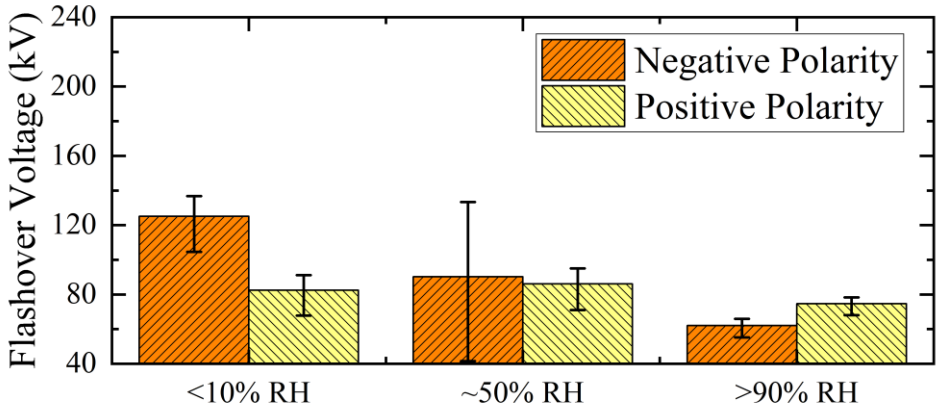

(a)

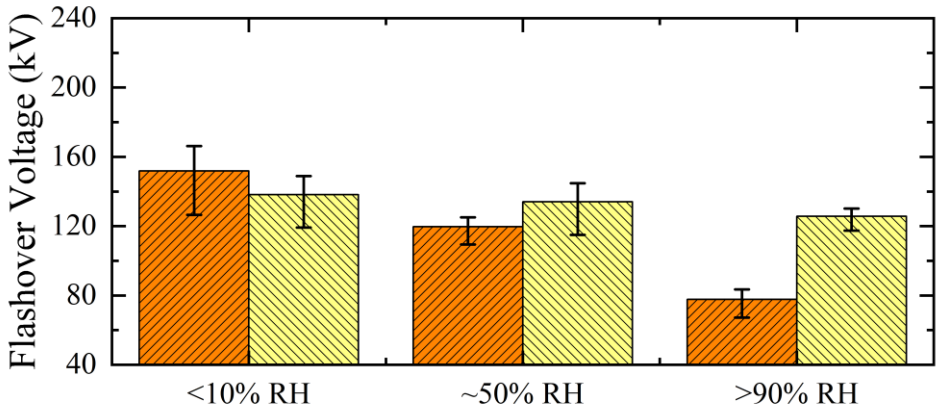

(b)

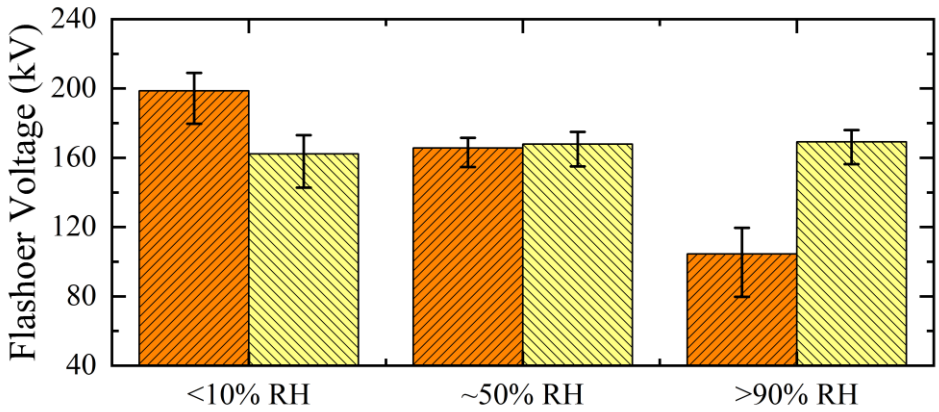

(c)

Figure 5.8 - Flashover voltages with a smooth, machined Polyetherimide spacer at <10% RH, ~50% RH and >90% RH, under negative and positive polarity impulse voltages, at (a) -0.5 bar gauge, (b) 0 bar gauge and (c) 0.5 bar gauge. Each bar represents the average of 20 breakdown voltages and the errors bars show the 95.4% spread of data in relation to the 2-parameter Weibull distribution of each data set

Figure 5.8a shows the Polyetherimide insulation system results for changing humidity and polarity at a constant pressure of -0.5 bar gauge. As the humidity increases, the V_{50} flashover voltage for both positive and negative polarity is shown to generally decrease. However, the added humidity exhibits much larger effect on the negative polarity flashover voltages than the positive. For positive polarity, although the >90% RH value is lower than that for <10% RH, the highest V_{50} flashover voltage occurs, marginally, at ~50% RH. The difference in V_{50} between positive polarity and negative polarity decreases with the addition of humidity into the environment from <10% RH to ~50% RH. At >90% RH, the value of V_{50} for positive polarity is higher than that for negative polarity. The maximum V_{50} for Polyetherimide at -0.5 bar gauge was under negative polarity, at <10% RH, with a flashover voltage of ~125 kV. The minimum V_{50} flashover voltage was measured at ~60 kV, under negative polarity and in a >90% RH environment.

Figure 5.8b shows the Polyetherimide insulation system results for changing humidity and polarity, at a pressure of 0 bar gauge. As the humidity increases, there is a downward trend in the V_{50} flashover voltage for both positive and negative polarity energisation, however, the changes are more significant for negative polarity tests. At <10% RH, the negative V_{50} breakdown voltage is seen to be greater than the positive, however, there are overlapping error bars. At ~50% RH, the positive polarity V_{50} flashover voltage is higher than the negative, however, the overlapping error bars show a similar behaviour. At >90% RH, the positive polarity V_{50} value is again higher than that of the negative polarity result, with no overlapping error bars indicating that the distributions are independent of each other, with 95.4% data spread. The maximum V_{50} breakdown voltage measured for Polyetherimide at 0 bar gauge was under negative polarity, at <10% RH, with a flashover voltage of ~150 kV. The minimum flashover voltage was measured at ~75 kV, also under negative polarity, but in a >90% RH environment.

Figure 5.8c shows the Polyetherimide insulation system results for changing humidity and polarity at a pressure of 0.5 bar gauge. As the humidity increases, the V_{50} flashover voltage for negative polarity is shown to decrease. The positive V_{50} values do not appear to change. At <10% RH the negative polarity V_{50} vale exceeds the positive value. At ~50% RH the two values are similar with overlapping error bars. At >90%

RH, the positive-polarity V_{50} value is greater than the negative polarity result, with no overlapping error bars, showing that the distributions are independent of each other, with 95.4% data spread. The maximum V_{50} breakdown voltage for Polyetherimide at 0.5 bar gauge was under negative polarity, at <10% RH, with a flashover voltage of ~200 kV. The minimum flashover voltage was measured at ~100 kV, also under negative polarity, in a >90% RH environment.

Overall, from the results shown in Figures 5.8a, 5.8b and 5.8c, due to the similar performance with increasing humidity, Polyetherimide would be a good choice for an insulation system subject to a wide range of humidity and pressure levels, if the system were positive polarity.

Further data highlighting the difference in the breakdown voltages of an insulation system bridged with a smooth Polyetherimide spacer is shown in Table 5.2. The 2-parameter Weibull distribution parameters are shown, as well as the V_{50} and $V_{0.01}$ values obtained from the CDF of each data set.

Table 5.2 – Values of α, β and $V_{0.01}$ for smooth Polyetherimide surfaces, for each set of environmental conditions and both polarities.

Polyetherimide Smooth	**Pressure**	**Negative**				**Positive**			
		α (kV)	**β**	**V_{50} (kV)**	**$V_{0.01}$ (kV)**	**α (kV)**	**β**	**V_{50} (kV)**	**$V_{0.01}$ (kV)**
-0.5 bar gauge	<10% RH	127.6	18.6	125.1	77.7	84.2	16.8	82.4	48.6
	~50% RH	98.3	4.3	90.2	11.5	88	17	86.1	51.1
	>90% RH	62.9	27.9	62.1	45.2	75.4	35.6	74.7	58.2
0 bar gauge	<10% RH	154.9	18.3	151.8	93.5	140.4	22.4	138.2	93.1
	~50% RH	120.8	37.2	119.6	94.3	136.3	21.5	134	88.9
	>90% RH	78.9	22.9	77.7	52.8	126.7	48.4	125.7	104.7
0.5 bar gauge	<10% RH	200.9	32.8	198.7	151.7	164.5	25.8	162.2	115.1
	~50% RH	166.9	48.3	165.7	138	169.4	41.1	167.7	135.4
	>90% RH	107.6	12.3	104.4	50.8	170.6	41.5	169.1	136.7

In Table 5.2 The impact of the conditioning effect at -0.5 bar gauge at 50% RH in negative polarity and 0.5 bar gauge at 90% RH in negative polarity can be seen clearly in the significantly lower values of beta. This indicates that the value for $V_{0.01}$ must be treated with caution. When comparing the calculated 0.01% probability of failure values, increasing the pressure, in general leads to an increase in the value of $V_{0.01}$ for

both positive and negative flashover voltages the exception being the result for 0.5 bar gauge at 90% RH in negative polarity which was impacted by the low β value. At <10% RH the values of $V_{0.01}$ are in general larger for negative polarity data. At ~50% RH the values are broadly similar and at >90%RH the values for positive energisation exceed those for negative energisation

For the -0.5 bar gauge results, the $V_{0.01}$ values show that with increasing humidity, the negative polarity results show no trend with the highest measured a <10% RH and the lowest at ~50% RH, again a product of the conditioning effect discussed. For positive polarity, with increasing humidity, the breakdown voltage increased also.

For the 0 bar gauge results in Table 5.2, the $V_{0.01}$ values show that with increasing humidity, the negative polarity results show no trend with the highest measured at ~50 % RH. For positive polarity, this also shows no trend with the highest measured a <10% RH and the lowest at ~50% RH,

For the 0.5 bar gauge results in Table 5.2, it is shown that there is opposing trends dependant on the polarity used with increasing humidity, the breakdown voltage decreases, but for positive polarity the breakdown voltage is shown to increase.

5.2.3. Polyoxymethylene (Delrin)

Figure 5.9, 5.10 and 5.11 shows 2-parameter Weibull plots for Polyoxymethylene samples tested at -0.5 bar gauge, 0 bar gauge and 0.5 bar gauge, at <10% RH, ~50% RH and >90% RH.

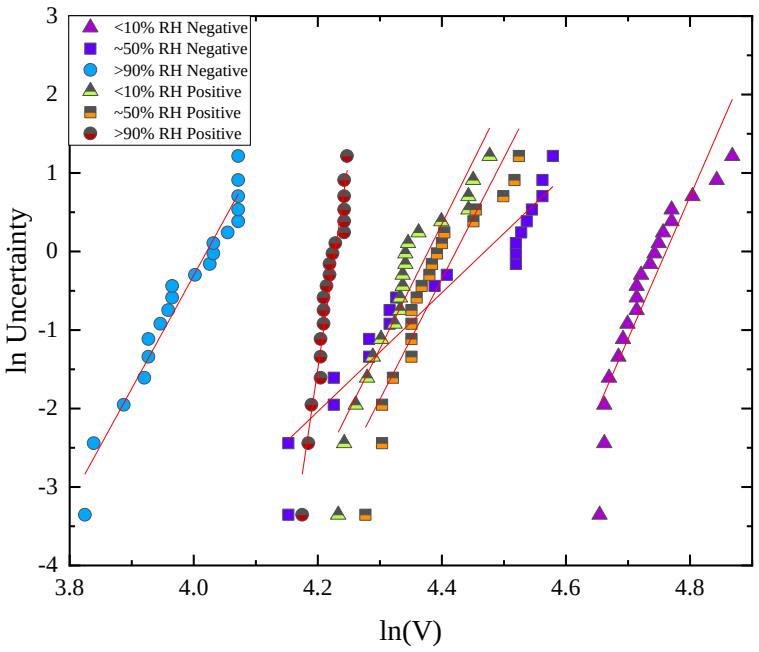

Figure 5.9 - Weibull plots and curve fits of breakdown voltage data for smooth Polyoxymethylene surface at <10% RH, ~50% RH and >90% RH, all at -0.5 bar gauge.

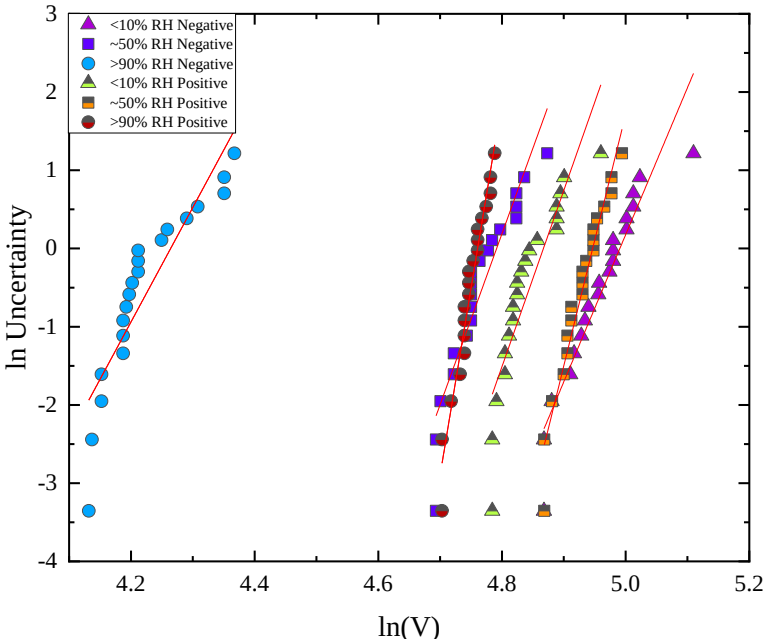

Figure 5.10 - Weibull plots and curve fits of breakdown voltage data for smooth Polyoxymethylene surface at <10% RH, ~50% RH and >90% RH, all at -0.5 bar gauge

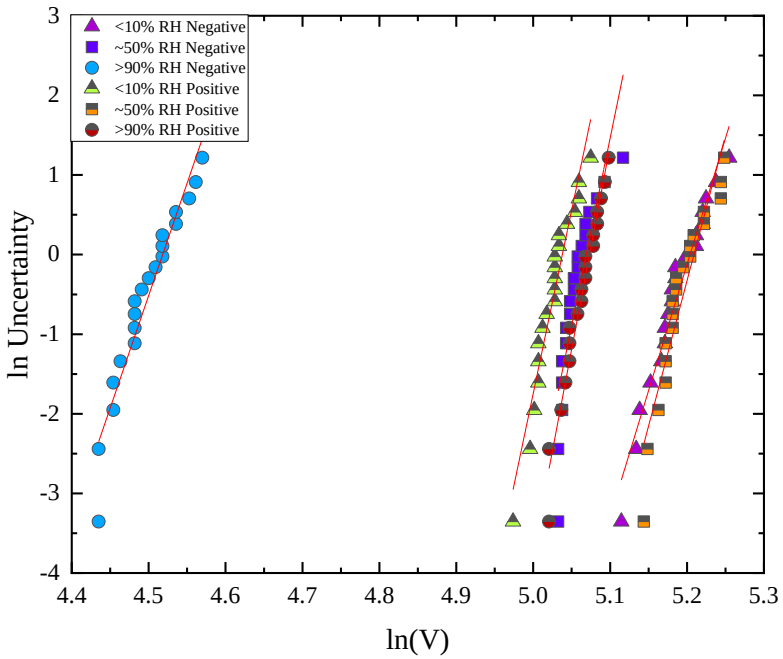

Figure 5.11 - Weibull plots and curve fits of breakdown voltage data for smooth Polyoxymethylene surface at <10% RH, ~50% RH and >90% RH, all at 0.5 bar gauge.

Analysing the Weibull distributions in Figure 5.9, 5.10 and 5.11, the V_{50} breakdown voltages and the spread (error bars) are shown in Figure 5.12a, 5.12b and 5.12c. Each bar represents the V_{50} from 20 impulsive breakdown voltages, and the error bars represent the 95.4% spread of the data.

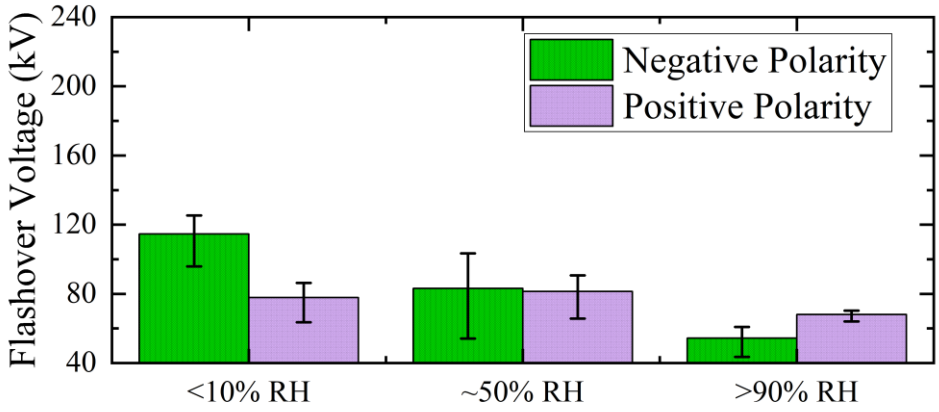

(a)

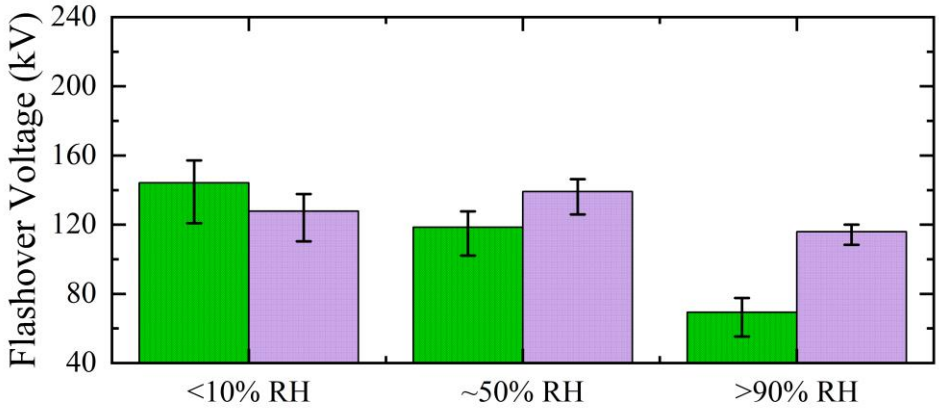

(b)

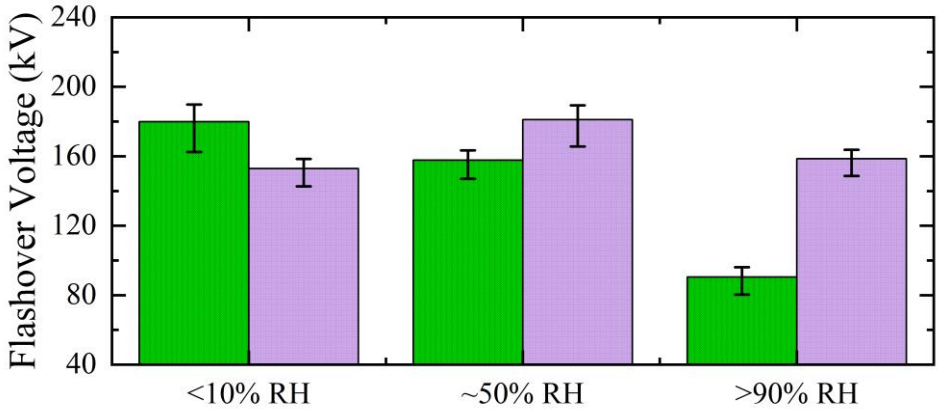

(c)

Figure 5.12 - Flashover voltages with a smooth, machined Polyoxymethylene spacer at <10% RH, ~50% RH and >90% RH, under negative and positive polarity impulse voltages, at (a) -0.5 bar gauge, (b) 0 bar gauge and (c) 0.5 bar gauge. Each bar represents the average of 20 breakdown voltages and the errors bars show the 95.4% spread of data in relation to the 2-parameter Weibull distribution of each data set.

Figure 5.12a shows the Polyoxymethylene insulation system results for changing humidity and polarity at a pressure of -0.5 bar gauge. Analysing the trends as the humidity increases, the V_{50} flashover voltage for both positive and negative polarity is shown to generally decrease. However, the added humidity exhibits a much larger effect on the negative polarity flashover voltages than the positive. Under positive polarity, although the value for >90% RH is smaller than that for, the highest V_{50} flashover voltage occurred, marginally, at ~50% RH. The difference between the positive and negative V_{50} flashover voltages changes with the addition of humidity into the environment, as the humidity is increased to ~50% RH, the difference in the V_{50} values decreases, resulting in overlapping error bars between the distributions. At >90% RH, however, the behaviour again changes, where the positive V_{50} value is higher than that of the negative polarity result, with no overlapping error bars, showing that the distributions are independent of one another, with 95.4% data spread. The maximum V_{50} breakdown voltage for Polyoxymethylene at -0.5 bar gauge was under negative polarity, at <10% RH, with a flashover voltage of ~115 kV. The minimum flashover voltage was measured at ~55 kV, again under negative polarity, although in a >90% RH environment.

Figure 5.12b shows the Polyoxymethylene insulation system results for changing humidity and polarity at a pressure of 0 bar gauge. As the humidity increases, for negative polarity, there is a general downward trend in the flashover voltage. However, under positive polarity, the highest V_{50} flashover voltage occurs at ~50% RH. At <10% RH, the negative V_{50} breakdown voltage is seen to be greater than that of the positive. There are, however, overlapping error bars. At ~50% RH, the positive polarity V_{50} flashover voltage is higher than the negative, however, again the error bars overlap. At >90% RH, the positive V_{50} value is significantly larger than that of the negative polarity result, with no overlapping error bars showing that the distributions are independent of each other, with 95.4% data spread. The maximum V_{50} breakdown voltage measured for Polyoxymethylene at 0 bar gauge was under negative polarity, at <10% RH, being ~145 kV. The minimum flashover voltage was measured at ~70 kV, again under negative polarity, but in a >90% RH environment.

Figure 5.12c shows the Polyoxymethylene insulation system results for changing humidity and polarity at a constant pressure of 0.5 bar gauge. Observing the behaviour

as the humidity increases, the flashover voltage for negative polarity is seen to generally decrease. However, for positive polarity, the change in trend is evident where the highest V_{50} flashover voltage occurs at ~50% RH, which then decreases at >90% RH, but <10% RH shows the lowest flashover voltage, but each result exhibits overlapping error bars. Looking at the differences between the positive and negative V_{50} flashover voltages, as the humidity is increased to ~50% RH, the positive V_{50} becomes higher than the negative, with no overlap of the error bars. At >90% RH, the difference becomes more pronounced, with much higher positive V_{50} than negative, with no overlapping error bars showing that the distributions are independent of each other, with 95.4% data spread. The maximum V_{50} breakdown voltage for Polyoxymethylene at 0.5 bar gauge was under positive polarity, at ~50% RH, being ~175 kV. The minimum V_{50} breakdown voltage of ~85 kV was measured under negative polarity, in a >90% RH environment.

Further data highlighting the difference in the breakdown voltages of an insulation system bridged with a smooth Polyoxymethylene spacer is shown in Table 5.3. The 2-parameter Weibull distribution parameters are shown, as well as the calculated V_{50} and $V_{0.01}$ values obtained from the CDF of each data set.

Table 5.3 – Values of α, β and $V_{0.01\%}$ for smooth Polyoxymethylene surfaces, for each set of environmental conditions and both polarities.

Polyoxymethylene Smooth	**Pressure**	**Negative**				**Positive**			
		α (kV)	**β**	**V_{50} (kV)**	**$V_{0.01}$(kV)**	**α (kV)**	**β**	**V_{50} (kV)**	**$V_{0.01}$(kV)**
<10% RH	-0.5 bar gauge	116.9	18.2	114.6	70.4	79.7	15.9	77.9	44.6
	0 bar gauge	87.3	7.6	83.2	25.8	83.3	15.4	81.3	45.8
	0.5 bar gauge	55.8	14.4	54.4	29.5	68.6	53.6	68.1	57.7
~50% RH	-0.5 bar gauge	147	18.8	144.2	90.1	129.9	22.5	127.8	86.3
	0 bar gauge	120.5	21.9	118.5	79	140.7	32.1	139.1	105.6
	0.5 bar gauge	71.1	14.7	69.4	37.9	116.8	47.8	115.9	96.3
>90% RH	-0.5 bar gauge	182	31.7	179.9	136.1	154.1	46.1	152.9	126.2
	0 bar gauge	159	47.1	157.8	130.7	182.9	36.5	181.1	142.1
	0.5 bar gauge	91.7	28.2	90.5	66.2	159.7	51.2	158.5	133.4

When comparing the calculated 0.01% probability of failure values in Table 5.3, increasing the pressure increases the values derived under all conditions of polarity and pressure. At <10%RH the values of $V_{0.01}$ are greater for negative energisation but

the opposite is true for ~50% and >90% RH.For the -0.5 bar gauge results, the $V_{0.01}$ values show with increasing humidity, the negative polarity results show no trend with the highest measured a <10% RH and the lowest at ~50% RH, again a product of the conditioning effect discussed. For positive polarity, with increasing humidity, the breakdown voltage increased also.

For the 0 bar gauge results, it is shown that for, the $V_{0.01}$ values show with increasing humidity, the negative polarity results show a decrease the breakdown voltage. For positive polarity, this also shows no trend with the highest measured at ~50% RH,

For the 0.5 bar gauge results, with the increase of humidity, the breakdown voltage decreases, whereas for positive polarity, no trend is resultant with the highest breakdown voltage measured at ~50% RH.

5.3. Effect of Physical and Environmental Parameters on Flashover

Based on the results in Section 5.2, the effect of physical parameters on the flashover process will now be discussed.

5.3.1. Dielectric Material

Comparing the results by material highlights the effect that the relative permittivity of the solid spacer had on certain tests. Under negative polarity, the performance of the system was shown to follow a relationship of higher flashover strengths for lower permittivity. This behaviour was consistently observed for all levels of pressure at <10% RH, ~50% RH and >90% RH, as shown by analysing Figures 5.4, 5.8 and 5.12. This observation is based on the values of V_{50}, although, the error bars do overlap in many cases. However, it is understood that this decrease in flashover voltage is due to the field enhancement associated with increasing relative permittivity of the spacer material, resulting in lower flashover voltages [6], [7], although the plasma channel was shown to change location dependant on environmental conditions. As the humidity increased, it was shown that the permittivity had more of an effect on the flashover voltage for negative polarity, which is hypothesised as being due to the probability of surface flashover increasing with higher humidity, changing the location

of the plasma discharge towards the spacer surface, as each material was shown to decrease in comparison to an open-air gap. This will be further discussed in relation to comparison of the results to those for an open-air gap system, in Section 5.4.

Under positive polarity, however, the same effect was not observed. At <10% RH and ~50% RH, although the flashover voltages recorded were very similar for each material, no trend in relation to relative permittivity of material was apparent. The biggest difference was at >90% RH, with large differences in the flashover performance of each system, due to other factors such as the hydrophobicity and hydrophilicity of the materials in very high humidity environments. This behaviour is potentially due to different breakdown processes affecting the initiation and propagation of the discharge, including higher probability of bulk air breakdown, away from the surface of the spacer [1], [3], [8], at the higher humidity levels tested in this study, which was shown to be dependent on material properties; again, this behaviour will be discussed in Section 5.3.2.

5.3.2. Impulse Polarity

As discussed in Chapter IV, a polarity effect was evident throughout testing due to the asymmetric field distribution. From visual inspection, the plasma channel at breakdown was seen to initiate and terminate at different points in the electrode system, dependent upon the test parameters. The different test conditions resulted in two distinct flashover behaviours:

- a surface flashover, with the discharge coupled closely to the surface of the solid spacer.
- a flashover at the higher-field regions associated with the electrode edges, away from the surface of the solid spacer.

These two discharge path provides a potential reason for the differences between positive- and negative-polarity breakdown voltages, as the increase of humidity when a dielectric spacer bridges the electrodes can alters the discharge location. This behaviour was evident for specific sets of environmental conditions, at ~50% RH and >90% RH, where the potential increase of the conductivity in the vicinity of the surface

of the added dielectric spacer could cause breakdown to occur along the surface, rather than in air at the lower levels of <10% RH.

At <10% RH, the lack of moisture introduced into the system resulted in an asymmetric performance between positive and negative polarity. This resulted in the differences in breakdown voltage being higher for negative polarity for all materials at all pressures tested. It is hypothesised that this is due to the discharge having been initiated at the high-field regions of the system (electrode edges) for all three materials in the range of pressures tested. However, the increase in pressure was also shown to influence the symmetry between positive and negative flashover voltages as discussed in Section 4.4.1. An example of an electrode edge flashover is shown in Figure 5.13.

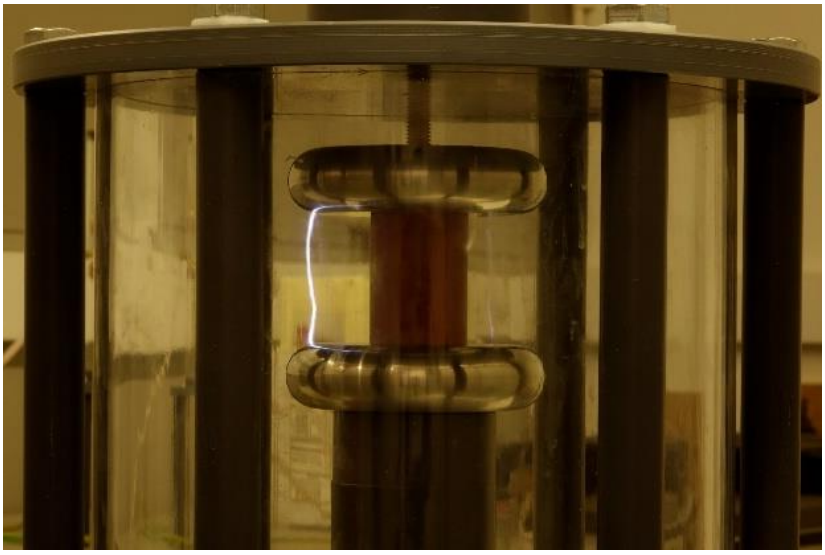

Figure 5.13 – Plasma channel location at rounded edge of electrode in a bulk air breakdown event with an Polyetherimide spacer at 0 bar gauge and <10% RH.

At >90% RH, negative streamers generally propagated along the surface of all spacer materials. This was also the case for positive streamers in HDPE, for other materials under positive energisation a bulk air breakdown were observed. The effect of this can be clearly seen, particularly in Figures 5.8, and 5.12, where the positive-polarity flashover voltages at >90% RH are higher than those for negative polarity, for Polyetherimide and Polyoxymethylene spacers. There is supporting evidence for this, as the flashover voltage was lower than that for an open-air gap for the same

environmental conditions, as discussed in Section 5.4.3. Therefore, the system can be viewed as being symmetrical when the solid spacer is formed from HDPE.

Another difference between positive and negative polarity is that, for positive polarity, the flashover voltage generally increased with increasing humidity, particularly from <10% RH to ~50% RH. Whereas, for negative polarity, the flashover voltages decreased with increasing RH. This can be attributed to the fact that humidity inhibits the inception and development of positive impulsive discharges but exerts minimal influence upon negative streamers [9].

Overall, the influence of RH on the breakdown voltage can be explained by the following phenomena. Firstly, differences in hydrophobicity and hydrophilicity of the materials can change the way that water accumulates on the surfaces of the different spacer materials, in a very high humid environment. When water droplets accumulate on an insulator surface, this can increase the electric field strength, [10]. For hydrophobic materials such as HDPE, the accumulation of water droplets on the surface can result in higher field enhancement of the electrical field strength in comparison to hydrophilic materials. This is particularly evident for negative polarity, where the flashover voltage in relation to the open-air gap decreases, giving evidence for propagating over the surface of the material. For Polyetherimide and Polyoxymethylene, the hydrophilic performance results in a smaller contact angle, but with the increased permittivity of the materials, for negative polarity also initiates the discharge to propagate over the material surface which also shows a decrease in comparison to open gap. For positive polarity, within the same high humid environment, the absorption of electrons which are important for the positive streamer development process is hindered by the increase in water droplet appearing on the spacer surface, which initiates the discharge at the electrode edges, for Polyetherimide and Polyoxymethylene. However, the hydrophobic performance of the HDPE spacer has enough of an effect on the electric field strength that the positive polarity discharge also propagates across the spacer surface. The increase in breakdown voltage with increasing RH could be due to the lesser amount of space charge generated under positive polarity at high humidity, where the increase of humidity inhibits the

inception and development of positive impulsive discharges but exerts minimal influence upon negative streamers [9]. There is experimental evidence, [11] – [13], that supports the notion that positive space charge diminishes with increasing humidity. Results reported in [14] also show a difference in corona inception voltages, with negative inception voltages being lower than positive, due to the effect of humidity. Additionally, it has been reported in [15] that positive breakdown voltages are hindered at high levels of RH, as photoionisation processes are important in the positive-streamer breakdown mechanism, where high-energy photons are absorbed by water molecules at high levels of relative humidity, [16], this effect results in an increase in the positive polarity breakdown voltage.

The presence of water molecules at higher levels of RH also increases the attachment coefficient of the air, due to the electronegative nature of the water molecules [17]. At higher pressures, the flashover voltages could be higher at ∼50% RH, due to the attachment coefficient increasing compared to that at <10% RH. Further increase of the humidity to >90% RH, however, will lead to a decrease in breakdown voltage from that at ∼50% RH, due to water droplets formed on the electrodes at >90% RH, creating high-field regions and decreasing the average breakdown voltage, as the disruptive discharge voltage becomes irregular [18]. It has also been shown, in [19], that the rate of increase of the attachment coefficient is considerably greater than that of the ionisation coefficient, as the partial pressure of water vapour is increased. In addition, the secondary ionisation coefficient was found to decrease with increasing water-vapour pressure [19]. In consequence, an increase in applied voltage is required to attain the same ionisation efficiency and affect breakdown.

Additionally, another potential reason for this performance is charge deposition from surface discharges accumulating on the surface of the solid spacer, culminating in an abundance of induced polarization charges, causing field distortions that can affect the avalanche process close to the spacer surface [8]. This could be attributed to the application of impulses that did not result in breakdown from the ‘step up’ process but contributed to an increase in surface charge. This is also seen in [20], where the surface charge has been shown to increase with the number of impulses the dielectric is subject to. In the present study, the negative-polarity breakdown voltages were found to decrease drastically at elevated (>90% RH) humidity levels. This results in a higher

positive-polarity flashover voltage compared to that for negative polarity, due to the initiation and termination points of the plasma channel during flashover. However, further work will be required in order to understand the charge accumulation on the spacer surface with increased humidity.

Differences in flashover behaviour were also evident when comparing spacer material. As the humidity was elevated to >90% RH, HDPE was found to have similar performance for both, positive and negative, polarity. This similar behaviour at >90% RH is thought to be due to the consistent discharge path for HDPE at each level of pressure, with all discharges emanating from the triple junction, irrespective of polarity. There is supporting evidence for this, as the flashover voltage was lower than that for an open-air gap for the same environmental conditions, as discussed in Section 5.4.3. Therefore, the system can be viewed as being symmetrical when the solid spacer is formed from HDPE. However, with Polyoxymethylene and Polyetherimide spacers, there is a clear polarity effect, correlating with observations on the discharge path changing as the humidity increases. This polarity effect for Polyetherimide and Polyoxymethylene is thought to be due to the fact that surface flashover was generally observed under elevated RH for negative polarity, whereas bulk breakdown of the humid air at >90% RH, away from the solid surface, was generally observed for positive polarity. This behaviour has been discussed in [1], [3], which show that positive impulsive discharges develop away from the surface of the insulating spacer.

The negative-polarity breakdown voltages were found to decrease drastically at elevated (>90% RH) humidity levels. This results in a higher positive-polarity flashover voltage compared to that for negative polarity, due to the initiation and termination points of the plasma channel during flashover. If a discharge is initiated at the insulator surface, all materials under negative polarity impulse and HDPE in positive polarity impulse, this decreases in comparison to an open-air gap as the humidity increases to >90% RH, water accumulates on the spacer surfaces, creating a more conductive surface over the length of the solid dielectric [21]. Therefore, the resistivity associated with the air-solid interface will decrease, as a conductive path has been established between HV and ground where the flashover voltage will decrease accordingly, this was confirmed by visual inspection during testing. For

discharges across the electrode edges, the performance will show similarities to the open gap performance.

Overall, the effect of RH on the flashover voltage can be discussed in the context of the negative polarity voltages presented in Section 5.2. With no solid spacer ('air'), the discharge is initiated from the high-field region at the electrode edges, as shown in Chapter IV. Comparing the results at >90% RH, there is a clear reduction in the average flashover voltage of the gap when bridged by a solid (HDPE, Polyoxymethylene or Polyetherimide) spacer, which can be correlated with an increased tendency for the discharge to propagate closer to the material surface. The effect is less for HDPE due to the hydrophobicity of the material, which increases the surface flashover voltage, as previously discussed. For positive polarity, where the flashover voltage of the open-air gap is similar to that with Polyoxymethylene and Polyetherimide spacers, corresponding to the propagation of the discharge through the bulk air during these tests. For HDPE, however, flashover is initiated at much lower voltages, suggesting a discharge path close to the surface of the solid. This was confirmed by visual inspection during testing. Effect of moisture absorbing electrons at the triple junction point with the shallow angles created by the water droplets on the surface of the material could be resultant of the discharges emanating across the electrode edge. Whereas for HDPE which is the most hydrophilic of the materials, creates sharp angles between the dielectric surface and air which has a direct effect on the electric field produced as shown in [10], which will overcome the absorption effect of the added humidity resulting in discharges being produced at the spacer surface.
The tendency for matching discharge processes between negative and positive polarity breakdown with HDPE under high humidity results in the symmetrical performance at >90% RH, where the maximum difference between negative- and positive-polarity breakdown voltages over the three pressures tested was 7 kV, at 0 bar gauge. When comparing this to Polyetherimide and Polyoxymethylene at >90% RH, the maximum difference between polarities were 65 kV and 68 kV, respectively, both at 0.5 bar gauge. The consistent occurrence of discharges at the surface of the HDPE spacer could be due to the larger contact angles of any droplets that form near the triple junction point (TJP) in the high humidity environment (>90% RH), as shown in Figure

3.6, creating a higher electric field at the spacer surface, and resulting in a surface flashover event.

5.3.3. Air Pressure

For all tested conditions at <10% RH, ~50% RH and >90% RH, increasing the pressure resulted in increased flashover voltage. As the gas pressure increases, the electron mean free path decreases, and the collision frequency increases. Electrons will gain less energy between collisions, which means that a higher applied field is required for free electrons to gain sufficient energy to cause an ionisation event [22].

5.4. COMPARISON BETWEEN OPEN GAP AND SMOOTH SPACERS

Throughout the testing phase with smooth (machined) spacers bridging the electrodes, the environment in the test cell influenced the discharge region and plasma channel location, which dictated the maximum holdoff voltages. In this section, at each relative humidity, volt-time graphs are presented, aiding the discussion on the relative performance of each insulation system. Comparison of the flashover voltages associated with the air-solid insulation systems with those for open gaps (Chapter IV) revealed some interesting cases when the flashover voltage of the air-solid insulation system was higher than that for an open-air gap.

The information used in this section in terms of numerical values is in Appendix 2.

5.4.1. <10% RH

When comparing the negative polarity results between air-solid and open gap arrangements, as the humidity is increased, the difference in breakdown voltage changes as the water content increases within the test-cell. Firstly, looking at direct comparisons between no spacer and with spacer tests at <10% RH, the magnitude of the breakdown/flashover voltage value is generally consistent for both.

Figures 5.14, 5.15 and 5.16 show the volt-time graphs for this data, where there are clear groupings of positive and negative data. These groupings illustrate the similar

behaviour of air-solid gaps and open-air gaps for each polarity. The numerical values associated with Figures 5.14, 5.15 and 5.16 are shown in Tables AP2c, AP2d and AP2e in Appendix 2.

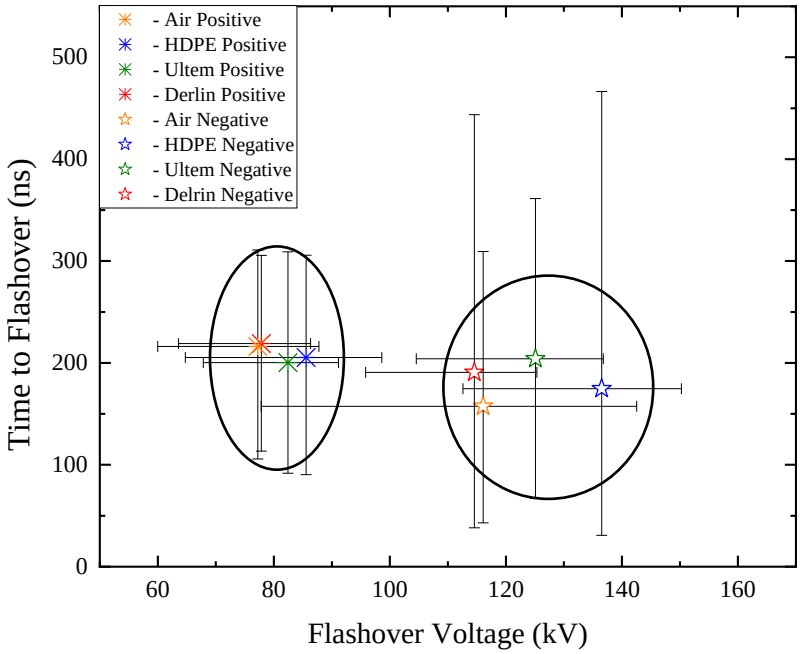

Figure 5.14 - Volt-time graphs for negative and positive polarity energisation, for open air, HDPE, Polyetherimide and Polyoxymethylene at <10% RH and -0.5 bar gauge.

From Figure 5.14, for all comparisons performed, there were overlapping error bars. This could be attributed to the plasma discharge location generally being at the electrode edges, due to the absence of a significant amount of water vapour to cause local increases in the electric field, in the low-humidity environment. Due to the discharge always initiating from the rounded electrode edge, the asymmetric polarity effect described in Chapter IV is evident for all insulation systems, with a difference in the positive and negative breakdown voltages in this environment. The change in the V_{50} flashover voltages of the air-solid insulation systems in comparison to an open gap (air) was +20.4 kV for HDPE, +9 kV for Polyetherimide and -1.5 kV for Polyoxymethylene for negative polarity; and +8.4 kV for HDPE, +5.2 kV for Polyetherimide and +0.7 kV for Polyoxymethylene for positive polarity.

As shown in Figure 5.14, there are two clear regions dictated by positive and negative polarity where overlapping error bars between air and HDPE, Polyetherimide and Polyoxymethylene show that the mechanisms are similar during the flashover process.

As there is a clear trend shown, this implies these insulation systems follow the same mechanisms as for an open gap system in Chapter IV.

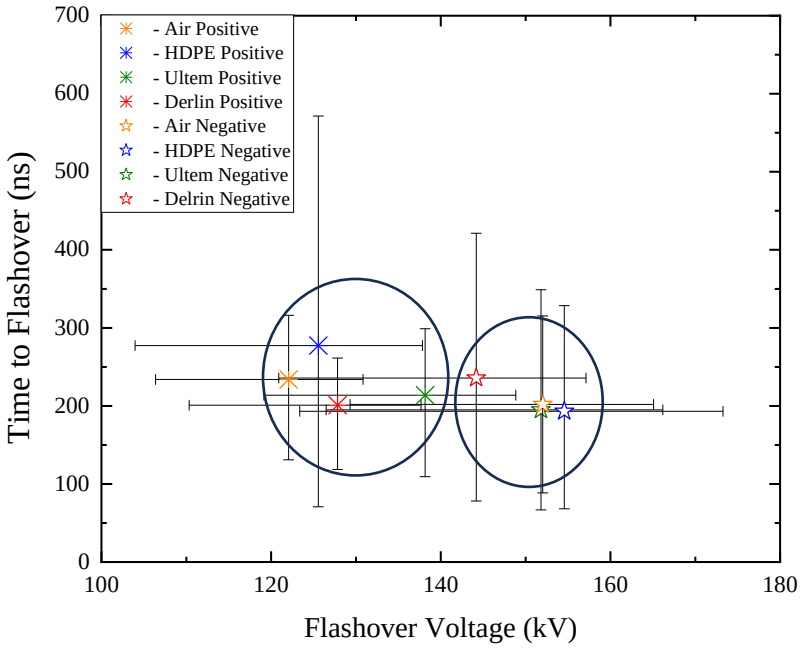

Figure 5.15 - Volt-time graphs of negative and positive polarity energisation, for open air, HDPE, Polyetherimide and Polyoxymethylene at <10% RH and 0 bar gauge.

From Figure 5.15, for all comparisons performed, there are overlapping error bars. This follows the same behaviour seen at -0.5 bar gauge. In Chapter IV, the increase in air pressure also resulted in a more symmetrical performance of the insulation system when discharges were initiated from the electrode edges, and this behaviour was also seen for the solid-bridged gaps in this environment. With the discharge always initiating from the electrode edge, the asymmetric polarity effect that is thoroughly described in Chapter IV was evident for all air-solid insulation systems. The differences in the V_{50} flashover values in comparison to those for open gap (air) were +2.6 kV for HDPE, -0.2 kV for Polyetherimide and -7.8 kV for Polyoxymethylene for negative polarity; and +3.5 kV for HDPE, +16.1 kV for Polyetherimide and, +5.7 kV for Polyoxymethylene for positive polarity.

Again, similar to the -0.5 bar gauge results, for 0 bar gauge in Figure 5.15, although the positive and negative flashover voltages have become closer, particularly when considering error bars, there are two distinct regions of positive and negative polarity data points. For negative polarity, the open-air gap breakdown voltage is similar to

that with spacers of HDPE, Polyetherimide, and Polyoxymethylene, suggesting a consistent breakdown mechanism, with breakdown generally occurring at the electrode edges. For positive polarity, an Polyetherimide spacer is shown to have a nominally higher flashover voltage in comparison to the open-air gap, but with overlapping error bars. As there is a clear trend shown, this implies these insulation systems follow the same breakdown mechanisms described for open gap systems in Chapter IV.

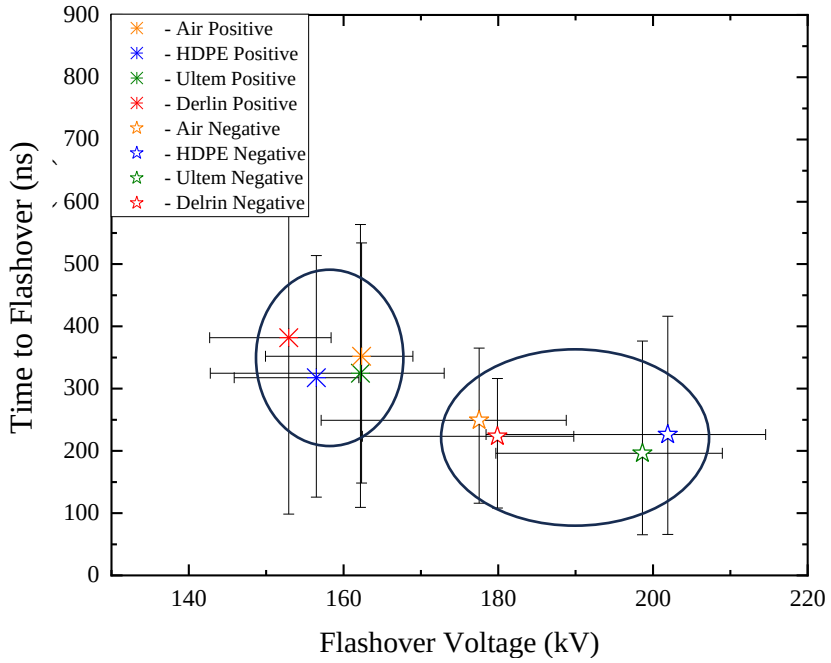

Figure 5.16 - Volt-time graphs of negative and positive polarity energisation, for open air, HDPE, Polyetherimide and Polyoxymethylene at <10% RH and 0.5 bar gauge.

From Table Figure 5.16, it can be seen that for all comparisons performed, there are overlapping error bars. This follows the same behaviour seen at the lower pressures, with the discharges generally occurring at the electrode edges due to the low amount of water vapour at <10% RH. The differences in the V_{50} flashover voltages for air-solid gaps in comparison to an open gap (air) were +24.4 kV for HDPE, +21.2 kV for Polyetherimide and +2.4 kV for Polyoxymethylene for negative polarity; and -5.8 kV for HDPE, -0.1 kV for Polyetherimide and, -9.6 kV for Polyoxymethylene for positive polarity.

For the 0.5 bar gauge results shown in Figure 5.16, again looking at positive and negative energisation separately, there is a clear correlation between the open-air gap

breakdown voltage and those with HDPE, Polyetherimide and Polyoxymethylene spacers. What is interesting, however, is that for HDPE and Polyetherimide for negative energisation, the nominal flashover voltages are seen to increase in comparison to the open gap result, however these results have overlapping error bars. As there is a clear trend shown, this implies these insulation systems follow the same mechanisms described for an open gap system in Chapter IV.

5.4.2. ~50% RH

Figures 5.17, 5.18 and 5.19 show the volt-time graphs from the ~50% RH results, where there are generally, as before at <10% RH, groupings for positive and negative discharges. The numerical values associated with Figures 5.17, 5.18 and 5.19 are shown in Tables AP2f, AP2g and AP2h in Appendix 2.

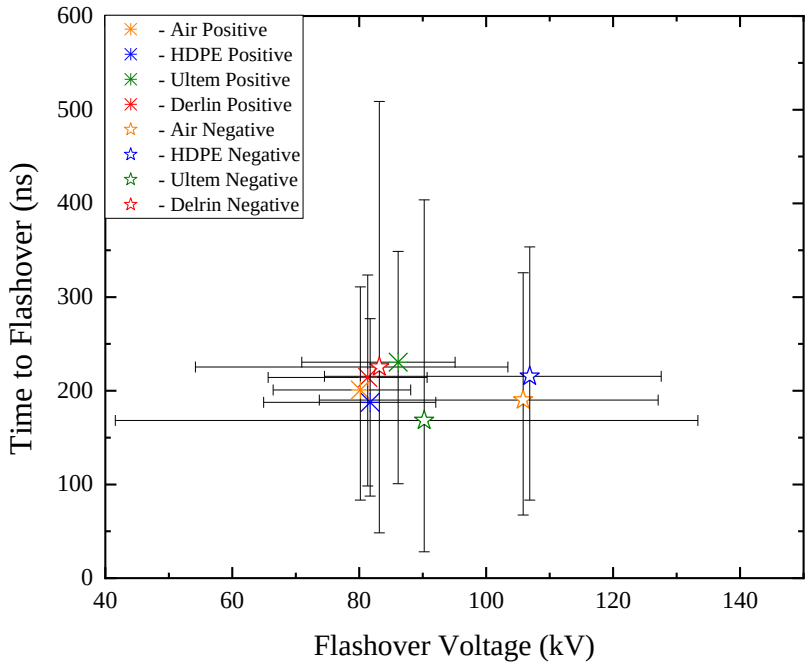

Figure 5.17 - Volt-time graphs of negative and positive polarity energisation, for open air, HDPE, Polyetherimide and Polyoxymethylene at ~50% RH and -0.5 bar gauge.

From Figure 5.17, it can be seen that for all comparisons performed, there are overlapping error bars. This follows the same trend seen at <10% RH, where the discharges tended to form at the electrode edges. As shown for open gaps in Chapter IV, increasing humidity resulted in a more symmetrical performance of the insulation system. Due to the increased moisture at ~50% RH, however, some discharges

initiated across the surface of the material, particularly for HDPE and Polyetherimide spacers, making the difference between the positive and negative V_{50} values wider than at <10% RH. In some instances, the V_{50} flashover voltage decreases in comparison to that for an open-air gap, with large error bars, implying that discharges also occurred at the insulator surface during the 20 flashovers in each data set. The difference in the V_{50} flashover values in comparison to an open gap (air) were +1.1 kV for HDPE, -15.6 kV for Polyetherimide and -22.6 kV for Polyoxymethylene for negative polarity; and +1.5 kV for HDPE, +5.9 kV for Polyetherimide and, +1.1 kV for Polyoxymethylene for positive polarity.

In comparing the open gap and solid-bridged insulation systems in Figure 5.17, when comparing the positive and negative results separately, the open gap breakdown voltage is similar for all materials under positive polarity, implying that the discharges are generally occurring over the electrode edges. However, for negative polarity, the presence of the Polyetherimide and Polyoxymethylene spacers is shown to decrease the holdoff voltage in comparison to that for an open-air gap, with the HDPE spacer resulting in a very similar V_{50} to that for the open-air gap. These decreases in the flashover voltage could be due to the increasingly humid environment in the test cell, creating a more conductive region in the vicinity of the spacer surface. As the HDPE spacer is more hydrophobic, this could result in any accumulation of moisture at the triple junction that occurs for the other materials being mitigated, with the moisture being able to move across the surface, which ultimately lowers the field at the triple junction, resulting in a higher breakdown voltage. The Polyetherimide and Polyoxymethylene spacers have hydrophilic surfaces, meaning that water droplets cannot readily move along the surface, which could cause a higher field at the triple junction, promoting surface flashover. This behaviour accounts for the large error bars for these tests, with the discharge initiation point changing between the electrode edge and flashover across the spacer surface as the humidity was increased, due to the hydrophilicity of the spacer in the increasingly humid environment, particularly for Polyetherimide.

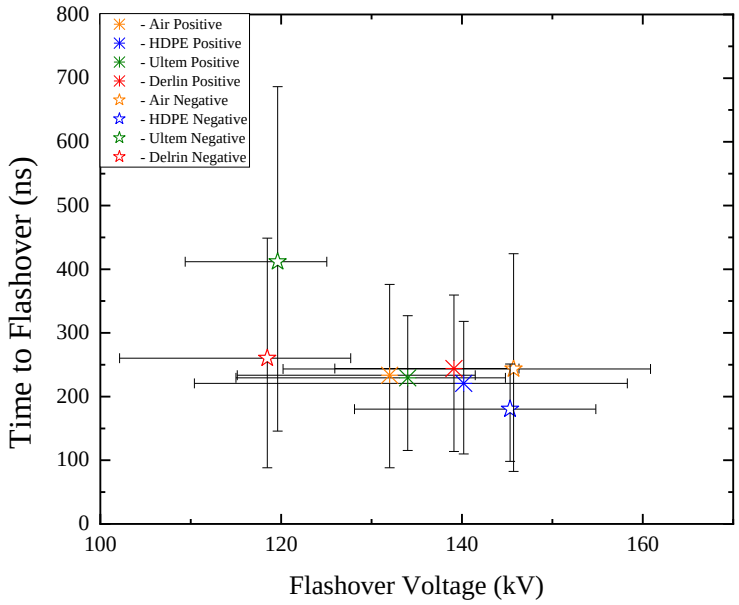

Figure 5.18. - Volt-time graphs of negative and positive polarity energisation, for open air, HDPE, Polyetherimide and Polyoxymethylene at ~50% RH and 0 bar gauge.

From Figure 5.18, for all compared tests, there are overlapping error bars. The difference in the V_{50} flashover values in comparison to those for an open gap (air) are -0.4 kV for HDPE, -26.1 kV for Polyetherimide and -27.2 kV for Polyoxymethylene for negative polarity; and +8.2 kV for HDPE, +2 kV for Polyetherimide and, +7.1 kV for Polyoxymethylene for positive polarity.

In comparing the open gap and solid-bridged insulation system results in Figure 5.18, as seen at -0.5 bar gauge (Figure 5.17), the positive polarity results reflect that the breakdown voltage of an open gap is very similar to those for air-solid insulation systems bridged with HDPE, Polyetherimide and Polyoxymethylene spacers, implying that the discharges are initiating across the rounded edge of the electrodes. However, for negative polarity, as seen at -0.5 bar gauge, there are two separate groupings. The V_{50} values with Polyetherimide and Polyoxymethylene surfaces are shown to decrease in comparison to that for the open gap, whereas with HDPE, V_{50} is similar to that for the open gap. This implies that there are different breakdown mechanisms which are causing the drop in flashover voltage for Polyetherimide and Polyoxymethylene spacers. The decrease in the flashover voltage could be due to the increasingly humid environment in the test cell, resulting in the occurrence of surface discharges for the more hydrophilic Polyetherimide and Polyoxymethylene surfaces.

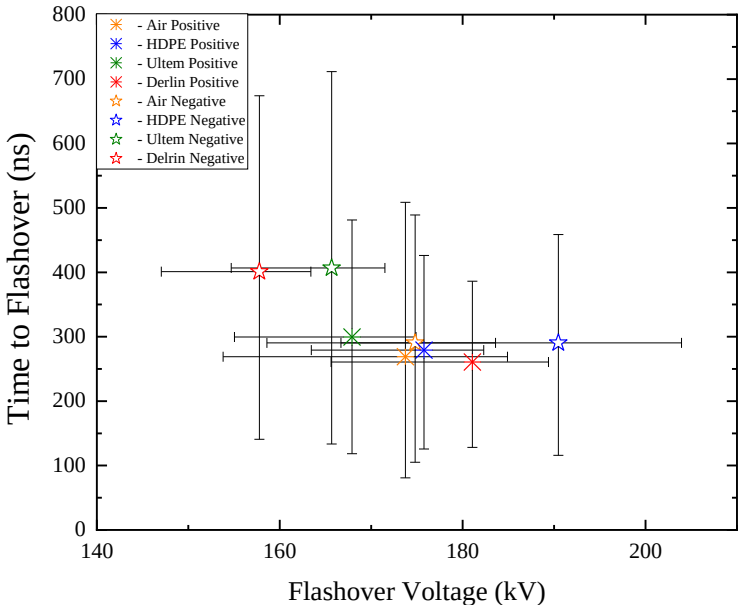

Figure 5.19. - Volt-time graphs of negative and positive polarity energisation, for open air, HDPE, Polyetherimide and Polyoxymethylene at ~50% RH and 0.5 bar gauge.

From Figure 5.19, it can be seen that for all compared cases, there are overlapping error bars. The results at 0.5 bar gauge follow the same trends seen at -0.5 bar gauge and 0 bar gauge, with discharges being initiated at the electrode edges. The differences in the V_{50} flashover values in comparison to those for an open gap (air) are +15.7 kV for HDPE, -9.1 kV for Polyetherimide and -17 kV for Polyoxymethylene for negative polarity; and +2.1 kV for HDPE, -6.2 kV for Polyetherimide and, +7.4 kV for Polyoxymethylene for positive polarity.

In comparing the open gap and solid-bridged insulation system data in Figure 5.19, as found at -0.5 and 0 bar gauge in Figures 5.17 and 5.18, the positive polarity results reflect that V_{50} for the open gap is very similar to those for gaps bridged by HDPE, Polyetherimide and Polyoxymethylene spacers, where discharges are generally initiating across the rounded electrode edges. For negative polarity, however, as was apparent at -0.5 bar gauge, the V_{50} values with Polyetherimide and Polyoxymethylene spacers nominally decrease in comparison to that for an open gap. This result implies that there are different breakdown mechanisms occurring with different spacer materials. The decrease in the flashover voltage with Polyetherimide and Polyoxymethylene spacers could be due to the synergistic effects of the increased moisture in the humid environment and of the increased pressure in the test cell, creating a more conductive surface on all spacer surfaces. With an HDPE spacer, V_{50}

is higher than that for the open-air gap, yielding the highest flashover voltage of all tests in this environment, however overlapping error bars are apparent between each distribution.

5.4.3. >90% RH

Figures 5.20, 5.21 and 5.22 show the volt-time graphs from the >90% RH results, where there is a clear decrease in breakdown voltage for both polarities, compared to those at <10% RH and ~50% RH. The decreasing V_{50} values in comparison to those for open air imply that the breakdown mechanism changes when a spacer is included in a high-humidity environment, with flashover across the surface occurring due to the increased conductivity in the vicinity of the spacer surfaces, which reduces the breakdown voltages compared to those where breakdown occurs at the electrode edges. The numerical values associated with Figures 5.20, 5.21 and 5.22 are shown in Tables AP2i, AP2j and AP2k in Appendix 2.

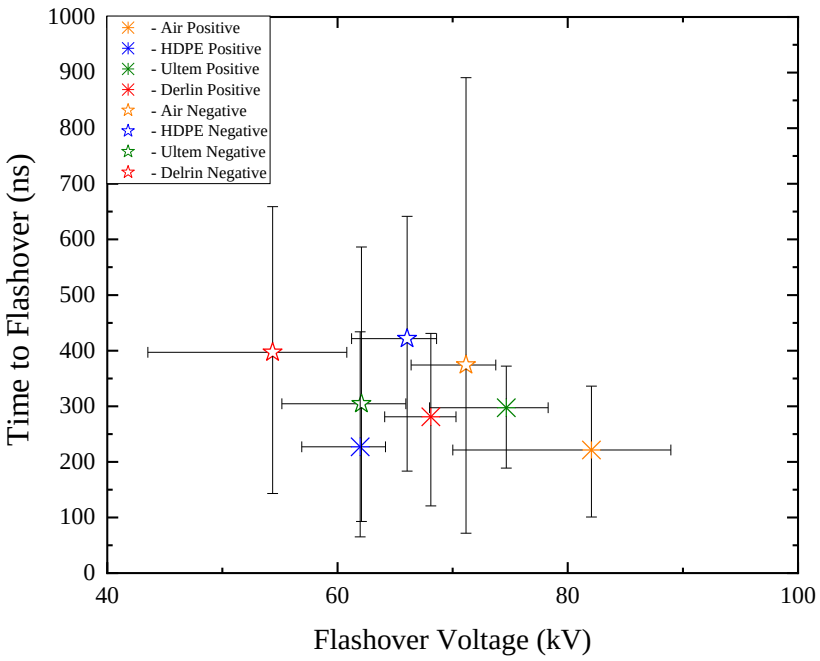

Figure 5.20 – Volt-time graphs of negative and positive polarity energisation, for open air, HDPE, Polyetherimide and Polyoxymethylene at >90% RH and -0.5 bar gauge.

From Figure 5.20, it can be seen that for negative polarity, there are overlapping error bars between the result for the HDPE spacer system and the open gap. For

Polyetherimide and Polyoxymethylene, however, V_{50} is lower than that for an open-air gap; further, the error bars do not overlap, signifying independence of each other to 95.4%. For positive polarity, however, the Polyetherimide and Polyoxymethylene spacers are shown to have overlapping error bars with the open-air gap, but the HDPE spacer is shown to decrease the breakdown voltage, to the point where their data sets are independent to ~95.4% spread. At >90% RH, the behaviour of the insulation systems was found to differ in comparison to at <10% RH and at ~50% RH, with the breakdown mechanism now being more consistent within a given test. This is supported by the shorter error bars characteristic of narrower distributions, which increase the probability that the error bars will not overlap when comparing tests. The change in the V_{50} flashover values in comparison to those for an open gap (air) were -5.2 kV for HDPE, -9.1 kV for Polyetherimide and -16.8 kV for Polyoxymethylene for negative polarity; and -20.1 kV for HDPE, -7.4 kV for Polyetherimide and, -14 kV for Polyoxymethylene for positive polarity.

In comparing the open gap and solid-bridged insulation system results in Figure 5.20, the positive polarity results show that the open gap has a higher breakdown voltage in comparison to that for gaps bridged by HDPE, Polyetherimide and Polyoxymethylene spacers. Also, the same behaviour is apparent for negative polarity, where the inclusion of a spacer made of HDPE, Polyetherimide or Polyoxymethylene results in a decrease in V_{50} in comparison to that of the open gap. This implies that there are different mechanisms for all spacers which are causing the drop in flashover voltage. These decreases in the flashover voltage could be due to the further increase of the humid environment up to >90% RH, creating a more conductive surface on all spacers.

For HDPE spacers, the similarity in the positive and negative breakdown voltages is hypothesised as being due to the initiation of the discharge channel at the triple junction, irrespective of polarity. As the water content is high in the humid environment, moisture accumulates on the surface of the spacer. Due to the hydrophobicity of HDPE, the contact angle of water droplets on the surface creates a high field region, [10], which results in propagation of the discharge channel over the spacer surface.

For Polyetherimide and Polyoxymethylene spacers, the positive breakdown voltage is hypothesised to be higher than the negative, as negative discharges initiate at the triple junction and propagate over the surface of the material, due to the increased conductivity of the wet spacer surface, while positive discharges initiate at the rounded electrode edges, and the discharge occurs away from the surface of the solids. The contact angles created by water droplets on the spacer surfaces are not severe enough (<90°) to initiate positive streamers at the sample surface, as the material is hydrophilic, coupled with absorption of the high energy photons important for photoionisation, [16], hinders the progress of positive streamers at the spacer surface. This leads to the discharge initiating and propagating over the electrode edges, increasing the positive polarity breakdown voltage compared to the negative. Another possible explanation for this result is due to charge deposition from surface discharges accumulating on the surface of the solid spacer, culminating in an abundance of induced polarization charges, causing field distortions that can affect the avalanche process close to the spacer surface, [8]. The increased humidity will also inhibit the accumulation of negative charge on the surface, leading to a higher probability of bulk air breakdown, away from the sample surface, for positive streamers. This was also discussed in Section 5.3.2.

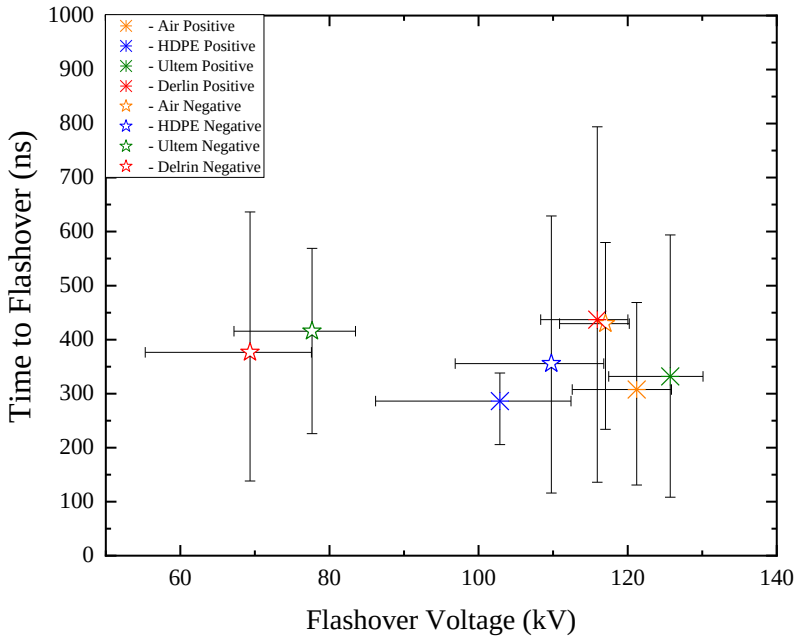

Figure 5.21 - Volt-time graphs of negative and positive polarity energisation, for open air, HDPE, Polyetherimide and Polyoxymethylene at >90% RH and 0 bar gauge.

Similar to at -0.5 bar gauge, it can be seen that for negative polarity, there are overlapping error bars between the distributions for an HDPE spacer system and an open gap. For Polyetherimide and Polyoxymethylene, however, V_{50} is reduced compared to that for the open-air gap, where the error bars between the distributions do not overlap, signifying independence of each other to 95.4%. For positive polarity, however, the Polyetherimide and Polyoxymethylene spacer are shown to have overlapping error bars with the open-air gap, but the HDPE spacer is shown to decrease the breakdown voltage to the point where their data sets are independent to ~95.4% spread. The changes in the V_{50} flashover values in comparison to those for an open gap (air) were -7.2 kV for HDPE, -39.3 kV for Polyetherimide and -47.6 kV for Polyoxymethylene for negative polarity; and -18.3 kV for HDPE, +4.5 kV for Polyetherimide and, -5.3 kV for Polyoxymethylene for positive polarity.

In comparing the data for the open gap and solid-bridged insulation systems in Figure 5.21, the positive polarity results show that the open gap has a similar breakdown voltage to that for the gaps bridged by Polyetherimide and Polyoxymethylene spacers, with the similar V_{50} values with overlapping error bars implying that the flashover mechanism is consistent, occurring at the rounded electrode edges. For HDPE, however, a significant decrease in V_{50} is seen compared to that for an open gap. For negative polarity, the inclusion of a spacer made from either HDPE, Polyetherimide or Polyoxymethylene results in a decreased V_{50} compared to that for the open gap; the flashover voltage is shown to greatly decrease with Polyetherimide and Polyoxymethylene spacers particularly, in the >90% RH environment.

Analysing the behaviour by material, for HDPE, the similarity in the positive and negative breakdown voltages is hypothesised to be due to the consistent initiation of discharges at the triple junction, resulting in the propagation of discharges over the surface of the solid. Due to the high aerosol content in the humid air, moisture accumulates on the surface of the spacer. Due to the hydrophobicity of HDPE, the contact angle creates a high field region which causes discharges to initiate at the triple junction, resulting in flashover of the spacer surface. The reason for the increased surface flashover voltage with HDPE at >90% RH in comparison to Polyoxymethylene and Polyetherimide is the hydrophobicity of the material, enabling the droplets to move under an applied electric field, therefore eliminating the high field

regions created and increasing the surface flashover voltage significantly. For Polyetherimide and Polyoxymethylene, similar to at -0.5 bar gauge, the similarity in the breakdown voltage is hypothesised as being due to the initiation of the plasma channel at the surface of the solid surface - as the water content is increased in the high-humidity environment, moisture accumulates on the surface of the spacer and due to the wettability of the material increasing, initiating surface flashover.

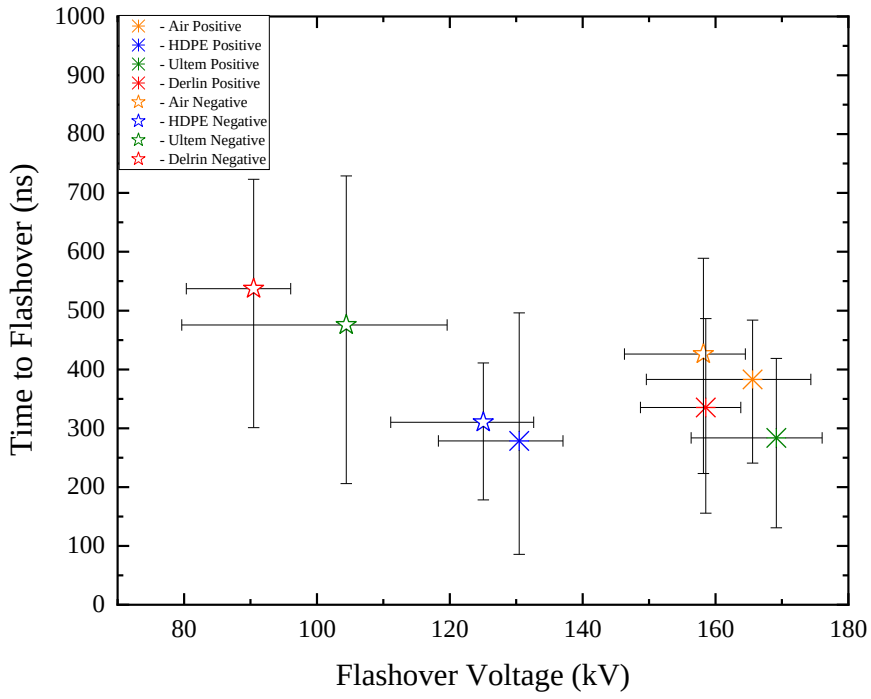

Figure 5.22 - Volt-time graphs of negative and positive polarity energisation, for open air, HDPE, Polyetherimide and Polyoxymethylene at >90% RH and 0.5 bar gauge.

From Figure 5.228, for each polarity, it can be seen that V_{50} for an open gap is higher than that for all solid-bridged insulation systems. For positive polarity, however, use of Polyetherimide or Polyoxymethylene spacers results in similar characteristics to that of the open-air gap, with overlapping error bars. The HDPE spacer is shown to result in a clear decrease in V_{50}, with the data sets being independent to ~95.4% spread.

The differences in the V_{50} flashover values in comparison to those for an open gap (air) were -33.1 kV for HDPE, -53.8 kV for Polyetherimide and -67.7 kV for Polyoxymethylene for negative polarity; and -35.1 kV for HDPE, +3.5 kV for Polyetherimide and, -7.1 kV for Polyoxymethylene for positive polarity.

In comparing the results for the open gap and solid-bridged insulation systems in Figure 5.22, similar to the results at 0 bar gauge, the positive polarity results show that gaps bridged by Polyetherimide and Polyoxymethylene spacers have similar V_{50} to that for the open gap, with the similar flashover voltage and overlapping error bars implying that flashover is occurring over the rounded electrode edges. For HDPE, however, a significant decrease in V_{50} was found in comparison to that for the open gap, consisted with discharges propagating along the surface of the material. For negative polarity, the HDPE, Polyetherimide and Polyoxymethylene spacers all resulted in a decreased V_{50} compared to the open gap result, with the flashover voltages particularly decreasing with Polyetherimide and Polyoxymethylene spacers.

5.5. SUMMARY

For tests in a <10% RH environment,

1. The best performance was exhibited by an HDPE spacer, for a negative polarity system over the three tested pressures. For positive polarity, an Polyetherimide spacer performed best. However, for both polarities, all materials performance similarly.
2. The breakdown channels were observed to initiate and propagate over the outside edges of the electrodes (away from the surface of the solid sample). At all pressures (-0.5, 0 and 0.5 bar gauge), it was found that the insulation systems bridged with a smooth (machined) HDPE, Polyetherimide or Polyoxymethylene spacer had similar behaviour to the ‘no spacer’ case, with the flashover voltages for each material being similar to those for the open gap.
3. With no other medium to significantly affect the field distribution in the gap, the plasma channel will likely initiate at the rounded electrode edges. Therefore, the permittivity of the material will have minimal effect on the flashover voltage of the insulation system, assuming that the triple junction point angle is not sufficient enough with the smooth machined surface spacers to enhance the local electric field (as shown from Figure 3.15).
4. This arrangement could be beneficial in system in long-term applications, where with the spacer being in a uniform field causes the discharge to occur

away from the spacer surface, which will thus not be directly affected by the plasma channel were failure to occur, maintaining the structural and electrical rigidity of the system.

For tests within a ~50% RH environment, it was found that –

1. The best performance was exhibited by an HDPE spacer, for a negative and positive polarity system over the three tested pressures. However, for both polarities, all material performance similarly.
2. The breakdown channels were generally observed to initiate and propagate over the outside edges of the electrodes (away from the surface of the solid sample). At all pressures (-0.5, 0 and 0.5 bar gauge), it was found that the insulation systems bridged with a smooth (machined) HDPE, Polyetherimide and Polyoxymethylene spacers had similar behaviour to the 'no spacer' case, with the flashover voltages for each material being similar to those for the open gap. However, the effect of humidity is shown to start to have an effect with the slight decrease in breakdown voltage with Polyetherimide and Polyoxymethylene spacer in negative polarity operation, with overlapping error bars.
3. With the increase of humidity within the gap, the plasma channel will likely initiate at the rounded electrode edges. However, with the higher humidity added, the probability of a surface flashover will increase, which may result in the permittivity of the materials having more of an impact on the flashover voltage of the insulation system than at <10% RH.

For tests at >90% RH, analysing the behaviour by material,

1. The best performance was exhibited by an HDPE spacer, for a negative polarity system over the three tested pressures. For positive polarity, an Polyetherimide spacer performed best.
2. The breakdown channels were observed to initiate and propagate either over the surface of the insulator or the outside edges of the electrodes (away from the surface of the solid sample), dependent upon the spacer material. Discharges propagating over the spacer for all materials in negative polarity, and across the surface for HDPE in positive polarity only.

3. For HDPE, the similarity in the positive and negative breakdown voltages, and the decrease in relation to the open-air gap results is hypothesised as being due to the consistent initiation of the discharge at the triple junction, and subsequent propagation over the surface of the solid spacer.
4. For Polyetherimide, the decrease in the flashover voltage in comparison to the open gap results for negative polarity implies the high humidity resulted in a surface flashover event. For positive polarity, the similarity between the flashover voltage and the breakdown voltage of the open-air gap implies a flashover over the outer edge of the electrodes.
5. Similarly, for Polyoxymethylene, the decrease in the flashover voltage in comparison to the open gap result for negative polarity implies the high humidity resulted in a surface flashover event. For positive polarity, the similarity between the flashover voltage and the breakdown voltage of the open-air gap implies a flashover over the outer edge of the electrodes.

5.6. CONCLUSIONS

The breakdown characteristics of gaps bridged by solids made of three different materials have been compared with those for open air gaps from Chapter IV. Following from the results outlined in sections 5.2.1, 5.2.2 and 5.2.3, the physical and environmental parameters have been discussed and explained, using hypotheses, visual confirmations and information gathered from previous literature on the subject.

Overall, this chapter will provide high-voltage system and component designers with practical information on typical processes and mechanisms which govern the flashover process of cylindrical smooth insulators in quasi-uniform pulsed power insulation systems, for use under varying environmental conditions.

5.7. CHAPTER V REFERENCES

[1] L. Lazaridis and P. Mikropoulos, ‘‘Positive impulse flashover along smooth cylindrical insulating surfaces under variable humidity,’’ IEEE Trans. Dielectr. Electr. Insul., vol. 18, no. 3, pp. 745–754, Jun. 2011.

[2] J. T. Krile, A. A. Neuber, J. C. Dickens, and H. G. Krompholz, ‘‘DC flashover of a dielectric surface in atmospheric conditions,’’ IEEE Trans. Plasma Sci., vol. 32, no. 5, pp. 1828–1834, Oct. 2004.

[3] L. Gao, ‘‘Comparison of long sparks in air and over an insulator surface,’’ in Proc. 11th Int. Symp. High-Voltage Eng. (ISH), London, U.K., 1999, pp. 31–34.

[4] H. Niu and T. Xu, ‘‘The relevance between dramatic declines of air gap breakdown voltage and fog-haze weather,’’ in Proc. IEEE Region Conf. (TENCON), Nov. 2015, pp. 1–4.

[5] T. S. Sudarshan and R. A. Dougal, ‘‘Mechanisms of surface flashover along solid dielectrics in compressed gases: A review,’’ IEEE Trans. Electr. Insul., vol. EI-21, no. 5, pp. 727–746, Oct. 1986

[6] N. Matsuoka, Y. Fuchi, M. Kozako, and M. Hikita, ‘‘Effect of permittivity variation on surface flashover of GIS epoxy spacer model in SF6 gas,’’ in Proc. IEEE Int. Conf. Dielectr. (ICD), Montpellier, France, Jul. 2016,pp. 96–99.

[7] D. L. Schweickart, H. Kirkici, L. C. Walko, and W. G. Dunbar, ‘‘Insulation and dielectric breakdown design considerations in sub-atmospheric environments,’’ in Proc. 16th IEEE Int. Pulsed Power Conf., Albuquerque, NM,USA, Jun. 2007, pp. 1661–1664.

[8] I. Gallimberti, G. Marchesi, and L. Niemeyer, ‘‘Streamer corona at an insulator surface,’’ in Proc. 7th Int. Symp. HV Eng., Dresden, Germany, 1991, Paper 41.10.

[9] D. E. Gourgoulis, P. N. Mikropoulos, C. A. Stassinopoulos, and C. G. Yakinthos, ‘‘Effects of negative DC pre-stressing on positive impulse breakdown characteristics of conductor-rod gaps,’’ IEE Proc. Sci., Meas. Technol., vol. 152, no. 4, pp. 155–160, Jul. 2005.

[10] Guan, L. Wang, B. Yang, X. Liang, and Z. Li, ‘‘Electric field analysis of water drop corona,’’ IEEE Trans. Power Del., vol. 20, no. 2, pp. 964–969,Apr. 2005, doi: 10.1109/TPWRD.2004.837672.

[11] A. J. Davies, J. Dutton, R. Turri, and R. T. Waters, ‘‘The effect of humidity on space charge growth in short air gaps,’’ in Proc. 5th Int. Symp. Gaseous Dielectr., Knoxville, TN, USA, vol. 58, 1987, pp. 249–254.

[12] N. L. Allen and G. Dring, ‘‘Effect of humidity on the properties of corona in a rod—Plane gap under positive impulse voltages,’’ Proc. R. Soc. Lond. A, Math. Phys. Eng. Sci., vol. 396, no. 1811, pp. 281–295, 1984.

[13] L. R. Group, ‘‘Positive discharges in long air gaps,’’ Electra, vol. 53, p. 97, 1977.

[14] T. Kondo, R. Ozaki, and K. Kadowaki, ‘‘Effect of superposed repetitive pulses onto DC voltage on discharge extension into fog water produced by electrospray,’’ in Proc. Int. Symp. Electr. Insulating Mater. (ISEIM), Toyohashi, Japan, Sep. 2017, pp. 390–393.

[15] A Yu Starikovskiy, E M Bazelyan and N L Aleksandrov “The influence of humidity on positive streamer propagation in long air gap” *Plasma Sources Science and Technology*, Volume 31, Number 11, 2022

[16] Alexandra Brisset, Pierre Tardiveau, Kristaq Gazeli, Blandine Bournonville, Pascal Jeanney, et al..”Experimental study of the effect of water vapor on dynamics of a high electric field non-equilibrium diffuse discharge in air”. *Journal of Physics D: Applied Physics*, 2021

[16] E. Kuffel, ‘‘Influence of humidity on the breakdown voltage of sphere-gaps and uniform-field gaps,’’ in Proc. IEE A, Power Eng., vol. 108, no. 40, pp. 295–301, Aug. 1961.

[17] High-Voltage Test Techniques—Part 1: General Definitions and Test Requirements, document EN 60060-1:2010.

[18] E. Kuffel, ‘‘Electron attachment coefficients in oxygen, dry air, humid air and water vapour,’’ Proc. Phys. Soc., vol. 74, p. 297, Sep. 1959.

[19] J. Deng, S. Matsuoka, A. Kumada, and K. Hidaka, ‘‘The influence of residual charge on surface discharge propagation,’’ J. Phys. D, Appl. Phys., vol. 43, no. 49, 2010, Art. no. 495203.

[20] R. K. Raiput, A Textbook PF Electrical Engineering Materials, vol. 171. Laxmi Publications Pvt Limited, 2004.

[21] L. G. Christophorou and L. A. Pinnaduwage, ‘‘Basic physics of gaseous dielectrics,’’ IEEE Trans. Electr. Insul., vol. 25, no. 1, pp. 55–74, Feb. 1990

6. CHAPTER VI

KNURLED SURFACE DIELECTRIC FLASHOVER

6.1. INTRODUCTION

A way in which the flashover voltage of a gas-solid insulation system can potentially be increased is to modify the surface finish. In Chapter VI, spacers made from the same materials as in Chapter V have been subjected to a knurling process and tested under the same conditions. Comparison of the results will enable the most suitable insulation system to be identified for different operating regimes (polarity and environmental conditions).

In addition to the surface modification discussed in Section 2.6.3.2, Characterising the effect of the introduction of modifications to spacer surfaces, whether achieved by simple roughening of the surface using sandpaper in 1980, [1], or via a more intricate PIII processing system in 2020, [2], has been an engineering challenge for many years, with designers attempting to increase the hold-off voltages of their insulation systems by means other than simply increasing the length of the spacer. Another common method of increasing the hold-off voltage is to modify the insulator geometry, to increase the path length that the discharge channel must traverse during the flashover process [3-8].

In this chapter, a novel 'knurling' method was implemented, to modify the surface of the insulator with set ~0.5 mm indentations across the spacer surface, as outline in Section 3.4.3.2. This manufacturing process provided a quick, consistent way of modifying a dielectric surface, with a view to increasing the flashover voltage.

Previous work on roughened/manipulated dielectric surfaces is detailed in [9]. The authors investigated the effect of modifying a dielectric surface using a sandblasting method, yielding surface roughness in the range 5 – 10 μm, within a SF_6/N_2 environment, under DC voltage. The authors found that, with an increasing surface roughness, the flashover voltage was increased by up to 13.3% for positive applied voltage, and by up to 24.7% for negative voltage. The authors proposed that higher

levels of surface roughness resulted in reduced probability of secondary electron emission, and higher breakdown voltage.

A study of the effect of the surface roughness of solid support insulators in an SF_6 environment was published in [10]. The barrel-shaped support insulators, made of epoxy resin with embedded copper connectors on both sides, were placed in a rod-plane electrode system, with the HV rod in contact with the upper connector, and the lower connector resting on the grounded metal plane. Lightning impulse flashover tests were conducted on insulators with varying surface roughness, and with varying gas pressure in the test cell. A decrease in the flashover voltage with an increase in the average surface roughness, R_a, was observed: the flashover voltage was highest for new, untreated, samples with R_a ~0.1 μm; however, as R_a was increased from ~0.1 μm to ~1.4 μm (for samples treated with sandpaper), the flashover voltage decreased by ~2% under positive polarity and by ~6% under negative polarity.

The authors of [11], show the effect of micro-profiling the shed on a Polyoxymethylene surface in atmospheric air, where the authors recorded increases in positive polarity flashover voltage in comparison to negative polarity flashover voltages by up to 26.5kV. Images captured using a high-speed camera showed that the progress of positive discharges was stopped by the modifications to the insulator surface, while negative discharges were not as affected by the modified surface. The related breakdown mechanisms are illustrated in Figures 6.1 and 6.2, adapted from [12], where the ‘corner effect’ on streamer propagation was introduced to explain the electric field decrease across the spacer surface.

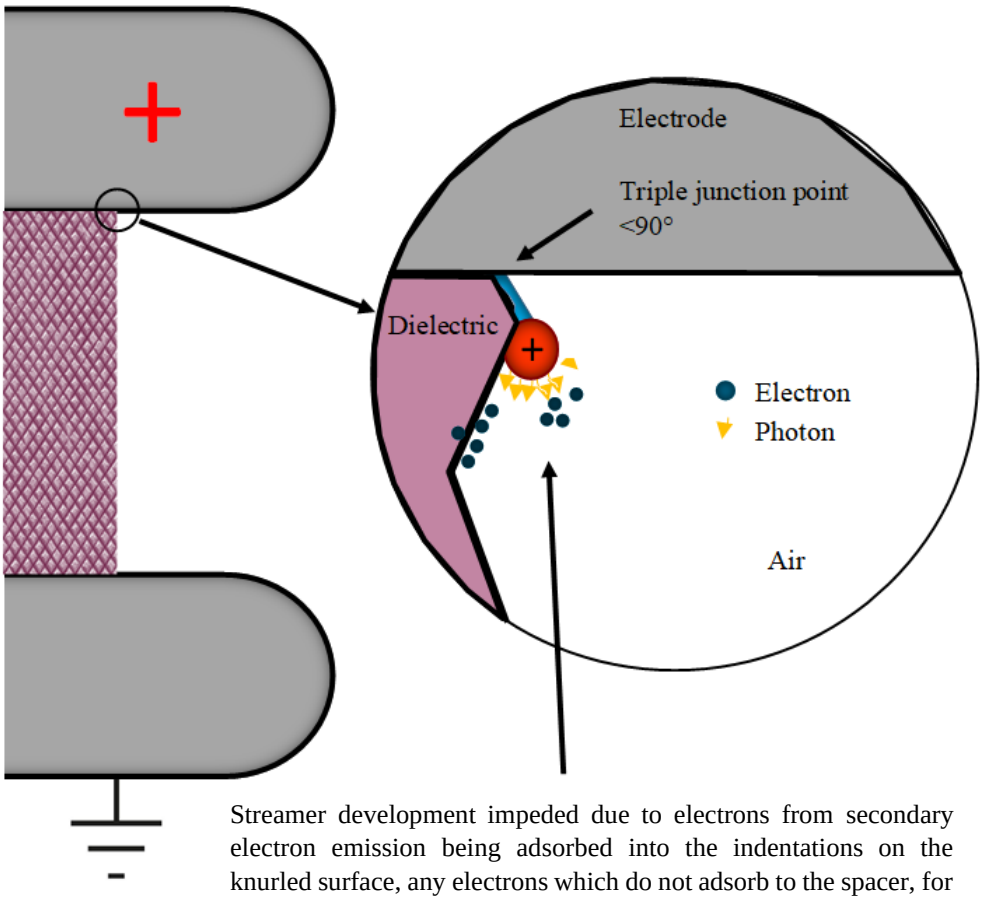

Streamer development impeded due to electrons from secondary electron emission being adsorbed into the indentations on the knurled surface, any electrons which do not adsorb to the spacer, for example those created by photoionisation, will expand the streamer head which will further weaken the field requiring a higher applied voltage to initiate a full surface flashover.

Figure 6.1. - Illustration and explanation of positive streamer development across a knurled surface.

As the positive streamer traverses the spacer surface, electrons gather at the indentations of the knurled surface due to secondary electron emission (SEE), and electrons are also produced in the gas by photoionisation at the streamer head. Due to these two simultaneous electron generation mechanisms, the streamer head expands, which results in a reduction in the field at the streamer head. This effect, along with the mitigation of free electrons by the knurled spacer surface, further weakens the field, as positive streamers need free electrons in the region of the spacer head for the field to be sufficient to allow the streamer to traverse the full length of the spacer surface. For this to happen, the applied voltage must be greater to overcome these field-reducing processes and leads to complete flashover of the insulator surface.

The discharge initiation process under negative energisation is illustrated in Figure 6.2. The negative flashover process is different from the positive, with the negative

streamer itself being a source of free electrons, removing the requirement of electrons at the streamer head to allow propagation across the spacer surface. Therefore, the field-reducing effects discussed in relation to Figure 6.1 have little consequence on the negative streamer formation, which can traverse the spacer at lower applied fields than those required for a positive streamer.

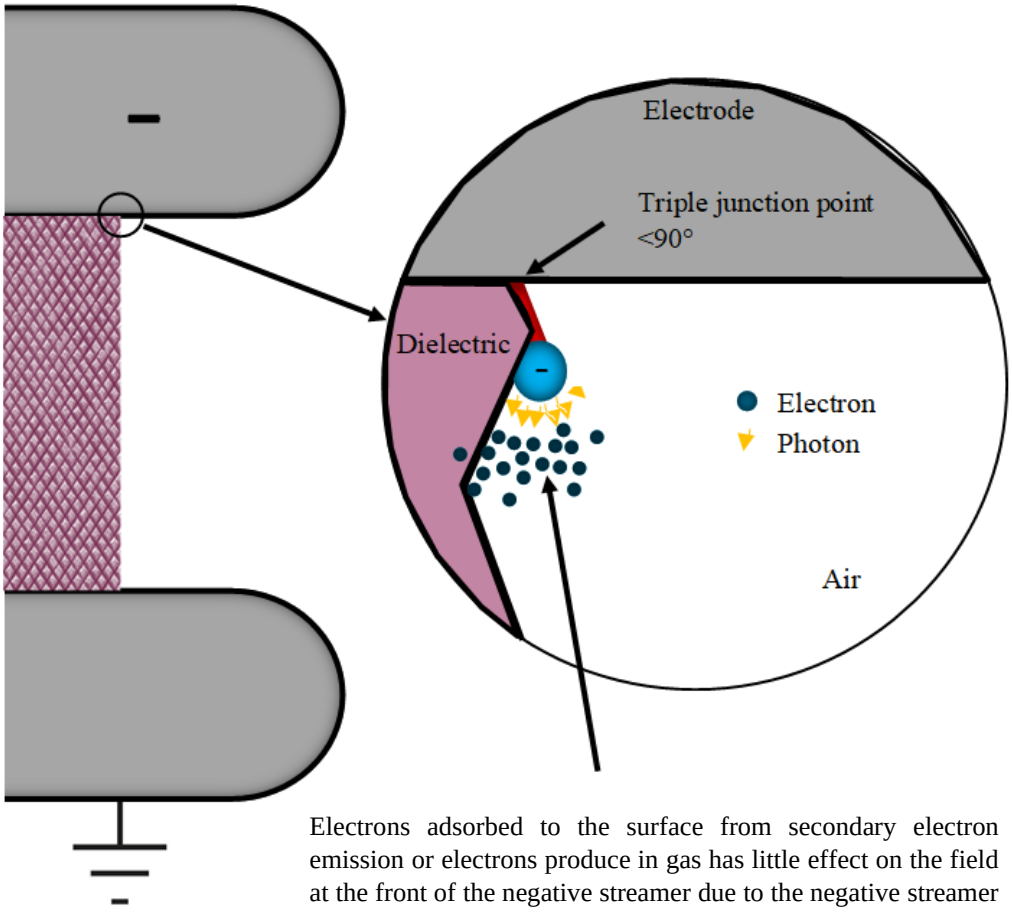

Electrons adsorbed to the surface from secondary electron emission or electrons produce in gas has little effect on the field at the front of the negative streamer due to the negative streamer head being a source of electrons.

Figure 6.2 - Illustration and explanation of negative streamer development across a knurled surface.

Considering the breakdown voltages of spacers with knurled surfaces, it is clear that the breakdown behaviour is different to that for smooth (machined) surfaces. This change can be attributed to differences in the discharge location, indicating that the difference in the positive and negative breakdown voltages is controlled mainly by the gas pressure and by the surface of the spacer. For knurled spacers, the discharge path tended to be across the sample surface, where the modification of the spacer surface

affects the angle between the spacer material and the surrounding air dielectric, which causes small TJP angles.

The authors of [13] detail the effect of the inclusion of surface deviations with larger dimensions, where different spacer geometries are proposed in an SF_6 environment, rather than subjecting the surfaces of cylindrical spacers to a roughening process. The authors concluded that the shape of spacer used in their study (cylindrical, concave and umbrella-shaped) largely affects the flashover process due to variation in the level of accumulated charge which is deposited on the spacer surface. Additionally, for surface deviations with larger dimensions in compressed air, a review can be found in [14], wherein different shapes of insulating spacers have been proposed.

In this chapter, a combination of these surface modification processes is adopted to the spacer surface, adding surface 'roughness' via a knurling manufacturing process. Cylindrical insulating spacers, in the form of rods 40 mm in length and 30 mm in diameter, were produced with a novel 'knurled' insulator surface finish (see Figure 3.9), to enable comparison with the breakdown behaviour of samples with a smooth (machined) insulator surface finish. The knurled surface finish consists of diamond-shaped indentations, machined on to the surface of the materials.

Again, as in Chapter V, the materials which will be tested in this chapter are as follows –

- HDPE (High Density Polyethylene)
- Polyetherimide (Ultem)
- Polyoxymethylene (Delrin)

Consistent with the approach in Chapters IV and V, the insulation systems were subject to changing environmental conditions of <10% RH, ~50% RH and >90% RH, and pressures of -0.5 bar gauge, 0 bar gauge and 0.5 bar gauge. Each insulation system was subjected to a 100/700 ns impulse voltage of both positive and negative polarity using the step-up testing procedure to determine the breakdown/flashover voltage for each insulation system.

As before and for ease of comparison, the results in this section will be shown in a bar graph arrangement, where each bar shows the average breakdown voltage from 20 tests at each combination of polarity and environmental conditions, following the 'step up' testing standard from ASTM D3426-97 which is explained in Section 3.6.4. The error bars characterise where ~95.4% of the spread of data lies to find the independency of each data set.

Overall, the results presented in this chapter will provide designers of pulsed-power systems and components with comparative data regarding -

- Which material will provide the highest flashover/breakdown voltage under various environmental conditions.
- Dependent upon material properties, how the discharge channel interacts with the spacer surface with changing humidity, pressure, permittivity, and polarity.
- How the breakdown characteristics of each of the air-solid insulation systems compares to the open-air gaps tested in Chapter IV.
- How each of the air-solid insulation systems, with knurled solid surfaces, performs in comparison to the equivalent smooth (machined) surface (Chapter V).

As previous literature has informed, the effect of multiple environmental parameters has an effect on the flashover voltage of a system, this will be discussed in terms of environmental parameters in Section 6.3 and in Section 6.4, how this compares to the open gap analysis shown in Chapter IV when comparing this to the smooth machined surfaces discussed in Chapter V.

6.2. EXPERIMENTAL RESULTS

The breakdown voltage and time results are presented here, separated by relative humidity, which, of the varying environmental parameters, resulted in the widest change in the observed behaviours.

The experimental results have been subjected to a 2-parameter Weibull statistical analysis, with α and β values extracted, and V_{50} and associated deviation (error bars

defining the spread of 95.4% of the data) determined from the cumulative distribution function (CDF) for each data set.

6.2.1. High Density Polyethylene (HDPE)

This section shows the results of the HDPE flashover voltages for knurled cylindrical spacers under the various combinations of test conditions.

Shown in Figures 6.3, 6.4 and 6.5 are Weibull plots of the data for electrodes bridged by knurled HDPE spacers at the three pressures considered.

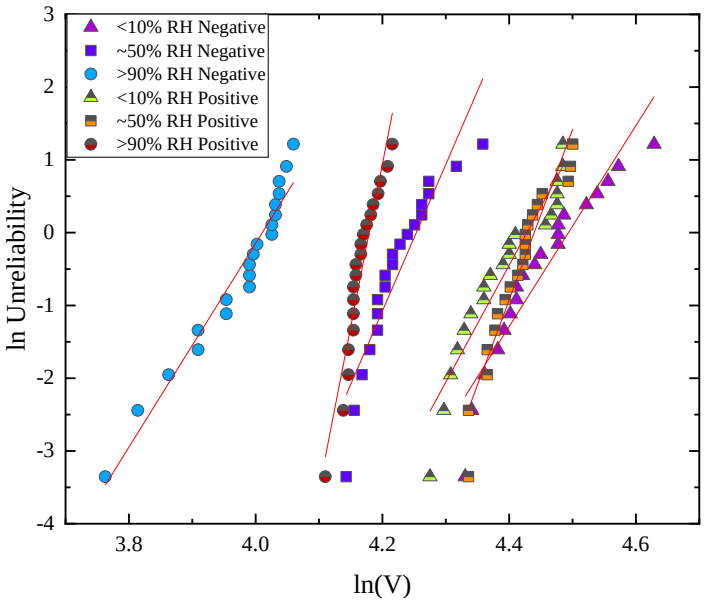

Figure 6.3. Weibull plots and curve fits of breakdown voltage data for knurled HDPE surfaces at <10% RH, ~50% RH and >90% RH, all at -0.5 bar gauge.

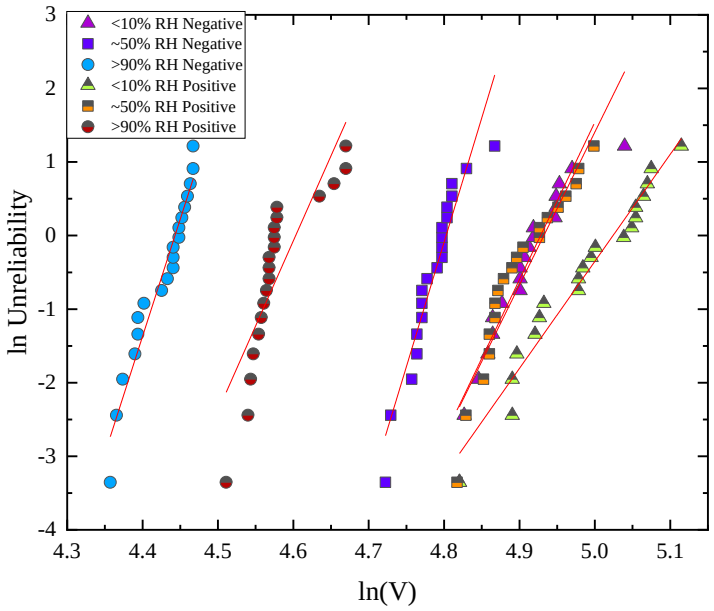

Figure 6.4. Weibull plots and curve fits of breakdown voltage data for knurled HDPE surfaces at <10% RH, ~50% RH and >90% RH, all at 0 bar gauge.

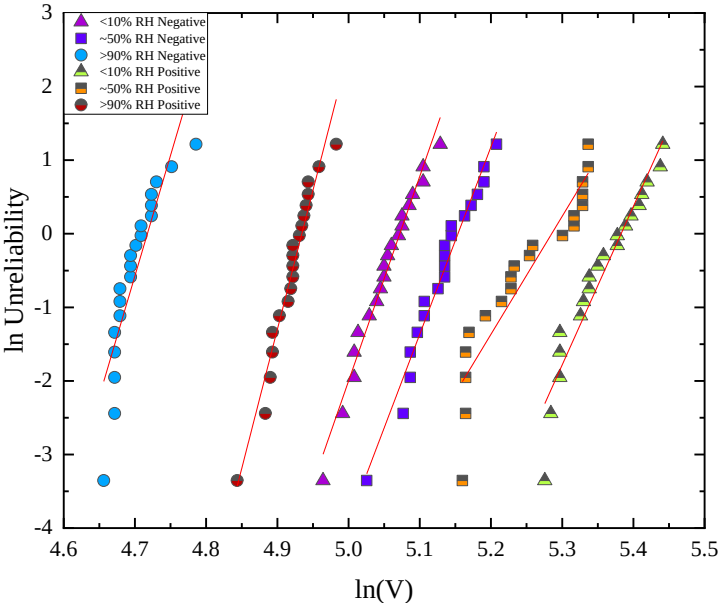

Figure 6.5. Weibull plots and curve fits of breakdown voltage data for knurled HDPE surfaces at <10% RH, ~50% RH and >90% RH, all at 0.5 bar gauge.

Analysing the Weibull distributions in Figure 6.3, 6.4 and 6.5, the V_{50} breakdown voltages and the spread (error bars) are shown in Figure 6.6a, 6.6b and 6.6c. Each bar represents the V_{50} from 20 impulsive breakdown voltages, and the error bars represent the 95.4% spread of the data.

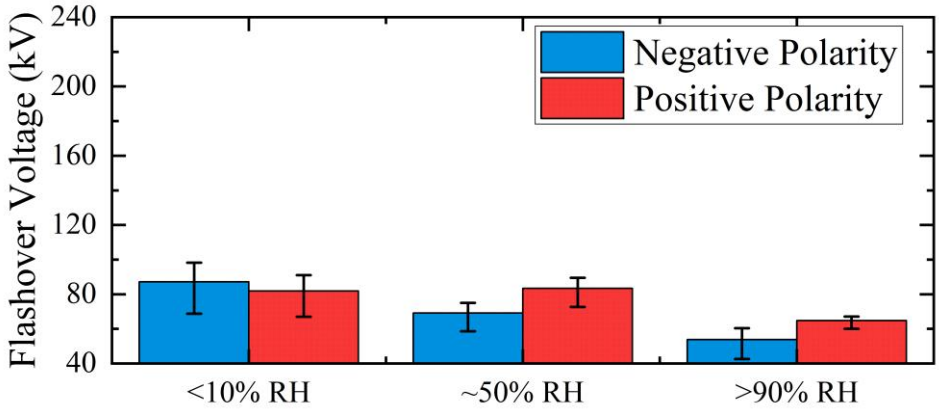

(a)

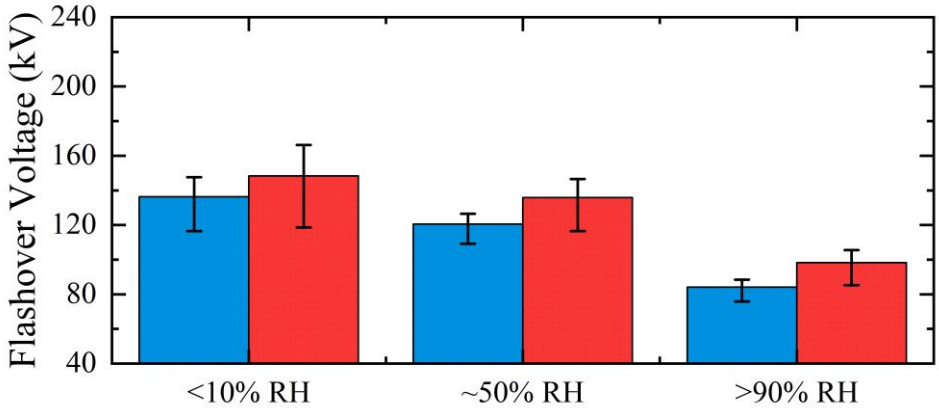

(b)

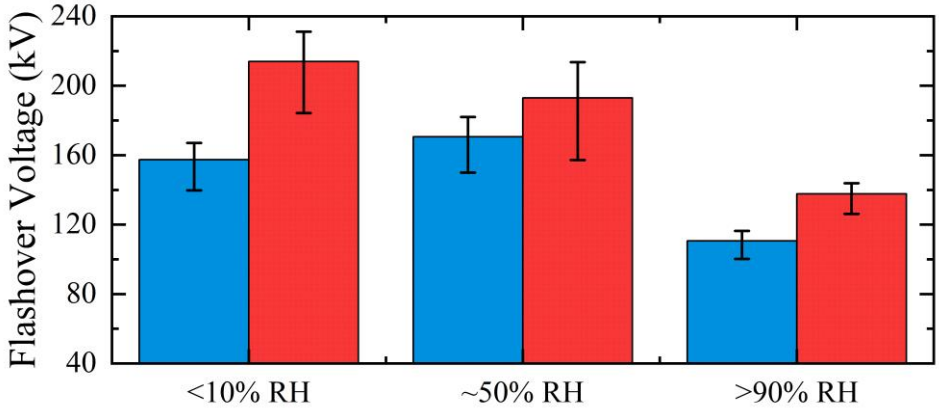

(c)

Figure 6.6. - Flashover voltages of pulsed power insulation system with a knurled Polyetherimide spacer at <10% RH, ~50% RH and >90% RH under negative and positive polarity impulse voltages, all at (a)-0.5 bar gauge, (b) 0 bar gauge and (c) 0.5 bar gauge. Each bar represents the average of 20 breakdown voltages and the errors bars show the 95.4% of the spread of data of each data set.

Figure 6.6a shows the HDPE insulation system results for changing humidity and polarity at -0.5 bar gauge. As the humidity increases, there is a clear downward trend in the negative-polarity flashover voltage. For positive polarity, however, as the humidity is increased from <10% RH to ~50% RH, the V_{50} flashover voltage is seen to marginally increase, with overlapping error bars. As the humidity increases to >90% RH, there is a clear decrease in the positive-polarity breakdown voltage. At <10% RH, the positive and negative polarity breakdown voltages are similar. The V_{50} value is higher for negative polarity, but with overlapping error bars with the positive result. At ~50% RH, the positive V_{50} is greater than the negative, but the distributions again have overlapping error bars. At >90% RH, the same general behaviour is apparent as at ~50% RH, with the positive V_{50} being higher than the negative. The maximum V_{50} with a knurled HDPE spacer at -0.5 bar gauge was for negative polarity at <10% RH, being ~87 kV, while the minimum V_{50} of 55 kV also occurred under negative polarity, but in a >90% RH environment.

Figure 6.6b shows the HDPE insulation system results for changing humidity and polarity at 0 bar gauge. There are clear downward trends in V_{50} for both negative and positive polarity. At each level of RH, the positive V_{50} is higher than the negative, with overlapping error bars in each case. The maximum V_{50} value with a knurled HDPE spacer at 0 bar gauge was under positive polarity at <10% RH, with a flashover voltage of ~135 kV, while the minimum V_{50} of ~85 kV occurred under negative polarity, but in a >90% RH environment.

Figure 6.6c shows the HDPE insulation system results for changing humidity and polarity at 0.5 bar gauge. As the humidity increases, for negative polarity, there is an increase in V_{50} between <10% RH and ~50% RH, however, when increasing to >90% RH, V_{50} decreases significantly. For positive polarity, as the humidity is increased from <10% RH to >90% RH, the V_{50} flashover voltage shows a clear decreasing trend. At <10% RH, the positive V_{50} is significantly higher than the negative, with no overlap of the error bars indicating that these data sets are independent of one another, within a 95.4% data spread. The positive flashover voltage is ~56 kV greater than negative. At ~50% RH, the positive V_{50} is again higher than the negative, however this comparison does exhibit overlapping error bars. At >90% RH, the same behaviour is recorded as that at <10% RH, where the positive V_{50} is higher than the negative by

~27 kV, with independent data sets. The maximum V_{50} value with a knurled HDPE spacer at 0.5 bar gauge was under positive polarity at <10% RH, with a flashover voltage of ~214 kV, while the minimum V_{50} of ~111 kV occurred under negative polarity, but in a >90% RH environment.

Further statistical data highlighting the differences in the breakdown-voltage distributions of electrodes bridged by knurled HDPE spacers is shown in Table 6.1. This table has been presented in the same format as those in Chapters IV and V, including $V_{0.01}$ values, for ease on comparison.

Table 6.1 – Values of α, β, V_{50} and $V_{0.01\%}$ for smooth HDPE surfaces, for each set of environmental conditions and both polarities.

HDPE Knurled	**Pressure**	**Negative**				**Positive**			
		α (kV)	**β**	**V_{50} (kV)**	**$V_{0.01}$ (kV)**	**α (kV)**	**β**	**V_{50} (kV)**	**$V_{0.01}$ (kV)**
-0.5 bar gauge	<10% RH	89.4	13.8	87.1	45.9	83.8	16.1	81.9	47.2
	~50% RH	70.3	20.2	69.1	44.5	84.7	23.4	83.4	57.2
	>90% RH	55.2	14	53.8	28.6	65.3	44.7	64.8	53.1
0 bar gauge	<10% RH	138.7	20.8	136.3	89.1	152	14.5	148.3	80.7
	~50% RH	121.8	33.8	120.5	92.8	138.1	21.4	135.8	89.8
	>90% RH	85	31.9	84.1	63.7	99.8	23.1	98.2	67
0.5 bar gauge	<10% RH	159.5	27.8	157.4	114.5	217.6	21.5	213.9	141.9
	~50% RH	173.1	25.5	170.6	120.5	197.4	16	192.9	111.1
	>90% RH	111.9	32.7	110.6	84.5	139	37.8	137.7	108.9

Analysing the calculated 0.01% probability of failure values (1 failure in 10,000), for the -0.5 bar gauge results in Table 6.1, it is shown that for the $V_{0.01}$ values, the increasing humidity is shown to decrease in the breakdown voltage for negative polarity, for positive polarity, there is no clear trend and with increasing humidity as the maximum 0.01% probability of failure value is measured at ~50% RH. For the 0 bar gauge results in Table 4.2, for both negative and positive polarity, there is no clear trend in the $V_{0.01}$ breakdown voltage as humidity increases, with the largest breakdown voltages appearing at ~50% RH. For the 0.5 bar gauge results, for negative polarity shows the 0.01% probability of failure value is maximum at ~50% RH and for positive polarity decreases with increasing humidity.

6.2.2. Polyetherimide (Ultem)

This section contains the results of the Polyetherimide flashover voltages for knurled cylindrical spacers under the various test conditions.

Shown in Figure 6.7, 6.8 and 6.9 are Weibull plots of the data for electrodes bridged by knurled Polyetherimide spacers, at -0.5 bar gauge.

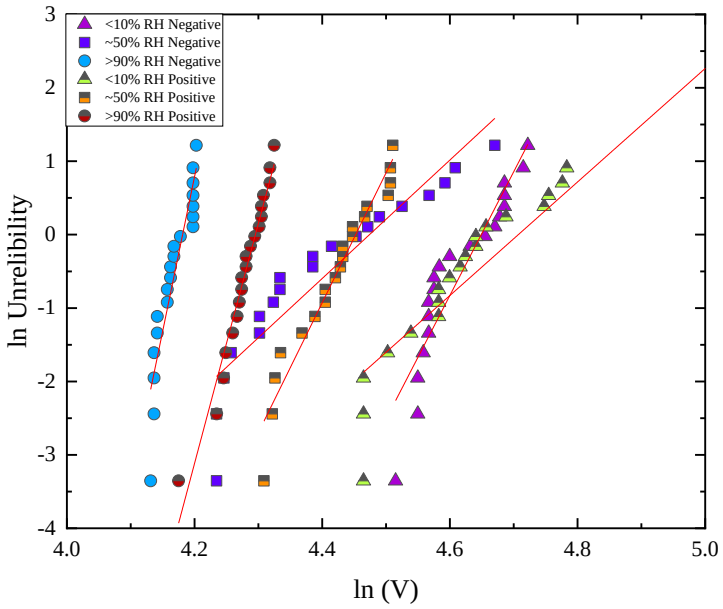

Figure 6.7. Weibull plots and curve fits of breakdown voltage data for knurled Polyetherimide surfaces at <10% RH, ~50% RH and >90% RH, all at -0.5 bar gauge.

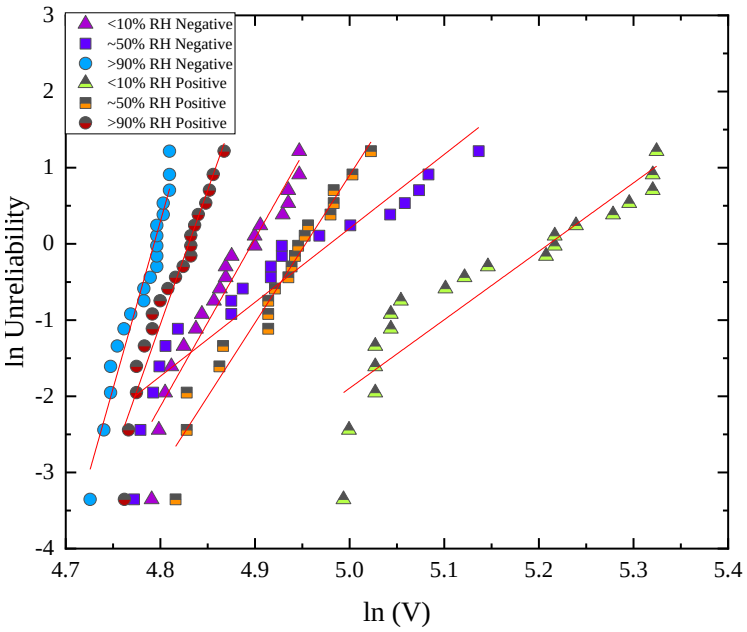

Figure 6.8 Weibull plots and curve fits of breakdown voltage data for knurled Polyetherimide surfaces at <10% RH, ~50% RH and >90% RH, all at 0 bar gauge.

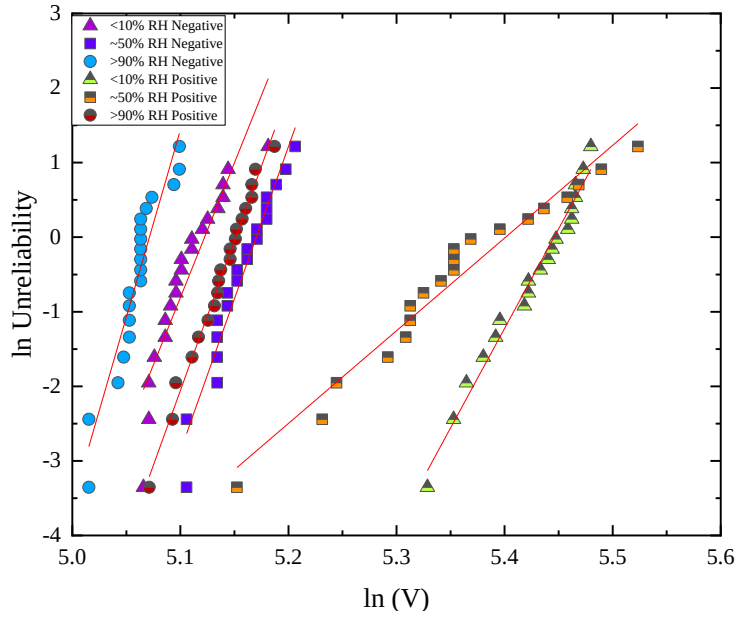

Figure 6.9 Weibull plots and curve fits of breakdown voltage data for knurled Polyetherimide surfaces at <10% RH, ~50% RH and >90% RH, all at 0.5 bar gauge

Analysing the Weibull distributions in Figure 6.7, 6.8 and 6.9, the V_{50} breakdown voltages and the spread (error bars) are shown in Figure 6.10a, 6.10b and 6.10c. Each bar represents the V_{50} from 20 impulsive breakdown voltages, and the error bars represent the 95.4% spread of the data.

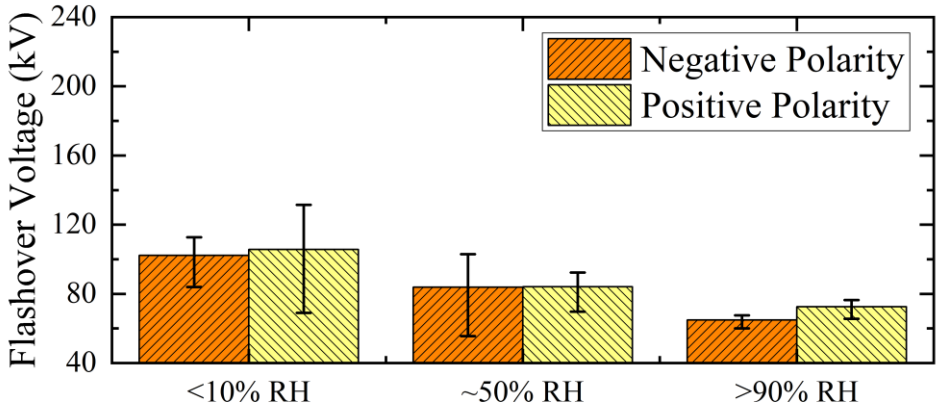

(a)

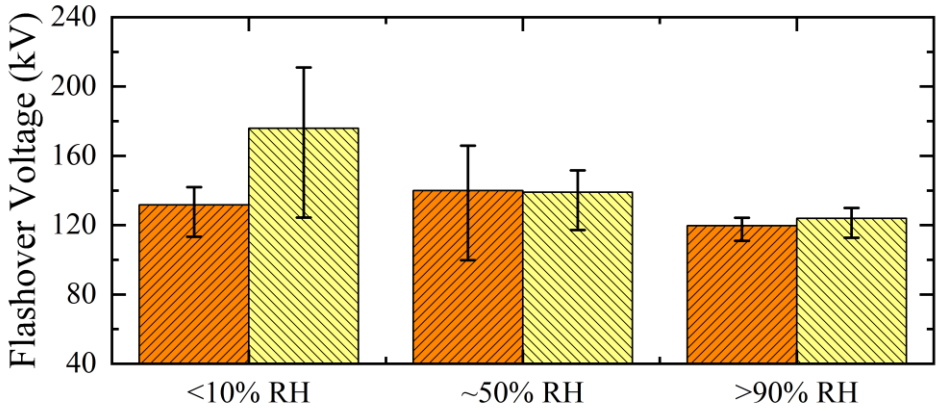

(b)

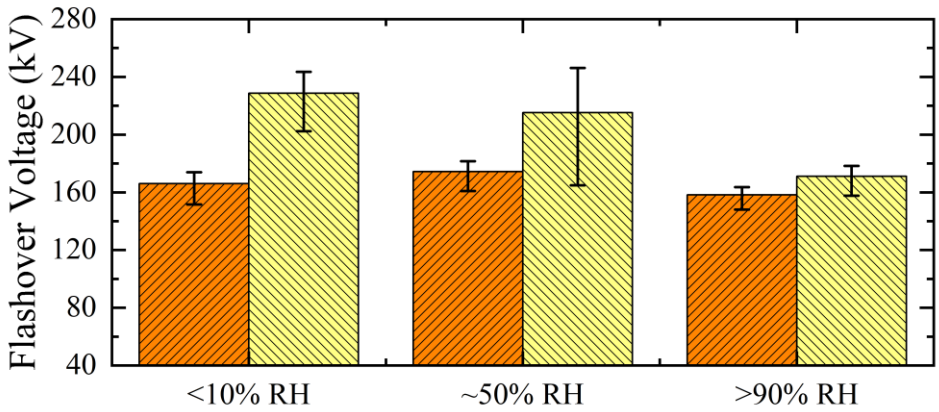

(c)

Figure 6.10. - Flashover voltages of pulsed power insulation system with a knurled Polyetherimide spacer at <10% RH, ~50% RH and >90% RH under negative and positive polarity impulse voltages, all at (a) -0.5 bar gauge, (b) 0 bar gauge and (c) 0.5 bar gauge. Each bar represents the average of 20 breakdown voltages and the errors bars show the 95.4% of the spread of data of each data set.

Figure 6.10a shows the Polyetherimide insulation system results for changing humidity and polarity at -0.5 bar gauge. It is clear that V_{50} decreases with increasing RH, for both positive and negative polarity. At all tested RH levels, V_{50} is very similar for both positive and negative voltages, with both distributions at each RH level exhibiting overlapping error bars. The V_{50} values are marginally higher for positive voltages in each case. The maximum V_{50} value for a knurled Polyetherimide spacer system at -0.5 bar gauge under positive polarity at <10% RH, with a flashover voltage of ~105 kV, while the minimum V_{50} was measured at ~65 kV, under negative polarity and at >90% RH.

Figure 6.10b shows the Polyetherimide insulation system results for changing humidity and polarity at 0 bar gauge. The V_{50} flashover voltage increases for negative polarity from <10% RH to ~50% RH, but then decreases when the humidity is further increased to >90% RH. For positive polarity, V_{50} decreases with increasing humidity. At <10% RH, the positive V_{50} is ~44 kV higher than the negative. The distributions do exhibit overlapping error bars. At ~50% RH and at >90% RH, the V_{50} values are very similar, with overlapping error bars in each case. At >90% RH, the error bars are shorter than at the lower RH levels, reflecting the narrower spread in the breakdown voltages. The maximum V_{50} with a knurled Polyetherimide spacer at 0 bar gauge was under positive polarity at <10% RH, being ~176 kV, and the minimum V_{50} of ~125 kV occurred under negative polarity at >90% RH.

Figure 6.10c shows the Polyetherimide insulation system results for changing humidity and polarity at 0.5 bar gauge. The positive V_{50} decreases with increasing RH level. Under negative polarity, the V_{50} flashover voltage increases slightly from <10% RH to ~50% RH, but then decreases slightly at >90% RH. What is evident from the negative polarity voltages is that V_{50} is fairly consistent, with short error bars, across the humidity range. At <10% RH, the positive V_{50} is much higher than the negative, by ~63 kV. The error bars also do not overlap, showing each distribution is independent of each other to ~95.4% spread of data. At ~50% RH, again, the positive V_{50} is higher than the negative, by ~41 kV, however the error bars are overlapping. At >90% RH, the positive V_{50} is again higher, but again with overlapping error bars. There exists a trend at 0.5 bar gauge whereas the humidity increases, the difference between the positive and negative V_{50} voltages becomes smaller. The maximum V_{50} with a

knurled Polyetherimide spacer at 0.5 bar gauge was under positive polarity at <10% RH, being ~230 kV, and the minimum V_{50} of ~158 kV occurred under negative polarity at >90% RH.

Further statistical data highlighting the differences in the breakdown-voltage distributions of electrodes bridged by knurled Polyetherimide spacers is shown in Table 6.2. This table has again been presented in the same format as those in Chapters IV and V, including $V_{0.01}$ values, for ease on comparison.

Table 6.2 – Values of α, β, V_{50} and $V_{0.01\%}$ for smooth Polyetherimide surfaces, for each set of environmental conditions and both polarities.

Polyetherimide Knurled	**Pressure**	**Negative**				**Positive**			
		α (kV)	**β**	**V_{50} (kV)**	**$V_{0.01}$ (kV)**	**α (kV)**	**β**	**V_{50} (kV)**	**$V_{0.01}$ (kV)**
-0.5 bar gauge	<10% RH	104.5	16.9	102.3	60.5	110.7	7.73	105.6	33.7
	~50% RH	87.7	8.1	83.8	28	85.8	17.7	84.1	51
	>90% RH	65.4	42.2	64.9	52.6	73.4	32.7	72.5	55.3
0 bar gauge	<10% RH	133.9	22	131.7	88.1	183.2	9	175.9	65.7
	~50% RH	145.3	9.7	139.9	56.3	141.7	19.4	139	88
	>90% RH	120.7	43.9	119.7	97.8	125.2	35.2	123.9	96.4
0.5 bar gauge	<10% RH	167.7	36.1	166	130	231.8	26.7	228.6	164.2
	~50% RH	176	40.8	174.4	140.4	221.6	12.4	215.2	105.6
	>90% RH	159.4	50.1	158.2	132.6	172.7	40.1	171.1	137.2

Analysing the calculated 0.01% probability of failure values (1 failure in 10,000), for the -0.5 bar gauge results in Table 6.2, it is shown that for the $V_{0.01}$ values, increasing humidity is shown to have no trend in the breakdown for positive polarity, with the maximum appearing at <10% and the minimum appearing at ~50% RH. For positive polarity, with increasing humidity the 0.01% probability of failure value increases with increasing humidity. For the 0 bar gauge results in Table 4.2, for both negative polarity, there is no clear trend in the $V_{0.01}$ breakdown voltage as humidity increases, with the largest breakdown voltages appearing at ~50% RH, for positive polarity the breakdown voltage increases with increasing humidity. For the 0.5 bar gauge results, for negative polarity shows the 0.01% probability of failure value is maximum at ~50% RH and for positive polarity is maximum at <10% RH, but minimum at ~50% RH, so both positive and negative polarity at 0.5 bar gauge shown no trend.

6.2.3. Polyoxymethylene (Delrin)

This section contains the results of the Polyoxymethylene flashover voltages for knurled cylindrical spacers under the various test conditions.

Shown in Figure 6.11, 6.12 and 6.13 are Weibull plots of the data for electrodes bridged by knurled Polyoxymethylene spacers, at -0.5 bar gauge, 0 bar gauge and 0.5 bar gauge.

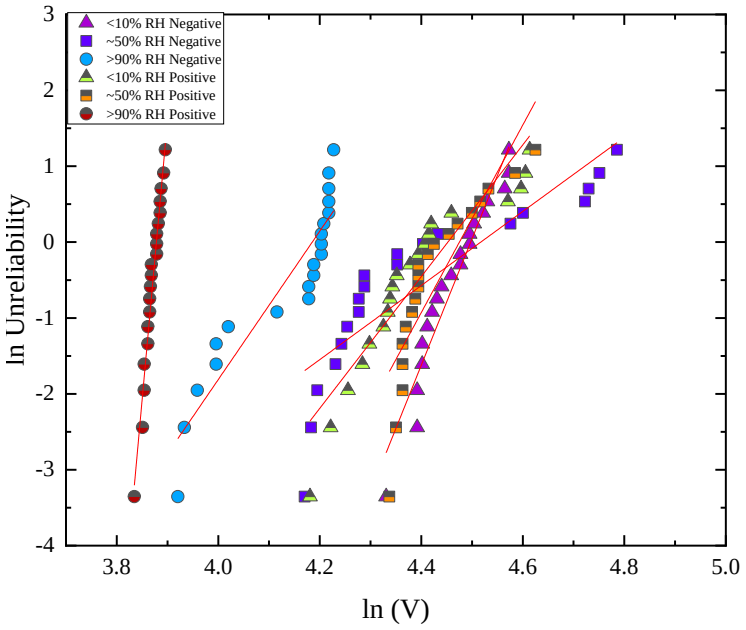

Figure 6.11. Weibull plots and curve fits of breakdown voltage data for knurled Polyoxymethylene surfaces at <10% RH, ~50% RH and >90% RH, all at -0.5 bar gauge.

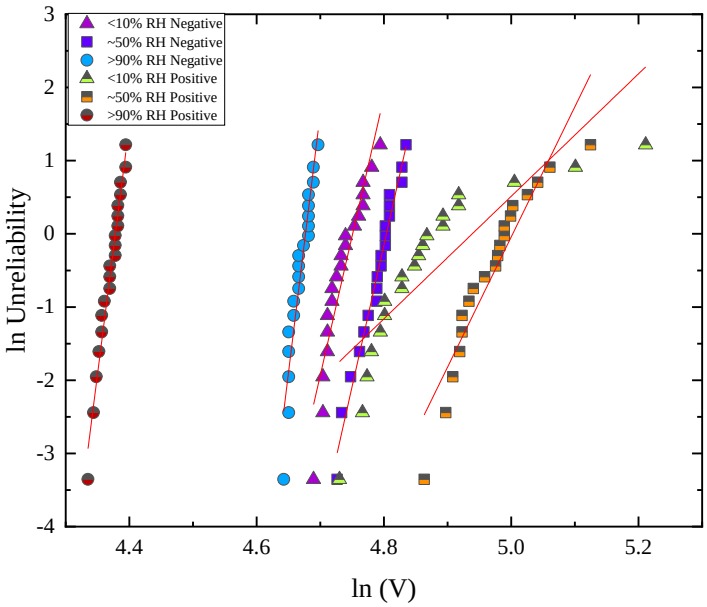

Figure 6.12. - Weibull plots and curve fits of breakdown voltage data for knurled Polyoxymethylene surfaces at <10% RH, ~50% RH and >90% RH, all at 0 bar gauge.

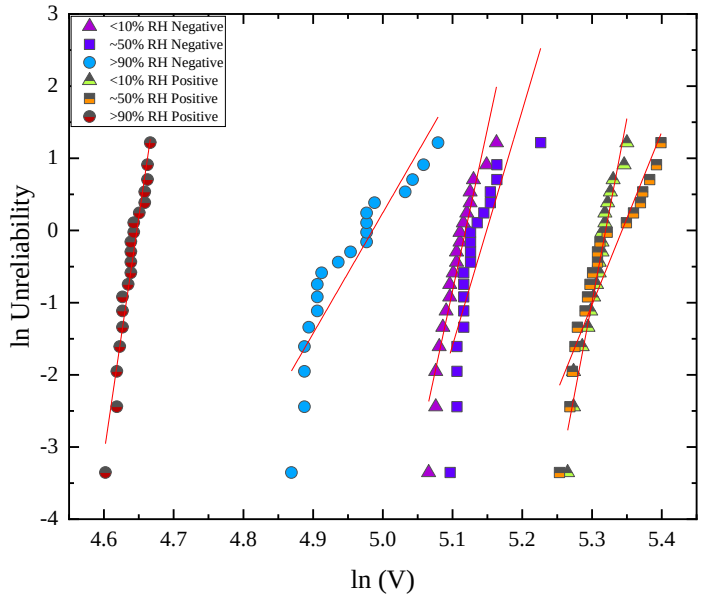

Figure 6.13. - Weibull plots and curve fits of breakdown voltage data for knurled Polyoxymethylene surfaces at <10% RH, ~50% RH and >90% RH, all at 0.5 bar gauge.

Analysing the Weibull distributions in Figure 6.11, 6.12 and 6.13, the V_{50} breakdown voltages and the spread (error bars) are shown in Figure 6.14a, 6.14b and 6.14c. Each bar represents the V_{50} from 20 impulsive breakdown voltages, and the error bars represent the 95.4% spread of the data.

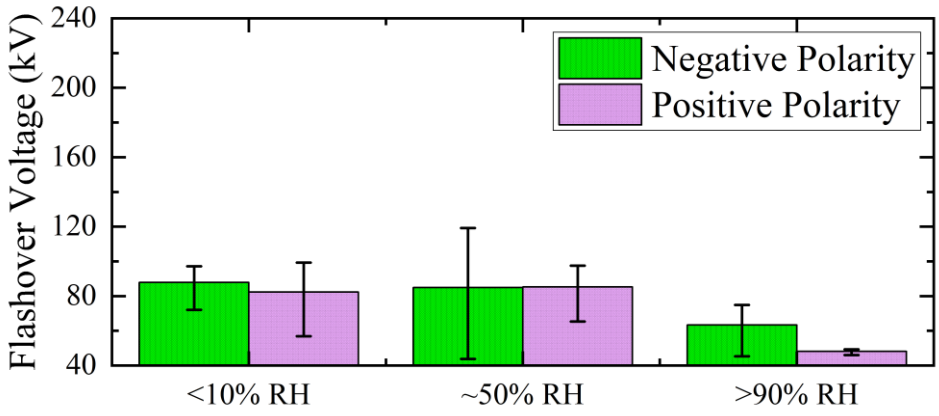

(a)

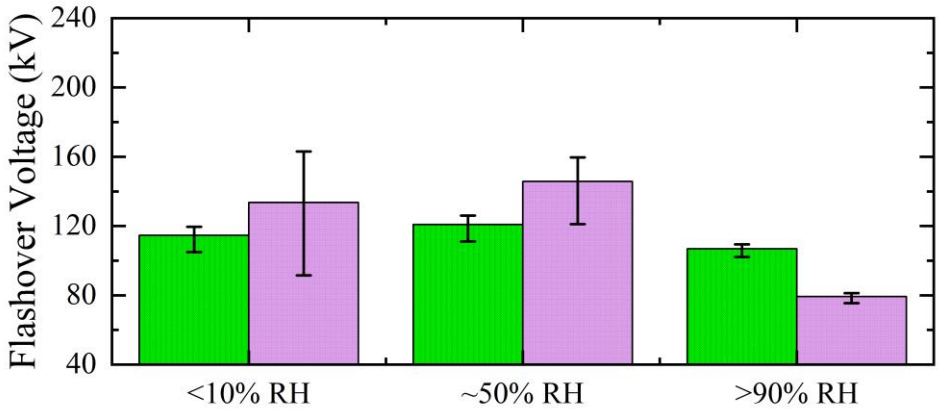

(b)

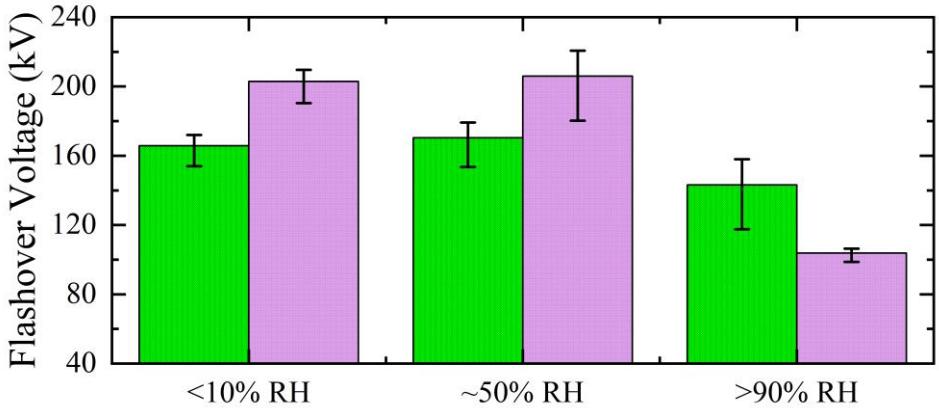

(c)

Figure 6.14. - Flashover voltages of pulsed power insulation system with a knurled Polyoxymethylene spacer at <10% RH, ~50% RH and >90% RH under negative and positive polarity impulse voltages, all at (a) -0.5 bar gauge, (b) 0 bar gauge and (c) 0.5 bar gauge. Each bar represents the average of 20 breakdown voltages and the errors bars show the 95.4% of the spread of data of each data set.

Figure 6.14a shows the Polyoxymethylene insulation system results for changing humidity and polarity at -0.5 bar gauge. Analysing the trends as the humidity increases, for negative polarity, there is a general downward trend in the flashover voltage. For positive polarity, however, V_{50} marginally increases as the humidity is increased from <10% RH to ~50% RH, and there are overlapping error bars. As the humidity increases to >90% RH, V_{50} significantly decreases. At <10% RH, the positive and negative polarity breakdown voltages are very similar, with the negative V_{50} being slightly higher, but with overlapping error bars. At ~50% RH, the positive and negative flashover voltages are very similar in magnitude, with overlapping error bars. At >90% RH, the negative V_{50} is seen to be higher than the positive, but with overlapping error bars. The maximum V_{50} with a knurled Polyoxymethylene spacer at -0.5 bar gauge was under negative polarity at <10% RH, with a flashover voltage of ~88 kV, and the minimum V_{50} of ~46 kV occurred under positive polarity, at >90% RH.

Figure 6.14b shows the Polyoxymethylene insulation system results for changing humidity and polarity at 0 bar gauge. Analysing the trends as the humidity increases, for both negative and positive polarity, as the humidity is increased from <10% RH to ~50% RH, the V_{50} flashover voltage is seen to increase. As the humidity increases to >90% RH, V_{50} decreases for both positive and negative polarity. For negative polarity, it can be seen that, irrespective of humidity, V_{50} is relatively consistent, whereas for positive polarity, V_{50} dramatically decreases at >90% RH. At <10% RH and at ~50% RH, the positive V_{50} is higher than the negative, by up to 25 kV at ~50% RH, although with overlapping error bars. At >90% RH, the negative V_{50} is seen to be ~28 kV higher than the positive, with no overlapping error bars, showing that these data sets are independent of one another, for ~95.4% spread of data. The maximum V_{50} of ~145 kV found with a knurled Polyoxymethylene spacer at 0 bar gauge was under positive polarity at ~50% RH, while the minimum V_{50} of ~80 kV was also under positive polarity, but in a >90% RH environment.

Figure 6.14c shows the Polyoxymethylene insulation system results for changing humidity and polarity at 0.5 bar gauge. For negative polarity, as the humidity is increased from <10% RH to ~50% RH, V_{50} is seen to slightly increase, but as the humidity increases to >90% RH, V_{50} decreases. For positive polarity, again, as the

humidity is increased from <10% RH to ~50% RH, V_{50} is seen to increase but again, as the humidity increases to >90% RH, V_{50} dramatically decreases. At <10% RH, the positive V_{50} is seen to be ~37 kV greater than the negative, with no overlapping error bars showing independent distributions for ~95.4% spread of data. At ~50% RH, V_{50} is again higher by ~36 kV for positive polarity, with no overlap of the error bars. At >90% RH the behaviour changes, with the negative V_{50} becoming ~39 kV higher than the positive, with no overlapping error bars. The maximum V_{50} of ~206 kV found with a knurled Polyoxymethylene spacer at 0.5 bar gauge was under positive polarity at ~50% RH, while the minimum V_{50} of ~104 kV was also under positive polarity, but in a >90% RH environment.

Further statistical data highlighting the differences in the breakdown-voltage distributions of electrodes bridged by knurled Polyoxymethylene spacers is shown in Table 6.3. This table has again been presented in the same format as those in Chapters IV and V, including $V_{0.01}$ values, for ease of comparison.

Table 6.3 – Values of α, β, V_{50} and $V_{0.01}$ for knurled Polyoxymethylene surfaces, for each set of environmental conditions and both polarities.

Polyoxymethylene **Knurled**	**Pressure**	**Negative**				**Positive**			
		***α* (kV)**	***β***	**V_{50} (kV)**	**$V_{0.01}$ (kV)**	***α* (kV)**	***β***	**V_{50} (kV)**	**$V_{0.01}$ (kV)**
<10% RH	<10% RH	89.8	16.7	87.8	51.7	85.8	8.7	82.3	29.7
	~50% RH	91.6	4.9	85	13.9	87.8	12.4	85.2	41.7
	>90% RH	65.7	9.8	63.3	25.6	48.3	73.7	48.1	42.7
~50% RH	<10% RH	115.7	38	114.6	90.8	139.6	8.4	133.6	46.4
	~50% RH	122	38.7	120.8	96.1	148.8	17.8	145.7	88.6
	>90% RH	107.4	71	106.9	94.3	79.7	68.2	79.3	69.6
>90% RH	<10% RH	167.1	44.9	165.7	136.1	204.3	50.9	202.8	170.5
	~50% RH	172.2	32.6	170.3	129.8	209.1	24	206	142.4
	>90% RH	146.2	16.7	143.1	115.8	104.3	65.6	103.7	90.6

Analysing the calculated 0.01% probability of failure values (1 failure in 10,000), for the -0.5 bar gauge results in Table 6.3, it is shown that for the $V_{0.01}$ values, increasing humidity is shown to have no trend in the breakdown voltage for negative polarity, where the maximum is measured at <10% RH, but at a minimum at ~50% RH. For positive polarity, as the humidity increases the breakdown voltage also increases. For the 0 bar gauge results in Table 4.2, for both negative and positive polarity, there is no

clear trend in the $V_{0.01}$ breakdown voltage as humidity increases, with the largest breakdown voltages appearing at ~50% RH. For the 0.5 bar gauge results, for both negative and positive polarity the 0.01% probability of failure value is shown to decrease with increasing humidity.

6.3. Effect of Physical and Environmental Parameters on Knurled Spacer Flashover

To explain the results outlined in Section 6.2, the physical and environmental parameters will now be discussed, drawing upon visual observations and information gathered from previous literature on the subject to develop explanations of the observed behaviours.

The effect of solely modifying the surfaces of spacer materials, without increasing the spacer length, will be elucidated by comparing the results to those for the open gap arrangement as a general reference, as well as to those for spacers with smooth (machined) surfaces.

6.3.1. Dielectric Material

When comparing the flashover results in Section 6.2 in terms of specific materials, for both negative and positive polarity, unlike with smooth (machined) surfaces, no correlation between the relative permittivity of the material and the flashover voltage level is evident. This could be due to the knurled surface creating low and high field regions at the surface of the spacer material, as well as at the triple junction point (TJP), resulting in a flashover voltage that is more dependent upon the location of the discharge. As shown previously in Figure 3.15, the electrostatic field simulations show that as the permittivity of the material is increased, the electric field at the TJP is increased. Overall, the results reflect no direct correlation between the material permittivity and the breakdown voltage during these tests.

Additionally, under changing environmental conditions, this could be affected by the process seen with smooth (machined) spacers, where lift-off of the plasma channel from the material surface occurs, and the discharge partly or fully propagates through the surrounding air. This lift-off could minimise the influence of the permittivity of

the solid on the breakdown voltage, with only those streamers which are local to the solid surface being affected. This behaviour is evident for all pressures and humidity levels.

6.3.2. Impulse Polarity

For tests undertaken at <10% RH, at -0.5 bar gauge, the positive and negative V_{50} values for each material were similar. This behaviour with knurled surfaces is different

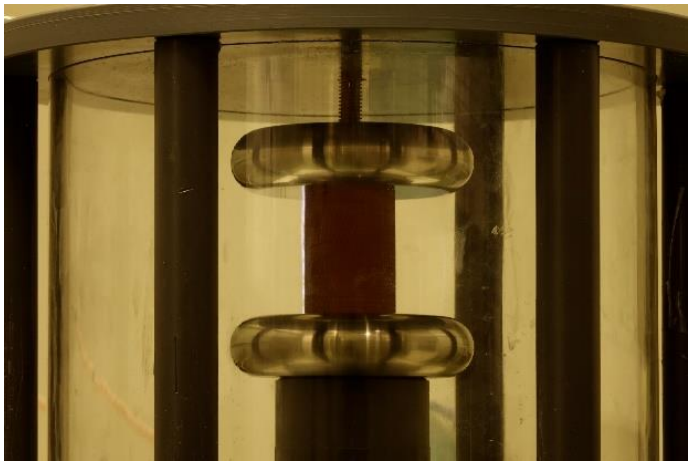

Figure 6.15 – surface flashover event of a knurled Ultem spacer at 0 bar gauge in <10% RH.

to that observed for smooth (machined) surfaces. Knurling of the material surfaces resulted in a decrease in the negative V_{50} compared to that for the corresponding smooth surface, for all materials. Under positive polarity, V_{50} for a knurled surface is relatively consistent with that for the corresponding smooth surface, for all materials. This could be attributed to the knurled surface creating a high field region at the TJP, initiating the flashover across the spacer surface (as shown in Figure 6.15) for both positive and negative polarity impulses, rather than across the electrode edges as occurred for the smooth (machined) surface tests (as shown in Figure 5.13), where, the behaviours and trends for smooth (machined) surface spacers generally follow those for the corresponding open gap arrangement, as was discussed in Section 5.3.2.

For knurled surfaces, however, due to the synergistic effect of the increased field region at the TJP and the low gas pressure at -0.5 bar gauge, the flashover voltage is similar for each polarity. As air pressure increases, an effect can also be seen from the flashover data at 0 bar gauge, where for all materials, the positive V_{50} starts to increase in comparison to the negative, but each comparison exhibits overlapping error bars.

However, as the pressure is further increased 0.5 bar gauge, a clear trend starts to appear where the positive polarity flashover voltages are significantly higher than the negative, for all materials. The widest difference occurred at 0.5 bar gauge for an Polyetherimide spacer, where the positive V_{50} was ~66 kV higher than the negative. An increase of at least 37 kV was evident for all materials at 0.5 bar gauge.

The modification of the spacer surface affects the TJP angle between the electrode, spacer material and the surrounding air dielectric. Over the circumference of the spacer, it is hypothesised that the contact angle produced will be decreased in certain regions due to the added indentations, resulting in an enhanced electric field strength at the triple junction point, as shown from the electrostatic field simulation results in Figure 3.15. Compared to the case with a smooth spacer surface this results in discharges tending to propagate along the sample surfaces.

The formation of positive streamers is hindered by the knurled surface, while the effect on negative streamers is minimal, as they do not rely as much on free electrons at the gas/spacer interface. This behaviour has been observed experimentally by another research group, in [11].

In order to explain this behaviour, the differences between the positive and negative flashover processes have to be discussed, where the mechanisms of positive and negative streamer growth and propagation are different when in the vicinity of a dielectric surface. For this comparison, it also has to be considered that the spacer surface itself can be an efficient source of free electrons [15]. Given that positive streamers need free electrons some distance ahead in order to propagate to the point of breakdown [16], and that the efficiency of secondary electron emission (SEE) could be limited, [17], by insulator surface roughness (in this case knurling), if the streamer is following the surface closely, the knurling will affect the full length of the streamer, which will be required to propagate a longer distance. This results in an increased voltage drop along the streamer length, reducing the voltage at the streamer front, and resulting in a reduction in the energy available to drive ionisation, [18].

This effect could increase the positive-polarity flashover voltage, which corresponds with empirical data found in this work. Additionally, electrons produced over the surface of the material from SEE processes, and electrons produced through

photoionisation at the head of the streamer in the bulk gas which are not adsorbed to the dielectric surface, will expand and further weaken the electric field at the positive streamer head, [12]. Due to the weakening of the electric field, a higher applied voltage will be required to initiate flashover, than that required for a non-profiled surface. The follows the hypothesis, which was made in Section 6.1, with the plasma channel discharging over the dielectric surface.

For tests at ~50% RH, at -0.5 bar gauge, positive and negative V_{50} values were similar, for each material. As the pressure is increased to 0 bar gauge, the positive V_{50} is higher than the negative for HDPE and Polyoxymethylene spacers. With an Polyetherimide spacer, the positive and negative V_{50} values are very similar, however there are overlapping error bars, for all materials. Increasing the pressure futher to 0.5 bar guage, all materials show higher nominal positive flashover voltage than negative. However, HDPE and Polyetherimide exhibit overlapping error bars. Generally, as the humidity is increased from <10% RH to ~50% RH, the differences between the average positive and negative breakdown voltages have become smaller, so that the average breakdown voltages are similar for positive and negative polarity, for each set of conditions. This could be attributed to the higher humidity creating an atmosphere in which the attachment coefficient is higher, due to the presence of water molecules, acting to increase the negative breakdown voltages. Also, the amount of charge deposition on the surface of the solid spacer is determined by the humidity. As there is a change in the amount of charge deposition between smooth and knurled samples of the same material at <10% RH, with less charge retained on the knurled surface, as shown (for roughened surfaces) by the authors of [19]. However, due to the humidity increase for tests undertaken at ~50% RH, there is a reduced charge deposition on both smooth and knurled surfaces, as discussed in Section 4.1, following discussion by the authors of [20], potentially explaining the increasingly (electrically) symmetrical breakdown performance.

Interestingly, at >90% RH, the knurled HDPE spacer and the knurled Polyoxymethylene spacer showed opposing behaviour in terms of positive and negative V_{50}, at all pressures. Analysing the insulation performance of each air-solid gap in relation to that for an open-air gap, use of HDPE as a spacer material resulted in flashover over the surface of the material being the dominant breakdown

mechanism under negative polarity, due to the increased field as a result of knurling and the hydrophobicity of the material as shown from equation 2.61. For Polyoxymethylene, also under negative polarity, flashover occurred at the electrode edges. These discharge paths were evident at all pressures. For positive polarity, similarly, surface flashover occurred with an HDPE spacer at all pressures, while flashover at the electrode edges occurred for a Polyoxymethylene spacer. Again, the different hydrophobic parameters of the materials may be the cause of this behaviour, for HDPE, with increased contact angles caused by the knurled surface, increases the electric field associated with water droplets near the TJP, promoting discharge at the surface. For Polyetherimide, as for Polyoxymethylene, flashover occurred at the electrode edges, irrespective of the humidity or pressure. Again, this could be attributed to the fact that the material is the most hydrophilic, resulting in a lesser field enhancement at the material surface compared to that for the other materials, as well as the knurled surface interrupting any conductive paths which could be formed on a smooth spacer surface, resulting in a breakdown voltage similar to that for an open air gap, with the addition of water vapour creating a more symmetrical system, as was discussed in-depth in Section 4.4.1.

These behaviours will be further analysed when comparing the smooth and knurled flashover results in Section 6.5.

6.3.3. Air Pressure

For all tested conditions, increasing the pressure resulted in increased flashover voltages, as expected. As the gas pressure increases, the electron mean free path decreases, and the collision frequency increases. Electrons will gain less energy between collisions, which means that a higher applied field is required for free electrons to gain sufficient energy to cause an ionisation event [21]. This is relevant for both surface flashover and bulk air breakdown mechanisms.

However, for the knurled material surface flashover tests in <10% RH air, with increasing air pressure, a clear effect can be seen from the difference between positive and negative flashover voltages. In terms of air pressure, the V_{50} flashover voltages for knurled surfaces are shown to be higher than those for smooth surfaces at 0 bar gauge

pressure, as seen in Figure 6.4, and at 0.5 bar gauge pressure, as seen in Figure 6.6. There is clearly less of an effect at −0.5 bar gauge, in Figure 6.2. A potential reason for this is that, as the pressure increases, the discharge tends to initiate closer to the TJP, as discussed in [22]. Based upon this, the development of positive and negative streamer discharges in the vicinity of dielectric surfaces is affected in different ways. The development of positive streamers is further impeded by the knurled surface with increasing pressure, due to the mechanisms for positive discharges near dielectric surfaces, decreasing the field at the head of the streamer. However, as negative discharges are wider and more diffuse, as discussed in [11], and with electrons emanating from the streamer head, there is minimal effect of the field at the front of the negative streamer, so therefore, the pressure, and the initial location of the discharge at the TJP has little effect on the flashover voltage.

6.4. COMPARISON WITH BREAKDOWN IN OPEN GAPS

In Chapter V, the smooth (machined) breakdown results were compared to those for open airs gaps. A similar analysis is now undertaken, but with the breakdown results with knurled surfaces compared to those with smooth (machined) surfaces (Section 6.5), and those for an open-air gap. These comparisons will give a clear outlook on the most optimal insulation system for each specific set of environmental conditions.

6.4.1. <10% RH

Figures 6.16, 6.17 and 6.18 show the volt-time graphs for this data, where there are clear groupings of positive and negative data. These groupings illustrate the similar behaviour of air-solid gaps and open-air gaps for each polarity.

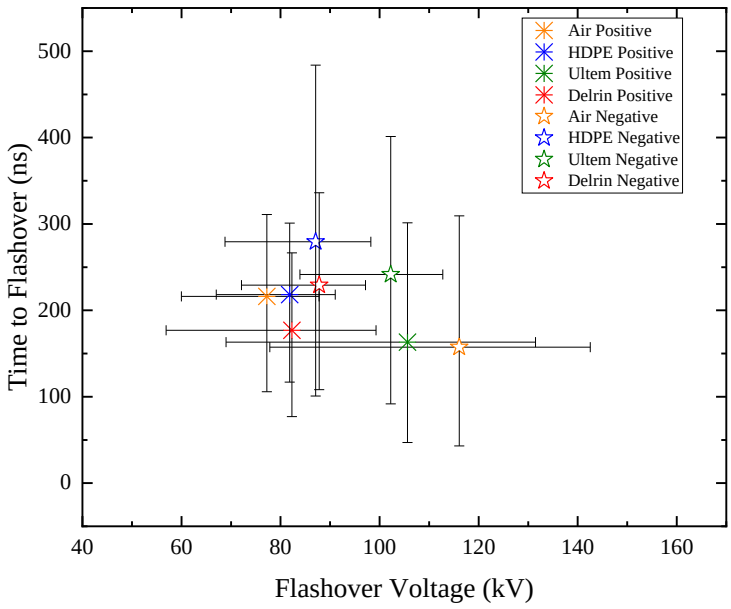

Figure 6.16. - Volt-time graphs for negative and positive polarity energisation, for open air, HDPE, Polyetherimide and Polyoxymethylene at <10% RH and -0.5 bar gauge.

From Figure 6.16, it can be seen that for all compared tests, there were overlapping error bars, for both negative and positive polarity. Analysis of the V_{50} values does reveal decreases from that for the open gap, with HDPE and Polyoxymethylene spacers, for both polarities. This could be attributed to the discharge location not only being at the edges of the electrode setup, but also at the TJP, due to the high field regions created by the knurled surface and the absence of any humidity to cause local increases in the electric field. Interestingly, for positive polarity, V_{50} is higher with the Polyetherimide spacer than for the open gap, however there are overlapping error bars. The difference in V_{50} for the air-solid insulation systems, referenced to V_{50} of the open gap (air) were -29 kV for HDPE, -13.8 kV for Polyetherimide and, -28.3 kV for Polyoxymethylene for negative polarity; and +4.7 kV for HDPE, +28.4 kV for Polyetherimide and, +5.1 kV for Polyoxymethylene for positive polarity.

Figure 6.16 shows the volt-time graphs from the <10% RH, - 0.5 bar gauge results. It can be seen that, in comparison to an open-air gap, there is a general increase in flashover voltage for all air-solid gaps under positive polarity, whereas all air-solid gaps cause a lower flashover voltage under negative polarity. It can also be seen in Figure 6.16 that, although there is a wide difference between the breakdown points for positive and negative open-air gaps, all data (positive and negative) for air-solid gaps is clustered.

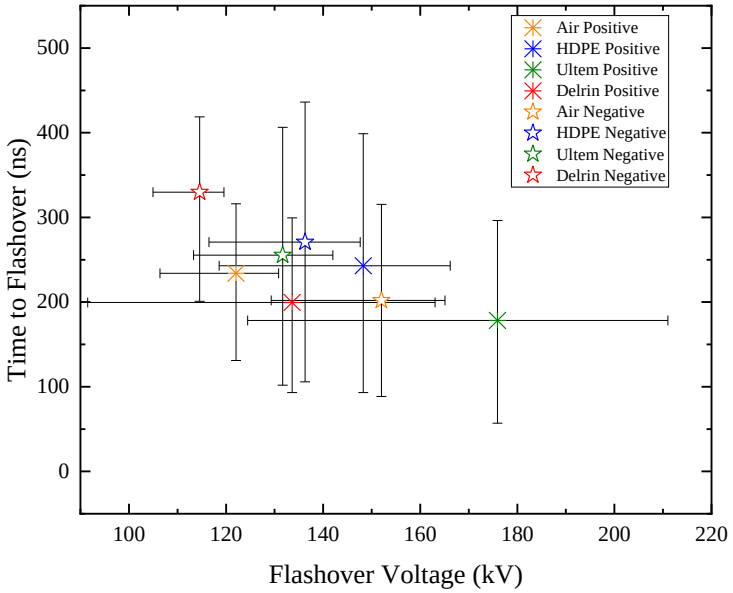

Figure 6.17. - Volt-time graphs of negative and positive polarity energisation, for open air, HDPE, Polyetherimide and Polyoxymethylene at ~10% RH and 0 bar gauge.

From Figure 6.17, there were overlapping error bars for most compared tests. Under negative polarity, however, V_{50} with a knurled Polyoxymethylene surface was significantly lower than that for the open-air gap. There are overlapping error bars between all compared tests. Evident from the negative polarity results is that the flashover voltages with any of the spacer materials are nominally lower than those for the open-air gap, while for positive polarity, they are nominally higher for air-solid gaps than for an open-air gap. This implies that there is a polarity effect at 0 bar gauge, also. The differences in the effect of the knurled surface on positive and negative breakdown were discussed and illustrated in Section 6.3.2. The differences in the nominal flashover voltages for air-solid gaps compared to the corresponding open gap (air) were -15.7 kV for HDPE, -20.3 kV for Polyetherimide and 37.4 kV for Polyoxymethylene for negative polarity; and +26.2 kV for HDPE, +53.9 kV for Polyetherimide and, +11.5 kV for Polyoxymethylene for positive polarity.

Figure 6.17 shows the volt-time graphs from the <10% RH, 0 bar gauge results, where there are clear trends for positive and negative insulation performance. When a knurled surface of any material bridges the electrodes, the positive flashover voltage increases compared to that for an open gap, while the negative flashover voltage decreases.

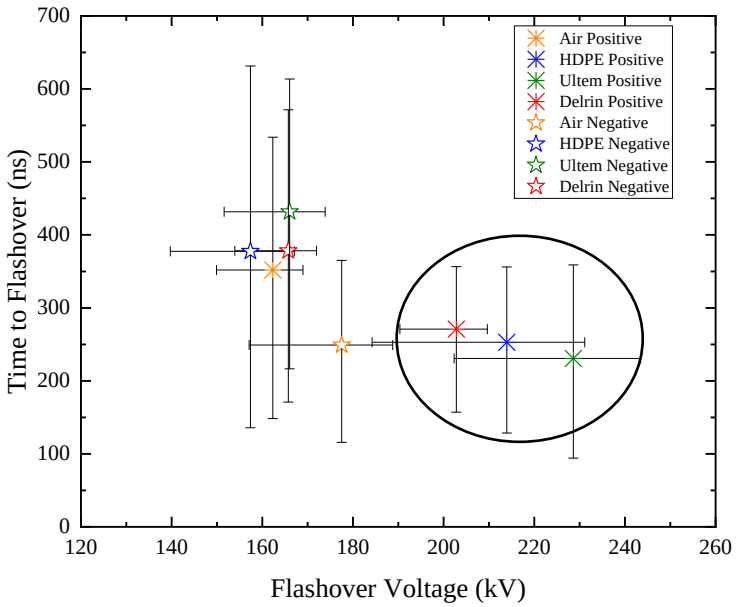

Figure 6.18. - Volt-time graphs of negative and positive polarity energisation, for open air, HDPE, Polyetherimide and Polyoxymethylene at ~10% RH and 0.5 bar gauge.

From Figure 6.18, there are overlapping error bars for all compared tests, under negative polarity, where the discharge interaction with the TJP and the knurled surface did not have much of an effect on the negative flashover voltages but had a large effect on the positive polarity flashover voltages, as discussed in Section 6.3.2. However, the time to flashover under negative polarity has increased in comparison to that for the open gap, implying a potentially different breakdown mechanism. For positive polarity, the presence of knurled spacer surfaces is shown to increase V_{50} compared to that for an open gap, suggesting that there are different underlying mechanisms dictating the flashover process, as discussed in Section 6.3.2. The differences in the V_{50} values with the knurled surfaces in comparison to that for the open gap (air) were -20.1 kV for HDPE, -11.5 kV for Polyetherimide and -11.8 kV for Polyoxymethylene for negative polarity; and +51.6 kV for HDPE, +66.3 kV for Polyetherimide and, +40.5 kV for Polyoxymethylene for positive polarity. Figure 6.18 shows the volt-time graphs from the <10% RH, 0.5 bar gauge results, where there is a clear trend for positive and negative insulation performance. As at 0 bar gauge, when a knurled surface of any material bridges the electrodes, the positive flashover voltage increases compared to that for an open gap, while the negative flashover voltage decreases.

Figure 6.18, in particular, highlights the influence that the discharge path has on the breakdown voltage and time to flashover. Due to the high field regions created by the knurled surface at the interface with the electrode, negative streamers can traverse the full length of the surface at a lower applied voltage, and at long times to flashover. For positive polarity, the knurled surface blocks the development of the positive streamer, necessitating a higher applied field to cause breakdown.

For tests in a <10% RH environment, the breakdown channels were observed to initiate and propagate both, over the surface of the material, and between the edges of the electrodes (away from the surface of the solid sample), different to what was seen with smooth (machined) surfaces in Chapter V, where all discharges occurred between the electrode edges.

Summarising the key findings with respect to applied voltage polarity at <10% RH:

- At -0.5 bar gauge, no polarity effect was observed, where for each material, the negative and positive error bars overlap
- For tests at 0 bar gauge, there is a slight polarity effect with knurled surfaces, where the positive polarity breakdown voltages were higher than the negative (with overlapping error bars for all materials), which is opposite to the behaviour seen with smooth (machined) solids, and with open gaps.
- Upon increasing the pressure further to 0.5 bar gauge, a polarity effect on the measured breakdown voltages is evident, with positive flashover voltages being higher than negative for gaps bridged by solid spacers with knurled surfaces, for all materials. This result is particularly interesting since this behaviour opposes the polarity effect observed with no spacer, where the average negative breakdown voltage of the open-air gap is higher than that for positive polarity. This is hypothesised as being due to the discharge path changing, propagating across the spacer surfaces, increasing the positive flashover voltage.

Further discussion is made in Section 6.5.1 where possible mechanisms for the increased flashover voltage in comparison to an open gap as well as a smooth machined spacer arrangement.

6.4.2. ~50% RH

Figures 6.19, 6.20 and 6.21 show the volt-time graphs from the ~50% RH, -0.5, 0 and 0.5 bar gauge results, where there are generally, as before at <10% RH, groupings for positive and negative discharges.

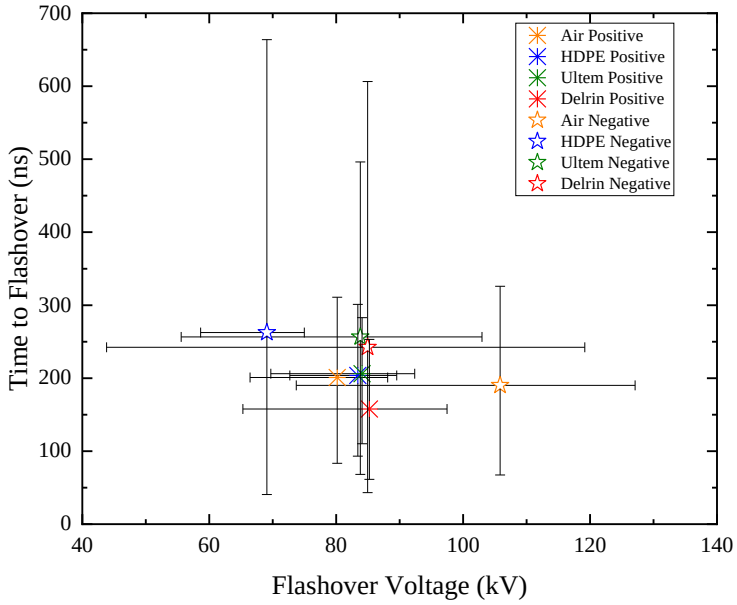

Figure 6.19. - Volt-time graphs of negative and positive polarity energisation, for open air, HDPE, Polyetherimide and Polyoxymethylene at ~50% RH and -0.5 bar gauge.

From Figure 6.19, it can be seen that for all compared tests for each polarity, there are overlapping error bars. This follows the same behaviour seen at <10% RH. The negative V_{50} flashover voltages do decrease with spacers of any material compared to an open gap, whereas for positive polarity, the V_{50} magnitudes with spacers are similar to that for the open gap.

As shown for open gaps at -0.5 bar gauge in Chapter IV, increasing humidity resulted in a more (electrically) symmetrical performance of the insulation system, when discharges occurred at the rounded electrode edges. However, at ~50% RH, the addition of a spacer reduces the breakdown voltage under negative polarity, particularly for HDPE and Polyetherimide spacers, so the difference between the positive and negative voltages increases again. Due to the increased humidity at ~50% RH, the discharges initiated both, across the surface of the material, and between the electrode edges, manifested in decreases in the flashover voltage - with large error bars

- in comparison to that for an open-air gap. The differences in the V_{50} flashover values in comparison to that for an open gap (air) were -36.7 kV for HDPE, -22 kV for Polyetherimide and -20.8 kV for Polyoxymethylene for negative polarity; and +3.2 kV for HDPE, +3.9 kV for Polyetherimide and, +5 kV for Polyoxymethylene for positive polarity.

Figure 6.20 shows the volt-time graphs from the ~50% RH, 0 bar gauge results, where there is a clear grouping of positive data (including the open-air gap), whereas the negative data shows a clear decrease in the flashover voltage with all spacers, compared to that for the open gap.

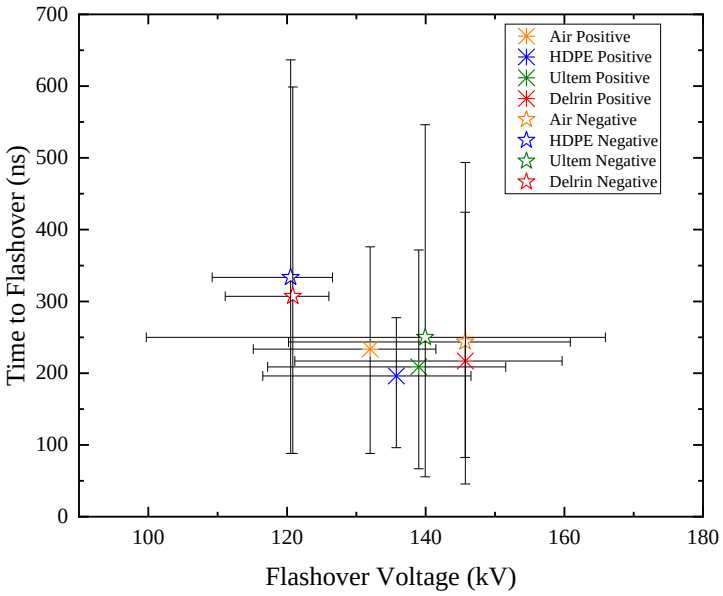

Figure 6.20. - Volt-time graphs of negative and positive polarity energisation, for open air, HDPE, Polyetherimide and Polyoxymethylene at ~50% RH and 0 bar gauge.

From Figure 6.20, it can be seen that for all compared cases for each polarity, there are overlapping error bars. This follows the same pattern seen at -0.5 bar gauge, where the inclusion of a spacer of any material decreases the nominal negative breakdown voltage compared to that for an open gap, but there is no such reduction for positive polarity. The differences in the nominal flashover values in comparison to those for open gaps (air) were: -25.2 kV for HDPE, -5.8 kV for Polyetherimide and -24.9 kV for Polyoxymethylene for negative polarity; and +3.8 kV for HDPE, +7 kV for Polyetherimide and, +13.7 kV for Polyoxymethylene for positive polarity.

Figure 6.26 shows the volt-time graphs from the ~50% RH, 0 bar gauge results, where there are clear groupings for the positive insulation systems. This close grouping of similar flashover voltage/time to flashover provide a clear visualisation of the behaviours, with similar performance for all air-solid systems and the open gap for positive polarity, while for negative polarity, there are two distinct groupings, due to the decrease in the flashover voltage of HDPE and Polyoxymethylene air-solid systems compared to that for the open gap, but a similar performance for Polyetherimide.

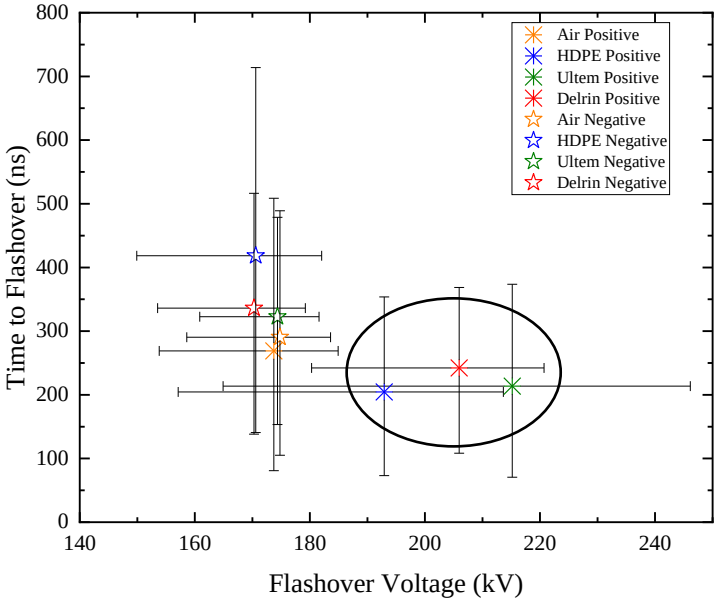

Figure 6.21. - Volt-time graphs of negative and positive polarity energisation, for open air, HDPE, Polyetherimide and Polyoxymethylene at ~50% RH and 0.5 bar gauge.

From Figure 6.21, it can be seen that there are overlapping error bars for all compared tests, for each polarity. This follows the same pattern seen at -0.5 and 0 bar gauge, where the inclusion of a spacer of any material decreases the nominal negative breakdown voltage compared to that for an open gap. However, for positive polarity, a large increase in the flashover voltage on comparison to air is resultant - The differences in the nominal flashover values in comparison to that for the corresponding open gap (air) were -4.2 kV for HDPE, -0.4 kV for Polyetherimide and -4.5 kV for Polyoxymethylene for negative polarity; and +9.2 kV for HDPE, +41.5 kV for Polyetherimide and, +32.3 kV for Polyoxymethylene for positive polarity.

Figure 6.21 shows the volt-time graphs from the ~50% RH, 0 bar gauge results, where there is a clear grouping for negative insulation performance. This close grouping of similar flashover voltage/time to flashover shown in Figure 6.21 supports the theory outlined in Section 6.3.2, where the interaction with the knurled surface for negative polarity discharges results in similar performances to an open gap system, while for positive polarity the increase in V_{50} shows the effect of the interaction of the knurled surface with positive polarity discharges.

In terms of polarity, the key findings for tests within a ~50% RH environment were –

- At -0.5 bar gauge for each insulation system, it was found that for HDPE, the positive polarity flashover voltage was greater than the negative, whereas no polarity effect was observed for Polyetherimide and Polyoxymethylene.
- For 0 bar gauge tests, there was an decrease in the positive and negative flashover voltages for HDPE and Polyoxymethylene in negative polarity, where the positive polarity voltages were higher than those under negative polarity; for Polyetherimide, however, no polarity effect was observed.
- When increasing the pressure further to 0.5 bar gauge, a polarity effect on the measured breakdown voltages was evident, with positive flashover voltages being higher than negative for gaps bridged by solid spacers with knurled surfaces of all materials.

Further discussion is made in Section 6.5.2 where possible mechanisms for the increased flashover voltage in comparison to an open gap as well as a smooth machined spacer arrangement.

6.4.3. >90% RH

Figures 6.22, 6.23 and 6.24 shows the volt-time graphs for this data, where there are distributions of positive and negative data. These points illustrate the similar behaviour of air-solid gaps and open-air gaps for each polarity.

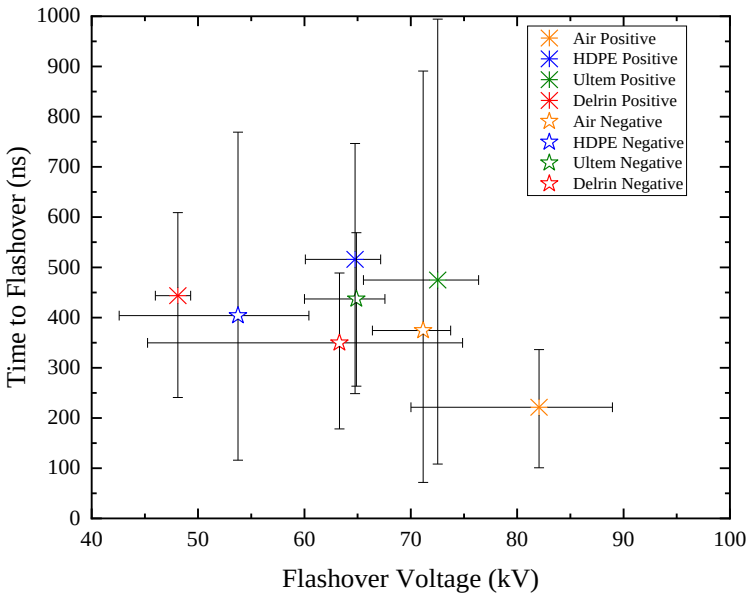

Figure 6.22. - Volt-time graphs of negative and positive polarity energisation, for open air, HDPE, Polyetherimide and Polyoxymethylene at >90% RH and -0.5 bar gauge.

From Figure 6.22 it can be seen that for negative polarity, there are overlapping error bars between the open gap test and those for air-solid gaps with Polyetherimide and Polyoxymethylene spacers, while for HDPE, the breakdown voltage is lower than that for the open-air gap, with no overlap of the error bars. For positive polarity, there are overlapping error bars between the tests with an Polyetherimide spacer and the open-air gap, while the HDPE and Derlin spacers result in a decreased breakdown voltage compared to that for an open gap, with no overlap of the error bars (~95.4% spread of data). The differences in the nominal flashover values in comparison to that for the corresponding open gap (air) were -17.4 kV for HDPE, -6.3 kV for Polyetherimide and -7.9 kV for Polyoxymethylene for negative polarity; and -17.3 kV for HDPE, -9.6 kV for Polyetherimide and, -34 kV for Polyoxymethylene for positive polarity.

Figure 6.22 shows the volt-time graphs from the >90% RH, -0.5 bar gauge results, highlighting the clear decrease in V_{50} compared to that for the corresponding open gap for both positive and negative insulation systems. These decreases reflect changes in the breakdown mechanism in the high humidity environment, with flashover of the spacer surfaces occurring at lower voltages than those for breakdown at the electrode edges in the open gaps, due to the increased conductivity in the vicinity of the spacer surfaces.

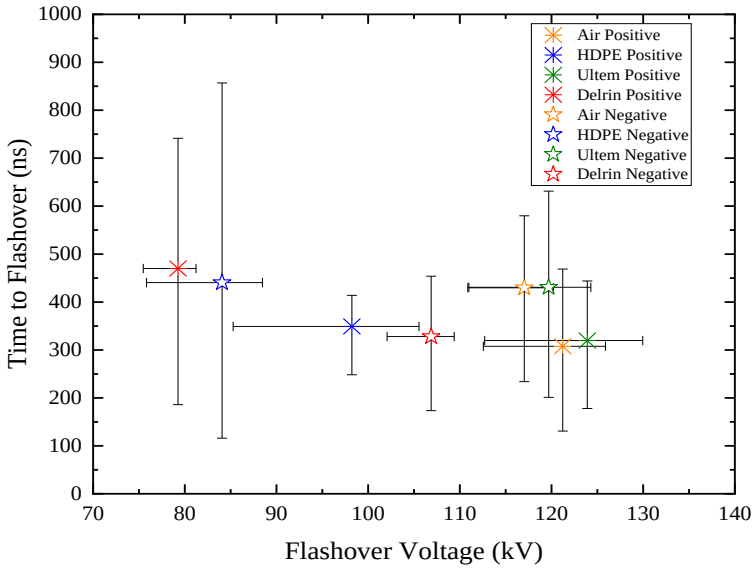

Figure 6.23. - Volt-time graphs of negative and positive polarity energisation, for open air, HDPE, Polyetherimide and Polyoxymethylene at >90% RH and 0 bar gauge.

From Figure 6.23, it can be seen that for negative polarity, there are overlapping error bars between the tests with an Polyetherimide spacer and an open gap - for HDPE and Polyoxymethylene, however, the breakdown voltage is reduced compared to that for an open gap, with no overlap of the error bars, signifying no overlap of the distributions (95.4% spread of data). For positive polarity, the same behaviours to those for negative polarity are evident in this case, for all materials. The differences in the nominal flashover values in comparison to that for the corresponding open gap (air) were -32.9 kV for HDPE, +2.7 kV for Polyetherimide and -10.1 kV for Polyoxymethylene for negative polarity; and -23 kV for HDPE, +2.7 kV for Polyetherimide and, -41.9 kV for Polyoxymethylene for positive polarity.

As shown from the graph in Figure 6.23, it is evident that there is a decrease in the positive and negative flashover voltages, compared to that for an open gap, with HDPE and Polyoxymethylene spacers in the high humidity environment, while Polyetherimide shows a similar performance to the open gap, for both polarities.

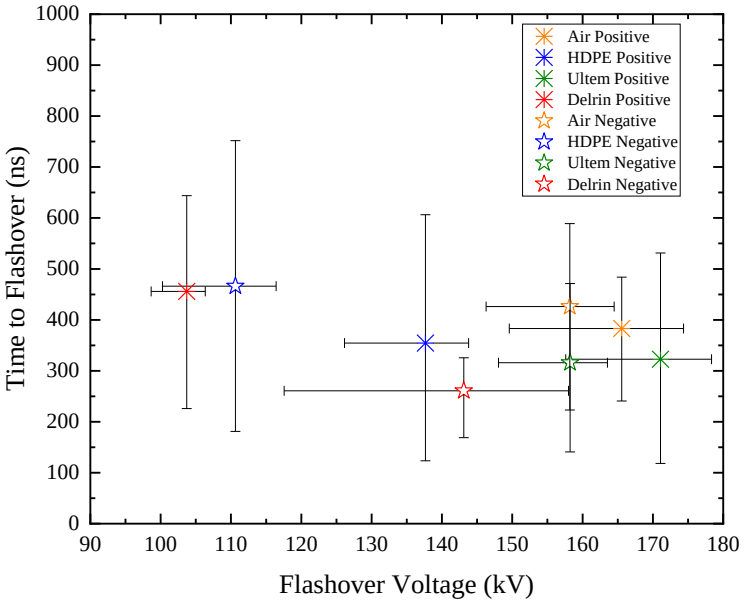

Figure 6.24. - Volt-time graphs of negative and positive polarity energisation, for open air, HDPE, Polyetherimide and Polyoxymethylene at >90% RH and 0.5 bar gauge.

From Figure 6.24, it can be seen that for negative polarity, there are overlapping error bars between the data for insulation systems with Polyetherimide and Polyoxymethylene spacers and the open gap - for HDPE, however, the breakdown voltage is reduced compared to that for an open-air gap, with no overlap of the error bars. For positive polarity, there are overlapping error bars between the tests with an Polyetherimide spacer and the open gap, but the HDPE and Derlin spacers are shown to decrease the breakdown voltage and their data sets are not overlapping to a ~95.4% spread. The differences in the nominal flashover values in comparison to that for the corresponding open gap (air) were -47.6 kV for HDPE, +0 kV for Polyetherimide and -15.1 kV for Polyoxymethylene for negative polarity; and -27.9 kV for HDPE, +5.5 kV for Polyetherimide and, -61.9 kV for Polyoxymethylene for positive polarity.

Figure 6.24 shows the volt-time graphs from the >90% RH, 0.5 bar gauge results. Where the breakdown voltages are reduced compared to that for the corresponding open gap, this is potentially due to flashover of the solid surfaces becoming the dominant breakdown mechanism for most tests in the high humidity environment, with increased conductivity in the vicinity of the surfaces. However, for Polyetherimide, the similarities between the open-gap breakdown results for both positive and negative polarity indicate a flashover on the outer electrode edge.

Summarising the key findings in terms of voltage polarity for tests within a >90% RH environment, it was found that –

- At -0.5 bar gauge for each insulation system, for HDPE and Polyetherimide, the positive polarity flashover voltage was greater than the negative, whereas for Polyoxymethylene, it was found that the negative polarity flashover voltage was greater than the positive.
- For 0 bar gauge tests, the positive flashover voltage was higher than the negative with an HDPE spacer; for Polyetherimide there was no statistical difference between positive and negative polarity flashover voltages; and for Polyoxymethylene, the negative flashover voltage was higher than the positive.
- At 0.5 bar gauge, for HDPE and Polyetherimide, it was shown that the positive flashover voltage was higher than the negative, whereas for Derlin, the negative flashover voltage is higher than the positive.

These results are discussed further in Section 6.5.3 where hypotheses have been made in relation to the increased flashover voltage in comparison to an open gap as well as smooth machined spacer arrangement.

6.5. COMPARISON WITH BREAKDOWN CHARACTERISTICS OF AIR-SOLID GAPS WITH SMOOTH (MACHINED) SPACER SURFACES

In order to characterise the effect that modifying the surface of the spacer alone has on the flashover voltage of the system, this section will provide direct comparison between the average breakdown voltage magnitude values that were measured during the testing process. The results in each section are compared in terms of relative humidity and pressure, to check if, under certain circumstances, the flashover voltage of the insulation system was increased *only* by modifying the surface of the insulator.

6.5.1. <10% RH

When comparing the negative polarity results between knurled dielectric surface and smooth machined surface arrangements, as the humidity is increased, the difference in breakdown voltage changes as the water content increases within the test-cell. Firstly, looking at direct comparisons between no spacer and with spacer tests at <10% RH, the magnitude of the breakdown/flashover voltage value is generally consistent for both.

Figures 6.25, 6.26 and 6.27 show the volt-time graphs for this data. The numerical values associated with Figures 6.25, 6.26 and 6.27 are shown in Table AP2u in Appendix 2.

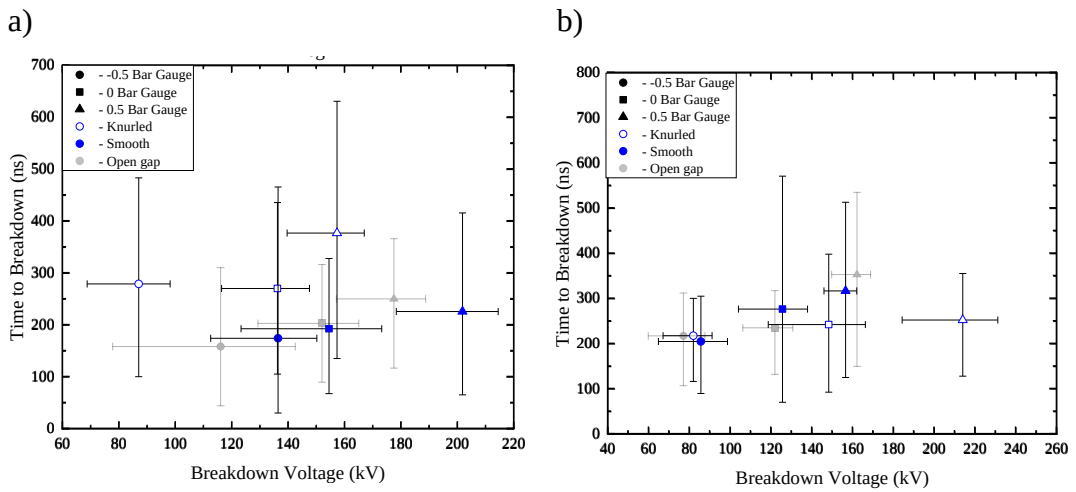

Figure 6.25. - Volt-time plots for HDPE smooth (machined) and knurled surfaces, in comparison to open gap breakdown for a) negative polarity and b) positive polarity.

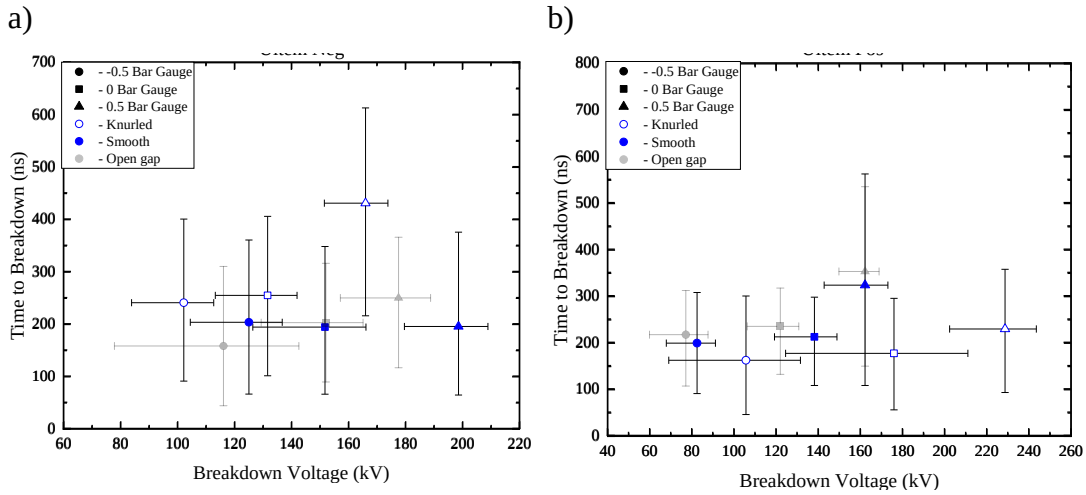

Figure 6.26. - Polyetherimide smooth machined and knurled surface in comparison to open gap breakdown for a) negative polarity and b) positive polarity

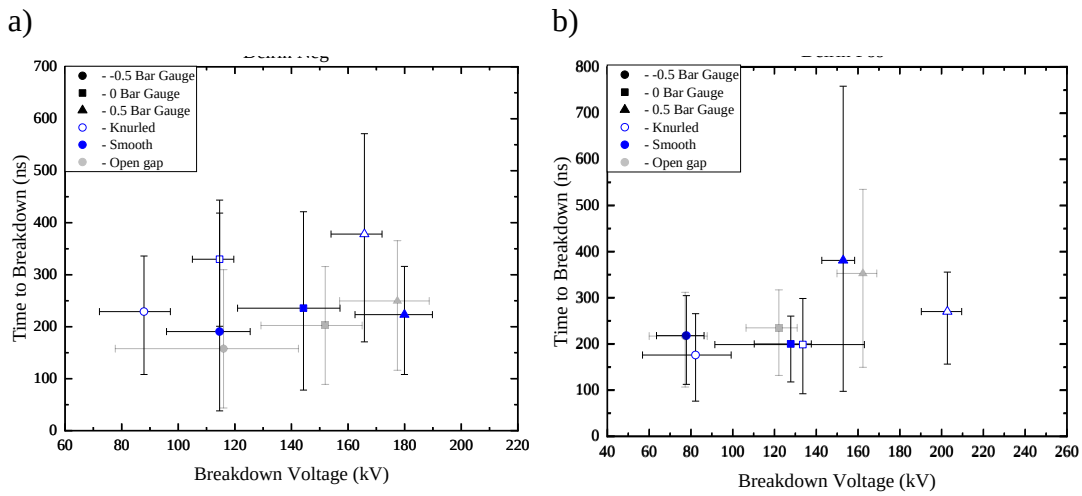

Figure 6.27. Polyoxymethylene smooth machined and knurled surface in comparison to open gap breakdown for a) negative polarity and b) positive polarity

Comparing the results for HDPE spacers from Figure 6.25, when the material surface is knurled, there is a change in the performance of the insulation system with respect to polarity, compared to when the HDPE surface is smooth. For negative polarity, the average breakdown voltage for knurled surfaces is always seen to be lower than that for smooth surfaces, irrespective of pressure. The opposite effect is observed under positive polarity impulses, where knurled HDPE surfaces have higher average breakdown voltages than smooth surfaces at 0 and 0.5 bar gauge pressures. At −0.5 bar gauge, there are overlapping error bars between the results for smooth and knurled surfaces for positive polarity, also showing a change from negative polarity energisation. The differences in the V_{50} flashover voltages for HDPE knurled surface insulation systems in comparison to a smooth machined surface were -49.4 kV for -0.5 bar gauge, -18.3 kV for 0 bar gauge and -44.5 kV for 0.5 bar gauge for negative polarity; and -3.7 kV for -0.5 bar gauge, +22.7 kV for 0 bar gauge and, +57.4 kV for 0.5 bar gauge for positive polarity.

Polyetherimide results follow a very similar trend to those of HDPE, where, again, for negative polarity, Polyetherimide spacers with smooth (machined) surfaces always have a higher average flashover voltage than those for knurled surfaces. For positive polarity, however, Polyetherimide spacers with knurled surfaces show higher average flashover voltages than smooth (machined) surfaces, at all pressures. As a result, just changing the energisation polarity changes the behaviour of the system with an Polyetherimide spacer: the smooth surfaces have higher average breakdown voltage than knurled for negative polarity; while the knurled surfaces have higher average breakdown voltage than smooth for positive polarity, for all tested pressures. The differences in the V_{50} flashover voltages for Polyetherimide knurled surface insulation systems in comparison to a smooth machined surface were -22.8 kV for -0.5 bar gauge, -20.1 kV for 0 bar gauge and -32.7 kV for 0.5 bar gauge for negative polarity; and +23.2 kV for -0.5 bar gauge, +37.7 kV for 0 bar gauge and, +66.4 kV for 0.5 bar gauge positive polarity.

For Polyoxymethylene, irrespective of pressure, the average negative flashover voltages are always higher for smooth machined surfaces, similar to the behaviour of HDPE. For positive polarity, Polyoxymethylene spacers with knurled surfaces show average flashover voltages higher than those for smooth (machined) surfaces, however

with overlapping error bars at −0.5 bar gauge and 0 bar gauge. At 0.5 bar gauge, however, there is a large increase in the average flashover voltage for a knurled surface spacer under positive polarity. The differences in the V_{50} flashover voltages for Polyoxymethylene knurled surface insulation systems in comparison to a smooth machined surface were -26.8 kV for -0.5 bar gauge, -29.6 kV for 0 bar gauge and -14.2 kV for 0.5 bar gauge for negative polarity; and +4.4 kV for -0.5 bar gauge, +5.8 kV for 0 bar gauge and, +49.9 kV for 0.5 bar gauge positive polarity.

These behaviours can be visualised by plotting the volt-time graphs for each material (smooth and knurled) and comparing with the baseline data for the corresponding open gap, where discharges always occurred at the electrode edges. The additional information on the time to breakdown will aid in the discussion of the dominant discharge mechanism for different tests.

Comparing the results for HDPE spacers only in Figure 6.25, it can be seen that, when the material surface is knurled, there is a change in the performance of the insulation system with respect to polarity, compared to when the HDPE surface is smooth. For smooth surfaces, the average positive breakdown voltage is always seen to be lower than that for negative polarity, irrespective of pressure, shown from the figures in Section 6.2.1. The opposite effect is observed when the HDPE surfaces are knurled, at higher pressures, with the average positive flashover voltage seen to be much higher than that for negative polarity, especially at 0.5 bar gauge, as shown in the figures in Section 6.2.1.

The data points in Figures 6.25a and 6.25b show that for negative polarity, the open gap results are similar to those with smooth (machined) surfaces, whereas with knurled surfaces, the flashover voltages are lower in magnitude, as well as having a longer time to flashover. This shows that the dominant breakdown mechanism with smooth (machined) surfaces is flashover over the rounded edges of the electrodes, as occurs in the open gap. For knurled surfaces, the magnitude of the flashover voltage is lower, due to discharges occurring across the spacer surfaces. As the indentations on the knurled surfaces have a small effect on the formation of negative streamers, the flashover voltages decrease in magnitude compared to those for the open gap and with smooth (machined) surface spacers.

For positive polarity, the data points at -0.5 bar gauge show a very similar performance for an open gap, and gaps with smooth and knurled spacers. However, when the pressure is increased, the difference in the performance of the different insulation systems becomes apparent. At 0 bar gauge, the breakdown voltages with knurled spacer surfaces start to increase in magnitude in comparison to those for both, open gaps and gaps with smooth spacer surfaces. Moving to 0.5 bar gauge, the knurled spacer surfaces clearly result in much higher flashover voltages than for the other gaps. This is hypothesised as being due to the combined effects of discharges at the TJP at high field regions, and the effective ionisation zone created at each specific pressure on streamer development. As the pressure increases, the effect of the TJP on the charge concentration in the developing discharge is not sufficient enough to result in flashover, due to the charge mitigation of electrons on the knurled surface, as discussed in Section 6.3.1 At lower pressures, the effective ionisation zone is increased, and the TJP has less of an effect on the discharge initiation, which results in flashover at a lower voltages, reflected in the 0 bar gauge and -0.5 bar gauge results.

Viewing the Polyetherimide results in Figure 6.26, these follow a very similar trend to those for HDPE. Again, Polyetherimide spacers with smooth (machined) surfaces always had a higher average negative flashover voltage than positive. At higher pressures (particularly 0.5 bar) with a knurled surface finish, the average positive breakdown voltage is higher than the negative.

The data points in Figures 6.26a and 6.26b reflect a very similar performance to that of HDPE insulation systems at <10% RH. For negative polarity, the results with smooth (machined) spacers bridging the gap are similar to those for an open gap, whereas for knurled spacers, the flashover voltages are lower in magnitude, as well as having a longer time to flashover.

For positive polarity, the data points at -0.5 bar gauge show a very similar performance for an open gap, and for gaps bridged by smooth spacers, and knurled spacers. When the pressure is increased, however, the difference in the insulation performance becomes apparent. At 0 bar gauge, the breakdown voltages with knurled spacers begin to increase in magnitude in comparison to those for both, open gap, and gaps with

smooth (machined) spacers. At 0.5 bar gauge, the knurled spacer is shown to have a much higher flashover voltage.

In Figure 6.27, Polyoxymethylene shows a very similar performance to that of HDPE and Polyetherimide, where, irrespective of pressure, the average negative breakdown voltages are always higher than the positive, for smooth (machined) surfaces. For Polyoxymethylene spacers with knurled surfaces, the average flashover voltage is seen to be higher for positive polarity than for negative at higher pressures, especially, again, at 0.5 bar gauge.

Overall, as the insulation systems with spacers made of the three different materials show very similar behaviour, it is clear that the surface of the material is affecting the discharge location, which is having a direct effect on the flashover performance of the insulation systems at <10% RH. It is apparent that, at <10% RH, the performance of the smooth machined insulation system is generally governed by the electrode arrangement and gas pressure under negative and positive energisation , while for knurled spacer surfaces, the flashover performance is generally governed by the impulse polarity and gas pressure.

6.5.1.1. Discussion

What is evident from Figures 6.25, 6.26 and 6.27, is that with a knurled spacer surface, as the pressure increases, not only does the knurled surface provide a higher flashover voltage than a smooth spacer surface, but also a higher flashover voltage than an open gap system, due to discharges initiating from the rounded electrode edge at <10% RH in smooth machined surfaces and open gap at <10% RH. Therefore, in addition to the discussion in Section 6.3.2., the difference between positive and negative energisation is shown have an effect on the plasma channel as it traverses the dielectric surface under knurled surface modification. For a smooth (machined) surface, the plasma channel was located at the outer electrode edge for all breakdowns (Fig. 5.13), irrespective of polarity and material. This is due to the TJP angle resulting in the highest electric field residing at the rounded edge of the electrode, which was shown in Figure 3.15. This behaviour manifests in the similar V_{50} voltages for air-solid insulation systems with smooth (machined) surfaces and the corresponding open-air gap, with similar processes governing the breakdown event discussed in Section 5.3.2,

and also in 5.3.1, showing that the relative permittivity of the solid has little effect on V_{50} for these conditions, as the tests exhibit overlapping error bars.

For knurled surfaces, the behaviour of the insulation system is more complex, with the occurrence of discharges closely coupled to the (knurled) sample surface (Figure 6.15) due to the high electric field regions produced as shown from the changing TJP angle, Figure 3.15., as well as discharges propagating between the electrode edges (Figure 5.13). Viewing the experimental results reported here as a whole, encompassing breakdown voltage data and the visual observations, it is clear that the process of knurling the sample surfaces can result in an increased positive V_{50} flashover voltage for certain environmental conditions, linked with a change in the discharge mechanism. This indicates the occurrence of competing breakdown mechanisms, where discharges are initiated at both, the high field region associated with the TJP, and that associated with the electrode edge. One of these discharges will bridge the gap first, leading to breakdown. Researchers in [23] showed that the addition of a screening electrode can increase the breakdown voltage when surface flashover and bulk air breakdown processes are competing. This is particularly relevant in relation to the results generated at 0.5 bar gauge in Figures 6.6c, 6.10c and 6.14c herein, where the positive V_{50} values for knurled surfaces of all tested materials (with different ε_r), are higher than those for smooth (machined) surfaces, as well as those for an open-air gap, despite the increasing field at the TJP with increasing ε_r.

However, the same performance is not seen under negative polarity. To explain this, the differences between the positive and negative flashover processes have to be discussed, where the mechanisms of positive and negative streamer growth and propagation are different when in the vicinity of a dielectric surface as discussed in 6.3.2 This effect could increase the positive-polarity flashover voltage, which corresponds with empirical data found in this work.

For positive polarity, electrons produced over the surface of the material from SEE processes, and electrons produced through photoionisation at the head of the streamer in the bulk gas which are not adsorbed to the dielectric surface, will expand and further weaken the electric field at the positive streamer head, [12]. Due to the weakening of the electric field, a higher applied voltage will be required to initiate flashover, than

across a non-profiled surface. This effect of positive streamer development has been seen in previous research on profiled dielectric surfaces tested under positive polarity impulse voltages, [11], where discharges were observed by a high-speed camera to propagate only partially across insulator surfaces. For the formation of negative streamers, however, they do not rely as much on adsorbed electrons from the gas-solid interface, where any electrons which are adsorbed by the surface will have little effect of the field at the front of the streamer as the electrons emanate from the streamer head in the gas/solid interface, manifesting in a lower applied voltage to initiate flashover.

Another possible mechanism leading to higher positive breakdown voltages in the case of knurled dielectric spacers, as compared with smooth spacers and open-air breakdown voltages is proposed. Due to the plasma streamer(s) propagating some distance over the dielectric surface, similar to as shown visually in [11], the electric field in the whole system can be re-distributed resulting in a decrease in the field on the electrode edge. An axisymmetric electrostatic model was created using the QuickField finite element solver and the field distribution in the current setup has been obtained in two different cases. The simulation results are shown in Figure 6.28. It must be noted that this is a limited axisymmetric model the geometry of which is not representative of the physical system.

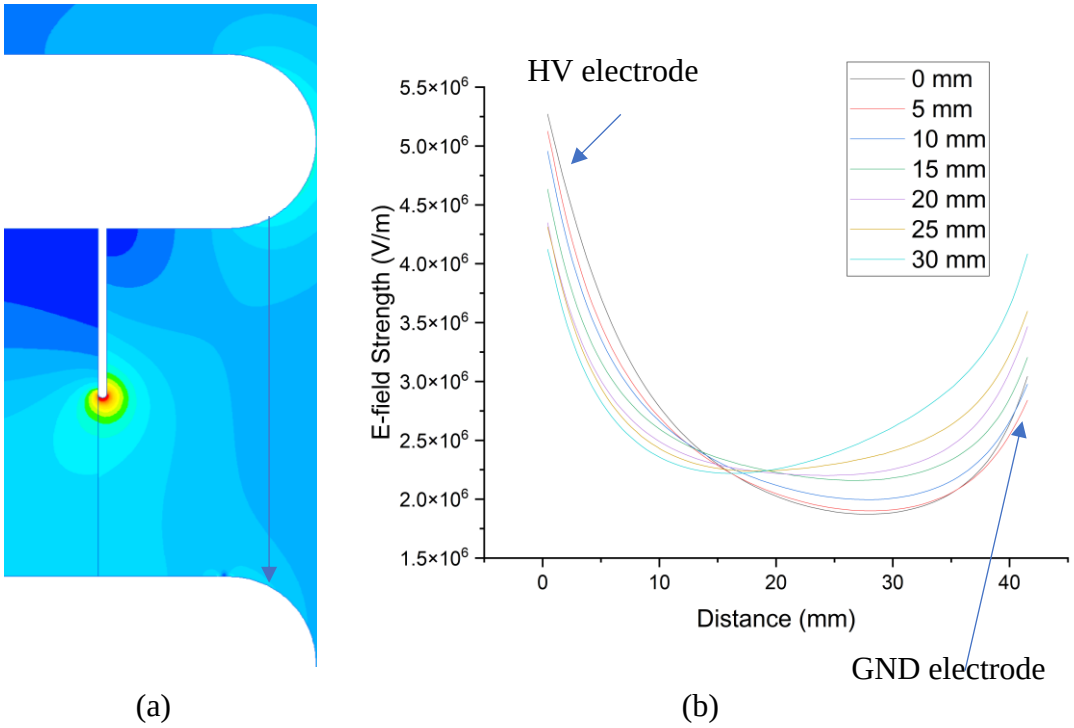

(a) (b)

Figure 6.28 – a) Axisymmetric electrostatic simulation of discharge channel partially across the dielectric surface, in this representation the discharge channel is 20 mm long b) the resultant electric field distribution across the gap as shown by the contour line in a), from 5 – 30 mm, in increments of 5 mm. an applied voltage of 100 kV was applied to this model.

The baseline field distribution was obtained for a smooth dielectric, with no streamer(s) propagating. It is shown that the maximum field in this case is achieved at the electrode edge. However, when a streamer starts to propagate across the air/dielectric interface, the field at the electrode edge started to reduce. The streamer initiated at the triple junction was modelled as a 1 mm wide conducting channel attached to the high voltage electrode, and this channel (streamer) is at the same potential as the HV electrode. As the streamer increases in length (l_p), along the dielectric surface, this results in a decrease in the field at the electrode edge by 6% at l_p =10 mm, by 18% at l_p =20 mm and by 23% at l_p = 30 mm, in comparison to the 'no streamer' electric field distribution, reducing the probability for the development of a "competitive" streamer(s) which can cross the gap though the bulk air at the electrode edge. The change in electric field at the rounded electrode edge in comparison to a streamer development across the dielectric surface from Fig.6.28b is shown more clearly in in Figure 6.29.

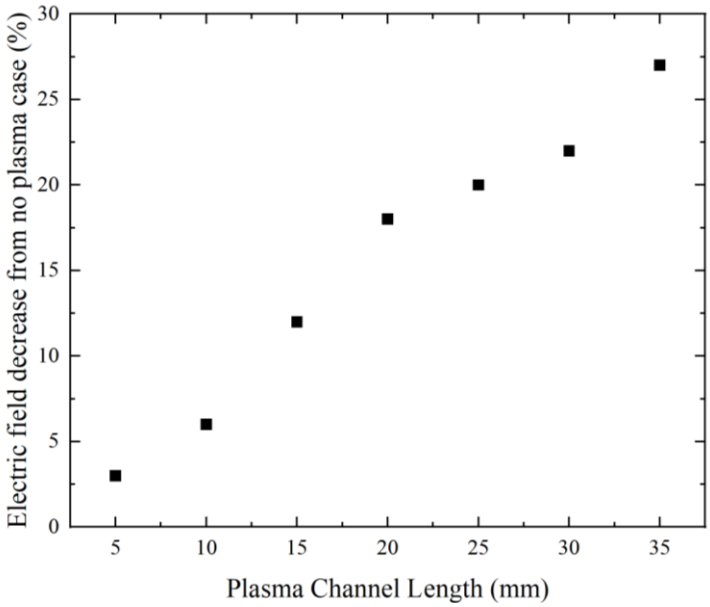

Figure 6.29 – Reduction in field at rounded edge of electrode as plasma channel traverses' different lengths across the dielectric surface.

Thus, in the case of the knurled surface, the streamer is initiated at the triple junction and propagates across the air/dielectric interface, however its development requires an increased applied voltage as the streamer will have a longer length (compared with the case of the smooth spacer) and larger voltage drop across its "body". This increases the breakdown/flashover voltage of the insulation system, leading to either an eventual flashover over the full surface of the knurled insulator, or breakdown in bulk air at the electrode edge (both at a higher applied voltage), giving a potential reason for the higher positive V_{50} for knurled surfaces compared to for smooth surfaces and open-air gaps.

In terms of air pressure, the V_{50} flashover voltages for knurled surfaces are shown to be higher than those for smooth surfaces at 0 bar gauge pressure, as seen in Figure 6.6b, and at 0.5 bar gauge pressure, as seen in Figure 6.6c. There is clearly less of an effect at −0.5 bar gauge, in Figure 6.6a. A potential reason for this is that, as the pressure increases, the discharge tends to initiate closer to the TJP, as discussed in [22]. Based upon this, the development of positive and negative streamer discharges in the vicinity of dielectric surfaces is affected in different ways. The development of positive streamers is further impeded by the knurled surface with increasing pressure, due to the mechanisms of positive discharges near dielectric surfaces in Section 6.3.2., decreasing the field at the head of the streamer. However, as negative discharges are

wider and more diffuse, as discussed in [11], and with electrons emanating from the streamer head, there is minimal effect of the field at the front of the negative streamer, so therefore, the pressure, and the initial location of the discharge at the TJP has little effect on the flashover voltage.

6.5.2. ~50% RH

Figures 6.30, 6.31 and 6.32 show the volt-time graphs from the ~50% RH results. The numerical values associated with Figures 6.30, 6.31 and 6.32 are shown in Table AP2v Appendix 2.

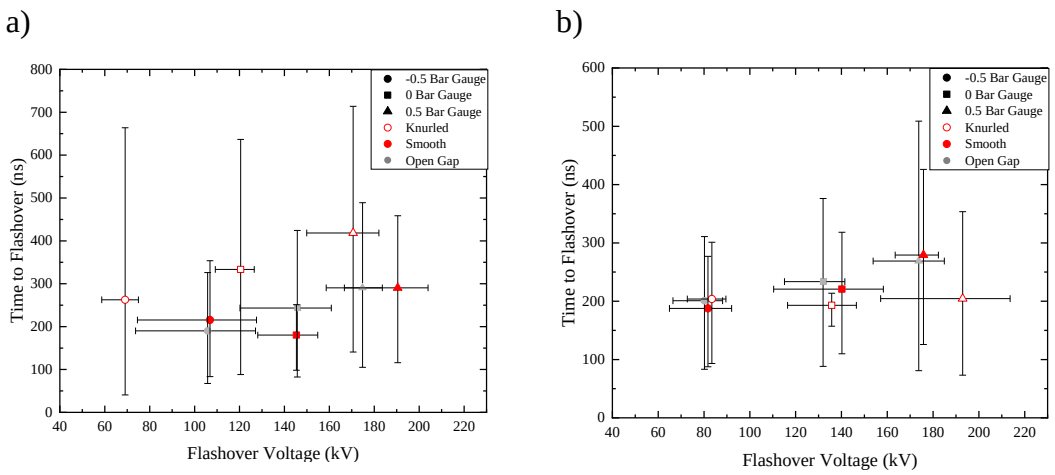

Figure 6.30. Volt-time plots for HDPE smooth (machined) and knurled surfaces, in comparison to open gap breakdown for a) negative polarity and b) positive polarity.

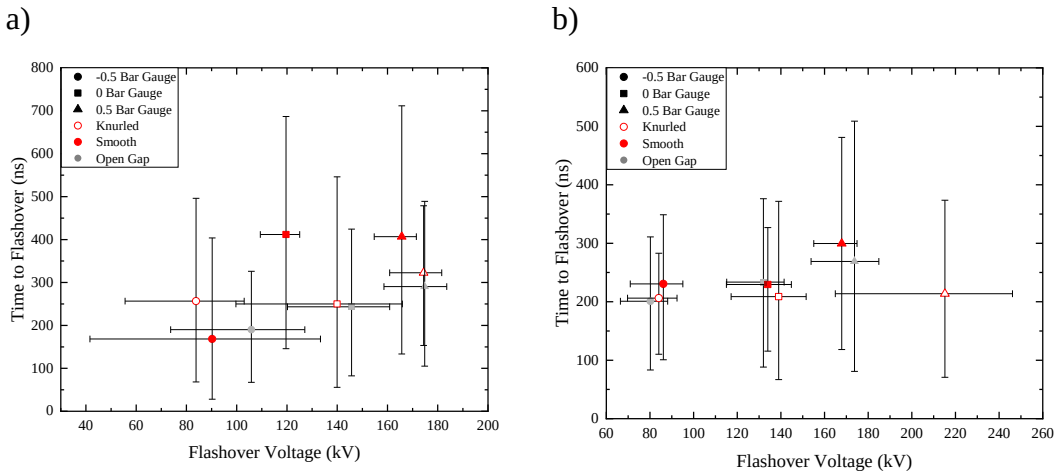

Figure 6.31. Volt-time plots for Polyetherimide smooth (machined) and knurled surfaces, in comparison to open gap breakdown for a) negative polarity and b) positive polarity.

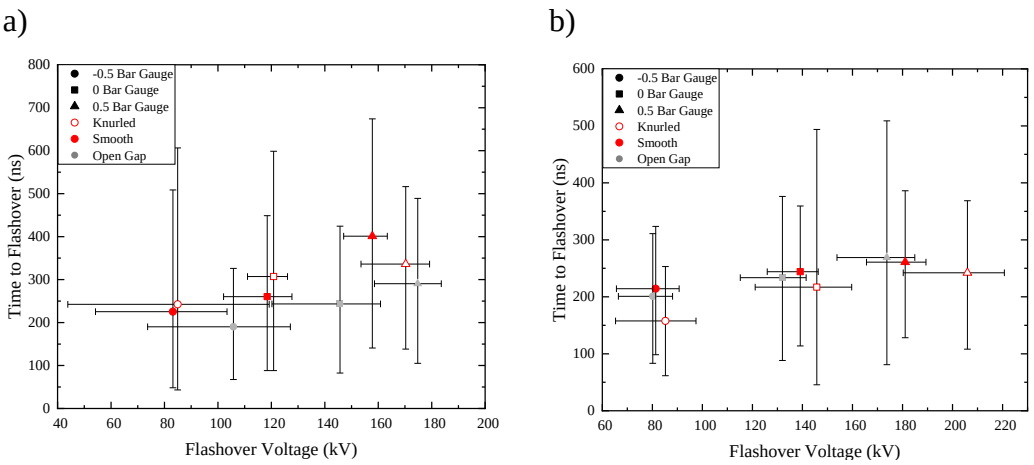

Figure 6.32. Volt-time plots for Polyoxymethylene smooth (machined) and knurled surfaces, in comparison to open gap breakdown for a) negative polarity and b) positive polarity.

Comparing the behaviour of the smooth and knurled HDPE spacers in Figure 6.30, again, the change in behaviour of the insulation system is evident for negative polarity. Under negative polarity energisation, the smooth surface had a higher average flashover voltage than knurled, for all tested pressures. However, for positive polarity energisation, at -0.5 and 0 bar gauge, there is a small difference between the flashover performance of smooth and knurled spacers, with the difference becoming more pronounced at 0.5 bar gauge, where the knurled spacer shows a higher V_{50} flashover voltage than the smooth spacer. The differences in the V_{50} flashover voltages for HDPE knurled surface insulation systems in comparison to a smooth machined surface were -37.8 kV for -0.5 bar gauge, -24.8 kV for 0 bar gauge and -19.9 kV for 0.5 bar gauge for negative polarity; and +1.7 kV for -0.5 bar gauge, -4.4 kV for 0 bar gauge and, +17.1 kV for 0.5 bar gauge for positive polarity.

For Polyetherimide spacers, under negative polarity energisation, for all pressures, there were similar results for the smooth (machined) surface and the knurled surface, with increasing breakdown voltages for knurled spacers as pressure increases. For positive polarity, at −0.5 and 0 bar gauge, there was a small differences in the average breakdown voltage for smooth and knurled surfaces. Increasing the pressure to 0.5 bar gauge, the knurled surface has a better performance than the smooth surface, with a higher average breakdown voltage. However, the range describing the ~95.4% spread of data is shown to increase greatly at 0.5 bar gauge. The differences in the V_{50} flashover voltages for Polyetherimide knurled surface insulation systems in

comparison to a smooth machined surface were -6.4 kV for -0.5 bar gauge, +20.3 kV for 0 bar gauge and +8.7 kV for 0.5 bar gauge for negative polarity; and -2 kV for -0.5 bar gauge, +5 kV for 0 bar gauge and, +47.3 kV for 0.5 bar gauge for positive polarity.

Finally, for Polyoxymethylene, the difference in performance for smooth and knurled surfaces is less irrespective of polarity. Similar to the Polyetherimide results, under negative polarity energisation, for all pressures, the breakdown voltages for the smooth (machined) surface and the knurled surface were similar, but with higher V_{50} for knurled spacers as pressure increases. For positive polarity energisation, again, at −0.5 and 0 bar gauge, there is a small difference only between the V_{50} values for smooth and knurled surfaces. However, again, at 0.5 bar gauge, the average breakdown voltage of the knurled surface exceeds that of the smooth (machined) surface. The differences in the V_{50} flashover voltages for Polyoxymethylene knurled surface insulation systems in comparison to a smooth machined surface were +1.8 kV for -0.5 bar gauge, +2.3 kV for 0 bar gauge and +12.5 kV for 0.5 bar gauge for negative polarity; and +3.9 kV for -0.5 bar gauge, +6.6 kV for 0 bar gauge and, +24.9 kV for 0.5 bar gauge for positive polarity.

Figures 6.30 (HDPE), 6.31 (Polyetherimide) and 6.32 (Polyoxymethylene) show the difference in volt-time characteristics at ~50% RH of open gaps, gaps with smooth spacers, and gaps with knurled spacers, at all pressures.

Comparing the results for HDPE spacers only (plus the open gap, for reference) in Figure 6.36, it can be seen that, when the material surface is knurled, there is a clear change in the performance of the insulation system with respect to polarity, compared to when the HDPE surface is smooth. This is similar to the behaviour seen at <10% RH. For smooth surfaces, the average positive breakdown voltage is always seen to be lower than that for negative polarity, irrespective of pressure, shown from Figures 5.2, 5.4 and 5.6 in Section 5.2.1. The opposite effect is observed when the HDPE surfaces are knurled, at higher pressures, with the average positive flashover voltage seen to be generally higher than that for negative polarity, especially at 0.5 bar gauge, as shown in Figures 6.6c, 6.10c and 6.14c in Section 6.2.1.

Similar to the HDPE results shown for <10% RH in Figure 6.30a and 6.30b, the data points in Figures 6.30a and 6.30b show that, for negative polarity, the open gap results are similar to those with the smooth (machined) surface, whereas for a knurled surface, the flashover voltages are lower in magnitude, as well as having a longer time to flashover.

For the Polyetherimide results shown in Figure 6.31a and 6.31b, the behaviour under negative polarity is shown to differ from that with HDPE insulation. The flashover voltages with both smooth and knurled Polyetherimide spacers are shown to be very similar to those for the open-air gap. This may be due to the hydrophilic nature of the Polyetherimide material, resulting in the creation of a more conductive layer over the length of the surface, which is shown to affect the flashover performance. This effect, linked with the negative discharge phenomena discussed previously, where the absorption of electrons by water molecules in the humid air has less of an effect on negative streamer formation (than positive), results in irregular discharges. For positive polarity, a similar performance to that for HDPE and the <10% RH results is evident. The breakdown voltages for the open gap and for a gap with a smooth Polyetherimide surface are similar, while the breakdown voltage increases with a knurled Polyetherimide surface - this increase is due to the increased attachment coefficient in the humid air, and the mitigation of electrons on the knurled surface, requiring a higher applied voltage to cause breakdown.

The results for Polyoxymethylene spacers are shown in Figures 6.32a and 6.32b. Under negative polarity, the breakdown characteristics are very similar for the open gap, and for gaps incorporating smooth and knurled Polyoxymethylene surfaces. Although there is a slight decrease in V_{50} in comparison to that for the open gap, the larger error bars for all tests reflect that the humid air results in a more irregular discharge pattern, due to the hydrophilic nature of the material creating a more conductive surface. The flashover voltages of gaps with both knurled and smooth Polyoxymethylene surfaces are very similar to that for the open-air gap, with no clear trends evident.

For positive polarity however, a similar performance to that for HDPE and Polyetherimide spacers, and to the Polyoxymethylene results at <10% RH, is apparent.

6.5.2.1. Discussion

From the results shown in Figures 6.30, 6.31 and 6.32, as the humidity is increased from <10% RH to ~50% RH, the differences between the positive and negative V_{50} breakdown voltages have become smaller, so that they are similar, for each set of conditions, however there are still similarities to the results shown for <10% RH in Section 6.5.1. This could be attributed to the higher humidity creating an atmosphere in which the attachment coefficient is higher, due to the presence of water molecules, acting to increase the negative breakdown voltages. The amount of charge deposition on the surface of the solid spacer is determined by the humidity. As previously hypothesised, there is a potential change in the amount of charge deposition between smooth and knurled samples of the same material at <10% RH, with less charge being retained on the knurled surface, similar to the explanation given by the authors of [24] for roughened surfaces, or with charge being trapped within the indentations, creating an absorption or blocking effect, as discussed in [17]. However, due to the humidity increase for tests undertaken at ~50% RH, there is a further reduced charge deposition on both smooth and knurled surfaces, as discussed for similar work in [25], potentially explaining the increasingly (electrically) symmetrical breakdown performance.

The dependency of the material surface and the polarity of the discharge is also shown to have similarities to that at <10% RH, where the increase of pressure is shown to increase the difference between the negative and positive polarity flashover voltages, as well as increasing over an open-gap, due to similarities in the open-gap and smooth machined surface flashover mechanisms, as discussed in Section 6.5.1.

6.5.3. >90% RH

Figures 6.33, 6.34 and 6.35 show the volt-time graphs from the ~50% RH results, where there are generally, as before at <10% RH, groupings for positive and negative discharges. The numerical values associated with Figures 6.33, 6.34 and 6.35 are shown in Table AP2w in Appendix 2.

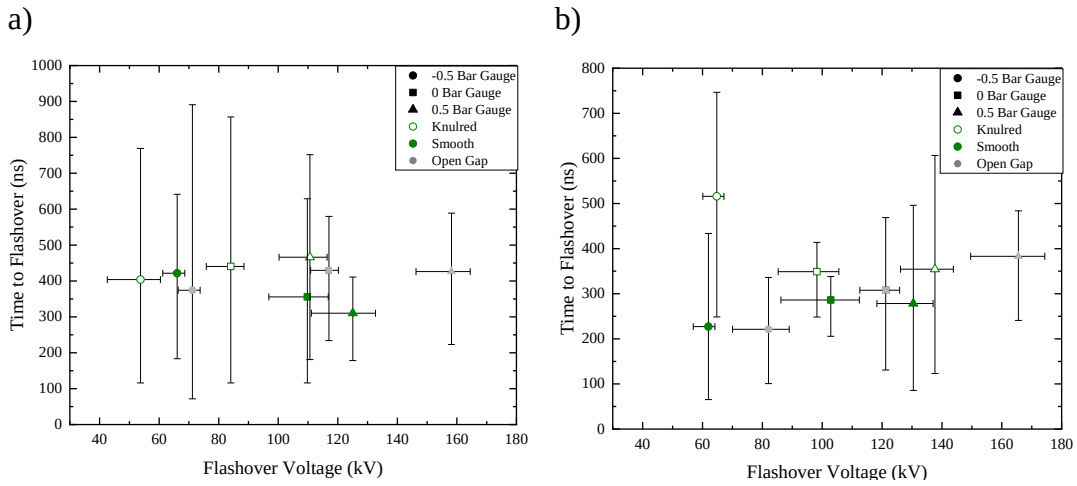

Figure 6.33. HDPE smooth machined and knurled surface in comparison to open gap breakdown for a) negative polarity and b) positive polarity

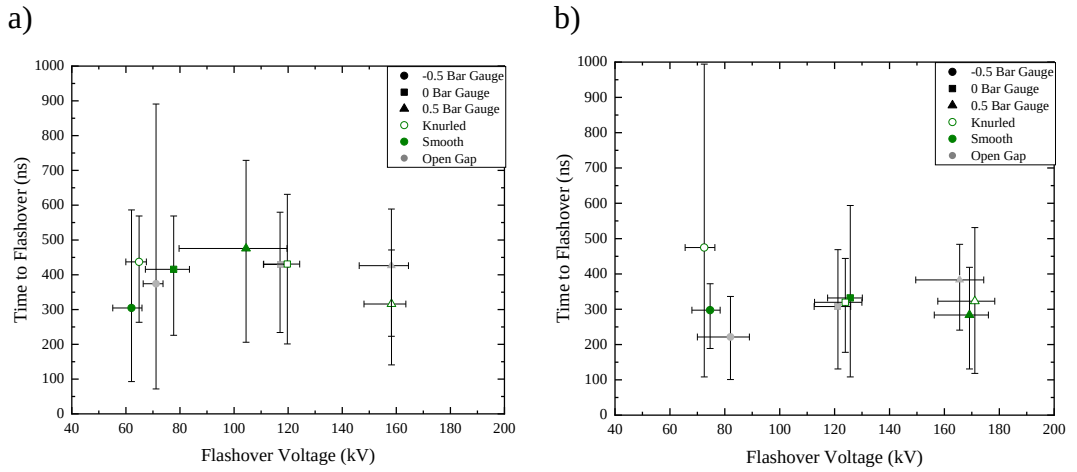

Figure 6.34. Polyetherimide smooth machined and knurled surface in comparison to open gap breakdown for a) negative polarity and b) positive polarity

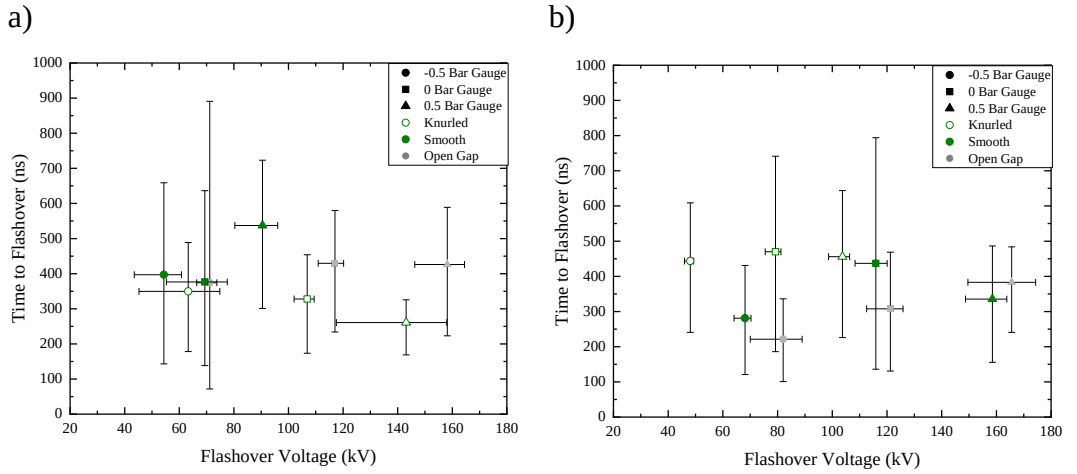

Figure 6.35. Polyoxymethylene smooth machined and knurled surface in comparison to open gap breakdown for a) negative polarity and b) positive polarity

When comparing the behaviour of the smooth and knurled surfaces of the HDPE spacers in Figure 6.33, the difference in performance of the insulation system for negative polarity is apparent, with smooth machined surfaces having higher flashover voltages than knurled, at all pressures. For positive polarity, there is very little difference between the smooth and knurled spacer average flashover voltages, at all pressures. The differences in the V_{50} flashover voltages for HDPE knurled surface insulation systems in comparison to a smooth machined surface were -12.2 kV for -0.5 bar gauge, -25.7 kV for 0 bar gauge and -14.5 kV for 0.5 bar gauge for negative polarity; and +2.8 kV for -0.5 bar gauge, -4.7 kV for 0 bar gauge and, +7.2 kV for 0.5 bar gauge for positive polarity.

For Polyetherimide spacers, under negative polarity, at −0.5 bar gauge, there is little difference in the breakdown characteristics for the smooth and knurled spacer surfaces. Increasing the pressure to 0 and 0.5 bar gauge, however, a knurled surface spacer is seen to have a higher flashover voltage. For positive energisation, there are minimal differences between the results for spacers with smooth (machined) surfaces, and those with knurled surface, for all pressures. The differences in the V_{50} flashover voltages for Polyetherimide knurled surface insulation systems in comparison to a smooth machined surface were +2.8 kV for -0.5 bar gauge, +42 kV for 0 bar gauge and +53.8 kV for 0.5 bar gauge for negative polarity; and -2.2 kV for -0.5 bar gauge, -1.8 kV for 0 bar gauge and, +2 kV for 0.5 bar gauge for positive polarity.

For Polyoxymethylene spacers, there is a similar performance to Polyetherimide under negative voltages - there is little difference in the breakdown characteristics with the smooth and knurled spacer surfaces at −0.5 bar gauge, whereas for 0 and 0.5 bar gauge, the knurled spacer shows as higher average flashover voltage. For positive polarity energisation, the smooth spacer performs better than the knurled spacer, at all tested pressures. The differences in the V_{50} flashover voltages for Polyoxymethylene knurled surface insulation systems in comparison to a smooth machined surface were +8.9 kV for -0.5 bar gauge, +37.5 kV for 0 bar gauge and +52.6 kV for 0.5 bar gauge for negative polarity; and -20 kV for -0.5 bar gauge, -36.6 kV for 0 bar gauge and, -54.8 kV for 0.5 bar gauge for positive polarity.

Figures 6.33 (HDPE), 6.40 (Polyetherimide) and 6.41 (Polyoxymethylene) show the difference in volt-time characteristics at ~50% RH of open gaps, gaps with smooth spacers, and gaps with knurled spacers, at all pressures.

Comparing the results for HDPE spacers in Figure 6.33, it can be seen that, when the material surface is knurled, there is a change in the performance of the insulation system with respect to polarity, compared to when the HDPE surface is smooth. For negative polarity in Figure 6.33a, the breakdown voltage is seen to become much more irregular to that with HDPE spacers at <10% RH and at ~50% RH. At -0.5 bar gauge and 0 bar gauge, the flashover voltage is shown to decrease in comparison to that for an open gap, with the difference between the two V_{50} values becoming wider as the pressure increases, particularly for a knurled spacer, which is shown to have the lowest flashover voltage for each test. These comparisons reflect that the dominant breakdown mechanism for knurled spacers was surface discharges at -0.5 bar gauge and 0 bar gauge, due to the synergistic effect of high field regions caused by the knurled surface and the high humidity environment. At 0.5 bar gauge, the similar breakdown characteristics for air-solid and open gaps suggest that breakdown preferentially occurred at the electrode edges, even with the solids bridging the electrodes.

For positive polarity, again the trends which were seen at <10% RH and at ~50% RH are not seen at >90% RH, due to the added humidity affecting the discharge characteristics in the insulation system. However, what is shown is that, unlike for negative polarity, the effect of the extra humidity is to decrease the flashover voltages of gaps with both knurled and smooth spacers in comparison to that for an open gap system. Therefore, it can be stated that surface flashover is the dominant breakdown mechanism with spacers of both types of surface finish.

Comparing the results for Polyetherimide spacers in Figure 6.34, it can be seen that, when the material surface is knurled, there is a change in the performance of the insulation system with respect to polarity, compared to when the Polyetherimide surface is smooth. For negative polarity in Figure 6.34a, as already seen for HDPE spacers, the breakdown voltage becomes much more irregular compared to the Polyetherimide results found at <10% RH and ~50% RH. At -0.5 bar gauge, the

breakdown characteristics are very similar for the open gap, and gaps with smooth and knurled spacers, indicating that the discharges predominantly occurred between the rounded electrode edges. Increasing the pressure to 0 bar gauge and 0.5 bar gauge, the flashover performance is very similar to the open gap results for knurled spacers, whereas there is a decrease in V_{50} in comparison to an open gap with smooth spacers, which increases in severity as the pressure increases. This behaviour can be attributed to the hydrophilic Polyetherimide surface resulting in lower electric fields local to the spacer surface, with the knurled surface essentially breaking up the conductive path formed by the surface wetness, leading to flashover over the electrode edges, whereas for smooth spacers, the lack of knurls/indentations to break up the conductive paths result in a lower flashover voltage, with breakdown occurring in the vicinity of the solid surface.

For positive polarity, three distinct regions for breakdown at -0.5 bar gauge, 0 bar gauge and 0.5 bar gauge can be seen, implying that the flashover mechanism is consistent at each level of pressure, with flashovers occurring at the electrode edges, since the results for open gap and for air-solid gaps are similar.

Comparing the results for Polyoxymethylene spacers in Figure 6.35, it can be seen that, when the material surface is knurled, there is a change in the performance of the insulation system with respect to polarity, compared to when the Polyoxymethylene surface is smooth. For negative polarity in Figure 6.35a, as also seen for HDPE and Polyetherimide spacers, the breakdown voltage is seen to become much more irregular to that with Polyoxymethylene spacers at <10% RH and at ~50% RH. At -0.5 bar gauge, the performance is shown to be very similar for open gap, and gaps with knurled and smooth (machined) spacers, indicating that the dominant discharge path is at the electrode edges. At 0 bar gauge and 0.5 bar gauge, the flashover performance is similar to the open gap results for knurled spacers, whereas there is a decrease in flashover voltage with smooth spacers in comparison to an that of an open gap, which increases in severity as the pressure increases. For Polyetherimide, the Polyoxymethylene performs similarly for Polyoxymethylene, where the hydrophilic nature of the surface results in lower local electric fields at the spacer surface, with the knurled surface essentially breaking up the conductive path formed by the surface wetness, leading to flashover over the rounded electrode edges, whereas for smooth

surface, the lack of knurls/indentations to break up the conductive paths result in flashover at the surface, at a lower voltage.

Under positive polarity, similar to for HDPE spacers, the flashover voltage greatly decreases with a knurled Polyoxymethylene spacer, in comparison to that for an open-air gap. This implies that surface flashover is the dominant breakdown mechanism for all knurled tests. However, for smooth (machined) surfaces, although V_{50} has decreased from that for the open gap, the similarity in the breakdown characteristics is due to bulk air breakdown at the electrode edges being the dominant breakdown mechanism. Comparing negative and positive energisation, it can be seen from Figures 6.35a and 6.35b that there is a clear change in performance for each system where, dependent on polarity, a knurled spacer results in higher V_{50} for negative polarity at 0 and 0.5 bar gauge. For positive polarity, smooth surfaces result in higher V_{50} than knurled surfaces. Due to the complex behaviour for these test conditions, this will now be discussed in Section 6.5.3.1.

6.5.3.1. Discussion

As shown from Figure 6.33, 6.34 and 6.35, although there are small fluctuations in the insulation performance with increasing pressure, there are similarities, so therefore, the behaviours will be discussed in relation to spacer material, as each reflects a unique performance.

For HDPE, any polarity effect is minimal compared to that observed for Polyetherimide and Polyoxymethylene. At very high levels of humidity (>90% RH), it was found via visual observation that all discharge channels propagated over the spacer surfaces, for both, positive and negative, polarities. This is hypothesised as being because HDPE is the most hydrophobic amongst all tested solid materials. Thus, the assumed accumulation of moisture on the surface of the HDPE spacer leads to the formation of surface droplets with small contact angles between the solid material and the surrounding air (this was not able to be imaged due to the highly humid environment in the air making it impossible to take clear images of the insulator surfaces, but it was reasonable to expect the build-up of water droplets on the spacer surface).. These droplets create high-field regions, leading to flashover irrespective of

the presence of surface modifications (created via the knurling process) - this results in similar positive and negative V_{50} flashover voltages. In [26], the authors show that surface roughness has an effect on the contact angle, depending upon how hydrophobic or hydrophilic the material is. The authors showed theoretically that if the material surface were hydrophobic, it would be even more hydrophobic after treatment to roughen the surface. Similarly, if the material surface were hydrophilic, it would be even more hydrophilic after treatment to roughen the surface. This result is in line with Wenzel's Equation (in equation 2.61), which shows that surface roughness treatment will amplify the surface wettability of certain materials. The effect of added roughness increasing the hydrophobicity of a hydrophobic material in also shown in [27]. Also due to the materials' hydrophobic or hydrophilic surface water droplet may accumulate in the knurled surface on the surface of the hydrophilic material and avoid these in the hydrophobic surface, further increasing or decreasing the angle associated with the water droplets.

As the contact angle of a water droplet increases, the electric field at the water droplet on the insulator surface increases, [28]. It is hypothesised that the local field enhancement on the spacer surface from the water droplets formed near to the HV electrode, as also shown by the authors of [29], results in a surface flashover event (i.e. preferential breakdown across the gas-solid interface rather than through the bulk of air) at a lower voltage. From Figure 6.15, the effect of the knurling process is evident, through comparison of the V_{50} breakdown voltages for the smooth and knurled HDPE spacers. Due to the anticipated increased hydrophobicity of the knurled HDPE surface, the resultant increase of the contact angle creates a higher local field region, leading to a surface flashover event, and lowering the breakdown voltage in comparison to those for Polyetherimide and Polyoxymethylene.

The results for Polyetherimide indicate that for positive polarity and smooth surfaces, the discharge location is at the electrode edges, due to the lower field at the surface created by the hydrophilic material, as well as the attachment of electrons to water molecules on the sample surface in the humid environment. Given the importance of the availability of secondary electrons for the development of positive streamers, this attachment of electrons to water molecules leads to the preferential development of the discharge in the gas at the electrode edges, away from the solid surface, resulting

in a similar breakdown voltage to that for the open air-gap. For negative polarity, however, the reduced significance of secondary electrons for streamer development, combined with the increased conductivity in the vicinity of the wet spacer surface, leads to the propagation of discharges across the surface of the material, and the flashover voltage is reduced.

For knurled Polyetherimide surfaces, irrespective of the voltage polarity, the breakdown of the insulation system occurs at the electrode edges. Where both, negative and positive, V_{50} breakdown voltages for knurled surfaces are similar to the corresponding open air-gap breakdown voltages. Following equation 2.61, it is hypothesised that the knurling process will create a more hydrophilic surface, which will decrease the contact angle further compared to that for a smooth surface, leading to a lower local field strength in the vicinity of the droplet, [28]. Unlike for a smooth surface, the surface indentations from the knurling process will also prevent a film of water from being produced over the length of the spacer surface, which could result in breakdown preferentially occurring at the electrode edges, resulting in both positive- and negative-polarity flashover voltages being similar to the corresponding voltage for an open air-gap.

An interesting phenomenon was witnessed with a Polyoxymethylene spacer in a high humidity environment, where changing the spacer surface was seen to have an opposite effect on the negative and positive polarity performance of the insulation system.

One possible explanation could be that the discharge channel may lift off from the Polyoxymethylene surface, due to the presence of secondary electrons playing a critical role in the formation of positive streamers. These secondary electrons attach themselves to water molecules, promoting the discharge's development in the gas near the electrode edges rather than on the solid surface. As a result, the breakdown voltage for this is similar to that of an open air-gap. Additionally, similar to Polyetherimide, Polyoxymethylene is a hydrophilic material, which, when moisture accumulates, creates a ‘flatter’ water droplet (reduced contact angle), leading to lower local field strength; in this case, only negative discharges initiate and propagate close to the surface of the material, meaning that the V_{50} breakdown voltage of smooth (machined)

samples is very similar for both Polyetherimide and Polyoxymethylene. This behaviour can be attributed to the fact that humidity inhibits the inception and development of positive impulsive discharges but exerts minimal influence upon negative streamers [30]. The development of water droplets at the surface of the spacer, therefore, is hypothesised to have more of an effect on the development of a positive discharge at the spacer surface, due to the synergistic effect of high humidity in the air as well as water droplets across the spacer surface, resulting in a preferential flashover at the rounded electrode edges.

Results reported in [25] show that the deposition of charge on solid spacer surfaces is also mitigated by the accumulation of water droplets on the surface of the spacer in a high-humidity environment. Referring to the results observed in the present study, such mitigation of surface charge will have a lager impact on positive streamer formation, with the reduced availability of secondary electrons meaning that higher applied fields will be required for the development of positive streamers in the vicinity of the spacer surface. This results in the effect, where under positive polarity, the V_{50} flashover voltage for a Polyoxymethylene spacer with a smooth surface finish is very similar to that for the open air-gap, indicative of the fact that the discharge channel propagated between the rounded edges of the electrodes, even in the presence of the Polyoxymethylene spacer. Under negative polarity, however, the V_{50} breakdown voltage is much lower than that for the open air-gap, indicating that surface flashover of the Polyoxymethylene spacer occurred.

From able 6.15, the negative V_{50} breakdown voltage for the knurled Polyoxymethylene spacer and that for the open gap are similar, whereas the positive V_{50} voltage is lower than that for the open gap. This shows that Polyoxymethylene spacers with a knurled surface finish behave differently to those with a smooth surface finish, which would suggest that the negative discharges propagated between the rounded electrode edges (higher breakdown voltages), while the positive discharges propagated over the spacer surface (lower breakdown voltages).

Comparing the results for a gap bridged by a knurled Polyoxymethylene spacer with those for the open air-gap, there is a large decrease in the positive polarity V_{50} flashover voltage when the spacer is included (~35% decrease at >90% RH),

supporting the theory that the discharge mechanism is surface flashover of the spacer, induced due to the high humidity.

Of interest here is the fact that the behaviour for knurled surfaces is opposite to that observed for the smooth (machined) surfaces. For smooth surfaces, the positive V_{50} voltage is significantly higher (by ~66 kV) than the negative for smooth surfaces. For knurled surfaces, however, the negative V_{50} voltage is ~40 kV higher than the positive.

In order to understand this strange phenomena produced by a Polyoxymethylene surface in >90% RH, some hypotheses have been made.

The opposite effect observed for knurled Polyoxymethylene surfaces compared to smooth Polyoxymethylene surfaces could be due to the water droplets deposited on the knurled surface in the high-humidity environment, coupled with the higher permittivity of the material ($\varepsilon_r = 3.8$) in comparison to that of Polyetherimide ($\varepsilon_r = 3$) and HDPE ($\varepsilon_r = 2.3$). For positive polarity, the presence of the water droplets in the vicinity of the surface of hydrophilicity (from equation 2.61) results in field enhancement at the HV electrode, leading to the development of auxiliary avalanches at the surface, resulting in the occurrence of a surface flashover at lower voltages than for negative polarity. For negative polarity, the presence of the water droplets could have the opposite effect, especially at the spacer surface, where the attachment of electrons to water molecules could be increased, leading to an increase in the breakdown voltage at the surface of the material and, alternatively, to the initiation of breakdown at the electrode edges. It must be noted, however, that this behaviour was not seen for the other tested materials, under the same environmental conditions.

Another potential reason for the differences in behaviour between smooth and knurled Polyoxymethylene surfaces is the resultant modification of the streamer propagation characteristics, due to the permittivity effect. In [31] and [32], the streamer velocities for discharges initiated near to a triple junction point are reported, for negative and positive polarity. The results demonstrated that the higher the permittivity, the greater the effect in terms of the streamer being attracted to the material surface, due to the increasing permittivity mismatch with the surrounding air. This effect is visually seen to be more prominent for a positive streamer, from the less diffuse nature of the discharge channel. In [31] and [32], it is shown that for both polarities, the polarisation

of the solid dielectric strengthens the electric field between the streamer and the solid, attracting the streamer towards the surface. The negative streamer propagates along the surface for 6 mm before becoming coupled to the surface, whereas this distance is only 2 mm for the positive streamer. There can be two reasons for this behaviour. Firstly, for negative streamers, electrons move away from the streamer channel, leading to the accumulation of negative surface charge on the dielectric; the presence of this surface charge then lowers the electric field between the streamer and the solid dielectric. Secondly, the negative streamer head has a larger radius and, therefore, a lower electrical field; this means that the negative streamer has lower and more spread-out charge density at its head, which leads to weaker electrostatic attraction to the surface, an effect that is further enhanced with increasing relative permittivity of the solid dielectric, [31], [32].

When the surface is modified, this has an effect on the streamer velocity, as reported in [18]. The authors of [18] showed that through modification of the surfaces of Lexan (polycarbonate) solid spacers, by the milling of 0.5 mm corrugations onto the surface (0.5 mm being the same indentation depth introduced by the knurling process used in the present study), the resulting profiled surface slowed the propagation of positive streamers such that, over a distance of 40 mm, the discharge took ~33% longer to reach the cathode than for a solid with a smooth surface finish. If the streamers follow the surface profile closely, the distance that the streamer needs to traverse is longer for a profiled surface than for a smooth surface. As the voltage drop along a streamer increases with the streamer length, there will be a reduction of the residual voltage at the streamer head and therefore less energy available to drive ionisation. Consequently, the advancement of the streamer towards the grounded electrode is slowed down with the profiled surface [18].

For modified surfaces, the authors of [18] found that negative breakdown voltages were higher than positive. Relating this to the simulation results in [32], when a streamer is initiated close to a material surface, a positive streamer is subjected to a greater force as the permittivity of the material is increased, with the attractive force between the streamer and the surface becoming stronger than that for a negative streamer. This effect can help to explain the higher negative breakdown voltages than positive observed for knurled Polyoxymethylene surfaces in the present study, due to

the higher permittivity of Polyoxymethylene. Additionally, the authors of [33] discuss local field enhancement resulting in the formation of discharges in the vicinity of water droplets, with positive discharges in air being initiated more readily than negative.

6.6. CHAPTER VI REFERENCES

[1] J. D. Smith and L. L. Hatfield, "Measurement of the effects of surface roughness on flashover," 1988. Annual Report., *Conference on Electrical Insulation and Dielectric Phenomena*, 1988, pp. 47-52, doi: 10.1109/CEIDP.1988.26307.

[2] J. O. Rossi, M. Ueda, A. R. Silva and L. P. S. Neto, "Improvement on UHMWPE and PMMA Surface Flashover Under Atmospheric Pressure Using PIII Processing," in *IEEE Transactions on Plasma Science*, vol. 48, no. 10, pp. 3386-3391, Oct. 2020, doi: 10.1109/TPS.2020.3007735.

[3] M. Dhofir, R. N. Hasanah and H. Suyono, "The Leakage Current and Flashover Voltage of Polyethylene Insulator with Different Contour Surfaces," *2020 12th International Conference on Electrical Engineering (ICEENG)*, 2020, pp. 17-22, doi: 10.1109/ICEENG45378.2020.9171763.

[4] L. LIU *et al*., "The Influence of Electric Field Distribution on Insulator Surface Flashover," *2018 IEEE Conference on Electrical Insulation and Dielectric Phenomena (CEIDP)*, 2018, pp. 255-258, doi: 10.1109/CEIDP.2018.8544732.

[5] H. -. Lee, T. Egashira and M. Hara, "Improvement of particle-initiated DC flashover characteristics by using electrode and surface shapes in SF6 gas," *[1991] Proceedings of the 3rd International Conference on Properties and Applications of Dielectric Materials*, 1991, pp. 529-532 vol.1, doi: 10.1109/ICPADM.1991.172114

[6] C. Sun *et al*., "Characteristics of nanosecond pulse dielectric surface flashover in high pressure SF6," in *IEEE Transactions on Dielectrics and Electrical Insulation*, vol. 25, no. 4, pp. 1387-1392, August 2018, doi: 10.1109/TDEI.2018.006759

[7] X. Yang *et al*., "Research on forming mechanism of surface discharge paths for solid dielectric with different shapes under micro-second impulse in liquid nitrogen," in *IEEE Transactions on Dielectrics and Electrical Insulation*, vol. 24, no. 6, pp. 3452-3459, Dec. 2017, doi: 10.1109/TDEI.2017.006769.

[8] J. Xue, H. Wang, J. Chen, K. Li, Y. Liu, B. Song, J. Deng, and G. Zhang, "Effects of surface roughness on surface charge accumulation characteristics and surface

flashover performance of alumina-filled epoxy resin spacers", *Journal of Applied Physics* 124, 083302 2018 https://doi.org/10.1063/1.5043239

[9] P. Xue, S. Zhao, D. Xiao, L. Zhu and Y. Wu, "Experimental Research on Flashover Characteristics of Insulator with N2," in *IEEE Electrical Insulation Conference (EIC)*, San Antonio, TX, 2018, pp. 60-63. doi: 10.1109/EIC.2018.8480897.

[10] Y. Qin et al., "A Study on Flashover Characteristics of Supporting Insulators in SF6 under Lightning Impulse," in *IEEE 11th International Conference on the Properties and Applications of Dielectric Materials (ICPADM).* Page 604 – 607, 2015 doi: 10.1109/ICPADM.2015.7295344.

[11] H. K. Meyer, R. Marskar, H. Osberg and F. Mauseth, "Surface Flashover over a Micro-Profiled Cylinder in Air," in *IEEE Transactions on Dielectrics and Electrical Insulation*, doi: 10.1109/TDEI.2023.3277413

[12] F. Wang, L. Wang, S. Chen, Q. Sun and L. Zhong, "Effect of Profiled Surface on Streamer Propagation and the Corner Effect," in *IEEE Transactions on Dielectrics and Electrical Insulation*, vol. 28, no. 6, pp. 2186-2194, December 2021, doi: 10.1109/TDEI.2021.009866.

[13] Z. Jia, B. Zhang, X. Tan and Q. Zhang, "Flashover Characteristics along the Insulator in SF6 Gas under DC Voltage," *2009 Asia-Pacific Power and Energy Engineering Conference*, Wuhan, China, 2009, pp. 1-4, doi: 10.1109/APPEEC.2009.4918383.

[14] A. H. Cookson, "Review of high-voltage gas breakdown and insulators in compressed gas," inIEE Proceedings A - *Physical Science, Measurement and Instrumentation, Management and Education* - Reviews, vol. 128, no. 4, pp. 303-312, May 1981.

[15] M. Akyuz, L. Gao, V. Cooray, T. G. Gustavsson, S. M. Gubanski, and A. Larsson, "Positive streamer discharges along insulating surfaces," *IEEE Transactions on Dielectrics and Electrical Insulation*, vol. 8, no. 6, pp. 902–910, 2001.. doi: 10.1109/94.971444.

[16] A. A. Dubinova, 'Modeling of streamer discharges near dielectrics', Doctor of Philosophy, Applied Physics and Science Education, University of Eindhoven 2016.

[17] J. Xue, H. Wang, J. Chen, K. Li, Y. Liu, B. Song, J. Deng, and G. Zhang, "Effects of surface roughness on surface charge accumulation characteristics and surface flashover performance of alumina-filled epoxy resin spacers", *Journal of Applied Physics* 124, 083302 2018 https://doi.org/10.1063/1.5043239

[18] H. K. H. Meyer, R. Marskar, H. Gjemdal and, F. Mauseth "Streamer propagation Along a Profiled Dielectric Surface" in *Plasma Sources Sciences and Technology*, vol 29, no 11 pp. 115015, 2020, doi: 10.1088/1361-6595/abbae2

[19] Effects of Roughening Insulator Surface on Charging and Flashover Characteristics of a Long Glass Insulator in Vacuum January 2006 *IEEJ Transactions on Fundamentals and Materials* 126(8):769-774

[20] Amer, Mohammed & Laninga, Jeff & Mcdermid, William & Swatek, D.R. & Kordi, Behzad. (2019). New experimental study on the DC flashover voltage of polymer insulators: combined effect of surface charges and air humidity. *High Voltage*. 4. 316-323. 10.1049/hve.2019.0094.

[22] J. M. Meek and J. D. Craggs, Electrical Breakdown of Gases. London: Clarendon Press,1953.

[23] C. Tran Duy, N. Bonifaci, A. Denat, O. Lesaint, L. Caliap, A. Girodet, B. Gelloz, P. Ponchon, "Partial discharges at a triple junction metal/solid insulator/gas and simulation of inception voltage", *Journal of Electrostatics*, Vl 66, Is. 5–6, 2008, pp. 319-327, https://doi.org/10.1016/j.elstat.2008.01.011

[24] A. Xu, Y. Shi, Y. Cheng and L. Chen, "Influence of Screening Electrode on Surface Flashover in Atmospheric Environment," in *IEEE Transactions on Dielectrics and Electrical Insulation*, vol. 30, no. 2, pp. 580-584, April 2023, doi: 10.1109/TDEI.2023.3235309.

[25] O. Yamamoto et al "Effects of Roughening Insulator Surface on Charging and Flashover Characteristics of a Long Glass Insulator in Vacuum" January *2006 IEEJ Transactions on Fundamentals and Materials* 126(8):769-774

[26] M. Amer, J. Laninga, W. McDermid, D. R. Swatek, and B. Kordi, “New experimental study on the DC flashover voltage of polymer insulators: combined effect of surface charges and air humidity”. *High Voltage*, 4: 316-323. 2019

[27] J. Xue, H. Wang, J. Chen, K. Li, Y. Liu, B. Song, J. Deng, G. Zhang; “Effects of surface roughness on surface charge accumulation characteristics and surface flashover performance of alumina-filled epoxy resin spacers”. *Journal of Applied Physics* 28 August 2018; 124 (8): 083302.

[28] L. B. Boinovich, A. M. Emelyanenko, “Hydrophobic materials and coatings: Principles of design, properties and applications”. *Russian Chemical Reviews*. 77. 583 (2008)

[29] Waluyo, P. M. Pakpahan and Suwarno, "Influences of Water Droplet Size and Contact Angle on the Electric Field and Potential Distributions on an Insulator Surface," *2006 IEEE 8th International Conference on Properties & applications of Dielectric Materials*, Bali, Indonesia, 2006, pp. 889-892, doi: 10.1109/ICPADM.2006.284320.

[29] Y. Liu, X. Kong, Y. Wu and B. Du, "Dynamic Behavior of Droplets and Flashover Characteristics for CFD and Experimental Analysis on SiR Composites," in *IEEE Access*, vol. 7, pp. 8095-8101, 2019, doi: 10.1109/ACCESS.2018.2889075.

[30] D. E. Gourgoulis, P. N. Mikropoulos, C. A. Stassinopoulos, andC. G. Yakinthos, ‘‘Effects of negative DC pre-stressing on positive impulse breakdown characteristics of conductor-rod gaps,*’’IEE Proc. Sci., Meas.Technol*., vol. 152, no. 4, pp. 155–160, Jul. 2005

[31] X. Li, A. Sun and J. Teunissen, "A computational study of negative surface discharges: Characteristics of surface streamers and surface charges," in *IEEE Transactions on Dielectrics and Electrical Insulation*, vol. 27, no. 4, pp. 1178-1186, Aug. 2020, doi: 10.1109/TDEI.2020.008880.

[32] X. Li. A. Sun, G. Zhang and J. Teunissen, “A computational study of positive streamers interacting with dielectrics*.” Plasma Sources Sci. Technol*. 29 IOP publishing, IS 5, VL 29, 2020

[33] S. Nijdam, J. Teunissen and U. Ebert “The physics of streamer discharge phenomena”- *Plasma Sources Science and Technology*, 2020, IOP Publishing, IS - 10, VL - 29

7. CHAPTER VII

CONCLUSIONS AND FURTHER WORK

This thesis has detailed the impulsive high-voltage testing of gas-solid insulation, where different spacer materials, surface finishes, and environmental parameters were investigated, with a view to providing insights into the breakdown and flashover processes relevant to the insulation of outdoor pulsed power systems, operating in rapidly changing environments. This information is imperative in the design process of any pulsed power system, where it is critical to understand the variation in the values of failure voltages evident under different applied voltage regimes or operational conditions. A sub-μs (100 ns rise time) voltage waveform was applied for all tests. As such, a view into the breakdown characteristics with different dielectric materials, tested under identical experimental conditions, has yielded useful information specifically for pulsed power system operators, additional to the general information on DC, AC or lightning impulse breakdown voltages typically available in the literature.

To ensure a thorough evaluation of the flashover performance of the three chosen solid dielectric materials, comprehensive tests were conducted under both positive and negative voltage stress. The reason for conducting tests with varying impulse polarities was the quasi-uniform field distribution with one electrode grounded, and the different breakdown mechanisms associated with each polarity. Additionally, the effect of moisture content in the air on bulk breakdown behaviour and discharge location was carefully examined, with changing air pressure above and below atmospheric. The effect of relative humidity under pulsed power conditions has not been extensively studied in the published literature. Thus, including this investigation in the thesis was of utmost importance, as it can provide valuable information for designers and operators of outdoor power and pulsed power equipment. The insights gained from this study have practical implications for improving the performance and reliability of this equipment.

Also contained within this thesis is a comparative study of the flashover performance of air-solid gaps bridged by spacers with smooth (machined) and knurled surfaces. These tests were performed under different environmental conditions, with the surrounding air insulation under varying pressure and humidity conditions. The significance of this work lies in addressing the lack of research on the synergistic effects of multiple environmental parameters on the flashover behaviour of these materials, particularly in nanosecond pulsed power conditions. Most published studies focus on solid dielectric materials and their response to a single environmental condition. To ensure comprehensive coverage of this aspect, the insulation systems were subjected to sub-μs impulses with the same voltage waveform as that applied in the baseline open-air gap breakdown study.

Both positive and negative impulses were used during the experiments. The breakdown study not only recorded the breakdown parameters of test samples where interfacial flashover was observed, but also those experiencing breakdown through the bulk air dielectric at the electrode edges, which in these instances in relation to a practical pulsed power system can be seen as an advantage as the plasma channel is developed away from the surface which will minimise the degradation of the dielectric surface over time. This approach provided valuable information on two critical aspects: the voltage level required to cause breakdown of the bulk air or surface flashover of the insulation system, and the probability associated with these events, as physical and environmental parameters are changed and compared to an open gap arrangement. This data is highly relevant to designers of electrical machines, as it informs the coordination of insulation to minimise the likelihood of catastrophic failure due to surface flashover or bulk air breakdown events, in practical electrode arrangements.

7.1. CONCLUSION OF THE OPEN GAP AIR DIELECTRIC STUDY

Initially, in order to provide baseline breakdown characteristics, the plane-parallel electrode system designed was characterised as an open-air gap, with no solid spacer bridging the electrodes. This work investigated the breakdown characteristics of zero grade air ‘as received’, with a measured relative humidity of <10% RH, when stressed

with a sub-µs 100/700 ns impulse voltage. As the experiments were conducted using a parallel-plane electrode configuration with one electrode earthed, with a 40 mm gap distance to facilitate 100s kV breakdown voltages, a moderately divergent electric field was resultant, prompting impulses of both positive and negative polarity to be used during tests. Within the changing environmental conditions, the effects of air humidity and air pressure were investigated. For these parameters, three discrete levels of pressure and humidity were tested. The pressure was set to values of -0.5, 0 and 0.5 bar gauge, in order to monitor the effect of pressures at, and above and below atmospheric pressure. In terms of relative humidity, levels of <10% RH, ~50% RH and >90% RH were tested, in order to cover the full spectrum.

For open air gaps, the discharge always occurred at the electrode edges, due to the enhanced electric field strength. The differences between the negative and positive polarity breakdown voltages were also shown to vary with the environmental conditions. Three types of behaviour were evident from these tests:

- higher negative breakdown voltage,
- similar breakdown voltage, irrespective of polarity,
- higher positive breakdown voltage.

As the electrode setup exhibited a weakly divergent field, there was a polarity effect witnessed during the comparison of positive and negative tests. For <10% RH and ~50% RH tests, at a pressure of -0.5 bar gauge, there was a large increase in the negative polarity breakdown voltage in comparison to positive polarity, with <10% RH showing the largest nominal difference of ~39 kV (and ~26 kV at ~50% RH). At >90% RH, there was a higher positive breakdown voltage than negative, where the difference was ~11 kV.

As the pressure was increased from -0.5 bar gauge to 0.5 bar gauge, for all levels of humidity, the polarity effect was found to decrease, with the positive and negative breakdown voltages being closer in magnitude. At 0.5 bar gauge, the differences were ~15 kV at <10% RH, ~1 kV at ~50% RH, and ~7 kV at >90% RH. These results are important as they provide baseline data to compare with that for the air-solid insulation systems. Therefore, to frame the following conclusions for air-solid gaps, it is important to emphasise –

- The polarity effect witnessed with the parallel plane electrode system with one electrode earthed, due to moderate divergent fields.
- The reduction in the polarity effect with increasing air pressure.
- The reduction in the polarity effect with increasing air humidity.
- The results can be compared with the gas-solid insulation systems, where breakdown voltages can be compared to the flashover voltages under the same environmental conditions, to see if any similarities arise, giving evidence to similar breakdown mechanisms over the electrode edge, away from the spacer.

7.2. CONCLUSION OF THE AIR-SOLID INSULATION DIELECTRIC STUDY

The air-solid insulation systems consisted of a cylindrical spacer between the two parallel plane electrodes, surrounded by air. The solid polymers tested were:

- High-density Polyethylene (HDPE)
- Polyetherimide (Ultem)
- Polyoxymethylene (Derlin)

For systems in a dry (<10% RH) environment, at −0.5 bar gauge, when the applied impulses were of negative polarity, smooth (machined) spacers were shown to have the highest hold-off voltages, with HDPE being the best choice of material of those tested at ~136 kV. For positive polarity, all materials showed similar flashover voltages irrespective of spacer surface, with knurled Polyetherimide surfaces reflecting the highest U_{50} flashover voltage at ~106 kV. At 0 bar gauge, for both positive and negative polarity impulses, all materials reflected similar performance in the insulation system, irrespective of surface finish. The results show that smooth HDPE surfaces are the best choice for negative polarity at ~155 kV, while knurled Polyetherimide surfaces offer the highest breakdown voltages for positive polarity ~176 kV. At 0.5 bar gauge, under negative polarity, the highest U_{50} values were recorded for spacers with smooth (machined) surfaces, in particular HDPE at ~202 kV, whereas for positive energisation, the highest breakdown voltages were for knurled spacers, in particular for Polyetherimide spacers at ~230 kV.

It was found that, in the case of changing environments, the specific failure mechanism of the insulation system varied, with the effect of knurling the surface in comparison to smooth machined surfaces created high electrical field regions at the triple junction point, which initiated flashover across the surface of the material. This was particularly interesting for positive polarity in a <10% RH environment, where the knurled spacer was shown to increase the hold-off voltage by up to 66 kV in comparison to a smooth (machined) surface. For smooth (machined) spacers of all materials at <10% RH, the discharge generally occurred across the outside edges of the electrodes, similar to the open gap case, showing a similar hold-off voltage for each material tested, at all pressures. For knurled spacers, the pressure was seen to have an effect on the flashover voltage of each material, where the same trend was evident for each tested material. At -0.5 bar gauge, the knurled surface was seen to have a similar performance to the smooth (machined) surface, with the hold-off voltages being similar. As the pressure was increased, however, the breakdown voltage with the knurled spacer started to increase in comparison to that for a smooth (machined) spacer at 0 bar, increasing to a maximum value at 0.5 bar gauge. The enhanced electric field at the triple junction point in the case of the knurled surfaces of all three materials can increase the hold-off voltage of the insulation system.

For systems at ~50% RH, at −0.5 bar and 0 bar gauge, the results show that a smooth HDPE surface offered the best performance at ~107 kV and ~145 kV. For positive energisation, all materials showed similar flashover voltages, irrespective of surface finish, however Polyetherimide smooth at -0.5 bar gauge with ~86 kV and Polyoxymethylene knurled at ~146 kV. For 0.5 bar gauge, under negative energisation, HDPE shows the best performance at ~190 kV as at −0.5 bar gauge and 0 bar gauge. For positive-polarity energisation, nominally, the knurled spacer surfaces of all materials performed better, with higher breakdown voltages for knurled Polyetherimide surfaces with an increase a maximum of ~215 kV. A gain, similar to <10% RH, this provided interesting results where the knurled spacer was shown to increase in comparison to a smooth machined spacer by up to ~47 kV.

For insulation systems in a high (>90%) RH environment, at −0.5 bar gauge and for negative polarity, each material performed similarly, with Polyetherimide surfaces, either smooth or knurled, offering the highest breakdown voltages with a maximum

of ~66 kV. For positive energisation, the Polyetherimide spacers performed the best overall, irrespective of surface finish, offering the highest breakdown voltages with a maximum of ~75 kV. At 0 bar gauge, an Polyetherimide spacer with a knurled surface provided the highest negative flashover voltage at offering the highest breakdown voltages with a maximum of ~120 kV, whereas for positive energisation, again, the Polyetherimide spacers performed the best overall, irrespective of surface finish with a maximum of ~126 kV. Finally, at 0.5 bar gauge, performing very similarly to at 0 bar gauge, an Polyetherimide spacer with a knurled surface provided the highest negative flashover voltage of 158 kV, whereas for positive energisation, the Polyetherimide spacer performed the best overall, irrespective of surface finish, with a flashover voltage of~171 kV.

The results have demonstrated that modifying physical factors (material, surface finish, and impulse polarity) as well as environmental conditions (pressure and relative humidity) has a significant impact on the effectiveness of a pulsed power insulation system. The results presented herein detail the behaviour of spacers made from each of three different materials under varied environmental conditions, enabling designers to select the best solution for their application.

The main findings showed that the as the insulation systems and their surrounding environments were changed, there were dramatic changes in the breakdown characteristics of the pulsed power insulation systems. For different sets of conditions, the discharge location changed, which had a profound effect on the hold-off voltage of each insulation system. The development of surface discharges across smooth machined surfaces, which occurred mainly at >90% RH, resulted in the flashover voltage decreasing in comparison to that for an open gap system, whereas development across the surface of knurled spacers at <10% RH was shown to increase the flashover voltage compared to that for an open gap and smooth machined surface insulation system.

7.3. MAJOR RESEARCH FINDINGS

From the work undertaken during this thesis, a number of key research findings have been made, these can be summarised as follows:

- For knurled spacers of all materials, at <10% RH, for negative polarity, the performance was shown to be generally comparable to the open gap results. For positive polarity, however, the breakdown voltage of the system dramatically increased in comparison to those with smooth (machined) surfaces and the open gap.
- At ~50% RH, the flashover results for smooth (machined) spacers were similar to those at <10% RH for negative polarity, but due to the increased humidity, different breakdown mechanisms were apparent, particularly at higher pressures.
- At >90% RH, the accumulation of water on the dielectric surface had a direct effect on the location of the plasma discharge, which dictates the flashover voltage of the system. As the pressure increases, for negative polarity, HDPE and Polyoxymethylene exhibited a decrease in the flashover voltage in comparison to an open gap, while Polyetherimide showed similarities to an open gap performance. This was evident for both polarities.
- For air-solid gaps bridged by spacers with smooth (machined) surfaces, at <10% RH, the breakdown characteristics are comparable to those for open gaps, reflective of similar discharge mechanisms. This behaviour was consistent for all materials, and both polarities. However, the flashover voltage was shown to increase in comparison to that for an open gap with HDPE and Polyetherimide spacers.
- At ~50% RH, the flashover results for smooth (machined) spacers were similar to those at <10% RH, but due to the increased humidity, different discharge mechanisms occurred, resulting in slight differences in flashover performance, particularly at higher pressures. For positive polarity flashovers, for all pressures, the performance of all materials exhibited similar breakdown

characteristics to an open-air gap, showing that the increase in humidity to ~50% RH results in polarity-dependant behaviour.

- At >90% RH, the effect of the accumulation of water droplets on the dielectric surface was seen to have a direct effect to the location of the plasma discharge, which dictates the flashover voltage of the system. As the pressure increases, for negative polarity, all materials exhibited a decrease in the flashover voltage in comparison to an open gap, with significant decreases with Polyoxymethylene and Polyetherimide spacers. For positive polarity, the breakdown behaviour was similar to that of an open gap for Polyoxymethylene and Polyetherimide, showing the effect the material properties have on the location of discharge. A significant decrease in breakdown voltage with HDPE spacers was found under positive polarity, however, particularly at higher pressures. This also shows that the flashover characteristics of the insulation systems at >90% RH are polarity and material dependent.
- The polarity effect observed in open gaps generally decreased with increasing pressure and humidity of the air dielectric.

7.4. FURTHER WORK

Further pre-treatment procedures and modifications to the electrode/sample geometry that will make it easier to reduce the power consumption of future pulsed-power systems are two areas in which additional research is required to broaden the knowledge base. Further electrostatic field analysis could be used to model a wide range of geometries in order to analyse the local field enhancements that are likely to occur in practical systems due to charge injection from the electrodes, it is necessary to include the influence of space charge in both the air and solid dielectric, thereby producing a Multiphysics model of the current system in order to characterise the streamer propagation across the smooth and knurled surfaces, when initiated at different areas of the electrode, and the shielding effect.

Additional environmental conditions should be probed in order to simulate the variable conditions in which outdoor pulsed power systems must operate, such as wind speed and air quality. The effect of sand/dust particles on the flashover performance

of the tested systems, and any synergistic effect with the physical parameters and environmental conditions tested herein, should be investigated.

A systematic study of the pre-breakdown streamer currents would assist in correlating the discharge location with the measured breakdown characteristics, assisting in discussion of the breakdown mechanisms. Pre-breakdown current measurements could also help to explain the interesting results in relation to the difference in the flashover strength of spacers with smooth (machined) and knurled surfaces, as well as the polarity effect observed within an open gap topology, making it an interesting future work objective.

With the intention of developing a comprehensive picture of streamer development at air-solid interfaces to build upon the open shutter photographs taken in the current study, the implementation of a fast optical detection system that incorporates a fast, intensified charge coupled device (ICCD) camera would provide intriguing future research opportunities, where streamer development, particularly across knurled surfaces, could be imaged, enabling the correlation of the discharge development with the increased flashover voltage in comparison to smooth machined surfaces and open-gap system. Additionally, imaging of the discharge initiation location would be useful to investigate the behaviour of competing discharges, where simultaneous discharges could ignite at multiple regions around the circumference of the spacer.

In conclusion, the experimental results, and their interpretation and discussion, presented herein may serve as a foundation for the development of more robust selection criteria, which can eventually lead to the creation of reliable design rules and test procedures for use under pulsed power conditions, comparable to those used in the power industry.

LIST OF PUBLICATIONS AND PRESENTATIONS

Journal Publications

1. **R. W. Macpherson**, M. P. Wilson, I. V. Timoshkin, S. J. Macgregor and M. J. Given, "Impulsive Flashover Characteristics and Weibull Statistical Analysis of Gas-Solid Interfaces With Varying Relative Humidity," in ***IEEE Access*****, vol. 8, pp. 228454-228465, 2020, doi: 10.1109/ACCESS.2020.3046088.**

2. **R. W. Macpherson**, M. P. Wilson, I. V. Timoshkin, M. J. Given and S. J. MacGregor, "Flashover of Smooth and Knurled Dielectric Surfaces in Dry Air," in *IEEE Transactions on Dielectrics and Electrical Insulation*, doi: 10.1109/TDEI.2023.3313571.

Conference Publications

3. **R. W. Macpherson**, M. P. Wilson, I. V. Timoshkin, S. J. MacGregor and M. J. Given, "The Effect of Relative Humidity on the Flashover Strength of Solid Insulation," ***2019 IEEE Pulsed Power & Plasma Science (PPPS)*****, Orlando, FL, USA, 2019, pp. 1-4, doi: 10.1109/PPPS34859.2019.9009915.**

4. **R. W. Macpherson**, M. P. Wilson, I. V. Timoshkin, S. J. Macgregor and M. J. Given Given "Effect of Surface Deviation of Solid Insulation on Impulsive Flashover Voltages Under Varying Environmental Conditions" in ***2020*** **IEEE Conference on Electrical Insulation and Dielectric Phenomena, 2020 NY, USA (Virtual conference) pp 1-4, 2021**

5. **R. W. Macpherson**, M. P. Wilson, I. V. Timoshkin, S. J. Macgregor and M. J. Given **"**Statistical Analysis of Impulsive Flashover Voltages Across Solid-Air Interfaces" in ***2020*** **IEEE Conference on Electrical Insulation and Dielectric Phenomena, 2020 NY, USA (Virtual conference) pp 1-4, 2021**

Presentations

1. **R. W. Macpherson**, M. P. Wilson, I. V. Timoshkin, S. J. MacGregor and M. J. Given "Effect of Air Humidity on the Flashover Strength of Solid Insulation" **2018 UHVnet Poster presentation**

2. **R. W. Macpherson**, M. P. Wilson, I. V. Timoshkin, S. J. MacGregor and M. J. Given, "The Effect of Relative Humidity on the Flashover Strength of Solid Insulation," ***2019 IEEE Pulsed Power & Plasma Science (PPPS)*****, Orlando, FL, USA oral presentation**

3. **R. W. Macpherson**, M. P. Wilson, I. V. Timoshkin, S. J. Macgregor and M. J. Given **"**Statistical Analysis of Impulsive Flashover Voltages Across Solid-Air Interfaces" in ***2020*** **IEEE Conference on Electrical Insulation and Dielectric Phenomena, 2020 poster presentation**

4. **R. W. Macpherson**, M. P. Wilson, I. V. Timoshkin, S. J. Macgregor and M. J. Given Given "Effect of Surface Deviation of Solid Insulation on Impulsive Flashover Voltages Under Varying Environmental Conditions" in ***2020*** **IEEE Conference on Electrical Insulation and Dielectric Phenomena poster presentation**

5. **R. W. Macpherson**, M. P. Wilson, I. V. Timoshkin, S. J. MacGregor and M. J. Given "Flashover of Smooth and Knurled Solid Insulation Systems Energised with Fast dV/dt Impulse Voltages in Varying Environmental Conditions **in 2022 University of Strathclyde showcase poster presentation**

APPENDIX 1: BREAKDOWN AND FLASHOVER DATA

Appendix 1 shows the breakdown/flashover results by number during the first 20 failures. In order to test the validity of the values, 2-parameter Weibull statistical analysis has been conducted for the first 10 shots and second 10 shots in order to test the spread of the data. For all tests overlapping error bars were conclusive for all test regimes to 95.4% spread.

For each test arrangement, the legend for each figure shows -

- -0.5 bar gauge breakdown and flashover data in blue
- 0 bar gauge breakdown and flashover data in red
- 0.5 bar gauge breakdown and flashover data in black

Open gap

Negative

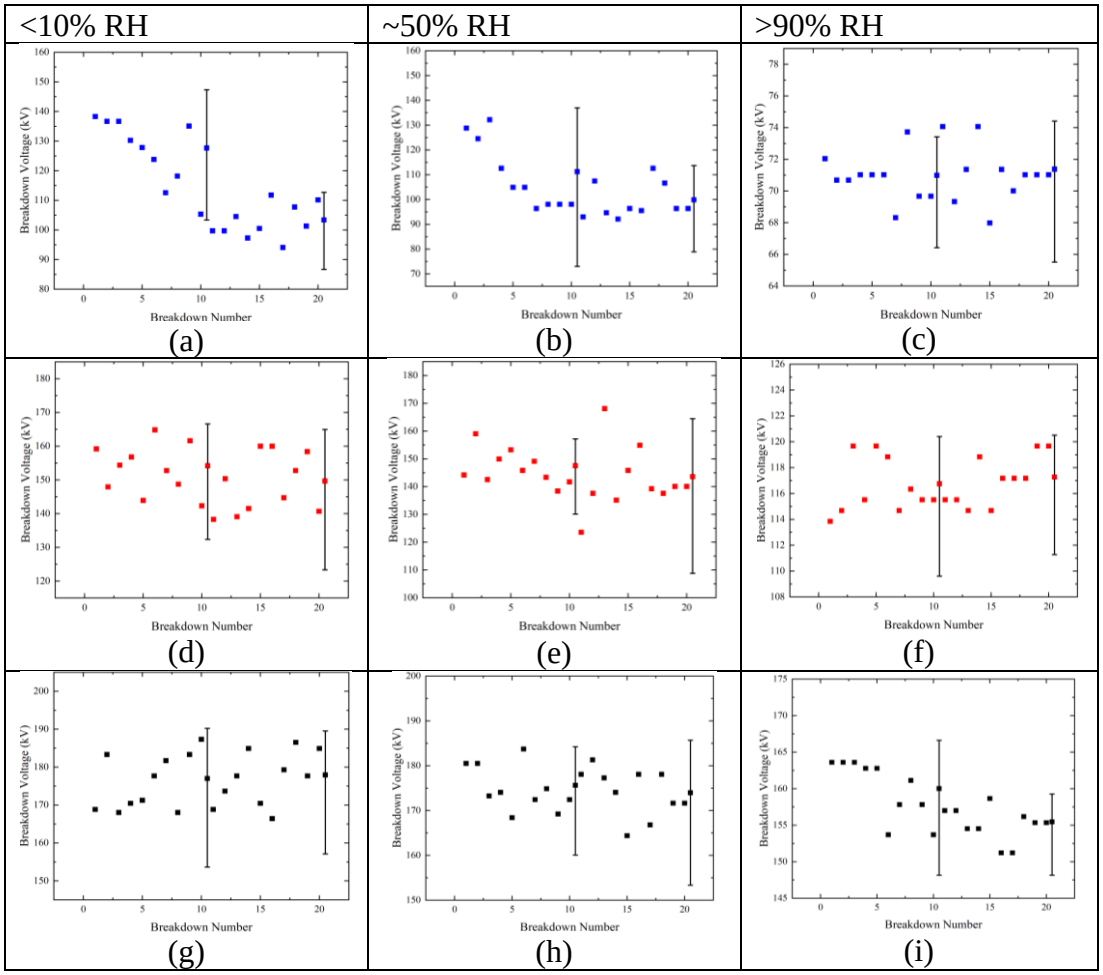

Figure AP1 – Open gap negative polarity breakdown voltage with corresponding breakdown number across the 20 events for a) -0.5 bar gauge at <10% RH, b) 0 bar gauge at <10% RH, c) 0.5 bar gauge at <10% RH, d) -0.5 bar gauge at ~50% RH, e) 0 bar gauge at ~50% RH, f) 0.5 bar gauge at ~50% RH, g) -0.5 bar gauge at >90% RH, h) 0 bar gauge at >90% RH and i) 0.5 bar gauge at >90% RH. Error bars show the 95.4% spread of data between the first 10 and second 10 shots, and all tests exhibit overlapping error bars.

Positive

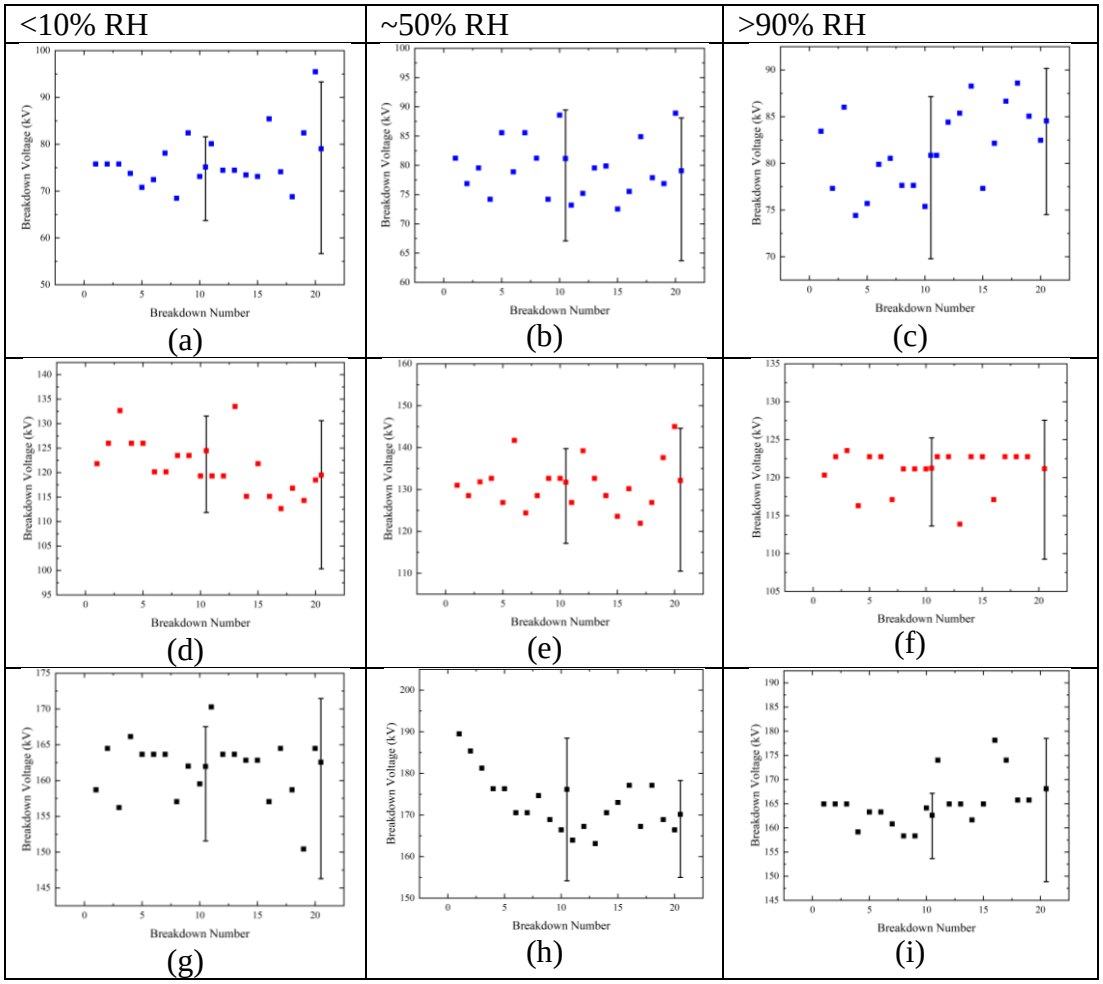

Figure AP2 - Open gap positive polarity breakdown voltage with corresponding breakdown number across the 20 events for a) -0.5 bar gauge at <10% RH, b) 0 bar gauge at <10% RH, c) 0.5 bar gauge at <10% RH, d) -0.5 bar gauge at ~50% RH, e) 0 bar gauge at ~50% RH, f) 0.5 bar gauge at ~50% RH, for g) -0.5 bar gauge at >90% RH, h) 0 bar gauge at >90% RH and i) 0.5 bar gauge at >90% RH. Error bars shows the 95.4% spread of data between the first 10 and second 10 shots of data, all tests exhibit overlapping error bars.

HDPE

Negative Smooth Machined

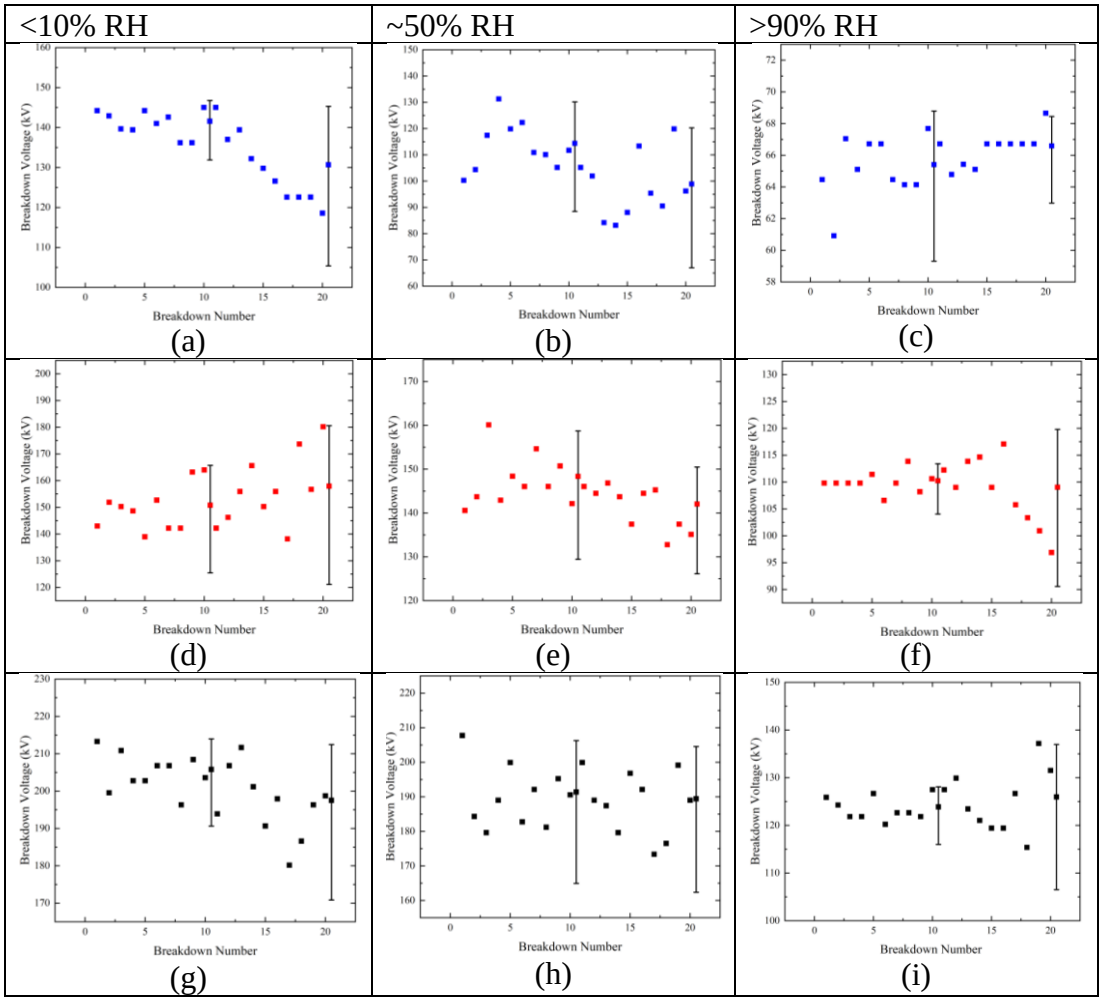

Figure AP3 – Smooth machined HDPE negative polarity breakdown voltage with corresponding breakdown number across the 20 events for a) -0.5 bar gauge at <10% RH, b) 0 bar gauge at <10% RH, c) 0.5 bar gauge at <10% RH, d) -0.5 bar gauge at ~50% RH, e) 0 bar gauge at ~50% RH, f) 0.5 bar gauge at ~50% RH, for g) -0.5 bar gauge at >90% RH, h) 0 bar gauge at >90% RH and i) 0.5 bar gauge at >90% RH. Error bars shows the 95.4% spread of data between the first 10 and second 10 shots of data, all tests exhibit overlapping error bars.

Negative Knurled

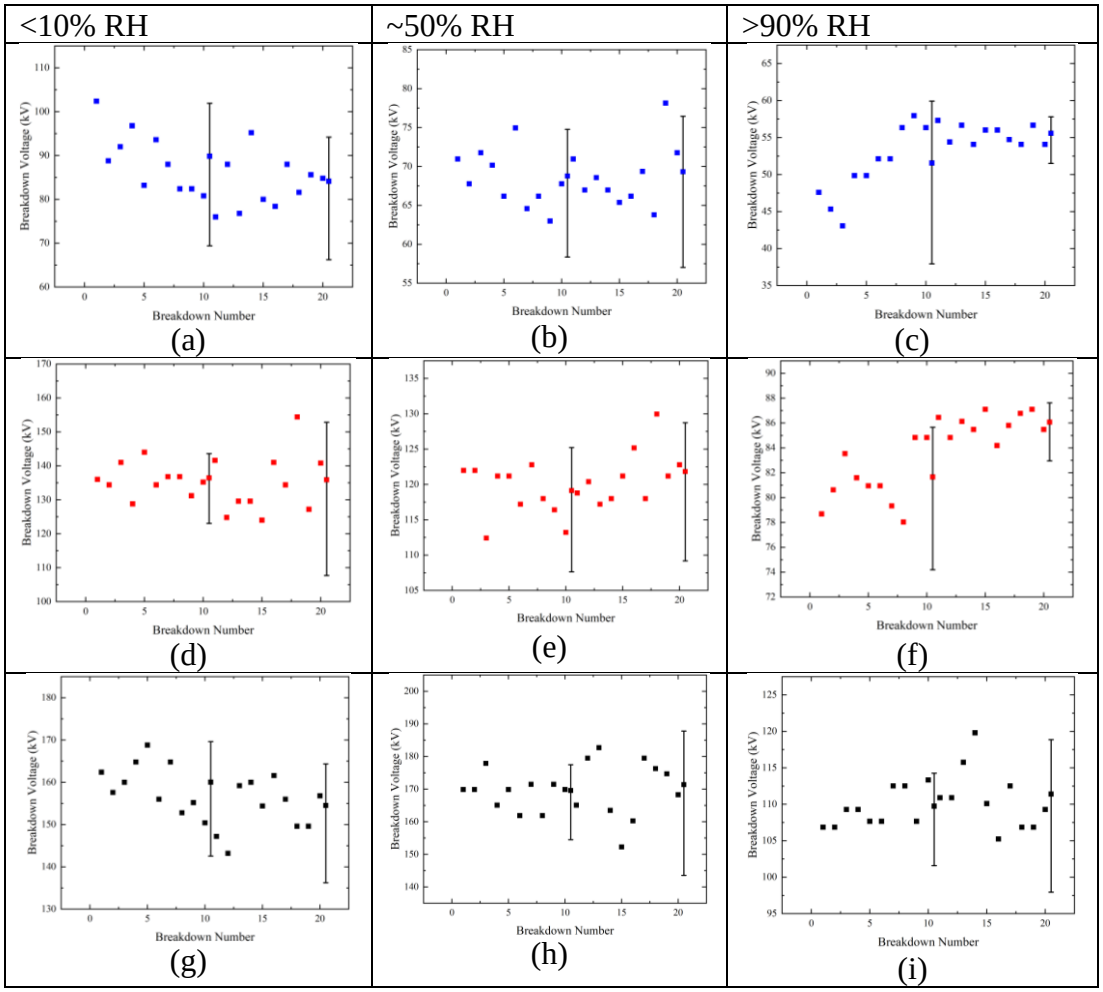

Figure AP4 - Knurled HDPE negative polarity breakdown voltage with corresponding breakdown number across the 20 events for a) -0.5 bar gauge at <10% RH, b) 0 bar gauge at <10% RH, c) 0.5 bar gauge at <10% RH, d) -0.5 bar gauge at ~50% RH, e) 0 bar gauge at ~50% RH, f) 0.5 bar gauge at ~50% RH, for g) -0.5 bar gauge at >90% RH, h) 0 bar gauge at >90% RH and i) 0.5 bar gauge at >90% RH. Error bars shows the 95.4% spread of data between the first 10 and second 10 shots of data, all tests exhibit overlapping error bars.

Polyetherimide

Negative Smooth Machined

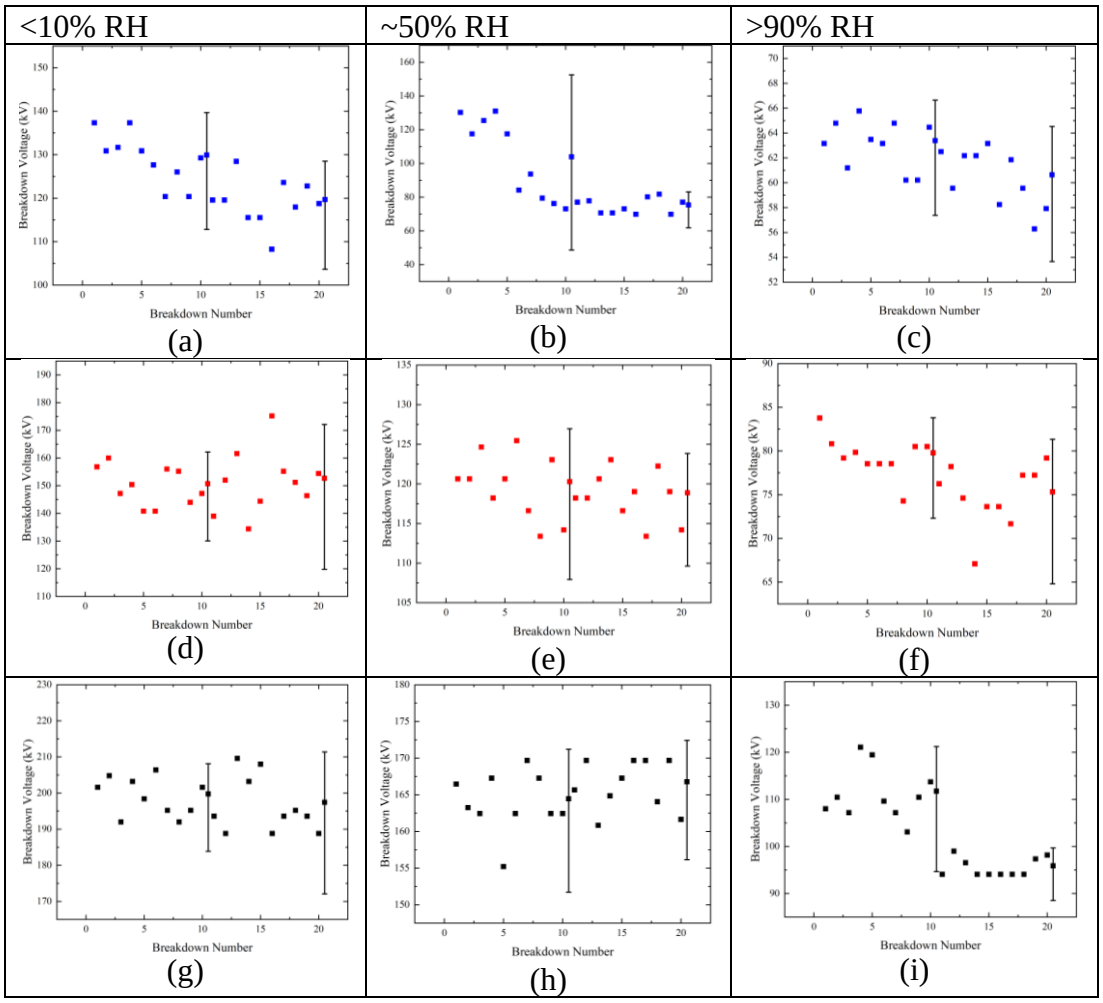

Figure AP5 - Smooth machined Polyetherimide negative polarity breakdown voltage with corresponding breakdown number across the 20 events for a) -0.5 bar gauge at <10% RH, b) 0 bar gauge at <10% RH, c) 0.5 bar gauge at <10% RH, d) -0.5 bar gauge at ~50% RH, e) 0 bar gauge at ~50% RH, f) 0.5 bar gauge at ~50% RH, for g) -0.5 bar gauge at >90% RH, h) 0 bar gauge at >90% RH and i) 0.5 bar gauge at >90% RH. Error bars shows the 95.4% spread of data between the first 10 and second 10 shots of data, all tests exhibit overlapping error bars.

Negative Knurled

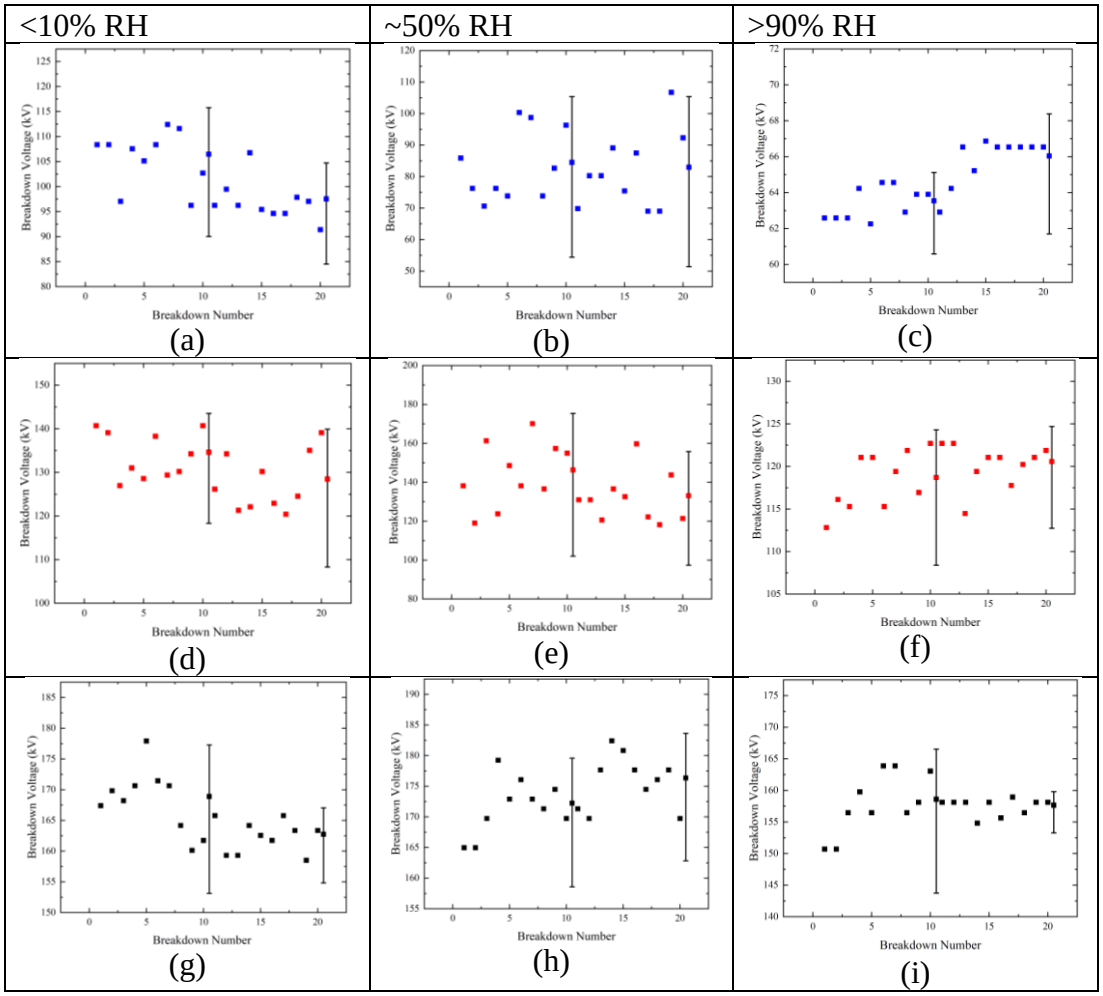

Figure AP6 - Knurled Polyetherimide negative polarity breakdown voltage with corresponding breakdown number across the 20 events for a) -0.5 bar gauge at <10% RH, b) 0 bar gauge at <10% RH, c) 0.5 bar gauge at <10% RH, d) -0.5 bar gauge at ~50% RH, e) 0 bar gauge at ~50% RH, f) 0.5 bar gauge at ~50% RH, for g) -0.5 bar gauge at >90% RH, h) 0 bar gauge at >90% RH and i) 0.5 bar gauge at >90% RH. Error bars shows the 95.4% spread of data between the first 10 and second 10 shots of data, all tests exhibit overlapping error bars.

Polyoxymethylene

Negative Smooth Machined

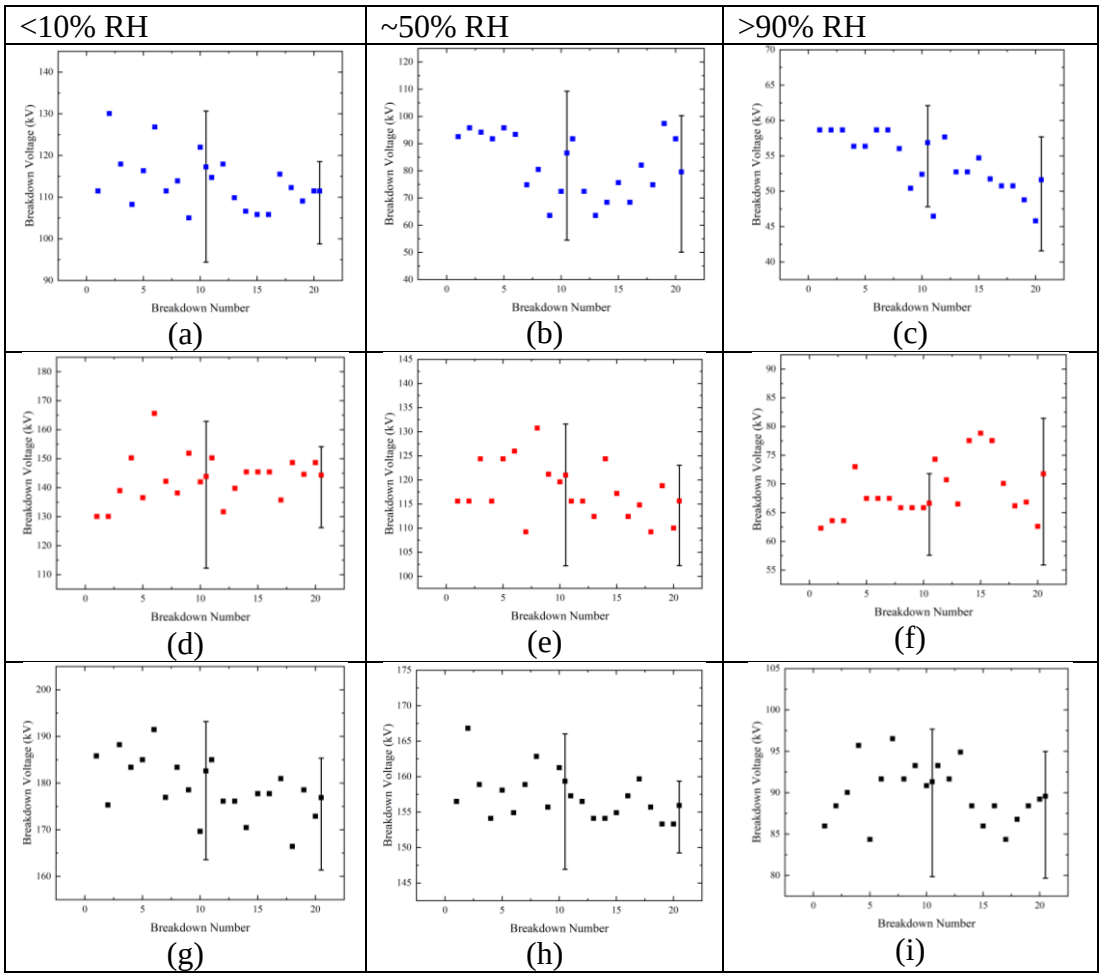

Figure AP7 - Smooth machined Polyoxymethylene negative polarity breakdown voltage with corresponding breakdown number across the 20 events for a) -0.5 bar gauge at <10% RH, b) 0 bar gauge at <10% RH, c) 0.5 bar gauge at <10% RH, d) -0.5 bar gauge at ~50% RH, e) 0 bar gauge at ~50% RH, f) 0.5 bar gauge at ~50% RH, for g) -0.5 bar gauge at >90% RH, h) 0 bar gauge at >90% RH and i) 0.5 bar gauge at >90% RH. Error bars shows the 95.4% spread of data between the first 10 and second 10 shots of data, all tests exhibit overlapping error bars.

Negative Knurled

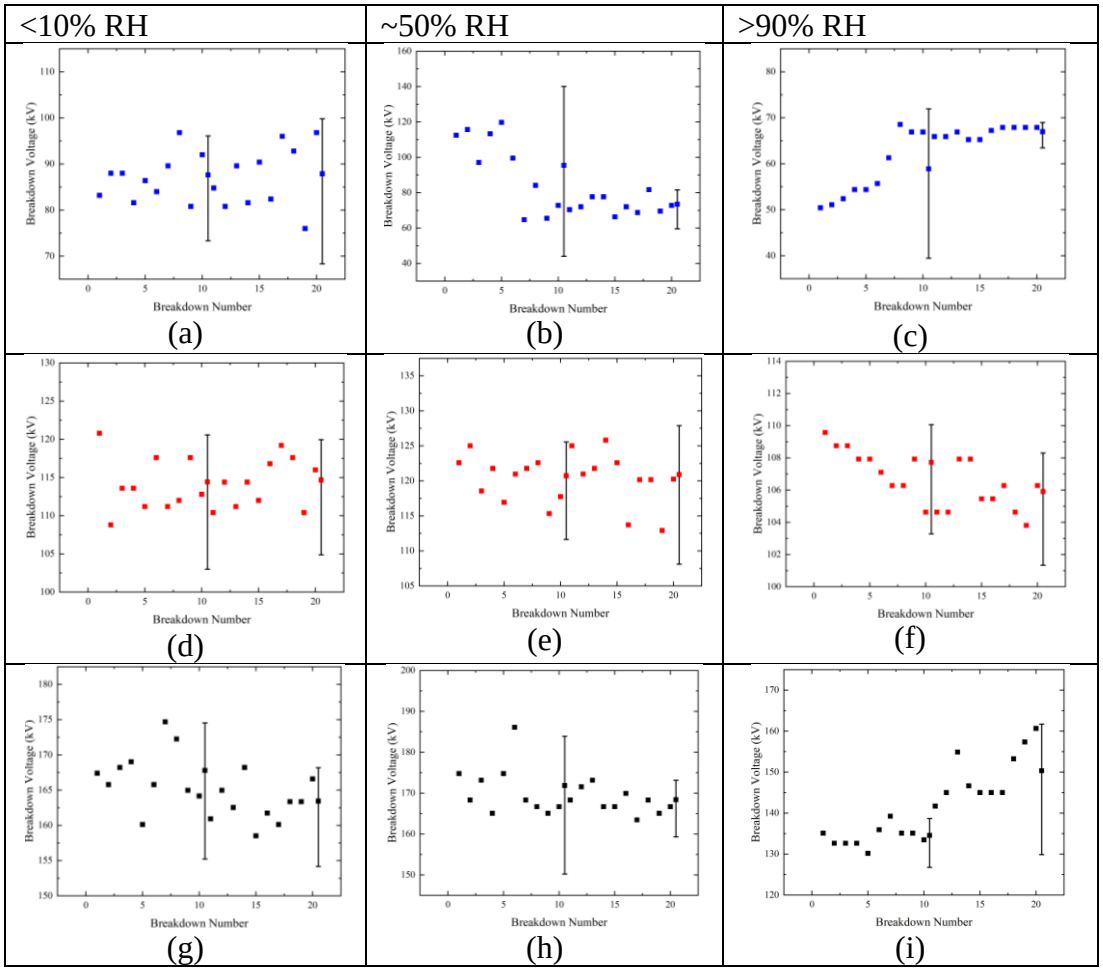

Figure AP8 - Knurled Polyoxymethylene negative polarity breakdown voltage with corresponding breakdown number across the 20 events for a) -0.5 bar gauge at <10% RH, b) 0 bar gauge at <10% RH, c) 0.5 bar gauge at <10% RH, d) -0.5 bar gauge at ~50% RH, e) 0 bar gauge at ~50% RH, f) 0.5 bar gauge at ~50% RH, for g) -0.5 bar gauge at >90% RH, h) 0 bar gauge at >90% RH and i) 0.5 bar gauge at >90% RH. Error bars shows the 95.4% spread of data between the first 10 and second 10 shots of data, all tests exhibit overlapping error bars.

HDPE

Positive Smooth Machined

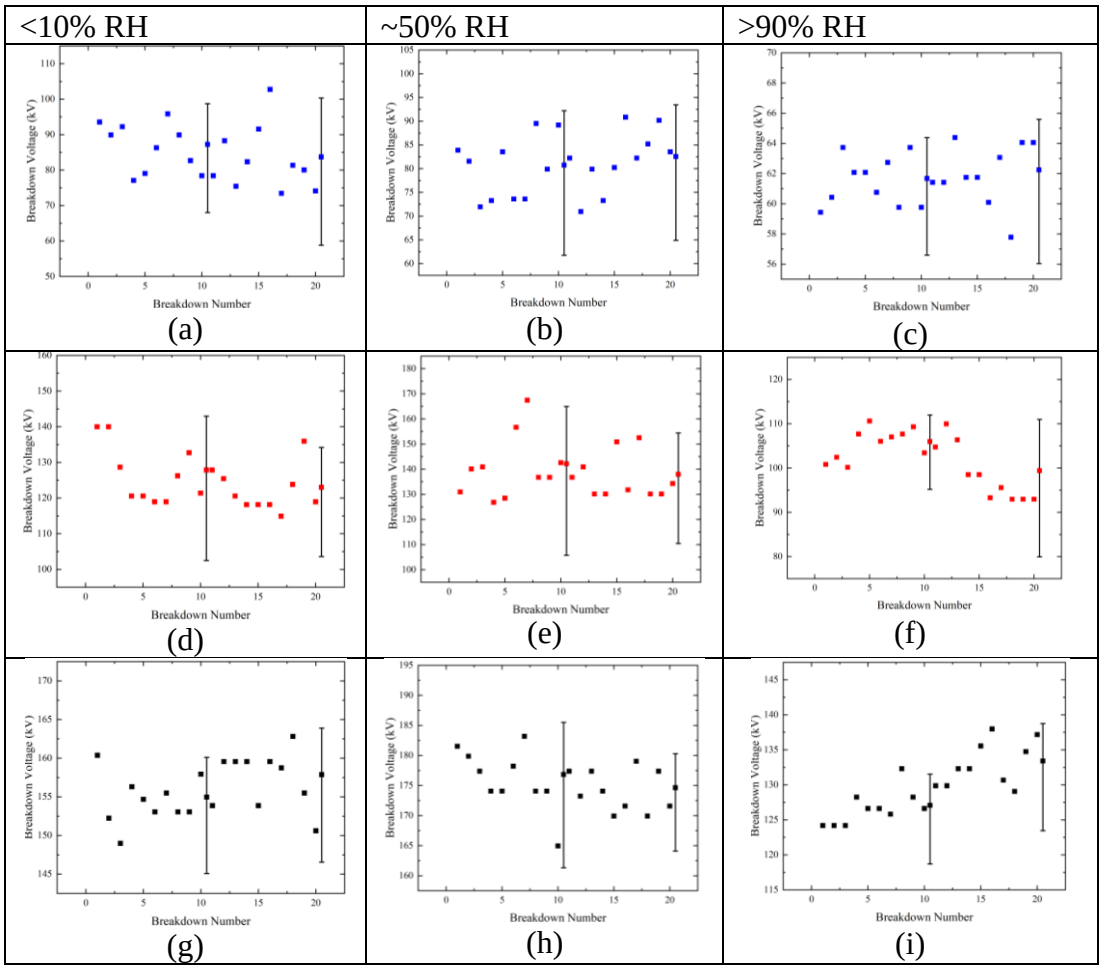

Figure AP9 - Smooth machined HDPE positive polarity breakdown voltage with corresponding breakdown number across the 20 events for a) -0.5 bar gauge at <10% RH, b) 0 bar gauge at <10% RH, c) 0.5 bar gauge at <10% RH, d) -0.5 bar gauge at ~50% RH, e) 0 bar gauge at ~50% RH, f) 0.5 bar gauge at ~50% RH, for g) -0.5 bar gauge at >90% RH, h) 0 bar gauge at >90% RH and i) 0.5 bar gauge at >90% RH. Error bars shows the 95.4% spread of data between the first 10 and second 10 shots of data, all tests exhibit overlapping error bars.

Positive Knurled

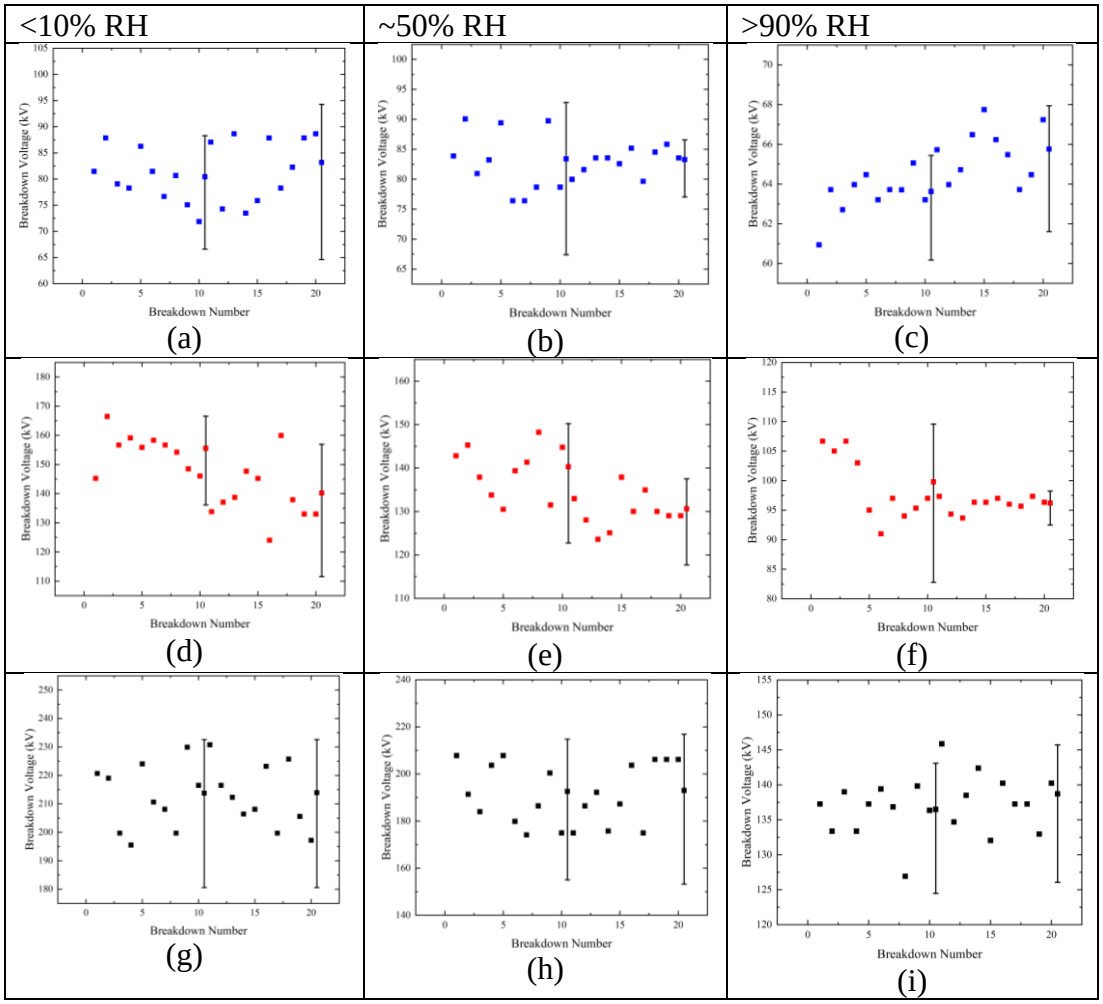

Figure AP10 - Knurled HDPE positive polarity breakdown voltage with corresponding breakdown number across the 20 events for a) -0.5 bar gauge at <10% RH, b) 0 bar gauge at <10% RH, c) 0.5 bar gauge at <10% RH, d) -0.5 bar gauge at ~50% RH, e) 0 bar gauge at ~50% RH, f) 0.5 bar gauge at ~50% RH, for g) -0.5 bar gauge at >90% RH, h) 0 bar gauge at >90% RH and i) 0.5 bar gauge at >90% RH. Error bars shows the 95.4% spread of data between the first 10 and second 10 shots of data, all tests exhibit overlapping error bars.

Polyetherimide

Positive Smooth Machined

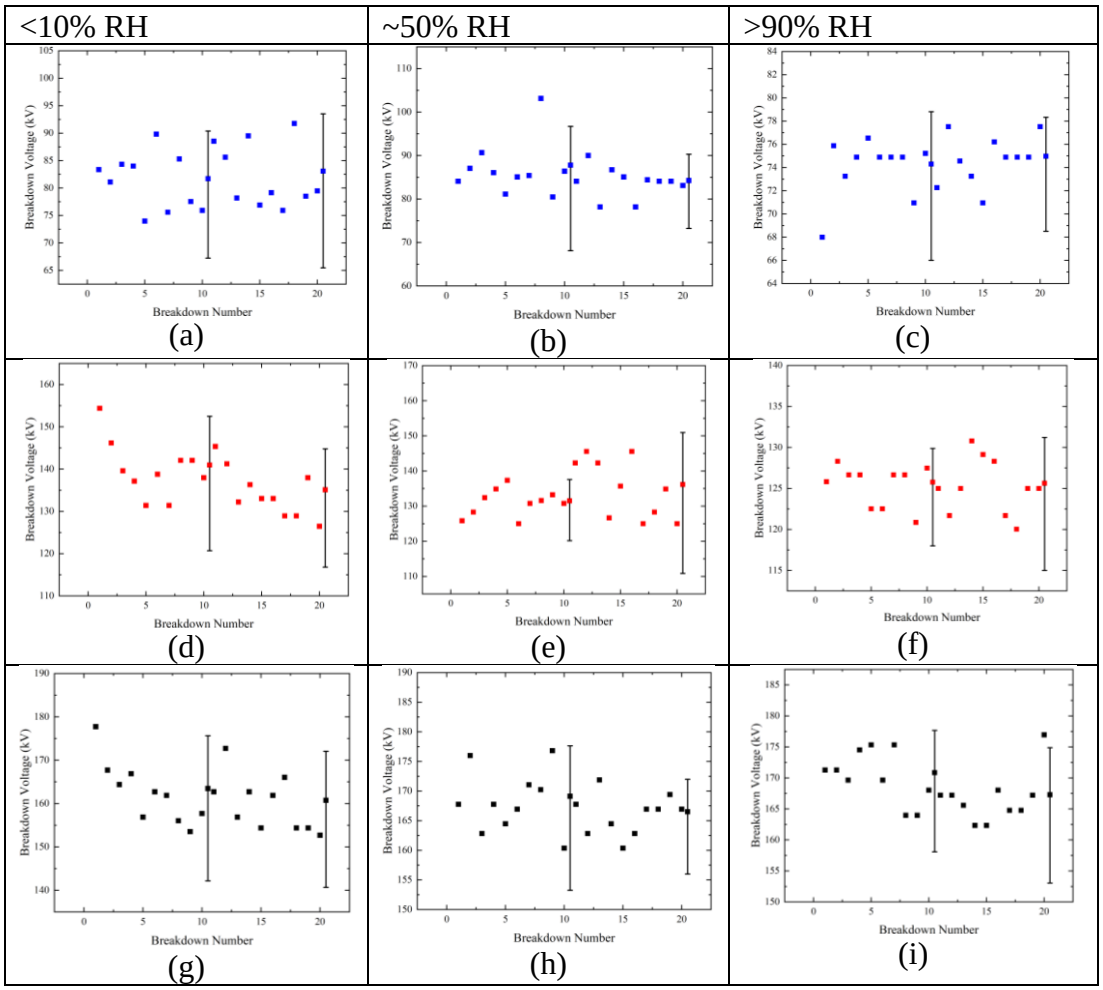

Figure AP11 - Smooth machined Polyetherimide positive polarity breakdown voltage with corresponding breakdown number across the 20 events for a) -0.5 bar gauge at <10% RH, b) 0 bar gauge at <10% RH, c) 0.5 bar gauge at <10% RH, d) -0.5 bar gauge at ~50% RH, e) 0 bar gauge at ~50% RH, f) 0.5 bar gauge at ~50% RH, for g) -0.5 bar gauge at >90% RH, h) 0 bar gauge at >90% RH and i) 0.5 bar gauge at >90% RH. Error bars shows the 95.4% spread of data between the first 10 and second 10 shots of data, all tests exhibit overlapping error bars.

Positive Knurled

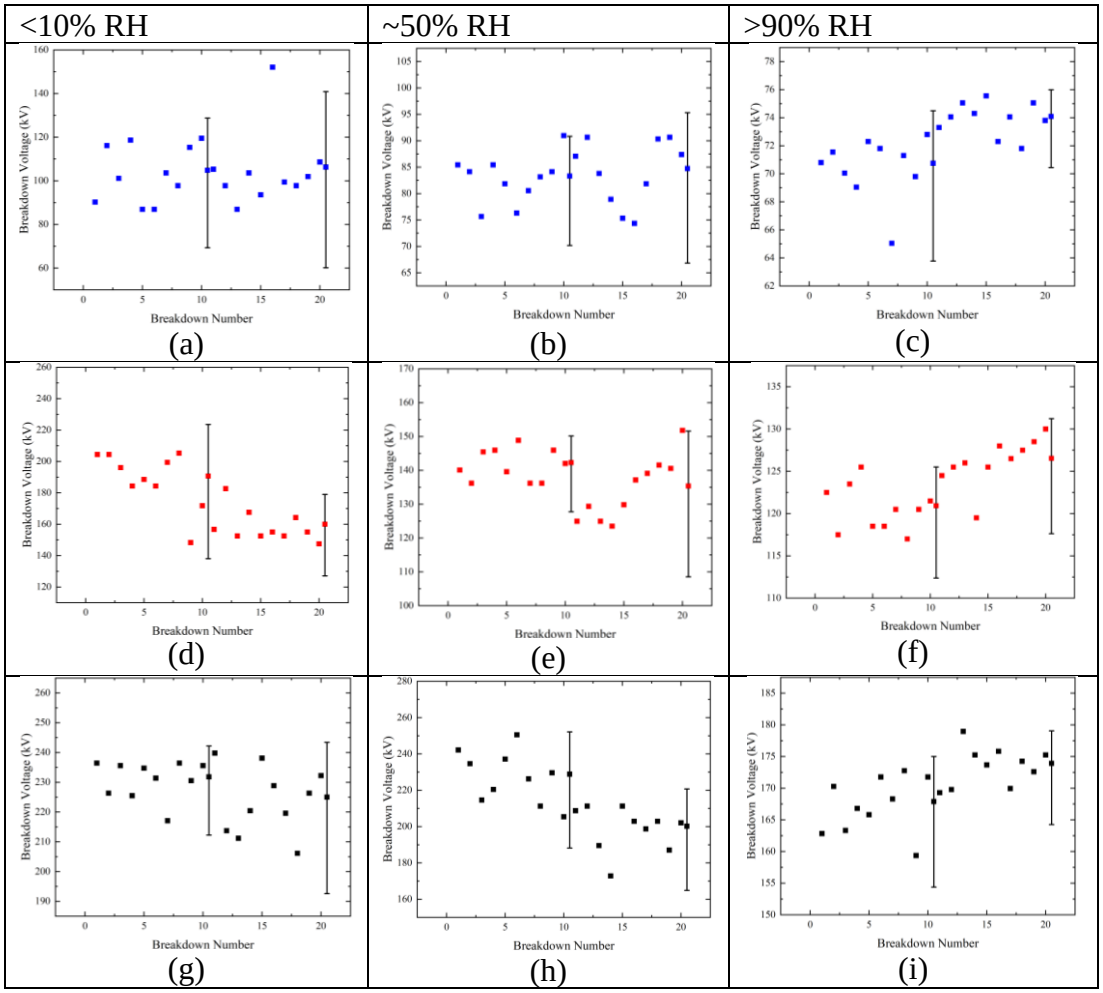

Figure AP12 - Knurled Polyetherimide positive polarity breakdown voltage with corresponding breakdown number across the 20 events for a) -0.5 bar gauge at <10% RH, b) 0 bar gauge at <10% RH, c) 0.5 bar gauge at <10% RH, d) -0.5 bar gauge at ~50% RH, e) 0 bar gauge at ~50% RH, f) 0.5 bar gauge at ~50% RH, for g) -0.5 bar gauge at >90% RH, h) 0 bar gauge at >90% RH and i) 0.5 bar gauge at >90% RH. Error bars shows the 95.4% spread of data between the first 10 and second 10 shots of data, all tests exhibit overlapping error bars.

Polyoxymethylene

Positive Smooth Machined

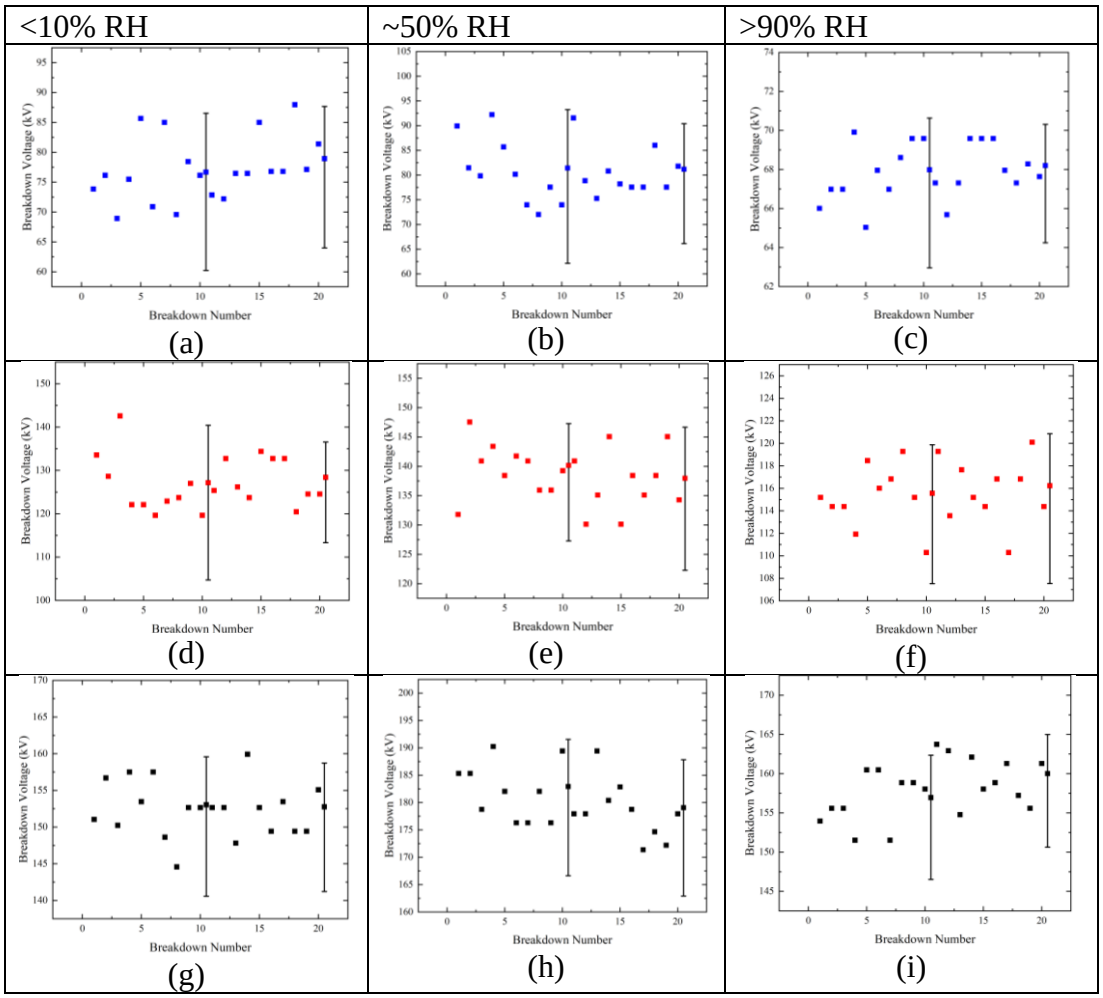

Figure AP13 - Smooth machined Polyoxymethylene positive polarity breakdown voltage with corresponding breakdown number across the 20 events for a) -0.5 bar gauge at <10% RH, b) 0 bar gauge at <10% RH, c) 0.5 bar gauge at <10% RH, d) -0.5 bar gauge at ~50% RH, e) 0 bar gauge at ~50% RH, f) 0.5 bar gauge at ~50% RH, for g) -0.5 bar gauge at >90% RH, h) 0 bar gauge at >90% RH and i) 0.5 bar gauge at >90% RH. Error bars shows the 95.4% spread of data between the first 10 and second 10 shots of data, all tests exhibit overlapping error bars.

Positive Knurled

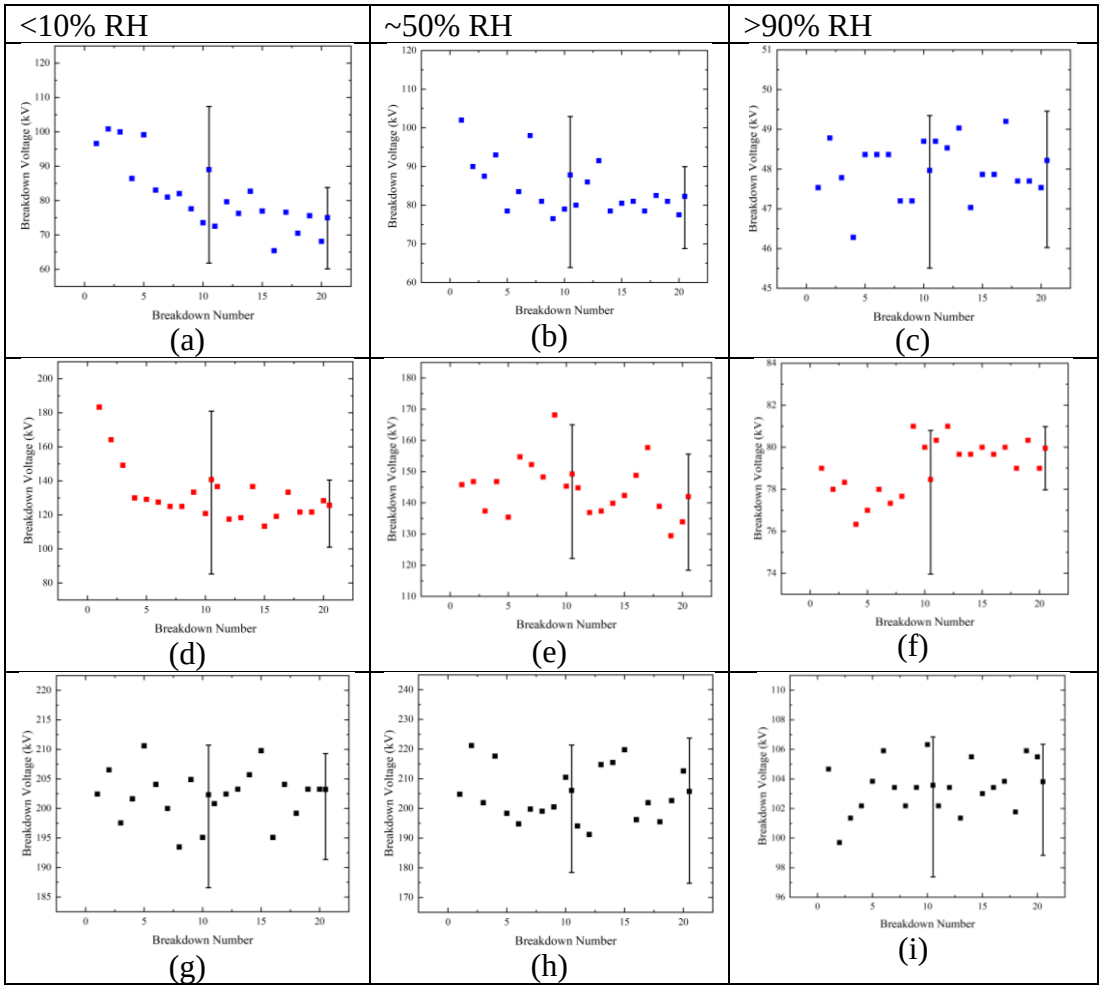

Figure AP14 – Knurled Polyoxymethylene positive polarity breakdown voltage with corresponding breakdown number across the 20 events for a) -0.5 bar gauge at <10% RH, b) 0 bar gauge at <10% RH, c) 0.5 bar gauge at <10% RH, d) -0.5 bar gauge at ~50% RH, e) 0 bar gauge at ~50% RH, f) 0.5 bar gauge at ~50% RH, for g) -0.5 bar gauge at >90% RH, h) 0 bar gauge at >90% RH and i) 0.5 bar gauge at >90% RH. Error bars shows the 95.4% spread of data between the first 10 and second 10 shots of data, all tests exhibit overlapping error bars.

APPENDIX 2: VOLT-TIME TABLE DATA

This section provides numerical data associated with the volt-time graphs in Chapters IV, V and VI.

Table AP2a. Breakdown voltage and time to breakdown at -0.5 bar gauge, 0 bar gauge and 0.5 bar gauge, and at <10% RH, ~50% RH and >90% RH.

Relative Humidity	Air pressure (Bar gauge)	Breakdown Voltage, V_{50} (kV)	Time to breakdown, t_{50} (ns)
<10%	**-0.5**	$116.1^{(+26.46)}_{(-38.25)}$	$157.45^{(+151.85)}_{(-114.36)}$
	0	$152.0^{(+13.07)}_{(-22.7)}$	$202.0^{(+113.32)}_{(-113.49)}$
	0.5	$177.5^{(+11.25)}_{(-20.43)}$	$249.1^{(+116.05)}_{(-133.2)}$
~50%	**-0.5**	$105.8^{(+21.28)}_{(-32.12)}$	$190.1^{(+135.9)}_{(-122.6)}$
	0	$145.7^{(+15.15)}_{(-25.5)}$	$243.5^{(+180.8)}_{(-160.9)}$
	0.5	$174^{(+8.8)}_{(-16.2)}$	$290.5^{(+198.6)}_{(-185.3)}$
>90%	**-0.5**	$71.2^{(+2.58)}_{(-4.77)}$	$376.1^{(+516.9)}_{(-302.3)}$
	0	$117^{(+3.2)}_{(-6.2)}$	$429.7^{(+150.2)}_{(-195.9)}$
	0.5	$158.2^{(+6.3)}_{(-12)}$	$426^{(+162.9)}_{(-202.9)}$

Table AP2b - Breakdown voltage and time to breakdown at -0.5 bar gauge, 0 bar gauge and 0.5 bar gauge, and at <10% RH, ~50% RH and >90% RH.

Relative Humidity	Air pressure (Bar gauge)	Breakdown Voltage, V_{50} (kV)	Time to breakdown, t_{50} (ns)
<10%	**-0.5**	$77.2^{(+10.54)}_{(-17.24)}$	$216.2^{(+94.7)}_{(-110.45)}$
	0	$122.1^{(+8.77)}_{(-15.68)}$	$233.9^{(+82.23)}_{(-103)}$
	0.5	$162.3^{(+6.64)}_{(-12.41)}$	$351.8^{(+)}_{(-12)}$
~50%	**-0.5**	$80.2^{(+7.93)}_{(-13.73)}$	$200.9^{(+110.02)}_{(-117.61)}$
	0	$132^{(+9.47)}_{(-16.86)}$	$233.5^{(+142.56)}_{(-145.3)}$
	0.5	$173.7^{(+11.16)}_{(-19.93)}$	$268.9^{(+239.88)}_{(-188.03)}$
>90%	**-0.5**	$82.1^{(+6.91)}_{(-12.04)}$	$221.3^{(+114.85)}_{(-120.44)}$
	0	$121.2^{(+4.66)}_{(-8.65)}$	$307.7^{(+161.1)}_{(-176.8)}$
	0.5	$165.6^{(+8.78)}_{(-15.99)}$	$382.9^{(+100.95)}_{(-142.01)}$

Table AP2c - Comparison of open-air gap arrangement and each air-solid insulation system at <10% RH and 0.5 bar gauge. 'Air' refers to the open air gap having optimum performance, 'Smooth' refers to the specific air-solid gap having optimum performance, and results with '*' refer to overlapping error bars between the open-air gap and air-solid insulation system distributions.

Material	Negative polarity smooth	Time to breakdown, t_{50} (ns)	Air or smooth	Positive polarity smooth	Time to breakdown, t_{50} (ns)	Air or smooth
HDPE	$136.5^{(+13.7)}_{(-23.9)}$	$174.7^{(+291.7)}_{(-143.9)}$	Smooth*	$85.6^{(+13.1)}_{(-20.8)}$	$205.4^{(+100.4)}_{(-115.1)}$	Air*
Polyetherimide	$125.1^{(+11.7)}_{(-20.6)}$	$204.1^{(+157.2)}_{(-137.2)}$	Smooth*	$82.4^{(+8.7)}_{(-14.6)}$	$200.3^{(+108.8)}_{(-108.5)}$	Air*
Polyoxymethylene	$114.6^{(+10.8)}_{(-18.8)}$	$190.7^{(+253)}_{(-152.5)}$	Air*	$77.9^{(+8.5)}_{(-14.3)}$	$219^{(+86.6)}_{(-105.6)}$	Smooth*
Air	$116.1^{(+26.5)}_{(-38.3)}$	$157.5^{(+151.9)}_{(-114.4)}$	-	$77.2^{(+10.5)}_{(-17.3)}$	$216.2^{(+94.7)}_{(-110.5)}$	-

Table AP2d - Comparison of open-air gap arrangement and each air-solid insulation system at <10% RH and 0 bar gauge. 'Air' refers to the open air gap having optimum performance, 'Smooth' refers to the specific air-solid gap having optimum performance, and results with '*' refer to overlapping error bars between the open-air gap and air-solid insulation system distributions.

Material	Negative polarity smooth	Time to breakdown, t_{50} (ns)	Air or smooth	Positive polarity smooth	Time to breakdown, t_{50} (ns)	Air or smooth
HDPE	$154.6^{(+18.7)}_{(-31.2)}$	$193.2^{(+135.3)}_{(-124.9)}$	Smooth*	$125.6^{(+12.3)}_{(-21.6)}$	$277.3^{(+294.3)}_{(-206.5)}$	Smooth*
Polyetherimide	$151.8^{(+14.4)}_{(-25.3)}$	$194.9^{(+154.1)}_{(-128)}$	Air*	$138.2^{(+10.7)}_{(-19)}$	$213.7^{(+85.2)}_{(-104.4)}$	Smooth*
Polyoxymethylene	$144.2^{(+12.9)}_{(-23.3)}$	$235.7^{(+185.5)}_{(-157.6)}$	Air*	$127.8^{(+9.8)}_{(-17.5)}$	$200.9^{(+60.4)}_{(-82.4)}$	Smooth*
Air	$152^{(+13.1)}_{(-22.7)}$	$202^{(+113.3)}_{(-113.5)}$	-	$122.1^{(+8.77)}_{(-15.68)}$	$233.9^{(+82.2)}_{(-103)}$	-

Table AP2e - Comparison of open-air gap arrangement and each air-solid insulation system at <10% RH and 0.5 bar gauge. 'Air' refers to the open air gap having optimum performance, 'Smooth' refers to the specific air-solid gap having optimum performance, and results with '*' refer to overlapping error bars between the open-air gap and air-solid insulation system distributions.

Material	Negative polarity smooth	Time to breakdown, t_{50} (ns)	Air or smooth	Positive polarity smooth	Time to breakdown, t_{50} (ns)	Air or smooth
HDPE	$201.9^{(+12.7)}_{(-23.5)}$	$226.3^{(+190)}_{(-160.5)}$	Smooth*	$156.5^{(+5.5)}_{(-10.6)}$	$317.4^{(+196.3)}_{(-191.6)}$	Air*
Polyetherimide	$198.7^{(+10.3)}_{(-19)}$	$196.2^{(+180.2)}_{(-131)}$	Smooth*	$162.2^{(+10.8)}_{(-18.8)}$	$324.7^{(+238.8)}_{(-215.4)}$	Air*
Polyoxymethylene	$179.9^{(+9.9)}_{(-17.5)}$	$223.3^{(+92.9)}_{(-115.1)}$	Smooth*	$152.9^{(+5.5)}_{(-10.2)}$	$381.7^{(+377.4)}_{(-283.4)}$	Air*
Air	$177.5^{(+11.3)}_{(-20.4)}$	$249.1^{(+116.1)}_{(-133.2)}$	-	$162.3^{(+6.6)}_{(-12.4)}$	$351.8^{(+182.1)}_{(-203.4)}$	-

Table AP2f - Comparison of open-air gap arrangement and each air-solid insulation system at ~50% RH and -0.5 bar gauge. 'Air' refers to the open air gap having optimum performance, 'Smooth' refers to the specific air-solid gap having optimum

performance, and results with '*' refer to overlapping error bars between the open-air gap and air-solid insulation system distributions.

Material	Negative polarity smooth	Time to breakdown, t_{50} (ns)	Air or smooth	Positive polarity smooth	Time to breakdown, t_{50} (ns)	Air or smooth
HDPE	$106.9^{(+20.7)}_{(-32.3)}$	$215.4^{(+138.2)}_{(-132.1)}$	Smooth*	$81.7^{(+10.3)}_{(-16.8)}$	$187.7^{(+89.2)}_{(-100.2)}$	Smooth*
Polyetherimide	$90.2^{(+43.1)}_{(-48.7)}$	$168.3^{(+235.4)}_{(-140.3)}$	Air*	$86.1^{(+9)}_{(-15.2)}$	$230.5^{(+118.2)}_{(-129.7)}$	Smooth*
Polyoxymethylene	$83.2^{(+20.2)}_{(-29)}$	$225.3^{(+283.4)}_{(-177)}$	Air*	$81.3^{(+9.4)}_{(-15.7)}$	$214.2^{(+109.3)}_{(-115.8)}$	Smooth*
Air	$105.8^{(+21.3)}_{(-32.1)}$	$190.1^{(+135.9)}_{(-122.6)}$	-	$80.2^{(+7.9)}_{(-13.7)}$	$200.9^{(+110)}_{(-117.6)}$	-

Table AP2g - Comparison of open-air gap arrangement and each air-solid insulation system at ~50% RH and 0 bar gauge. 'Air' refers to the open air gap having optimum performance, 'Smooth' refers to the specific air-solid gap having optimum performance, and results with '*' refer to overlapping error bars between the open-air gap and air-solid insulation system distributions.

Material	Negative polarity smooth	Time to breakdown, t_{50} (ns)	Air or smooth	Positive polarity smooth	Time to breakdown, t_{50} (ns)	Air or smooth
HDPE	$145.3^{(+9.5)}_{(-17.2)}$	$180.3^{(+70.7)}_{(-82)}$	Air*	$140.2^{(+18.1)}_{(-29.8)}$	$220.7^{(+97.5)}_{(-110.8)}$	Smooth*
Polyetherimide	$119.6^{(+5.4)}_{(-10.2)}$	$411.8^{(+274.8)}_{(-266.2)}$	Air*	$134^{(+10.8)}_{(-19)}$	$229.5^{(+97.4)}_{(-114.1)}$	Smooth*
Polyoxymethylene	$118.5^{(+9.2)}_{(-16.3)}$	$260.3^{(+188.6)}_{(-172.1)}$	Air*	$139.1^{(+7.2)}_{(-13.2)}$	$244^{(+115.4)}_{(-130.1)}$	Smooth*
Air	$145.7^{(+15.2)}_{(-25.5)}$	$243.5^{(+180.8)}_{(-160.9)}$	-	$132^{(+9.5)}_{(-16.9)}$	$233.5^{(+142.6)}_{(-145.3)}$	-

Table AP2h - Comparison of open-air gap arrangement and each air-solid insulation system at ~50% RH and 0.5 bar gauge. 'Air' refers to the open air gap having optimum performance, 'Smooth' refers to the specific air-solid gap having optimum performance, and results with '*' refer to overlapping error bars between the open-air gap and air-solid insulation system distributions.

Material	Negative polarity smooth	Time to breakdown, t_{50} (ns)	Air or smooth	Positive polarity smooth	Time to breakdown, t_{50} (ns)	Air or smooth
HDPE	$190.5^{(+13.5)}_{(-23.8)}$	$290.5^{(+168.2)}_{(-174.7)}$	Smooth*	$175.8^{(+6.5)}_{(-12.3)}$	$279.2^{(+147)}_{(-153.4)}$	Smooth*
Polyetherimide	$165.7^{(+5.8)}_{(-11)}$	$406.8^{(+304.7)}_{(-273.4)}$	Air*	$167.9^{(+7)}_{(-129)}$	$299.6^{(+181.6)}_{(-181.2)}$	Air*
Polyoxymethylene	$157.8^{(+5.6)}_{(-10.7)}$	$401.1^{(+272.9)}_{(-260.3)}$	Air*	$181.1^{(+8.3)}_{(-15.5)}$	$260.8^{(+125.4)}_{(-132.6)}$	Smooth*
Air	$174.8^{(+8.8)}_{(-16.2)}$	$290.5^{(+198.6)}_{(-185.3)}$	-	$173.7^{(+11.2)}_{(-19.9)}$	$268.9^{(+239.9)}_{(-188)}$	-

Table AP2i - Comparison of open-air gap arrangement and each air-solid insulation system at >90% RH and -0.5 bar gauge. 'Air' refers to the open air gap having optimum performance, 'Smooth' refers to the specific air-solid gap having optimum performance, and results with '*' refer to overlapping error bars between the open-air gap and air-solid insulation system distributions.

Material	Negative polarity smooth	Time to breakdown, t_{50} (ns)	Air or smooth	Positive polarity smooth	Time to breakdown, t_{50} (ns)	Air or smooth

HDPE	$66^{(+2.6)}_{(-4.8)}$	$421.5^{(+220)}_{(-238)}$	Air*	$62^{(+2.2)}_{(-5.1)}$	$227.1^{(+206.7)}_{(-161.9)}$	Air
Polyetherimide	$62.1^{(+3.9)}_{(-6.9)}$	$304.4^{(+282)}_{(-211.7)}$	Air	$74.7^{(+3.6)}_{(-6.7)}$	$297.4^{(+74.8)}_{(-108.6)}$	Air*
Polyoxymethylene	$54.4^{(+6.5)}_{(-10.8)}$	$397^{(+262)}_{(-253.8)}$	Air	$68.1^{(+2.2)}_{(-4)}$	$280.9^{(+150.1)}_{(-160.1)}$	Air*
Air	$71.2^{(+2.6)}_{(-4.8)}$	$374.1^{(+516.9)}_{(-302.2)}$	-	$82.1^{(+6.9)}_{(-12)}$	$221.3^{(+114.9)}_{(-120.4)}$	-

Table AP2j – Comparison of open-air gap arrangement and each air-solid insulation system at >90% RH and 0 bar gauge. 'Air' refers to the open air gap having optimum performance, 'Smooth' refers to the specific air-solid gap having optimum performance, and results with '*' refer to overlapping error bars between the open-air gap and air-solid insulation system distributions.

Material	**Negative polarity smooth**	**Time to breakdown, t_{50} (ns)**	**Air or smooth**	**Positive polarity smooth**	**Time to breakdown, t_{50} (ns)**	**Air or smooth**
HDPE	$109.8^{(+7)}_{(-12.9)}$	$355.5^{(+273.3)}_{(-239.7)}$	Air*	$102.9^{(+9.5)}_{(-16.7)}$	$286.1^{(+52.2)}_{(-80.6)}$	Air
Polyetherimide	$77.7^{(+5.8)}_{(-10.5)}$	$415.5^{(+153.4)}_{(-189.7)}$	Air	$125.7^{(+4.4)}_{(-8.3)}$	$331.9^{(+262)}_{(-223.6)}$	Smooth*
Polyoxymethylene	$69.4^{(+8.2)}_{(-14.1)}$	$376.6^{(+260)}_{(-238.3)}$	Air	$115.9^{(+4.1)}_{(-7.6)}$	$436.9^{(+357.2)}_{(-301.1)}$	Air*
Air	$117^{(+3.2)}_{(-6.2)}$	$429.7^{(+150.2)}_{(-195.9)}$	-	$121.2^{(+4.7)}_{(-8.7)}$	$307.7^{(+161.1)}_{(-176.8)}$	-

Table AP2k - Comparison of open-air gap arrangement and each air-solid insulation system at >90% RH and 0.5 bar gauge. 'Air' refers to the open air gap having optimum performance, 'Smooth' refers to the specific air-solid gap having optimum performance, and results with '*' refer to overlapping error bars between the open-air gap and air-solid insulation system distributions.

Material	**Negative polarity smooth**	**Time to breakdown, t_{50} (ns)**	**Air or smooth**	**Positive polarity smooth**	**Time to breakdown, t_{50} (ns)**	**Air or smooth**
HDPE	$125.1^{(+7.6)}_{(-13.9)}$	$310.3^{(+100.8)}_{(-132.1)}$	Air	$130.5^{(+6.6)}_{(-12.2)}$	$278.4^{(+217.8)}_{(-192.6)}$	Air
Polyetherimide	$104.4^{(+15.2)}_{(-24.8)}$	$475.6^{(+253.4)}_{(-269.7)}$	Air	$169.1^{(+6.9)}_{(-12.8)}$	$283.6^{(+135.2)}_{(-152.7)}$	Smooth*
Polyoxymethylene	$90.5^{(+5.6)}_{(-10.2)}$	$537.2^{(+186.2)}_{(-236.1)}$	Air	$158.5^{(+5.3)}_{(-9.8)}$	$335.4^{(+150.9)}_{(-179.6)}$	Air*
Air	$158.2^{(+6.3)}_{(-11.9)}$	$426.1^{(+162.9)}_{(-202.9)}$	-	$165.6^{(+8.9)}_{(-16)}$	$382.9^{(+101)}_{(-142)}$	-

Table AP2l. - Comparison of open-air gap arrangement and each air-(knurled) solid insulation system at <10% RH and -0.5 bar gauge. 'Air' refers to the open air gap having optimum performance, 'knurled' refers to the specific air-(knurled) solid gap having optimum performance, and results with '*' refer to overlapping error bars between the open-air gap and air-(knurled) solid insulation system distributions.

Material	**Negative polarity knurled**	**Time to breakdown, t_{50} (ns)**	**Air or knurled**	**Positive polarity knurled**	**Time to breakdown, t_{50} (ns)**	**Air or knurled**
HDPE	$87.1^{(+11.1)}_{(-18.3)}$	$279.4^{(+279.4)}_{(-204.4)}$	Air*	$81.9^{(+9.2)}_{(-14.8)}$	$218.1^{(+82.8)}_{(-101.2)}$	Knurled*
Polyetherimide	$102.3^{(+10.5)}_{(-18.3)}$	$241.5^{(+159.7)}_{(-149.8)}$	Air*	$105.6^{(+25.9)}_{(-36.6)}$	$163.3^{(+138.1)}_{(-116.4)}$	Knurled*
Polyoxymethylene	$87.8^{(+9.3)}_{(-15.7)}$	$229.2^{(+107)}_{(-121)}$	Air*	$82.3^{(+17)}_{(-25.4)}$	$176.9^{(+89.7)}_{(-100)}$	Knurled*
Air	$116.1^{(+26.5)}_{(-38.3)}$	$157.5^{(+151.9)}_{(-114.4)}$	-	$77.2^{(+10.5)}_{(-17.3)}$	$216.2^{(+94.7)}_{(-110.5)}$	-

Table AP2m - Comparison of open-air gap arrangement and each air-(knurled) solid insulation system at <10% RH and 0 bar gauge. 'Air' refers to the open air gap having optimum performance, 'knurled' refers to the specific air-(knurled) solid gap having optimum performance, and results with '*' refer to overlapping error bars between the open-air gap and air-(knurled) solid insulation system distributions.

Material	Negative polarity knurled	Time to breakdown, t_{50} (ns)	Air or knurled	Positive polarity knurled	Time to breakdown, t_{50} (ns)	Air or knurled
HDPE	$136.3^{(+11.4)}_{(-19.8)}$	$270.8^{(+165.5)}_{(-165)}$	Air*	$148.3^{(+17.9)}_{(-29.7)}$	$242.9^{(+155.9)}_{(-149.8)}$	Knurled *
Polyetherimide	$131.7^{(+10.3)}_{(-18.4)}$	$255.5^{(+151)}_{(-153.6)}$	Air*	$175.9^{(+35.1)}_{(-51.5)}$	$178.2^{(+118.2)}_{(-121.3)}$	Knurled *
Polyoxymethylene	$114.6^{(+5)}_{(-9.6)}$	$329.9^{(+88.9)}_{(-128.9)}$	Air	$133.6^{(+29.5)}_{(-42.1)}$	$199.5^{(+100)}_{(-106.5)}$	Knurled *
Air	$152^{(+13.1)}_{(-22.7)}$	$202^{(+113.3)}_{(-113.5)}$	-	$122.1^{(+8.77)}_{(-15.68)}$	$233.9^{(+82.2)}_{(-103)}$	-

Table AP2n - Comparison of open-air gap arrangement and each air-(knurled) solid insulation system at <10% RH and 0.5 bar gauge. 'Air' refers to the open air gap having optimum performance, 'knurled' refers to the specific air-(knurled) solid gap having optimum performance, and results with '*' refer to overlapping error bars between the open-air gap and air-(knurled) solid insulation system distributions.

Material	Negative polarity knurled	Time to breakdown, t_{50} (ns)	Air or knurled	Positive polarity knurled	Time to breakdown, t_{50} (ns)	Air or knurled
HDPE	$157.4^{(+9.7)}_{(-17.7)}$	$377.5^{(+253.9)}_{(-241.6)}$	Knurled*	$213.9^{(+17.8)}_{(-29.7)}$	$252.9^{(+103.2)}_{(-124.3)}$	Knurled
Polyetherimide	$166^{(+7.8)}_{(-14.5)}$	$431.6^{(+181.9)}_{(-215.1)}$	Knurled*	$228.6^{(+14.8)}_{(-26.3)}$	$230.7^{(+128.2)}_{(-136.4)}$	Knurled
Polyoxymethylene	$165.7^{(+6.2)}_{(-11.8)}$	$378.3^{(+193.1)}_{(-207.5)}$	Knurled*	$202.8^{(+6.8)}_{(-12.5)}$	$271^{(+85.6)}_{(-113.8)}$	Knurled
Air	$177.5^{(+11.3)}_{(-20.4)}$	$249.1^{(+116.1)}_{(-133.2)}$	-	$162.3^{(+6.6)}_{(-12.4)}$	$351.8^{(+182.1)}_{(-203.4)}$	-

Table AP2o. - Comparison of open-air gap arrangement and each air-(knurled) solid insulation system at |50% RH and -0.5 bar gauge. 'Air' refers to the open-air gap having optimum performance, 'knurled' refers to the specific air-(knurled) solid gap having optimum performance, and results with '*' refer to overlapping error bars between the open-air gap and air-(knurled) solid insulation system distributions.

Material	Negative polarity knurled	Time to breakdown, $t_{50\%}$ (ns)	Air or knurled	Positive polarity knulred	Time to breakdown, $t_{50\%}$ (ns)	Air or knurled
HDPE	$69.1^{(+5.9)}_{(-10.4)}$	$262.6^{(+401.3)}_{(-222)}$	Air*	$83.4^{(+6.1)}_{(-10.7)}$	$203.7^{(+97.4)}_{(-110.6)}$	Knurled*
Polyetherimide	$83.8^{(+19.2)}_{(-28.2)}$	$256.5^{(+239.6)}_{(-188.3)}$	Air*	$84.1^{(+8.3)}_{(-14.4)}$	$206.2^{(+76.7)}_{(-96.1)}$	Knurled*
Polyoxymethylene	$85^{(+34.3)}_{(-41.1)}$	$242.4^{(+364.1)}_{(-199.3)}$	Air*	$85.2^{(+12.2)}_{(-20)}$	$157.7^{(+95.4)}_{(-96.2)}$	Knurled*
Air	$105.8^{(+21.3)}_{(-32.1)}$	$190.1^{(+135.9)}_{(-122.6)}$	-	$80.2^{(+7.9)}_{(-13.7)}$	$200.9^{(+110)}_{(-117.6)}$	-

Table AP2p - Comparison of open-air gap arrangement and each air-(knurled) solid insulation system at ~50% RH and 0 bar gauge. 'Air' refers to the open-air gap having optimum performance, 'knurled' refers to the specific air-(knurled) solid gap having

optimum performance, and results with '*' refer to overlapping error bars between the open-air gap and air-(knurled) solid insulation system distributions.

Material	Negative polarity knurled	Time to breakdown, $t_{50\%}$ (ns)	Air or knurled	Positive polarity knurled	Time to breakdown, $t_{50\%}$ (ns)	Air or knurled
HDPE	$120.5^{+6}_{-11.3}$	$333.5^{+303.1}_{-245.2}$	Air*	$135.8^{+10.8}_{-19.3}$	$196.1^{+81.2}_{-99.8}$	Knurled*
Polyetherimide	$139.9^{+26}_{-40.2}$	$250^{+296.3}_{-194.3}$	Air*	$139^{+12.6}_{-21.8}$	$208.7^{+163.1}_{-141.9}$	Knurled*
Polyoxymethylene	$120.8^{+5.2}_{-9.8}$	$307.1^{+291.7}_{-218.8}$	Air*	$145.7^{+14}_{-24.6}$	$216^{+276.8}_{-171.4}$	Knurled*
Air	$145.7^{+15.2}_{-25.5}$	$243.5^{+180.8}_{-160.9}$	-	$132^{+9.5}_{-16.9}$	$233.5^{+142.6}_{-145.3}$	-

Table AP2q - Comparison of open-air gap arrangement and each air-(knurled) solid insulation system at ~50% RH and 0.5 bar gauge. 'Air' refers to the open-air gap having optimum performance, 'knurled' refers to the specific air-(knurled) solid gap having optimum performance, and results with '*' refer to overlapping error bars between the open-air gap and air-(knurled) solid insulation system distributions.

Material	Negative polarity knurled	Time to breakdown, $t_{50\%}$ (ns)	Air or knurled	Positive polarity knurled	Time to breakdown, $t_{50\%}$ (ns)	Air or knurled
HDPE	$170.6^{+11.5}_{-20.7}$	$418.4^{+295.6}_{-277.6}$	Air*	$192.9^{+20.7}_{-35.8}$	$204.5^{+149.1}_{-131.3}$	Knurled*
Polyetherimide	$174.4^{+7.2}_{-13.5}$	$322.6^{+156.1}_{-169.2}$	Air*	$215.2^{+31}_{-50.3}$	$213.6^{+160}_{-142.9}$	Knurled*
Polyoxymethylene	$170.3^{+8.9}_{-16.8}$	$336^{+180.4}_{-197.7}$	Air*	$206^{+14.8}_{-25.7}$	$242.2^{+126.5}_{-134}$	Knurled*
Air	$174.8^{+8.8}_{-16.2}$	$290.5^{+198.6}_{-185.3}$	-	$173.7^{+11.2}_{-19.9}$	$268.9^{+239.9}_{-188}$	-

Table AP2r - Comparison of open-air gap arrangement and each air-(knurled) solid insulation system at >90% RH and -0.5 bar gauge. 'Air' refers to the open-air gap having optimum performance, 'knurled' refers to the specific air-(knurled) solid gap having optimum performance, and results with '*' refer to overlapping error bars between the open-air gap and air-(knurled) solid insulation system distributions.

Material	Negative polarity knurled	Time to breakdown, $t_{50\%}$ (ns)	Air or knurled	Positive polarity knurled	Time to breakdown, $t_{50\%}$ (ns)	Air or knurled
HDPE	$53.8^{+6.7}_{-11.2}$	421.5^{+220}_{-238}	Air	$64.8^{+2.4}_{-4.7}$	$515.9^{+230.7}_{-267.3}$	Air
Polyetherimide	$64.9^{+2.7}_{-4.9}$	$304.4^{+282}_{-211.7}$	Air*	$72.5^{+3.8}_{-7}$	$474.7^{+519.7}_{-366.5}$	Air*
Polyoxymethylene	$63.3^{+11.6}_{-18}$	$349.7^{+139.1}_{-171.4}$	Air*	$48.1^{+1.2}_{-2.1}$	$443.6^{+165.3}_{-202.7}$	Air
Air	$71.2^{+2.6}_{-4.8}$	$374.1^{+516.9}_{-302.2}$	-	$82.1^{+6.9}_{-12}$	$221.3^{+114.9}_{-120.4}$	-

Table AP2s - Comparison of open-air gap arrangement and each air-(knurled) solid insulation system at |>90% RH and 0 bar gauge. 'Air' refers to the open-air gap having optimum performance, 'knurled' refers to the specific air-(knurled) solid gap having

optimum performance, and results with '*' refer to overlapping error bars between the open-air gap and air-(knurled) solid insulation system distributions.

Material	**Negative polarity knurled**	**Time to breakdown, $t_{50\%}$ (ns)**	**Air or knurled**	**Positive polarity knurled**	**Time to breakdown, $t_{50\%}$ (ns)**	**Air or knurled**
HDPE	$84.1\binom{+4.4}{-8.2}$	$440.6\binom{+416.2}{-324.7}$	Air	$98.2\binom{+7.3}{-13}$	$348.9\binom{+64.9}{-100.6}$	Air
Polyetherimide	$119.7\binom{+4.6}{-8.7}$	$430.8\binom{+200.5}{-229.9}$	Knurled*	$123.9\binom{+6}{-11.2}$	$319.6\binom{+124.2}{-141.6}$	Knurled*
Polyoxymethylene	$106.9\binom{+2.5}{-4.8}$	$328\binom{+125.8}{-154.6}$	Air	$79.3\binom{+2}{-3.8}$	$470\binom{+271.6}{-284.1}$	Air
Air	$117\binom{+3.2}{-6.2}$	$429.7\binom{+150.2}{-195.9}$	-	$121.2\binom{+4.7}{-8.7}$	$307.7\binom{+161.1}{-176.8}$	-

Table AP2t. Comparison of open-air gap arrangement and each air-(knurled) solid insulation system at |>90% RH and 0.5 bar gauge. 'Air' refers to the open-air gap having optimum performance, 'knurled' refers to the specific air-(knurled) solid gap having optimum performance, and results with '*' refer to overlapping error bars between the open-air gap and air-(knurled) solid insulation system distributions.

Material	**Negative polarity knurled**	**Time to breakdown, $t_{50\%}$ (ns)**	**Air or knurled**	**Positive polarity knurled**	**Time to breakdown, $t_{50\%}$ (ns)**	**Air or knurled**
HDPE	$110.6\binom{+5.8}{-10.4}$	$466.3\binom{+285.5}{-285.3}$	Air	$137.7\binom{+6.2}{-11.5}$	$354.5\binom{+252}{-231.2}$	Air
Polyetherimide	$158.2\binom{+5.3}{-10.2}$	$315.9\binom{+155.3}{-175.2}$	Knurled*	$171.1\binom{+7.3}{-13.5}$	$322.8\binom{+208.4}{-204.5}$	Knurled*
Polyoxymethylene	$143.1\binom{+14.9}{-25.5}$	$260.8\binom{+64.9}{-92.1}$	Air*	$103.7\binom{+2.6}{-5.1}$	$455.9\binom{+188}{-230.1}$	Air
Air	$158.2\binom{+6.3}{-11.9}$	$426.1\binom{+162.9}{-202.9}$	-	$165.6\binom{+8.9}{-16}$	$382.9\binom{+101}{-142}$	-

Table AP2u. - Comparison of air-solid insulation arrangements at <10% RH and −0.5, 0 and 0.5 bar gauge pressure. Outcomes are either: 'Smooth', indicating that the material with a smooth machined surface has the better performance, or 'knurled', meaning that the material with a knurled surface finish has the better performance; outcomes with '*' refer to overlapping error bars between the compared test results. The values listed are V_{50} flashover voltages for each arrangement, with the ± values shown representing the error bars for ~95.4% spread of data for each distribution.

		Average breakdown voltage (kV)			**Average breakdown voltage (kV)**		
Pressure	**Material**	**Negative polarity smooth**	**Negative polarity knurled**	**Outcome**	**Positive polarity smooth**	**Positive polarity knurled**	**Outcome**
−0.5	HDPE	$136.5\binom{+13.7}{-23.9}$	$87.1\binom{+11.1}{-18.3}$	Smooth	$85.6\binom{+13.1}{-20.8}$	$81.9\binom{+9.2}{-14.8}$	Smooth*
	Polyetherimide	$125.1\binom{+11.7}{-20.6}$	$102.3\binom{+10.5}{-18.3}$	Smooth*	$82.4\binom{+8.7}{-14.6}$	$105.6\binom{+25.9}{-36.6}$	Knurled*
	Polyoxymethylene	$114.6\binom{+10.8}{-18.8}$	$87.8\binom{+9.3}{-15.7}$	Smooth*	$77.9\binom{+8.5}{-14.3}$	$82.3\binom{+17}{-25.4}$	Knurled*
0	HDPE	$154.6\binom{+18.7}{-31.2}$	$136.3\binom{+11.4}{-19.8}$	Smooth*	$125.6\binom{+12.3}{-21.6}$	$148.3\binom{+17.9}{-29.7}$	Knurled*
	Polyetherimide	$151.8\binom{+14.4}{-25.3}$	$131.7\binom{+10.3}{-18.4}$	Smooth*	$138.2\binom{+10.7}{-19}$	$175.9\binom{+35.1}{-51.5}$	Knurled*
	Polyoxymethylene	$144.2\binom{+12.9}{-23.3}$	$114.6\binom{+5}{-9.6}$	Smooth	$127.8\binom{+9.8}{-17.5}$	$133.6\binom{+29.5}{-42.1}$	Knurled*
0.5	HDPE	$201.9\binom{+12.7}{-23.5}$	$157.4\binom{+9.7}{-17.7}$	Smooth	$156.5\binom{+5.5}{-10.6}$	$213.9\binom{+17.8}{-29.7}$	Knurled
	Polyetherimide	$198.7\binom{+10.3}{-19}$	$166\binom{+7.8}{-14.5}$	Smooth	$162.2\binom{+10.8}{-18.8}$	$228.6\binom{+14.8}{-26.3}$	Knurled
	Polyoxymethylene	$179.9\binom{+9.9}{-17.5}$	$165.7\binom{+6.2}{-11.8}$	Smooth*	$152.9\binom{+5.5}{-10.2}$	$202.8\binom{+6.8}{-12.5}$	Knurled

Table AP2v. - Comparison of air-solid insulation arrangements at ~50% RH and −0.5, 0 and 0.5 bar gauge pressure. Outcomes are either: 'Smooth', indicating that the material with a smooth machined surface has the better performance, or 'knurled', meaning that the material with a knurled surface finish has the better performance; outcomes with '*' refer to overlapping error bars between the compared test results. The values listed are V_{50} flashover voltages for each arrangement, with the ± values shown representing the error bars for ~95.4% spread of data for each distribution.

		Average breakdown voltage (kV)			Average breakdown voltage (kV)		
Pressure	**Material**	**Negative polarity smooth**	**Negative polarity knurled**	**Outcome**	**Positive polarity smooth**	**Positive polarity knurled**	**Outcome**
−0.5	HDPE	$106.9^{+20.7}_{-32.3}$	$69.1^{+5.9}_{-10.4}$	Smooth *	$81.7^{+10.3}_{-16.8}$	$83.4^{+6.1}_{-10.7}$	Knurled *
	Polyetherimide	$90.2^{+43.1}_{-48.7}$	$83.8^{+19.2}_{-28.2}$	Smooth *	$86.1^{+9}_{-15.2}$	$84.1^{+8.3}_{-14.4}$	Smooth *
	Polyoxymethylene	$83.2^{+20.2}_{-29}$	$85^{+34.3}_{-41.1}$	Knurled *	$81.3^{+9.4}_{-15.7}$	$85.2^{+12.2}_{-20}$	Knurled *
0	HDPE	$145.3^{+9.5}_{-17.2}$	$120.5^{+6}_{-11.3}$	Smooth *	$140.2^{+18.1}_{-29.8}$	$135.8^{+10.8}_{-19.3}$	Smooth *
	Polyetherimide	$119.6^{+5.4}_{-10.2}$	$139.9^{+26}_{-40.2}$	Knurled *	$134^{+10.8}_{-19}$	$139^{+12.6}_{-21.8}$	Knurled *
	Polyoxymethylene	$118.5^{+9.2}_{-16.3}$	$120.8^{+5.2}_{-9.8}$	Knurled *	$139.1^{+7.2}_{-13.2}$	$145.7^{+14}_{-24.6}$	Knurled *
0.5	HDPE	$190.5^{+13.5}_{-23.8}$	$170.6^{+11.5}_{-20.7}$	Smooth *	$175.8^{+6.5}_{-12.3}$	$192.9^{+20.7}_{-35.8}$	Knurled *
	Polyetherimide	$165.7^{+5.8}_{-11}$	$174.4^{+7.2}_{-13.5}$	Knurled *	$167.9^{+7}_{-12.9}$	$215.2^{+31}_{-50.3}$	Knurled *
	Polyoxymethylene	$157.8^{+5.6}_{-10.7}$	$170.3^{+8.9}_{-16.8}$	Knurled *	$181.1^{+8.3}_{-15.5}$	$206^{+14.8}_{-25.7}$	Knurled *

Table AP2w. - Comparison of air-solid insulation arrangements at >90% RH and −0.5, 0 and 0.5 bar gauge pressure. Outcomes are either: 'Smooth', indicating that the material with a smooth machined surface has the better performance, or 'knurled', meaning that the material with a knurled surface finish has the better performance; outcomes with '*' refer to overlapping error bars between the compared test results. The values listed are V_{50} flashover voltages for each arrangement, with the ± values shown representing the error bars for ~95.4% spread of data for each distribution.

		Average breakdown voltage (kV)			Average breakdown voltage (kV)		
Pressure	**Material**	**Negative polarity smooth**	**Negative polarity knurled**	**Outcome**	**Positive polarity smooth**	**Positive polarity knurled**	**Outcome**
−0.5	HDPE	$66^{+2.6}_{-4.8}$	$53.8^{+6.7}_{-11.2}$	Smooth	$62^{+2.2}_{-5.1}$	$64.8^{+2.4}_{-4.7}$	Knurled*
	Polyetherimide	$62.1^{+3.9}_{-6.9}$	$64.9^{+2.7}_{-4.9}$	Knurled*	$74.7^{+3.6}_{-6.7}$	$72.5^{+3.8}_{-7}$	Smooth*
	Polyoxymethylene	$54.4^{+6.5}_{-10.8}$	$63.3^{+11.6}_{-18}$	Knurled*	$68.1^{+2.2}_{-4}$	$48.1^{+1.2}_{-2.1}$	Smooth
0	HDPE	$109.8^{+7}_{-12.9}$	$84.1^{+4.4}_{-8.2}$	Smooth	$102.9^{+9.5}_{-16.7}$	$98.2^{+7.3}_{-13}$	Smooth*
	Polyetherimide	$77.7^{+5.8}_{-10.5}$	$119.7^{+4.6}_{-8.7}$	Knurled	$125.7^{+4.4}_{-8.3}$	$123.9^{+6}_{-11.2}$	Smooth*
	Polyoxymethylene	$69.4^{+8.2}_{-14.1}$	$106.9^{+2.5}_{-4.8}$	Knurled	$115.9^{+4.1}_{-7.6}$	$79.3^{+2}_{-3.8}$	Smooth
0.5	HDPE	$125.1^{+7.6}_{-13.9}$	$110.6^{+5.8}_{-10.4}$	Smooth	$130.5^{+6.6}_{-12.2}$	$137.7^{+6.2}_{-11.5}$	Knurled*
	Polyetherimide	$104.4^{+15.2}_{-24.8}$	$158.2^{+5.3}_{-10.2}$	Knurled	$169.1^{+6.9}_{-12.8}$	$171.1^{+7.3}_{-13.5}$	Knurled*
	Polyoxymethylene	$90.5^{+5.6}_{-10.2}$	$143.1^{+14.9}_{-25.5}$	Knurled	$158.5^{+5.3}_{-9.8}$	$103.7^{+2.6}_{-5.1}$	Smooth